OTTO VON GUERICKE
UNIVERSITÄT
MAGDEBURG

INTENSIFICATION OF THE SELECTIVE PROPANE DEHYDROGENATION IN INTEGRATED MEMBRANE REACTORS

Dissertation

zur Erlangung des akademischen Grades

Doktoringenieur
(Dr.-Ing.)

von
ANDREAS BRUNE
geboren am 06.10.1990 in Höxter

genehmigt durch die Fakultät für Verfahrens- und Systemtechnik der
Otto-von-Guericke-Universität Magdeburg

Promotionskommission:	Prof. Dr. rer. nat. Helmut Weiß	(Vorsitz)
	Prof. Dr.-Ing. Christof Hamel	(Gutachter)
	Prof. Dr.-Ing. Andreas Seidel-Morgenstern	(Gutachter)
	Prof. Dr.-Ing. Fausto Gallucci	(Gutachter)

Eingereicht am	25.08.2023
Promotionskolloquium am	19.01.2024

Abstract

The objective of this work is to investigate integrated membrane reactor concepts to improve the performance of processes for selective dehydrogenation of propane. Increasing the productivity of chemical processes can help to make the chemical industry more sustainable in times of global warming and the transition to renewable resources. In the field of process engineering, the means of process intensification can be used. In this work, in particular membranes are used for the control of local concentration profiles by reactant dosing and temperature control in heat-integrated apparatuses. The dehydrogenation of propane to propene was chosen as an industrially relevant model reaction. Highly selective endothermic thermal dehydrogenation (TDH), in which rapid catalyst deactivation is observed, is already in industrial use. In contrast, exothermic oxidative dehydrogenation (ODH) shows no deactivation but offers significantly lower selectivity. The different reaction enthalpies can be exploited for heat integration when both reactions are combined in one apparatus. A VO_x/Al_2O_3 catalyst is suitable to catalyze both reactions and is therefore used in this work.

In order to enable a model-based evaluation, laboratory experiments were carried out. Experiments were conducted in a laboratory fixed-bed reactor for the parameterization of the kinetic models of the main and side reactions. Regeneration and coking were specifically investigated in a TGA setup under precisely defined conditions. The main and side reactions could be described by a power law approach. Several monolayer multilayer coke-growth models were systematically evaluated using the Akaike Information Criterion. The deactivation behavior was described by three approaches of different complexity.

Based on this modeling, the complete cycle of reaction and regeneration phases in a tubular reactor was simulated using a 1D model. It was shown that the space-time yield of the process can be optimized by a specific choice of production and regeneration times. An incomplete regeneration proves to be advantageous. The utilization of 2D models allowed the investigation of complex transient axial and radial concentration profiles influenced by radial membrane dosing in integrated reactor concepts. Especially in the range of low oxygen concentrations, the simulations revealed that the use of a heat-integrated membrane reactor (PBMRint) provides better results than comparable fixed-bed reactors or membrane reactors. In transient simulations, the estimation of cycle times for an efficient reactor operation considering the complete process was possible. It became clear that distinct temperature and concentration profiles are formed, which can only be represented in elaborate 2D simulations.

Finally, the knowledge gained from the laboratory experiments and simulations was evaluated using a scale-up to pilot scale. In a step-wise increase in complexity, first a fixed-bed reactor cascade, and later a membrane reactor cascade with and without flow reversal for operando regeneration were investigated. Ultimately, a heat-integrated membrane reactor (PBMRint) was experimentally realized. The experimental studies in pilot scale confirmed the trends found in the simulations. In particular, the use of membranes increased the reactor performance. Flow reversal proved to be beneficial under certain circumstances.

Kurzfassung

Ziel dieser Arbeit ist die Untersuchung integrierter Membranreaktorkonzepte zur Steigerung der Leistung von Verfahren zur selektiven Dehydrierung von Propan. Die Steigerung der Produktivität von chemischen Prozessen kann dazu beitragen, die chemische Industrie in Zeiten der globalen Erwärmung und des Übergangs zu erneuerbaren Ressourcen nachhaltiger zu gestalten. Im Bereich der Verfahrenstechnik kann hierbei auf die Mittel der Prozessintensivierung zurückgegriffen werden. In dieser Arbeit werden insbesondere Membranen zur Steuerung von lokalen Konzentrationsprofilen durch Reaktandosierung und Temperaturregelung in wärmeintegrierten Apparaten eingesetzt. Als industriell relevante Modellreaktion wurde die Dehydrierung von Propan zu Propen gewählt. Bereits industriell angewendet wird die hochselektive endotherme thermische Dehydrierung (TDH), bei der eine schnelle Katalysatordeaktivierung zu beobachten ist. Die exotherme oxidative Dehydrierung (ODH) zeigt im Gegensatz dazu keine Deaktivierung bei deutlich geringerer Selektivität. Die unterschiedlichen Reaktionsenthalpien können bei der Kombination beider Reaktionen in einem Apparat im Sinne einer Wärmeintegration genutzt werden. Ein $\mathrm{VO_x/Al_2O_3}$ Katalysator ist in der Lage beide Reaktionen zu katalysieren und findet deshalb im Rahmen dieser Arbeit Anwendung.

Um eine modellgestützte Bewertung zu ermöglichen, wurden Laborversuche durchgeführt. Für die Parametrisierung der kinetischen Modelle der Haupt- und Nebenreaktionen wurden Versuche im Festbettreaktor realisiert. Regeneration und Verkokung wurden in einem TGA Aufbau unter präzise definierten Bedingungen gezielt untersucht. Die Haupt- und Nebenreaktionen konnten durch einen Potenzansatz beschrieben werden. Beim Koksaufbau wurden mehrere Monolayer-Multilayer-Coke-Growth-Modelle systematisch anhand des Akaike Informationskriteriums bewertet. Das Deaktivierungsverhalten wurde mit Hilfe dreier Ansätze unterschiedlicher Komplexität beschrieben.

Aufbauend auf dieser Modellbildung wurde der komplette Zyklus aus Reaktions- und Regenerationsphasen in einem Rohrreaktor im 1D-Modell simuliert. Es konnte gezeigt werden, dass sich die Raum-Zeit-Ausbeute des Prozesses durch gezielte Wahl der Produktions- und Regenerationszeiten optimieren lässt. Eine unvollständige Regeneration stellt sich als vorteilhaft heraus. In 2D-Modellen war es möglich, komplexere, transiente axiale und radiale Konzentrationsprofile zu untersuchen, die durch eine radiale membrangestützte Dosierung in integrierten Reaktorkonzepten verursacht werden. Insbesondere im Bereich niedriger Sauerstoffkonzentrationen zeigten die Simulationen, dass der Einsatz eines wärmeintegrierten Membranreaktors (PBMRint) bessere Ergebnisse liefert als bisher untersuchte Festbettreaktoren oder Membranreaktoren. In transienten Simulationen war die Abschätzung von Zykluszeiten für einen effizienten Reaktorbetrieb unter Berücksichtigung des Gesamtprozesses möglich. Es wurde deutlich, dass sich ausgeprägte Temperatur und Konzentrationsprofile ausbilden, die ausschließlich in aufwändigen 2D-Simulationen abgebildet werden können.

Die aus Laborversuchen und Simulationen gewonnenen Erkenntnisse wurden anschließend für die Maßstabsvergrößerung in den Pilotmaßstab eingesetzt. In einer schrittweisen Steigerung der Komplexität wurde zuerst eine Festbettreaktorkaskade, später eine Membranreaktorkaskade mit und ohne Strömungsumkehr zur operando Regeneration untersucht. Abschließend wurde ein wärmeintegrierter Membranreaktor (PBMRint) experimentell realsiert. Die Pilotversuche bestätigten die in den Simulationen gefundenen Trends. Insbesondere die Verwendung von Membranen steigerte die Reaktorleistung. Die Strömungsumkehr erwies sich unter bestimmten Umständen als vorteilhaft.

Preface

The main results presented in this dissertation have been acquired in the context of the DFG project *Control and intensification of chemical reactions due to periodically operating distributors* conducted by the Chair of Chemical Process Engineering at Otto von Guericke University Magdeburg and the Chair of Process Engineering at Anhalt University of Applied Sciences between 2018 and 2023. Parts of this thesis have been published in scientific journals. The connections between results in this thesis and journal papers are disclosed in the following list.

- Preliminary results proving the feasibility of membrane reactor concepts have been published in a paper by Brune, Wolff, et al. 2019. Due to a change of the catalyst dedicated to thermal dehydrogenation (TDH) from a chromium to a vanadium oxide based active mass the results of this paper are not directly presented in this thesis. Nevertheless, these results provided a proof of concepts for the reactor concepts studied in more detail in this thesis. The paper is therefore also listed here.

- Chapter 3 presents a systematic model discrimination and parameter estimation in order to parametrize the kinetics of the model reaction. Results of the parameter estimation for main and side reactions (Section 3.1) as well as coking and regeneration of the catalyst (Section 3.2) are presented by Brune, Seidel-Morgenstern, et al. 2020. Different coke based and phenomenological deactivation models have been established and published by Brune, Geschke, et al. 2021. A time based approach is presented by Walter, Brune, Seidel-Morgenstern, et al. 2021.

- The mathematical models have been used in Chapter 4 for reactor simulations on different levels of complexity. The 1D simulations presented in Section 4.1 have been published by Brune, Geschke, et al. 2021. The 2D reactor simulations (Section 4.2) are largely based on the cooperation with Jan Paul Walter (Walter, Brune, Seidel–Morgenstern, et al. 2021; Walter, Brune, Seidel-Morgenstern, et al. 2021).

The use of results obtained by the mentioned cooperation partners has been marked at the relevant places in this thesis. This refers in particular to the results of the 2D simulations in Chapter 4.

Journal articles containing results presented in this dissertation

- A. Brune, T. Wolff, A. Seidel-Morgenstern, C. Hamel (2019). “Analysis of Membrane Reactors for Integrated Coupling of Oxidative and Thermal Dehydrogenation of Propane”. In: *Chemie Ingenieur Technik* 56.2, p. 251

- A. Brune, A. Seidel-Morgenstern, C. Hamel (2020). “Analysis and Model-Based

Description of the Total Process of Periodic Deactivation and Regeneration of a VOx Catalyst for Selective Dehydrogenation of Propane". In: *Catalysts* 10.12, p. 1374

- A. Brune, A. Geschke, A. Seidel-Morgenstern, C. Hamel (2021). "Modeling and Simulation of Catalyst Deactivation and Regeneration Cycles for Propane Dehydrogenation - Comparison of Different Modeling Approaches". In: *Chemical Engineering and Processing: Process Intensification*, p. 108689

- J. P. Walter, A. Brune, A. Seidel–Morgenstern, C. Hamel (2021). "Model–based Analysis of Fixed–bed and Membrane Reactors of Various Scale". In: *Chemie Ingenieur Technik* 93.5, pp. 819–824

- J. P. Walter, A. Brune, A. Seidel-Morgenstern, C. Hamel (2021). "Process Intensification of the Propane Dehydrogenation Considering Coke Formation, Catalyst Deactivation and Regeneration—Transient Modelling and Analysis of a Heat-Integrated Membrane Reactor". In: *Catalysts* 11.9, p. 1056

Contents

Abstract i

Kurzfassung iii

Preface v

1 Introduction 3

2 Theoretical Background 7

2.1 Propane Dehydrogenation 7
  2.1.1 Steam Cracking 7
  2.1.2 On-purpose Dehydrogenation Processes 8
  2.1.3 Catalysts for Thermal Propane Dehydrogenation 12
  2.1.4 Oxidative Propane Dehydrogenation 13
2.2 Process Intensification 15
  2.2.1 Membrane Reactors 17
  2.2.2 Heat-Integrated Fixed Bed Reactors 23
2.3 Modeling 26
  2.3.1 Continuum Models 28
  2.3.2 Reaction Kinetics 36
  2.3.3 Coke Formation and Catalyst Deactivation 41
  2.3.4 Catalyst Regeneration 45
2.4 Interim Conclusion 47

3 Experimental Investigation and Parameter Estimation 49

3.1 Kinetics of Main and Side Reactions 49
3.2 Coke Formation and Catalyst Regeneration 53
  3.2.1 Coke Formation 54
  3.2.2 Catalyst Regeneration 66
  3.2.3 Model Validation 72
3.3 Catalyst Deactivation 77
  3.3.1 Experimental Results 78
  3.3.2 Phenomenological Approach for Deactivation 79
  3.3.3 Coke-Based Approach for Deactivation 83
  3.3.4 Time Dependent Approach for Catalyst Deactivation 92
3.4 Interim Conclusion 94

4 Simulation and Process Optimization 97

4.1 1D Simulations: Optimization of the Overall Production Process 97
4.2 2D Simulations 103
  4.2.1 Reactor Models 103
  4.2.2 2D Modeling Procedure 105

4.2.3 Steady State 2D Simulations . . . 107
4.2.4 Transient 2D Simulations . . . 112
4.3 Interim Conclusion . . . 115

5 Reactor Cascades and Integrated Reactor Concepts in Pilot Scale 117
5.1 Experimental Equipment and Operation Modes . . . 117
5.1.1 Experimental Equipment . . . 117
5.1.2 Operation Modes . . . 120
5.2 Scale-up and Comparison to Lab Scale Experiments . . . 123
5.3 Fixed Bed Reactor Cascade With and Without Membranes . . . 124
5.3.1 Fixed Bed Reactor Cascade With and Without Flow Reversal . . . 125
5.3.2 Membrane Reactor Cascade With and Without Flow Reversal . . . 130
5.4 Integrated Membrane Reactor . . . 142
5.5 Interim Conclusion . . . 147

6 Membrane Reactors in Extractor Configuration 149
6.1 Experimental Setup and Membrane Characterization . . . 149
6.2 Catalyst Characterization at Elevated Pressures and Reaction Tests With Membrane . . . 152
6.3 Interim Conclusion . . . 155

7 Conclusion and Outlook 157
7.1 Outlook . . . 159
7.2 Concluding Remarks . . . 159

Bibliography 161

A Appendix to Chapter 2 177
A.1 Details on the Momentum Balance Equations . . . 177
A.2 Heat Transfer and Heat Conduction Models . . . 177
A.2.1 The $\lambda(r)$ Model . . . 178
A.2.2 The α_w Model . . . 181

B Appendix to Chapter 3 183
B.1 Kinetic Investigation of the Reaction Network . . . 183
B.2 Akaike Information Criterion . . . 184
B.3 Bootstrapping of Confidence Intervals . . . 188
B.4 Periodic Experiments and Validation . . . 191
B.5 Experimental Results: Deactivation Experiments . . . 193
B.6 Phenomenological Approach . . . 197
B.7 Coke Based Approach . . . 198
B.7.1 Discretization . . . 198
B.7.2 Results . . . 199
B.8 Optimization . . . 201

C Appendix to Chapter 5 203
C.1 P&ID and Engineering Drawings of Pilot Scale Reactors and Pilot Plant . . 204
C.2 1D Simulations of Reactor Cascades in Pilot Scale . . . 208
C.2.1 FBR-FBR Reactor Cascade . . . 208
C.2.2 PBMR-FBR Reactor Cascade . . . 209

C.3 Experimental Results of Pilot Scale Experiments . . . 212
  C.3.1 Experiments Without Membrane Dosing . . . 212
  C.3.2 Experiments With Membrane Dosing . . . 214
  C.3.3 Experiments With Additional Membrane Dosing of CO_2 . . . 217
  C.3.4 Comparison of Experiments With and Without Membrane Dosing . 220
  C.3.5 Experiments with Integrated Packed Bed Membrane Reactor (PBM-Rint) . . . 224

D Appendix to Chapter 6 225
D.1 Pd-Ag Membrane Characterization . . . 225
D.2 Results of Reaction Tests With Pd-Ag Membrane . . . 226

1 Introduction

> Sustainable development is development that meets the needs of the present without compromising the ability of future generations to meet their own needs.
>
> ---
>
> OUR COMMON FUTURE
> *Report of the World Commission on Environment and Development (1987)*

Against the backdrop of the current global challenges, the concept of sustainability is commonplace in political and social discussions. Stakeholders generally agree that future developments must be *sustainable*. The term *sustainability* was first used in its current, broad, global context in the publication "Limits of Growth" by the Club of Rome in 1974 (Meadows et al. 1974). One of the main conclusions of the report is, that "the limits to growth on this planet will be reached sometime within the next one hundred years" and that it is still possible to "establish a condition of ecological and economic stability that is *sustainable* far into future". Here, the ecological and economic dimensions of sustainability are implied. In the 1972s issue of "The Ecologist" titled "A blueprint for survival", a social dimension of sustainability is addressed by the authors (Goldsmith and Allen 1972), who understood their work as a "proposal for creating a sustainable society". This approach of three dimensions of sustainability (see Fig 1.1) is nowadays commonly accepted in literature (Purvis et al. 2019) and has been adopted by the united nations (UN) in their resolution in 2015 titled "Transforming our World: the 2030 Agenda for Sustainable Development" (United Nations 2015a). In that resolution 17 Sustainable Developement Goals (SDG) are defined that are "integrated and indivisible and balance the three dimensions of sustainability". In order to achieve these goals, national governments have implemented their own strategies as for example the "German Sustainable Development Strategy 2021" by the German federal government (German Federal Government 2021).

The SDGs are closely related to the challenges connected to climate change, most prominent in SDG 13 that demands to "take urgent action to combat climate change and its impact". Other SDGs are also impacted indirectly, e.g. SDG 1 that aims to "end poverty in all its form everywhere", SDG 2 that demands to "end hunger, achieve food security" or SDG 6, that is to "ensure availability and sustainable management of water". These goals can be compromised by severe climate events e.g. droughts on the one hand and heavy rain on the other hand, as reported regularly by the Intergovernmental Panel on Climate change (IPCC) (Masson-Delmotte et al. 2021). The most significant contribution to human-induced climate change is the emission of greenhouse gases. With the Paris Climate Agreement, large parts of the international community committed themselves for the first time to limit climate change to below two degrees (Article 2, Paragraph 1a) (United Nations 2015b). That required individual parties to "prepare, communicate and

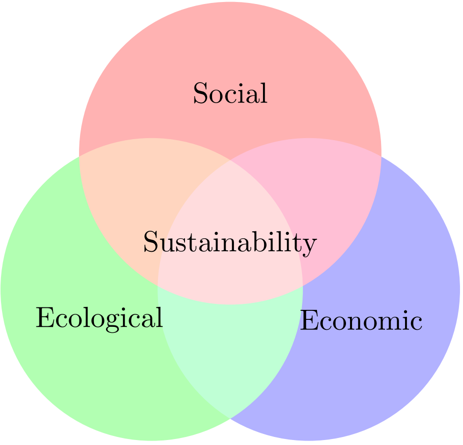

Figure 1.1: The three dimensions of sustainability (adapted from Purvis et al. 2019).

maintain successive nationally determined contributions" (NDCs) to that goal (Article 4, Paragraph 2). The parties are encouraged to adjust their NDCs "with a view to enhancing its level of ambition" (Articel 4, Paragraph 11).

The EU submitted the latest NDC for all member states in 2020. Its specific goals are also outlined in the European Green Deal (European Commission 2019). The EU aims to reduce the emission of green house gases (GHG) by 55 % until 2030 compared to the levels in 1990. This is accompanied by a reduction of the overall energy consumption of 36 %. The long term goal is to become the first climate neutral continent with net zero GHG emissions by 2050. These goals are also added to the European Climate Law (European Parliament and Council 2021). On national level the German federal government passed the National Climate Protection Plan 2050 (Bundesministerium für Umwelt, Naturschutz, Bau und Reaktorsicherheit 2016) to outline the the reduction steps required for meeting the purposes of the EU Green Deal and the Paris Agreement (Deutscher Bundestag 2019). Specific reduction goals for different sectors (Energy industry, buildings, traffic, agriculture, waste management and others) have later been defined in the first Federal Climate Protection Law (Bundes-Klimaschutzgesetz, KSG) and later been tightened with the first Act to Amend the Federal Climate Protection Law (Deutscher Bundestag 2021). The law now requires a reduction of the GHG emissions of 65 % until 2030 and 88 % until 2040 compared to 1990. Zero net emissions of GHG have to be achieved by 2045, five years earlier than planed by the UN and the EU. According to the law, German industry has to realize a reduction of 37 % compared to the emission level of 2020 which means 68 million tons CO_2 equivalent. These ambitious goals will not be met according to the Council of Experts on Climate Change (Expertenrat für Klimafragen, ERK) with the measures that are in place today. In its biennial report the ERK even reported increasing emissions of GHG by industry in Germany in the time period from 2010 until 2019.

Other stakeholders from industry also addressed emission reduction and sustainability against the backdrop of national and international laws. In chemistry, *Green Chemistry* approaches are increasingly being pursued. The principles of *Green Chemistry* aim for harm reduction, efficiency and sustainability on a fundamental level (atomic efficiency of chemical reactions, green solvents, etc.) (Anastas and Eghbali 2010). An industrial per-

spective on the topic is given by Dechema and VCI, who published a roadmap for emission reduction of the German chemical industry, where technologies and investment costs for different scenarios of GHG reduction are described, with net GHG neutrality until 2050 as most the ambitious scenario (Geres et al. 2019). To achieve GHG neutrality by 2050 the electricity consumption of the chemical industry in Germany will fourteen-fold to a total of 684 TWh/a according to their calculations. In 2018 the gross consumption of Germany was 595 TWh/a and the net electricity generation was 611 TWh/a with 216 TWh/a from renewable resources (Prognos et al. 2021). According to forecasts, the chemical industry in 2050 will need more electricity than Germany as a total in 2018. This electricity has to be produced from renewables, since otherwise there will be an emission of GHG gases connected to the burning of fossil fuels. A study commissioned by the Climate Neutrality Foundation about the feasibility of the energy transition projected a total industrial electricity consumption of 317 TWh/a in 2045, which includes not only chemical industry but also other every other energy demanding industry. The total consumption of electricity in Germany is extrapolated to be roughly 1017 TWh/a (Prognos et al. 2021). This example illustrates, that there is a large discrepancy between the energy needed by chemical industry and the amount that will be prospectively available to meet the needs of a sustainable economy and to be able to limit the global warming according to the Paris agreement.
There is a need for efficient process technology with the potential to decrease the energy needs of chemical industry. A prominent part of process engineering dealing with more efficient solutions by design of integrated concepts for reaction and separation is *Process Intensification* (PI) (A. Stankiewicz and J. A. Moulijn 2002). This work aims to contribute to the field of PI by studying reactor concepts for the on-purpose dehydrogenation of propane to propene.

The product propene of the chosen model reaction is one of the most important building blocks in chemical industry, mainly used to produce polypropylene (PP). The market share of PP is growing, since it can replace other plastics e.g. polyethylene (PE) in film and packaging applications and is able to be used as a replacement for technical thermoplastics, e.g. acrylonitrile butadiene styrene (ABS) and polyamide (PA) (Koltzenburg 2014). The production volume of polypropylene is predicted to increase from 56 million tons in 2018 to 88 million tons in 2026 (Tiseo 2021). Besides that it can be use for the production of propylene oxide or acrylonitrile (Zimmermann 2010). The extraction of shale gas has led to profound changes in the chemical industry (Siirola 2014). The abundance of lighter feedstock for crackers and a thereby shifted product spectrum towards ethene gave rise to on-purpose technologies in propene production (Amghizar et al. 2017). Tackling the problems of these on purpose methods is therefore relevant from an industrial perspective. Part of the efforts within the framework of the EU Green Deal is the development of a circular economy (European Commission 2020). Within this framework, recycling shares in the most important products, including packaging, are to become mandatory. This also appears to be reasonable against the background of the environmental impact of the extraction of fossil raw materials (European Commission 2019). Additionally, there is a focus on promoting the use of bio-based and biodegradable plastics in areas where their ecological benefits are evident. Since polypropylene is the main use of propene, it can be assumed that the direct dehydrogenation of propane is only a transitional technology on the way to fully recycled feedstock. Nevertheless, the methods developed by studying this model reaction can be used in the future to intensify other reactions. Also, thermal integration of an exothermic and an endothermic reaction as presented in this work can be applied in other contexts. The problem of catalyst deactivation and regeneration by coke burn-up, which has been discussed in detail, can be observed in other relevant reactions. Furthermore, a systematic scale-up to pilot scale is performed, the methodology of which can be applied to other reactions as well.

Experiment and theory are often regarded as classic pillars of science. Both constantly interact with each other. New experiments lead to new experimental approaches and vice versa (Weinzierl 2021). During the last decade a third pillar gained more and more attention (Pitac 2005). Some experiments can not be done for various reasons e.g. for being expensive or time intensive. On the theoretical side of science, some equations can not be solved on a blackboard because of the high complexity. Computer simulations are therefore regarded as a third pillar of science and can help to overcome these challenges.

Following this classification of the three pillars, this thesis is divided into the following parts:

- A first part that describes the necessary *theoretical* basics (Chapter 2),
- an experimental part to fit the presented models to *experimental* values (Chapter 3),
- a part that applies these models in *simulations* to predict promising operating parameters in scale-up (Chapter 4),
- and a last part deals with the *experimental* investigation of scale-up based on the previous experiments and simulations (Chapter 5 and 6).

2 Theoretical Background

> A good answer to a poor question [...] is little better than a poor answer to a poor question.
>
> Model Selection and Multimodel Inference
> *K. P. Burnham, D. R. Anderson*[1]

This chapter aims to provide the theoretical background on state of the art of propene production and on-purpose propane dehydrogenation (Section 2.1) but also recent developments and advances in the field of Process Intensification (PI) (Section 2.2). In that way, the relevance of the model reaction can be illustrated and the innovative reactor concepts evaluated later in this work are put into context. Membrane reactor concepts (Section 2.2.1) and heat integrated reactor concepts with and without flow reversal (Section 2.2.2) will be especially emphasized. Later, the balance equations necessary for reactor modeling and simulation will be introduced (Section 2.3).

2.1 Propane Dehydrogenation

2.1.1 Steam Cracking

The leading technology in olefin and therefore propene production today is steam cracking (SC) (Zimmermann and Walzl 2010). In steam cracking, different hydrocarbon feedstocks are cracked and dehydrogenated to form mainly ethene. Propene and other olefins are produced as by-products. The feedstock that is used for the process depends on the market situation and availability (Amghizar et al. 2017). Due to the shale gas abundance in the USA feedstock has shifted to shorter hydrocarbons which in consequence shifts the product spectrum towards ethene. This gives rise to on-purpose production processes for the production of propene.

Steam cracking is performed without catalyst and follows a radical mechanism (Zimmermann and Walzl 2010). Reaction temperatures are usually between 750 °C and 900 °C depending on the feed (Staszak et al. 2020). Shorter hydrocarbons require higher temperatures. Residence times in the cracking furnace are very short (0.08 s to 0.25 s). Longer residence times would support coking of the tubes due to the unsaturated compounds that are formed during the process. Steam is added to the reaction mixture to reduce the partial pressure of hydrocarbons, suppress coking and to deliver the heat necessary for the endothermic reaction. Due to coke depositions the furnace has to be decoked every 3 to 4 months.

---

[1] Burnham and Anderson 2004.

The steam cracking process needs to be constantly modified and the flexibility has to be increased to meet current market developments. One challenge is changing feedstocks, that can range from liquefied gas to vacuum distillate. There are approaches to use crude oil instead of naphta as a feed to reduce refining costs. Heating of the cracking furnace is realized by gas burners to be able to reach the required temperatures. To reduce the fossil fuel consumption, industry is currently testing electrically heated steam cracking processes, that will reduce the CO_2 emissions by 90 % according to industry (BASF SE and SABIC, Linde 2022).

According to the trends in fossil feedstocks and the growing worldwide demand for propene the importance of on-purpose production methods for propene is assumed to increase (Amghizar et al. 2017; Tiseo 2021). Catalytic propane dehydrogenation processes to produce propene are already well established in industry. The most important dehydrogenation processes will be described in the next chapter to present challenges and identify research needs in the context of these technologies.

2.1.2 On-purpose Dehydrogenation Processes

Today's industrial processes for on-purpose propane dehydrogenation are based on the highly endothermic thermal dehydrogenation reaction ($\Delta_R H = 124\,\mathrm{kJ\,mol^{-1}}$):

$$\mathrm{C_3H_8} \rightleftharpoons \mathrm{C_3H_6} + \mathrm{H_2} \tag{2.1}$$

The catalysts used in these processes provide a high selectivity but need to be regenerated regularly because of rapid deactivation due to coking. Details on catalysts are given in Section 2.1.3. Furthermore, the thermal dehydrogenation (TDH) is limited by chemical equilibrium. Efficient H_2 conversion or removal are promising to shift the equilibrium. Examples for enhancing this reaction using membranes will be presented later (see Section 2.2.1).

An alternative reaction is the oxidative dehydrogenation (ODH, Eq. (2.2)).

$$\mathrm{C_3H_8} + \frac{1}{2}\,\mathrm{O_2} \longrightarrow \mathrm{C_3H_6} + \mathrm{H_2O} \tag{2.2}$$

The ODH is not limited by chemical equilibrium. It is an exothermic reaction ($\Delta_R H = -118\,\mathrm{kJ\,mol^{-1}}$) that proceeds at lower temperatures than the TDH and in the presence of oxygen. That prevents coking, whereas the selectivity is significantly lower due to unwanted side reactions like total and partial oxidations. Details on the ODH reaction are part of Section 2.1.4.

A detailed reaction network including ODH, TDH and side reactions based on current literature will be presented in Section 2.3.2.

CATOFIN process One of the most common commercialized dehydrogenation processes is the CATOFIN process licensed by Lummus Technology (Lummus Technology 2022). The process stems from the Houdry process which was originally designed for catalytic cracking in refineries and has been commercialized in the 1940s (Staszak et al. 2020). The CATOFIN process utilizes 5 to 8 reactors in parallel that are used in cyclic operation. A typical cycle consists of a production and a regeneration phase (7 min to 15 min each) as illustrated in Fig. 2.1. Dehydrogenation takes place during the production process on a Cr_2O_3-catalyst on Al_2O_3 support. The regeneration phase consists of purging the reactor with steam, reheating of the catalyst bed and evacuation of the reactor and reduction of the catalyst with hydrocarbons or hydrogen. The energy needed for the endothermic dehydrogenation reaction is stored by the catalytic bed. The temperature of the catalyst decreases during the production phase and the catalyst deactivates. The heat, that is released during the regeneration phase by oxidizing the carbon deposits on the catalyst surface is then stored in the catalytic bed to provide the energy for the next production phase.

To further improve the heat exchange in the reactor metal oxides have been utilized as so called “heat generating materials” (HGM) (Staszak et al. 2020). This additional material of the same particle size than the catalyst does not react with reactants or products, so side reactions like cracking are not enhanced. Heat is released chemically by reducing the metal oxides during the production phase (Eq. (2.3)) and oxidize them during the regeneration phases (Eq. (2.4)).

$$\mathrm{MO}_x + x\,\mathrm{H}_2 \longrightarrow \mathrm{M} + x\,\mathrm{H}_2\mathrm{O} \qquad \Delta H < 0 \qquad (2.3)$$

$$\mathrm{M} + \frac{x}{2}\,\mathrm{O}_2 \longrightarrow \mathrm{MO}_\mathrm{x} \qquad \Delta H > 0 \qquad (2.4)$$

A total of nine Catofin process units for propene dehydrogenation are in use producing $5.000\,000 \times 10^6$ t of propene worldwide according to Lummus Technology (Lummus Technology 2022). An overview of the different propane dehydrogenation technologies is given in Tab. 2.1.

Oleflex process The Oleflex process has been commercialized in the 1980s. The first plant started production in 1990. The process uses three moving bed adiabatic reactors in series and leads to polymer grade propene. The heat for the endothermic reaction is provided by inter-stage heating. The catalyst moves continuously in co-current flow to the gases. The catalyst is regenerated in a separate regeneration unit after it leaves the last reactor. Platinum-based catalysts are used and are under ongoing developement (*Petrochemical Catalysts: Olefins* 2022). Due to the moving bed design, it is possible to replace the catalyst on the fly without shutting down the plant. The circulating catalyst bed furthermore has the advantage that the reactor does not need a separate regeneration phase. A simplified schematic of the process is shown in Fig. 2.1. The Oleflex process is together with the Catofin process the most widely applied propane dehydrogenation technology. All in all 19 Oleflex units produce $7.000\,000 \times 10^6$ t of propene worldwide.

Table 2.1: Comparison of important commercialized propane dehydrogenation processes (Bhasin et al. 2001; S. Chen et al. 2021; Lavrenov et al. 2015; Staszak et al. 2020; Zimmermann 2010).

	Catofin	Oleflex	STAR	Dow FCDh
Reactor	Fixed bed parallel reactors	3 - 4 moving-bed reactors in series, continuous catalyst regeneration	2 reactors: fixed bed tubular furnace and oxyreactor	1 fluidized reactor, 1 fluidized regenerator
Temperature	550 °C to 650 °C	525 °C to 705 °C	500 °C to 600 °C	550 °C to 600 °C
Pressure	0.016 MPa to 0.1 MPa	0.1 MPa to 0.6 MPa	0.6 MPa to 0.9 MPa	0.16 MPa to 0.25 MPa
Catalyst	Cr_2O_3/Al_2O_3	$Pt{-}Sn/Al_2O_3$	$Pt{-}Sn/NaAlO_2$	$Pt{-}Ga/Al_2O_3$
Catalyst lifetime	2 years to 4 years	1 years to 3 years	up to 7 years	no data
Catayst regeneration	Cyclic operation with regeneration phase	Continuous regeneration in separate regenerator	Cyclic regeneration of furnace	Regeneration in separate fluidized bed
Heating for reaction	Regenerative heating of catalyst bed	External interstage heating	Direct heating of furnace, recuperative heating of oxyreactor	Regenerative heating of circulating catalyst
Catalyst reaction residence time	7 min to 15 min	5 d to 10 d	7 h	<2 min
Conversion	45 %	25 %	40 %	45 %
Selectivity	88 %	89 % to 91 %	89 %	93 %

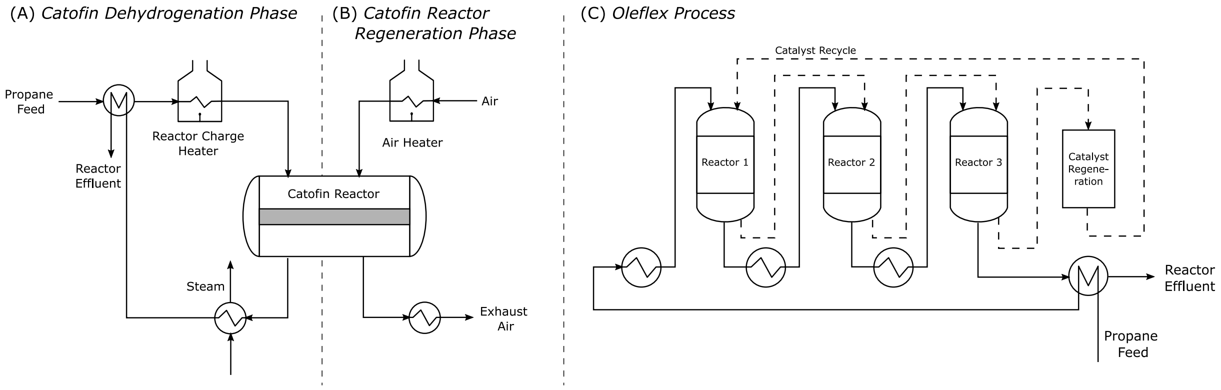
(A) *Catofin Dehydrogenation Phase*
(B) *Catofin Reactor Regeneration Phase*
(C) *Oleflex Process*
Propane Feed
Reactor Effluent
Reactor Charge Heater
Air
Air Heater
Catofin Reactor
Steam
Exhaust Air
Catalyst Recycle
Reactor 1
Reactor 2
Reactor 3
Catalyst Regene-ration
Reactor Effluent
Propane Feed

Figure 2.1: Commercialized dehydrogenation processes: a)-b) Catofin process; c) Oleflex process.

Star process The Star (*ST*eam *A*ctive *R*eforming) process was originally developed by Thyssen Krupp Uhde and can be used for dehydrogenation of different reactants similar the other dehydrogenation processes. A comparable process has been developed by BASF. Recently both companies worked together on improving their technology (BASF SE 2020; BASF SE and thyssenkrupp Industrial Solutions AG 2022). In the Star process steam is used to lower the partial pressure of propane to be able to get conversions as high as at vacuum conditions. Operating pressures of the other processes are usually lower (see Tab. 2.1 for a detailed comparison of the different dehydrogenation processes). The Star process follows a two stage concept. The feed gases are first fed to a directly heated multitubular reactor. In this reactor the feed gases react on a Pt-Sn/$NaAlO_2$. The second stage consists of a so called oxyreactor. The outlet gases of the first reactor, consisting of propane, propene, hydrogen and steam, are mixed with oxygen enriched air. In that way the hydrogen generated in the first reactor is oxidized according to Eq. (2.5) to shift the chemical equilibrium and to deliver heat for the dehydrogenation of unconverted propane (Staszak et al. 2020).

$$H_2 + \frac{1}{2} O_2 \longrightarrow H_2O \tag{2.5}$$

Regeneration of the first reactor is realized periodically. During catalyst regeneration another reactor is used to ensure continuous production.

FCDh process Dow is working on a Fluidized Catalytic Dehydrogenation (FCDh) process for propane dehydrogenation which is related to the design of a Fluidized Catalytic Cracking (FCC) unit. It consists of a reaction reactor and a regeneration reactor that are both realized as fluidized beds. The catalyst circulates regularly between the production and the regeneration bed to ensure catalyst activity. Advantages are a continuous operation and the possibility to change the catalyst during operation.

This overview does not claim to be complete. It also has to be stated that there are other on-purpose production processes besides dehydrogenation, e.g. methanol-to-olefin (MTO) processes, that are not discussed here. The discussion of other processes would go beyond the scope of this work and can be found in literature. Lavrenov et al. discusses the state of the art of propene production with special attention to Russian contributions in that field (Lavrenov et al. 2015). Additional dehydrogenation processes are described by Chen et al. (S. Chen et al. 2021). Current technologies including MTO, SC and dehydrogenation are described in more detail be Staszak et al. (Staszak et al. 2020). Amghizar et al. discusses the olefin production technologies with respect to future developments like shifting feedstocks and predicted global demands for olefins (Amghizar et al. 2017).

The processes described in this section illustrate the difficulties of the on-purpose propane dehydrogenation as already discussed at the beginning of this chapter and present different strategies to overcome these hurdles. All processes presented have different strategies to realize catalyst regeneration. This can be realized in a continuous (Oleflex, FCDh process) or a cyclic manner (CATOFIN, Star process). Understanding the kinetics of coking, deactivation, and regeneration of catalysts is critical to being able to rigorously optimize the overall production process. Another obstacle is the provision of heat, that is required for the process. Common strategies for heat supply are direct heating of the catalyst bed (Star process) or the gas streams (Oleflex) and regenerative heating of the catalyst bed (Catofin) or the circulating catalyst (FCDh process). Another field of continuous improvement is the catalyst used in the different processes. The next section will discuss the state of the art regarding dehydrogenation catalysts. After that, oxidative propane dehydrogenation as an alternative for currently industrilized processes are presented.

2.1.3 Catalysts for Thermal Propane Dehydrogenation

Catalysts for propane dehydrogenation processes are a subject of ongoing research. The catalysts that gain attention in research can be divided in different categories. Metal-based catalysts are the first category. Platinum is known to be the most promising active component. The Oleflex, STAR and Dow FCDh processes use Pt-based catalysts. The main problem of Pt-based catalyst is, that they also catalyze C-C cleavage and deep dehydrogenation (S. Chen et al. 2021). The consequence is severe coke formation. The active platinum clusters or nano-crystals are prone to sintering at high temperatures that usually occur during regeneration. During the Oleflex process redistribution of the platinum is ensured by addition of chlorine (Staszak et al. 2020). To overcome the disadvantages of Pt-based catalysts, different promoters are commonly used. It can be distinguished between metal promoters and oxide promoters (S. Chen et al. 2021). Different metals for alloys or composites with platinum have been used. Tin has gotten the most attention and is already utilized in the STAR and Oleflex processes. The mechanism of Sn as a promoters is not entirely clear. It is assumed that it assists in Pt redistribution or acts as an electron donor for Pt. Oxide promoters are also known to be beneficial. Small amounts of TiO_2 were found to mitigate coke formation but larger amounts enhance coking. Aside from promoters, there is a not negligible influence of the support on the catalyst performance. The mostly used support is Al_2O_3, which is employed in Oleflex and Dow FCDh processes. The use of other metal oxides is also possible as well, as using zeolites for exploiting their unique geometric properties. Since Pt is expensive, many non-noble metals have been tested for propane dehydrogenation e.g. Ni, Fe and Co. These metals still do not reach the performance of Pt-based catalysts (S. Chen et al. 2021). An advantage would be the high abundance of the metals, making them a more sustainable choice in the sense of green chemistry.

Besides metal catalysts, metal oxide-based catalysts are common in propane dehydrogenation. CrO_x is most prominently used for the Catofin and FBD4 processes (S. Chen et al. 2021). The mechanism of CrO_x as dehydrogenation catalyst is more complex than the mechanism of Pt-based catalysts, since CrO_x forms a variety of different valence states that all play a different role in dehydrogenation. Common disadvantages of CrO_x catalysts are rapid coke formation and low stability due to diffusion into the lattice of the support and Cr^{3+} aggregation (S. Chen et al. 2021).

VO_x is an alternative active component for metal oxide catalysts that has mainly be studied for oxidative dehydrogenation reactions (ODH) (Carrero et al. 2014; Grabowski 2006), but is also known to catalyze thermal dehydrogenation reactions (S. Chen et al. 2021; Xiong et al. 2019). Sokolov et al. proved that VO_x offers better stability and selectivity during cyclic TDH operation than CrO_x and Pt−Sn (Sokolov, Stoyanova, et al. 2012). The main reason of deactivation of VO_x catalysts during thermal dehydrogenation reactions is coking, which will be discussed later (see Section 2.3.3). Due to the ability of VO_x to catalyze both TDH and ODH reactions, it will be used in this work that aims to combine both reactions (see Chapter 3). Since the commercialized processes that have already been discussed in the previous sections mainly utilize the thermal dehydrogenation reaction, the next sections focuses on the oxidative dehydrogenation reaction.

2.1.4 Oxidative Propane Dehydrogenation

As stated in the beginning of this chapter, the oxidative dehydrogenation reaction has some remarkable advantages and disadvantages in comparison to the widely industrialized thermal dehydrogenation reaction. On the one hand the catalyst used in ODH reactions does not suffer from coking due to the presence of oxygen and is not limited by a chemical equilibrium. On the other hand consecutive side reactions are promoted (For details see Section 2.3.2). An example for a commercialized oxidative dehydrogenation process is the conversion of n-butane to maleic anhydrite on vanadium pyrophosphate (VPO). Oxidative dehydrogenation of propane can still not compete with already commercialized processes. Despite the fact that ODH of propane to propene has not been commercialized yet, there are ongoing research efforts to optimized the reaction and processes utilizing it (Cavani et al. 2007). Research on ODH can be divided into research on ODH catalysts, reaction kinetics and reaction equipment. Both catalysts and reaction equipment for ODH reactions will be discussed in the following paragraphs.

ODH catalysts Cavani et al. raised the question of how far ODH is from industrial use and gave an overview on catalysts for ODH of ethane and propane together with reactor configurations for ODH processes discussed in literature (Cavani et al. 2007). Most commonly catalysts based on vanadia and molybdenum oxide are used for selective dehydrogenation reactions. Due to the higher activity vanadium oxide based catalyst are most popular in literature. Besides that, zeolites and mixed metal oxides are mentioned (Grant et al. 2018). The exact mechanisms of alkane dehydrogenation on vanadia catalysts are still under discussion. Similar to TDH catalysts (Section 2.1.3) the catalysts support plays a role in catalyst performance as well as the structure and valence state of the active sites (Xiong et al. 2019; Zanthoff et al. 1999; Khodakov et al. 1999). Besides new catalyst systems, innovative reactor concepts are considered to enhance the ODH reaction, which is discussed in the next paragraph.

Innovative Reactor Concepts for ODH In terms of innovative reactor concepts, staged oxygen dosing, membranes and cyclic reactor operation is mentioned. These concepts aim to keep constantly low oxygen partial pressures to avoid consecutive partial and total oxidation of reactants and products. The use of membrane reactors will be discussed in more detail in Section 2.2.1. New concepts in reaction technology are short bed reactors, that operate at higher temperatures than conventional ODH processes. The catalyst in these concepts is used to start the reaction. The main conversion of the reactants occurs in the gas phase. This concept is characterized by shorter residence times and can be seen as a combination of catalytic reactions and thermal cracking reactions (Cavani et al. 2007).

As the use of CO_2 gains more and more attention in the context of emission reduction and the shift away from fossil fuels, oxidative dehydrogenation using CO_2 as a mild oxidant is also being investigated more and more. Since this work focuses on O_2 as an oxidizer, this topic will only be briefly summarized. Atanga et al. mainly review different catalysts used for ODH of propane with CO_2 in current literature (Atanga et al. 2018). The research on carbon dioxide as oxidant in a variety of different oxidation reactions is reviewed by Ansari et al. (Ansari and Park 2012). The authors point out that there are already investigations in pilot scale for production of styrene by dehydrogenation of ethyl benzene. Wang and Zhu summarize the catalytic conversion of different alkanes to olefins by oxidation with CO_2 (S. Wang and Z. H. Zhu 2004). All reviews point out the need for more in depth investigations of the reaction mechanisms and pathways of the reactions and the potential for industrial utilization. Different types of catalysts and supports for oxidative dehydrogenation using CO_2 are also under ongoing investigation (Müller et al. 2014; Gomez et al. 2018; Michorczyk et al. 2011; Valenzuela et al. 2000).

After introducing the model reaction and the state of the art in alkane dehydrogenation technology it becomes clear, that there are challenges connected to ODH and TDH reactions. The goal of this work is to find solutions to overcome these obstacles by using innovative reactor concepts and to illustrate ways to make the overall process more efficient. The field of *Process Intensification* (PI) deals in particular with the question of how processes can be made more efficient. For this purpose, several operations are often integrated into one apparatus. In the next section the concept of PI will be discussed and the concepts used within this work are explained.

2.2 Process Intensification

This chapter aims to present the current state of research and theoretical concepts in the field of process intensification. The reactor concepts used in this work will be classified and important preliminary work will be presented. First, general terms and trends in the field of *Process Intensification* (PI) are presented, before membrane reactor concepts and flow reversal reactors are addressed.
PI is an ongoing trend in chemical engineering. First systematic definitions of the term Process Intensification have been published in the 2000s but the underlying principles have been used decades before (A. Stankiewicz and J. A. Moulijn 2002; A. I. Stankiewicz and J. A. Moulijn 2000). The goal of PI is to create more efficient processes by following the principles stated by van Gerven and Stankiewicz (van Gerven and A. Stankiewicz 2009):

- Maximize the effectiveness of intramolecular and intermolecular events
- Provide all molecules the same process experience
- Optimize driving forces at all scales and maximize the specific surface areas to which they apply
- Maximize synergistic effects from partial processes

These principles can be applied to different domains as illustrated in Fig. 2.2.

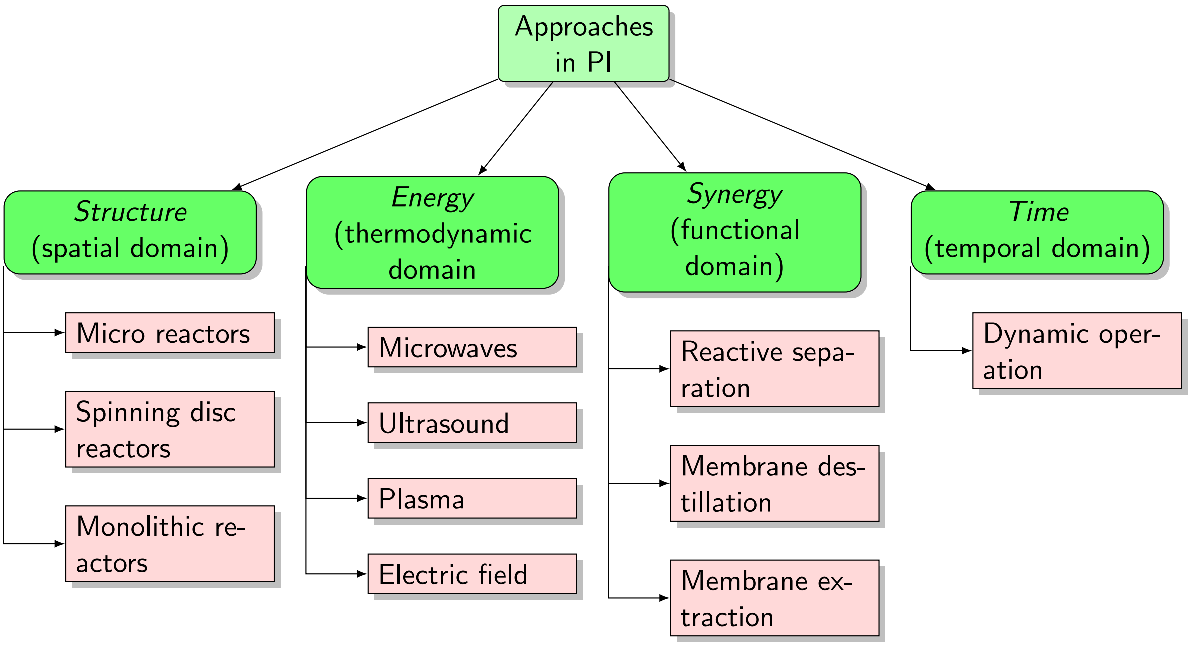
Approaches in PI
Structure (spatial domain)
Energy (thermodynamic domain
Synergy (functional domain)
Time (temporal domain)
Micro reactors
Spinning disc reactors
Monolithic reactors
Microwaves
Ultrasound
Plasma
Electric field
Reactive separation
Membrane destillation
Membrane extraction
Dynamic operation

Figure 2.2: Approaches in Process Intensification with practical examples (adopted from van Gerven and A. Stankiewicz 2009; Haase et al. 2022).

PI by improving the *structure* can refer to either the catalyst or the reactor itself. Examples are spinning disc reactors that offer better heat and mass transfer properties than conventional reactors (Beer et al. 2015; Chaudhuri et al. 2022). Another approach to enhance heat transfer properties are microreactors or micro structured reactors (Guettel and Turek 2010; Vernikovskaya et al. 2023; Wen et al. 2009). PI does not necessarily include reactions. A typical example for PI in structural domain are dividing-wall columns, which are able to reduce investment and energy consumption for the separation of mixtures into 3 or 4 fractions compared to conventional distillation columns (Dejanović et al. 2010). This example also illustrates that the principles of PI have been used decades before PI has been formally defined (Kaibel 1987). In terms of *energy*, current trends in PI include plasma reactors (X. Chen et al. 2017) and microwave reactors (Estel et al. 2017). These concepts aim to provide better heating and heat transfer. *Synergistic* effects are usually realized by combining separation and reaction in a single apparatus. An example is reactive distillation, which has already been utilized in industry (Keller 2014). Separation and reaction can also be combined in membrane reactors. This can include membrane distillation, membrane extraction, reactive membranes and membrane distribution (Keil 2018; Haase et al. 2022). Since membrane reactors are in the focus of this work, a detailed description of different membrane reactor configurations is given in Chapter 2.2.1. PI via improvements in *temporal* domain are mainly realized by periodic operation of reactors. This can include variation of temperature, concentration or pressure over time but also flow reversal. Felischak et al. showed how forced periodic operation of more than one input parameter is able to improve overall reactor performance for a homogeneous model reaction (Felischak et al. 2021). Ellwood et al. used the same principle for a photo-catalytic, heterogeneously catalyst reaction (Ellwood et al. 2021).

The term “Multifunctional Reactors” is also mentioned regularly within the context of PI. The idea of combining different functionalities in a single apparatus can be found in literature even before the term “Process Intensification” was coined (Agar and Ruppel 1988). According to Agar, multifunctional reactors can benefit from measures of PI (Agar 1999). This suggests the coexistence of two separate concepts. Utilizing the current definition of PI, the concept of multifunctional reactors can be grouped into the categories within PI as presented earlier. It presents a narrower concept than PI and describes reactors combining different unit operation besides reaction (Dautzenberg and Mukherjee 2001). Multifunctional reactors often perform process intensification in spacial domain (separation + reaction) and temporal domain (e.g. reverse flow reactors).

A more thorough description of the different approaches in PI is beyond the scope of this work. More details about process intensification is available in recent literature. Haase et al. describe the advances in PI in the different domains as presented in Fig. 2.2 (Haase et al. 2022). Tian et al. present the PI approaches in process systems engineering including a very comprehensive list of literature (Tian et al. 2018). Modeling of PI is the focus of a book edited by Keil (Keil 2007).

The reactor concepts in this work are intended to intensify the process through measures in the functional domain (membrane reactors, internal heat integration) and in time domain (periodic operation). In the next chapters, these two topics will be addressed in more detail.

2.2.1 Membrane Reactors

Membrane reactors are a well known concept in reaction engineering. First patents regarding membrane reactors date back to the 1960s and 1970s (Pfefferle 1966; Gryaznov et al. 1977). In the context of PI, membrane reactor concepts can be seen as modifications in the functional domain or in spatial domain (see Fig. 2.2). Membrane reactors can be categorized by their function as illustrated in Fig. 2.3. In this chapter, examples for all illustrated membrane reactor configurations will be given. Examples will mainly focus on dehydrogenation reactions, since the selective propane dehydrogenation is used as an industrial relevant model reaction in this work. The literature mentioned at the end of this chapter contains more examples. The interested reader may be referred to these reviews for further applications of membrane reactors.

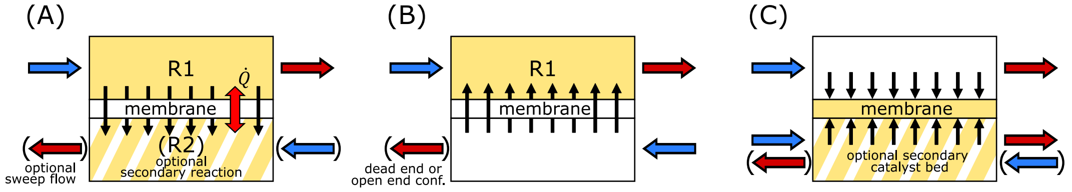

Figure 2.3: Membrane reactor concepts (Thomas et al. 2010; Dittmeyer and Caro 2008).

Fig. 2.3 (A) illustrates a membrane reactor with product extraction. An example for a reaction network that benefits from this kind of membrane reactor is shown in Eq. 2.6 and 2.7.

$$\text{R1:}\quad \mathrm{A} + \mathrm{B} \rightleftharpoons \mathrm{C} \tag{2.6}$$

$$\text{R2:}\quad \mathrm{C} + \mathrm{D} \longrightarrow \mathrm{E} \quad \text{(optional)} \tag{2.7}$$

Product extraction is especially beneficial if the main reaction R1 is limited by a chemical equilibrium. The chemical equilibrium can be shifted towards the products and higher conversions can be achieved by extracting the product C. An optional secondary reaction R2 for consumption of the extracted component can be used to keep the concentration difference between retentate and permeate high. This keeps the trans-membrane flux of the product high. If the secondary reaction R2 is exothermic, it can help to provide the heat needed for a endothermic reaction R1 and therefore further increase the reactor performance. On the permeate side the reactor can be designed with or without a sweep flow. A sweep flow enhances the transport of the permeate away from the membrane but has the disadvantage of diluting the permeate and therefore implicates an additional separation task, if it is a valuable product. Dilution can be avoided if a vacuum on the permeate side contributes to a quick removal of the permeate.

Besides equilibrium limited reactions it is also thinkable to utilize membrane extractors to extract a valuable product to avoid consecutive reactions, that limit the yield. An example is given in 2.8 and 2.9.

$$\text{R1:}\quad \mathrm{A} + \mathrm{B} \longrightarrow \mathrm{C} \tag{2.8}$$

$$\text{R1:}\quad \mathrm{C} + \mathrm{B} \longrightarrow \mathrm{D} \tag{2.9}$$

This consecutive reaction scheme is common for selective oxidation reactions that suffer from total and partial oxidation of the valuable product.

Another common principle in membrane reactors is dosing of reactants as illustrated in Fig. 2.3 (B). Consecutive reactions can often be mitigated by keeping the concentration of the reactant low. In case of selective oxidation reactions, this would be the oxidizing agent. A membrane reactor for reactant distribution can be realized in open end and dead end configuration. For distributor designs, the requirements concerning the membrane can be less challenging than in extractor configurations, depending on the specific design. Whereas in extractor configurations the selectivity of the membrane towards the product has to be guaranteed, a membrane distributor could be realized with non-selective membranes. Differences in membranes and the consequences for reactor design will be discussed later on.

In the distributor and extractor designs for membrane reactors discussed so far, the membranes are inert and only support the reaction, which is usually catalyzed in a packed bed. A third option to design membrane reactors is depicted in Fig. 2.3 C. In membrane contactors the membrane itself defines the reaction zone. This can be realized by impregnation of the membrane support or incorporation of catalytically active components into the membrane structure. Different combinations of this approach are thinkable and have been tested in literature. The catalytically active membrane can be combined with a catalyst bed. Flow directions and dead end/open end configurations can also be a variable. A variation of membrane contactors are pore through flow membrane reactors. The reactants flow through the pores of the catalytically active membranes. Membrane contactors can be used to bring liquid and gaseous reactants together at a large surface. In gas-gas reactions the separation provided by the membrane can have advantages in terms of safety since the gases are not premixed as in a conventional plug flow reactor. Pore through flow reactors allow to eliminate the diffusional resistance of conventional catalyst particles and to exploit the intrinsic catalytic properties of the catalyst and offer defined residence times (Dittmeyer and Caro 2008; Caro 2016a).

All these different membrane reactor setups impose different demands on the membranes used. Typical membrane parameters that have to match with the reaction are thermal, mechanical and chemical stability of the membrane, selectivity and permeance at the desired reaction temperature.

To assess the compatibility of H_2-selective membranes and reactions, van de Graaf compared the space-time yield (STY) of catalytic reactors with the performance of various H_2-selective membranes (van de Graaf et al. 1999). The area time yield (ATY) defined by Boudart, which is identical to the membrane flux, was used to evaluate the membrane (Boudart 1997). As a benchmark for industrial STYs, the “Window of reality” defined by Weisz is used, which indicates a space-time yield of $1\,\mathrm{mol\,m^{-3}\,s^{-1}}$ to $10\,\mathrm{mol\,m^{-3}\,s^{-1}}$ for industrial processes (Weisz 1982). An updated version of this comparison can be found in Fig. 2.4. For the Pd-based membranes, a pressure difference of 1 bar between permeate and retentate side was assumed (Fernandez, Helmi, Medrano, et al. 2017). For all other membranes the differential pressure is 1 bar to 2 bar (Dittmeyer and Caro 2008). By dividing the STY by the ATY, volume-specific surfaces can be calculated. In cylindrical reactors with the diameter d, the ratio between shell surface area and volume is $\frac{A}{V} = \frac{4}{d}$. A volume specific surface area of $\frac{A}{V} = 100\,\mathrm{m^{-1}}$ corresponds to a diameter of 4 cm of a cylindrical reactor and a volume specific surface area of $\frac{A}{V} = 10\,\mathrm{m}^{-1}$ corresponds to a reactor with a diameter of 40 cm. Both values can be assumed to be realistic against an industrial background and have also been plotted in Fig 2.4. It is clear that for all the H_2-selective materials shown, a combination of membranes and reactions in an industrial setting seems possible. It should be noted that this analysis is based purely on the mass transfer properties of the membranes. Other aspects such as long-term stability under reaction conditions are not considered in the presentation.

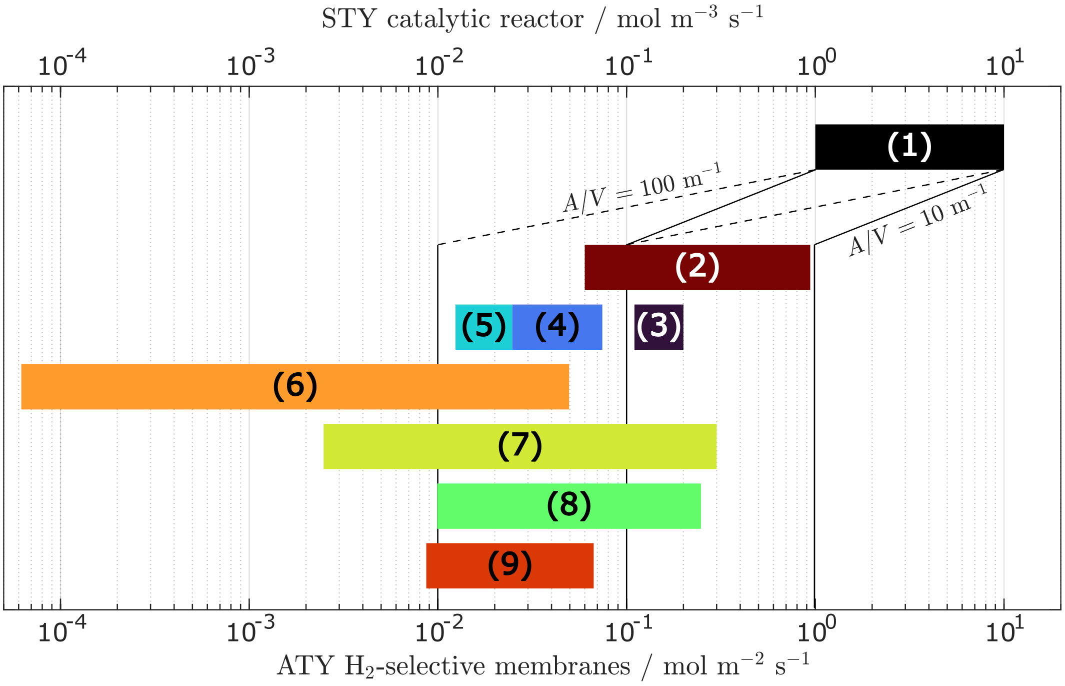

Figure 2.4: Updated comparison between the space-time yield of catalytic reactors (1) and the areal time yield of some organic and inorganic H_2-selective membranes ((2)-(9)) according to van de Graaf (van de Graaf et al. 1999). (1): "Window of reality" of catalytic reactors (Weisz 1982); (2): Pd-based membrane on ceramic support; (3): Pd-based membrane on metallic support; (4) solid polymer electrolyte membrane; (5): organic polymer membrane; (6): carbon molecular sieve membrane; (7): MFI zeolite membrane; (8): silica molecular sieve membrane; (9): single phase ceramic mixed H^+/e^- conducting membranes (Dittmeyer and Caro 2008; Fernandez, Helmi, Medrano, et al. 2017).

Comparing the original figure in the publication of van der Graaf and Fig. 2.4, the development of membranes over the last decades becomes clear. While van der Graaf assumed a permeate flux of $0.1\,\mathrm{mol\,m^{-2}\,s^{-1}}$ for palladium-based membranes, this value has increased almost tenfold for current membranes and makes a utilization of membranes in technical applications even more promising.

A common categorization of membranes is the distinction between selective and non-selective membranes. In the next paragraphs, both categories will be discussed in detail.

Selective membranes In the context of dehydrogenation reactions H_2-selective membranes raised a lot of attention in research. Selective membranes based on polymers, metals and microporous membranes are the most promising for H_2 separation. Selectivity in polymer membranes is usually determined by diffusivity and solubility of H_2 in the polymer material. Disadvantages of polymer membranes are low temperature limits and limitations in terms of H_2 selectivity. Due to the low temperature limits of the membranes a combination with reactions in one apparatus is rather challenging. The low selectivity towards hydrogen makes polymer unsuitable for applications where a hydrogen with high purity is necessary.

A well known alternative are metal based membranes, which basically have an infinite selectivity and lead to the production of ultra pure hydrogen. The temperature stability is better compared to polymer membranes. Most metal based membranes are based on Pd and Pd alloys and are still in the focus of research. Fernandez et al. review the latest advances in Pd-based membrane reactors in EU projects (Fernandez, Helmi, Medrano, et al. 2017). Pd-based membranes have been used to enhance water gas shift reaction, oxidative steam reforming, steam methane reforming, natural gas reforming, bioethanol reforming and biogas reforming. Some of the reactor concepts suggested by Fernandez et al. utilize fluidized beds for better mixing, heat transfer and less problems with concentration polarization. Long term stability in fluidized bed conditions has been studied by Nooijer et al. for different Pd-based membranes (Nooijer et al. 2019). Pinhole formation and therefore reduced selectivity is reported for long times on stream in fluidized beds. A major disadvantage is the fragility of the selective layer. A thin layer is needed to ensure high fluxes across the membrane. The membranes are therefore prone to leakages especially in environments with additional mechanical stress. An introduction of an additional protective ceramic layer results in enhanced coking of the membrane by alkanes and alkenes as present in propane dehydrogenation (Brencio, Fontein, et al. 2022; Brencio, Gough, et al. 2022; Sheintuch and Nekhamkina 2018).

Another alternative for H_2 separation are micro-porous membranes that usually offer a better resistance against mechanical stress than Pd based membranes. Selectivities vary greatly due to the very different preparation techniques of the membranes. Mass transport of different gases through the membrane is determined by the pore size and the kinetic diameter of the gases and is usually described by the dusty gas model (Mason et al. 1983; Karagöz et al. 2020).

Besides H_2 selective membranes, O_2 selective membranes are used in reaction engineering. Microporous membranes are usually not suitable for the purpose of O_2 separation since the difference in the kinetic diameter of N_2 and O_2 is not significant enough to result in the required selectivities. Mixed ionic-electronic conducting (MIEC) membranes are attractive for this purpose (X. Zhu and Yang 2017). The development of these materials with the purpose of O_2 production started in the 1980s. Perowskites are a prominent example of this category of materials. Oxygen is transferred through the material as O_2^{2-} ions by diffusion. Interfacial oxygen exchange at the permeate and retentate side is also part of the mechanism. Electrons are internally transferred in the opposite direction for charge balancing. Typical reactions that benefit from oxygen dosing via MIEC membranes are partial oxidation of methane to syngas (POM) as described by Caro et al. (Caro et al. 2007). The membranes are combined with a packed bed catalyst in that work. Other possible reactions are oxidative dehydrogenation reactions and oxidative coupling of methane.

Yan et al. used disc shaped oxygen permeable membranes based on $La_2Ni_{0.9}V_{0.1}O_{4+\delta}$ or $Ba_{0.5}Sr_{0.5}Co_{0.8}Fe_{0.2}O_{3-\delta}$. The membrane itself functioned as a catalyst for the reaction and a separate catalyst was not used (Yan et al. 2014). Alternative materials also used for dehydrogenation reactions are solid electolytes (SE) or oxygen ion conductors. These materials are not able to transport electrons and therefore need an external circuit for charge balancing which makes reactor setups more complicated. An advantage of this external circuit is that the oxygen permeation can be enhanced by applying an external voltage, known as oxygen pumping, as presented by Ye et al. for partial oxidation of *n*-butane (Y. Ye et al. 2005). Bortolotto and Dittmeyer utilized both H_2-selective as well as O_2-selective membranes in one apparatus to enhance the hydroxylation of benzene to phenol in a microstructured membrane reactor (Bortolotto and Dittmeyer 2010).

Non-selective membranes Generally, non-selective membranes are easier to manufacture and therefore cheaper than their selective counterparts. Due to the lack of selectivity, their field of application is usually limited to distributors and contactors. According to the IUPAC definition, membrane reactors must perform membrane-based separation with a reaction (Koros et al. 1996). This definition cannot be met with non-selective membranes. Nevertheless, reactors with non-selective membranes are also considered membrane reactors by the research community (Caro 2016b).

Lu et al. compared different reactors with distributed reactant dosing for a model reaction network consisting of parallel and consecutive reactions (Lu et al. 1997). Six different reactor setups containing both discrete multiple stage feeds and continuous membrane feeds have been compared. Furthermore uniform distribution and optimal distribution over the length of the reactor have been studied. It was shown that reactors with distributed dosing can outperform reactors in co-feed operation depending on the reaction order regarding the dosed reactant, the residence time and permeability and the dimensionless rate constant.

As mentioned above, selective oxidation reactions are commonly used as model reactions in experimental studies on membrane distributors. Ramos et al. performed the oxidative dehydrogenation in a membrane distributor on a VO_x/MgO catalyst. The distribution membrane consists of a modified alumina filtration tube, which illustrated the broad availability of materials that can be utilized as distributing membranes. Besides ceramic membranes, it is possible to use sinter metal membranes for non-selective dosing, which might be easier to seal and are not as fragile as ceramic membranes. More important than mechanical strength is the compatibility between reaction and transport properties of the membrane. A systematic investigation and comparison of sinter metal membranes and ceramic membranes has been performed by Hamel et al. for the deghydrogenation of ethane. The smaller pore sizes of ceramic membranes have shown to be beneficial for that specific reaction and reactor setup due to a higher trans membrane flow resistance that causes a higher pressure drop between shell side and tube side and avoids back diffusion (Hamel, Wolff, and Seidel-Morgenstern 2011).

Nonselective dosing offers an additional degree of freedom in reactor design through dilution of the reactant that is dosed through the membrane. A higher dilution has an influence on back permeation through the membrane and on the residence time distribution. Fig. 2.5 illustrates typical concentration and residence time profiles for FBR and PBMR for an reaction with the reactants A and B.

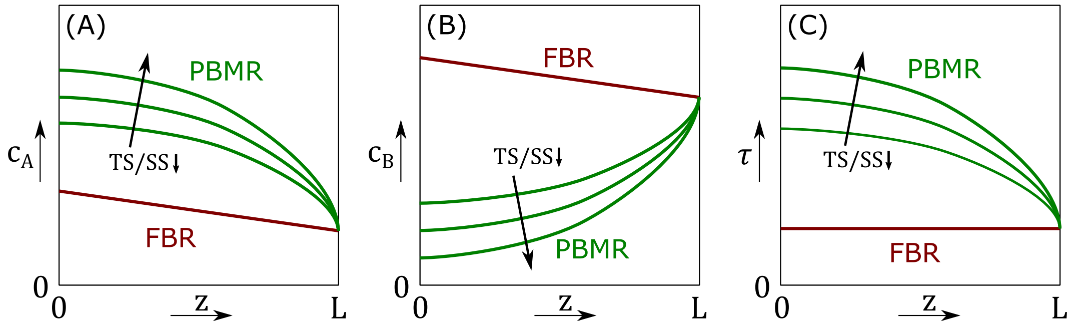

Figure 2.5: Schematic profiles over reactor length in fixed bed reactors (FBR) and packed bed membrane reactors (PBMR); (A) Concentration of reactant A fed on tube side; (B) Concentration of reactant B fed on shell side in PBMR and on tube side in FBR; (C) Residence time.

Component B is dosed through the porous membrane along the length of the reactor. The concentration of reactant A at the beginning of the reactor is apparently higher in the PBMR reactor than in the FBR (Fig. 2.5 A). Assuming a similar conversion in both reactors, the concentration of A is similar for FBR and PBMR at the end of the reactor. The concentration of B is lower at the beginning of the PBMR than at the beginning of the FBR, since B is dosed via the membrane and therefore accumulates over the length of the membrane (Fig. 2.5 B). The apparent residence time in the PBMR at the beginning is higher than in the FBR, since the total volumetric flow at the beginning of the PBMR is smaller than in the FBR. At the end of the reactors the total inlet flow is the same for both reactors for a fair comparison of the reactor concepts. The differences in residence times in the reactors and in the mean concentrations are the reasons for different reactor behavior. The variable determining the ratio between the flow through the membrane (shell side, SS) to the direct flow fed to the reactor tube inlet (tube side, TS) is the tube-side/shell-side ratio:

$$TS/SS = \frac{\dot{V}_{TS}}{\dot{V}_{SS}} \tag{2.10}$$

This ratio can be varied to provide the most favorable reaction conditions for the reaction conducted in the reactor. The consequences of a variation on the reactor behavior is also illustrated in Fig. 2.5. Kostanjac et al. studied the oxidative dehydrogenation of propane on a Ga_2O_3/MoO_3 catalyst (Kotanjac et al. 2010) and varied the dilution systematically to optimize the reaction conditions. To further increase the yield of a reactor with distributed dosing, a dosing profile can be beneficial as already shown by Lu (Lu et al. 1997). A continuous variation of the trans membrane flux over the length of the reactor can hardly be realized in experiments. Staged dosing profiles in a membrane reactor cascade are a more convenient implementation of that principle. This has already been analyzed both theoretically and experimentally for oxidative dehydrogenation of ethane in 3 stage membrane reactor cascade (Hamel, Tóta, et al. 2010; Hamel, Tóta, et al. 2008; Tóta et al. 2004). Staged membrane dosing showed better results than evenly distributed dosing in ethane ODH on VO_x/Al_2O_3 in ceramic membrane reactors.

Non-selective membranes are also frequently used for membrane contactors. Bottino and co-workers used membrane contactors for oxidative dehydrogenation of propane (Bottino, Capannelli, and Comite 2002). Active VO_x sites have been deposited on ceramic membranes (Al_2O_3, ZSM) for an experimental comparison of co-feed of C_3H_8 and O_2 and parallel feeding of O_2 via the membrane and C_3H_8 via the tube side with better results for the operation as a membrane contactor. Catalytically active alumina membranes activated with VO_x have also been combined with a Cr_2O_3 catalyst on alumina support to combine ODH and TDH (Brune, Wolff, et al. 2019). Pore through flow reactors have been used for the production of prebiotic galacto-oligosaccharides in liquid phase. A methacrylate based polymer monolith has been activated with β-galactosidase to catalyze the conversion of lactose, a reaction usually conducted in batch reactors. A scale-up and a long term stability test have been performed (Pottratz et al. 2022).

A broader overview on membrane reactors is given by literature, e.g. in a dedicated chapter in the Handbook of Heterogeneous Catalysis (Dittmeyer and Caro 2008). Further details on membrane reactors as distributors have been summarized in a book edited by Seidel-Morgenstern (Seidel-Morgenstern 2010). Comprehensive information on different keywords regarding membrane reactors can also be found in the Encyclopedia of Membranes edited by Drioli and Giorno (Drioli and Giorno 2016) or in more detail in another reference work edited by Drioli (Drioli 2010).

This work focuses on membrane reactors in distributor configuration. Besides reactant dosing a further intensification of the process is intended through heat integration. The next section aims to present the fundamentals of heat integration.

2.2.2 Heat-Integrated Fixed Bed Reactors

Heat integrated fixed bed reactors are well known for weakly exothermic reactions. The most intuitive case of heat integration is represented in counter-current fixed bed reactors as represented in Fig. 2.6 A. In that reactor concept the product stream of the reactor heats up the feed stream internally without the need of an external heat exchanger. With that, equipment cost can be reduced. Another well known alternative to utilize the heat released by an exothermic reaction is the reverse flow reactor as illustrated in Fig. 2.6 B. By reversing the flow of the gas stream after a certain time the heat front of the reaction is kept in the reactor and can be utilized to provide the heat necessary to perform the reaction in the next phase. Such a process is inherently dynamic and will be performed in a cyclic manner, which imposes special requirements on process control.

One of the first patents for a reactor based on this principle was issued in 1938 (Cottrell 1938). This reactor concept attracted greater attention with the work of Matros and his co-workers in the Boreskov Institute of Catalysis in Novosibirsk (Russia) in the 1970s (Boreskov and Matros 1983). Both modeling and experimental work on this principle has been in the focus of research since then (Bunimovich and Sapoundjiev 2013; Zagoruiko et al. 2021).

The concepts introduced so far use the principle of recovering heat released in an exothermic reaction to preheat the reactants and to keep the reaction at temperature. Another approach is to combine endo- and exothermic reactions. In that way, the heat released in an exothermic reaction can be used to provide the energy for the endothermic reac-

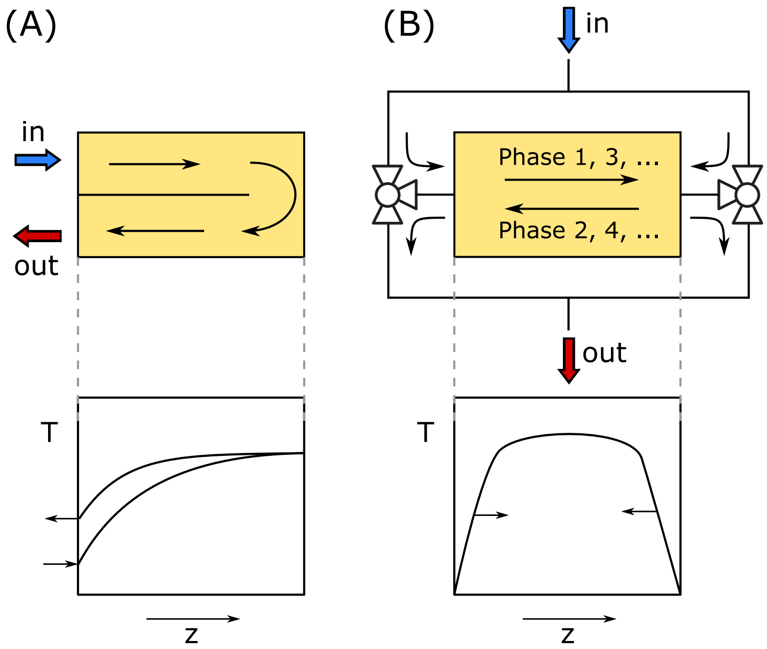

Figure 2.6: Heat integrated reactor concepts for exothermic reactions and typical temperature profiles (A) Counter-current fixed bed reactor, (B) Reverse flow reactor (with periodic steady state temperature).

tion. Kolios and co-workers introduced a system to categorize the different approaches (Kolios, Frauhammer, et al. 2000; Kolios, Gritsch, et al. 2005). The concepts relevant for this work are illustrated in Fig. 2.7. These reactors can be distinguished by the mechanism of heat transfer (recuperative and regenerative) and how the different reactions are performed (simultaneously in one compartment or asymmetrically in separated compartments). For further concepts please refer to (Kolios, Gritsch, et al. 2005). In simultaneous mode (A) and (B) the endothermic and exothermic reactions are not separated from each other. The reactants for both reactions are fed into the reactor together. In this case the conditions of both reactions have to be compatible e.g. in terms of temperature and pressure. Performing the reactions separately offers the advantage of being able to tune the reaction conditions of both reactions separately. Another disadvantage of performing both reactions simultaneously is the increased difficulty of downstream processing, since the reaction products are mixed at the reactor outlet. In (C) and (D) the reactions are conducted separately. In that way, the products are not mixed and the separation task is easier to perform. Side reactions between the reactants of the R1 and R2 are not possible in asymmetric operation. Concepts (A) and (C) realize the heat transfer between the reactions in recuperative mode. These processes are stationary. Concepts (B) and (D) utilize regenerative heat exchange which requires a cyclic process with flow reversal.

Different examples for both research as well as industrial application of these principles can be found. A process that uses simultaneous operation has been designed by Blanks et al. for Amoco (Blanks et al. 1990) combining steam reforming and methane combustion in one apparatus with flow reversal (Fig. 2.7 B). In his Danckwert's Memorial lecture Levenspiel proposed different heat integrated reactor concepts. For coal gasification the RE-GAS process was proposed consisting of exothermic coal combustion to provide the needed energy by heating up the catalyst bed and endothermic coal gasification in cyclic operation in

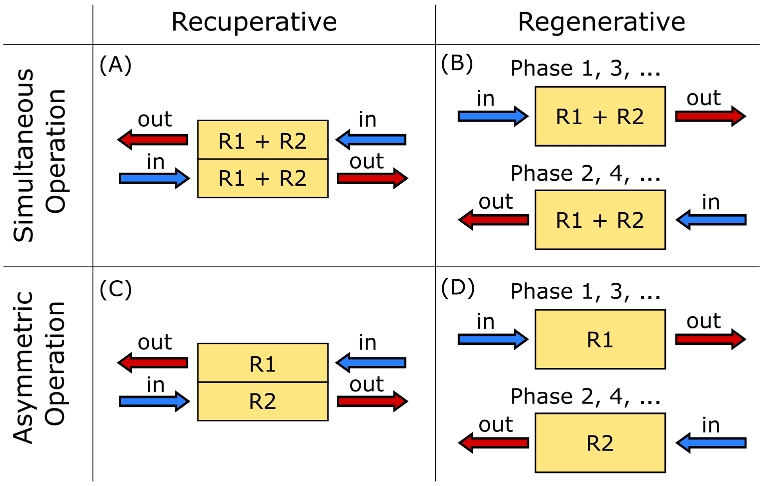

Figure 2.7: Different heat integrated reactor concepts for combining end- and exothermic reactions.

one reactor with regenerative heat exchange (Fig. 2.7 B) (Levenspiel 1988). Kulkarni and Duduković investigated the RE-GAS process theoretically in simulation studies (Kulkarni and Duduković 1996). An industrialized process that is performed in a asymmetric and regenerative manner (Fig. 2.7 D) is the Catofin process that has already been introduced in Section 2.1 (Won et al. 2010; Zeeshan Nawaz 2016). Levenspiel also introduced the EX-GAS process concept for coal gasification where both reactions are performed in asymmetric operation with recuperative heat exchange (Fig. 2.7 C) (Levenspiel 1988).

Detailed studies of asymmetric combinations of reactions with recuperative and regenerative heat transfer have been performed by van Sint Annaland (van Sint Annaland, Scholts, et al. 2002b; van Sint Annaland, Scholts, et al. 2002a). In that work the combination of non oxidative propane dehydrogenation with hydrocarbon burning was investigated. An additional advantage of this process is the regeneration of the catalyst during the exothermic reaction. The reactor concepts studied in that work are shown in Fig. 2.8.

For the sake of completeness, chemical looping must be mentioned at this point. Chemical looping can be understood as a material variant of the heat transfer concepts presented here. The principle describes a regenerative transfer of atoms with the aid of an auxiliary material instead of the transfer of latent heat stored in the reaction bed. In such a process it is possible to perform a full oxidation e.g. of a fuel in one phase of the process by reducing the chemical looping material. In a regeneration phase the material has to be reoxidized again. The goal of this process, known as Chemical Looping Combustion (CLC), is to produce heat by combustion of the fuel. The produced CO_2 is not diluted with air, which makes a consecutive CO_2 capture more efficient. H_2O can be easily separated by condensation. The same principle can be used for partial oxidation and selective oxidation and other processes as summarized by Zeng et al. (Zeng et al. 2018).

Goal of this thesis is the combination of the heat integration as introduced in Section 2.2.2 and membrane reactors in distributor configuration in Section 2.2.1. An evaluation of new reactor concepts, that are not easily set up in laboratory and pilot scale, by using modeling and simulation is an important step in reaction engineering. Avoiding unnec-

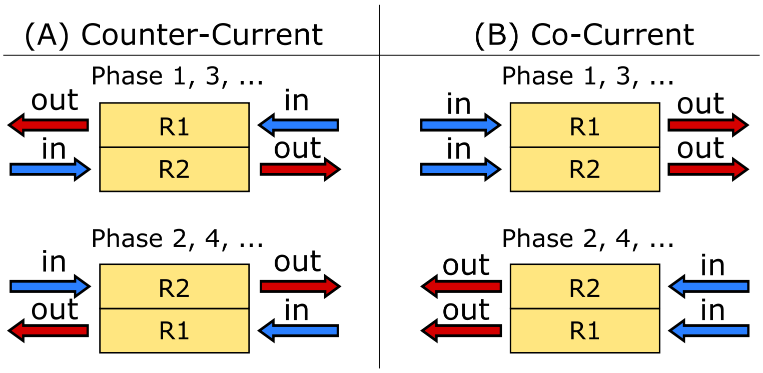

Figure 2.8: Flow regimes for asymmetric combination of endo- and exothermal reactions in a reactor with recuperative heat transfer proposed by van Sint Annaland (van Sint Annaland, Scholts, et al. 2002b; van Sint Annaland, Scholts, et al. 2002a).

essary experiments helps to save money and time in process design. The foundation of modeling and therefore simulation of chemical reactors are balance equations for mass, energy and momentum. The next chapter aims to provide the theoretical background on reactor modeling as conducted in this work. All necessary balance equations for both 1D and 2D modeling are derived and the kinetic expressions to describe chemical reactions are introduced (Section 2.3.2). Special emphasis is put on modeling approaches for coke build-up and deactivation of the catalyst (Section 2.3.3) as well as the consecutive catalyst regeneration (Section 2.3.4).

2.3 Modeling

Reactor modeling is a crucial part of chemical reaction engineering since the beginning of the discipline (Kockmann 2019). Different models for reactor modeling have evolved over time together with the computational capabilities. Fig. 2.9 gives an overview of the most prominent approaches for reactor modeling that differ in applicability, degree of detail, level of abstraction and the number of parameters involved (Stegehake, Riese, et al. 2019). The simplest modeling approaches are estimation methods that originate from process safety considerations and evaluate potential hazards, e.g. critical temperatures (AIChE 1995). These models do not intend to deliver a high degree of detail and are rather simple, which results in a high applicability for basic reactor design. The number of parameters needed is also low, which makes it possible to use them in early stages of the design process. Models following this approach are still widely used for specific fundamental considerations in reaction engineering.

For detailed reactor design more sophisticated methods are needed. The most common modeling methods are continuum methods. In these models the reactor is treated as a continuous model phase. Homogeneous continuum models and heterogeneous continuum models can be distinguished. Both use differentiable equations to describe concentration and temperature spatially and temporally. Transport properties and physical properties of solid and fluid phases are usually included. The different continuum models offer the

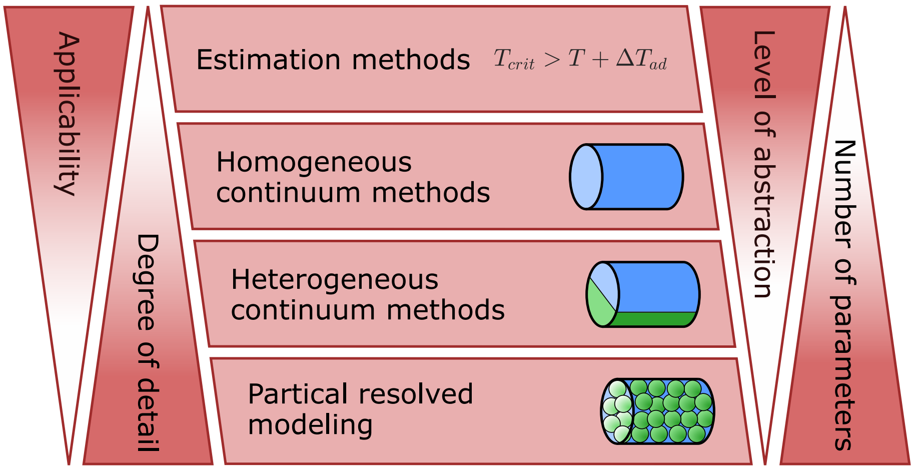
Applicability
Degree of detail
Estimation methods $T_{crit} > T + \Delta T_{ad}$
Homogeneous continuum methods
Heterogeneous continuum methods
Partical resolved modeling
Level of abstraction
Number of parameters

Figure 2.9: Classification of continuums models (adapted from Stegehake, Riese, et al. 2019).

possibility to realized models with a broad range of levels of detail, depending on the system, that has to be modeled (Iordanidis 2002). Since continuum models are still the most prominent and most widely used class of models, they will be discussed in more detail in Section 2.3.1.

A less common modeling approach are cell models. They have been introduced by Deans and Lapidus in the 1960 (Deans and Lapidus 1960a; Deans and Lapidus 1960b) and describe a chemical reactor as a combination of simpler systems, usually Contiuous Stirred Tank Reactors (CSTR). The dimension of the cells depends on catalyst particle size (Elnashaie 1994; Stegehake, Riese, et al. 2019). The number of cells also determines the back mixing properties of the system. A overview on early publications on cell models is presented by Elnashaie (Elnashaie 1994). Illustrations of different cell models including the governing equations have been published by Ioranidis (Iordanidis 2002).

A relatively new category of reactor models are particle resolved models (Fig. 2.9). They allow to take complex geometries into account and usually a high accuracy is possible. Dixon et al. give an overview on CFD approaches in reactor modeling that focuses on particle resolved modeling methods (Dixon et al. 2006). Jurtz et al. reviewed the latest advances in that field and present the steps involved in particle resolved methods in detail (Jurtz et al. 2019). Particle resolved methods hold great potential for future applications by delivering insights that can not be gained by more traditional approaches. It is for example possible to get information on temperature distributions on the surface of catalyst particles and inhomogenities of the reactor in general (Y. Dong et al. 2018). The biggest disadvantage of particle resolved methods is the high computational demand. Dong et al. report a computational time of several weeks on a computational cluster to model the oxidation of n-butane to maleic anhydride in an industrial size reactor geometry ($ID = 21\,\text{mm}$, $L = 50\,\text{cm}$, random packed hollow cylinder catalyst, network of seven reactions) (Y. Dong et al. 2018). All in all, it can be assumed that particle-resolved models will play a greater role in the future. At present, continuum models remain the main choice for mass applications.

In the following section continuum models will be described in more detail since they will be used in this work to model reactors of different sizes and geometries.

2.3.1 Continuum Models

Continuum models are the most common method for reactor modeling. They can be categorized according to Fig. 2.10. The structure of the catalyst bed is not exactly described by continuum models but is treated as a continuum instead. Principles of heat and mass transfer are considered in terms of effective parameters, that include the underlying mechanisms implicitly. Generally, homogeneous and heterogeneous continuum models can be distinguished.

Homogeneous models consider catalyst and fluid phase as one continuum without any gradients between solid and fluid phase whereas heterogeneous continuum models consider both catalyst and fluid as separate continuous phases. Therefore, the heat and mass transfer between the fluid phase and the catalyst have to be taken into account. Additionally, it is possible to consider internal gradients in the catalyst particle.
Both homogeneous and heterogeneous model approaches have their own specific advantages and disadvantages. Homogeneous models describe the reactor not as realistic as heterogeneous models. They are not able to distinguish between the temperature of the solid and the fluid phase separately. Since the reaction in catalyzed reactions takes place at the catalyst surface, the temperature of the catalyst has to be taken into account for kinetics. Especially in very exothermic or endothermic reactions, the temperature of the solid and the fluid can differ significantly. One downside of heterogeneous models is that more than twice as many parameters are needed for the calculations. This can lead to greater uncertainties, since all these parameters have to be determined experimentally. Homogeneous models, on the other hand, represent a good compromise between the level of detail and the computational effort.

Another category to differentiate reactor models is the spatial dimension. The homogeneous and the heterogeneous modeling approach can be used to set up 1D and 2D models. In a conventional tubular reactor for heterogeneously catalyzed reaction 1D models usually consider only the axial coordinate and 2D models both axial and radial dimensions. 2D models furthermore differ in the way they describe the heat transfer from the continuous phase inside the reactor to the reactor walls. Generally α_w and $\lambda(r)$ models can be distinguished. α_w models can be described as heat transfer models and $\lambda(r)$ models as heat conduction models (Winterberg and Tsotsas 2000; Winterberg, Tsotsas, et al. 2000). Both will be presented in the following section in more detail.
Further distinctions can be made between the flow characteristics of different models. The velocity of the gas flows in the reactor can be considered to be constant ($u = u_0$, plug flow) or it can differ along the radial coordinate due to differences in porosity and no slip boundary conditions ($u = f(r)$). Axial resolution of the flow velocity due to reaction and pressure losses is also possible ($u = f(r, z)$). Crucial for an accurate description of the reactor is also to consider thermodynamic properties of fluids and solids as non-constant. This is possible by implementing widely used empirical equations that can be found in different handbooks (Yaws 1999; VDI e. V. 2010; Hirschberg 1999). A comprehensive list of decision criteria to decide which level of detail and which modeling approach is available in literature (Stegehake, Riese, et al. 2019).

A more detailed overview of different reactor models focusing on continuum models is given by Stegehake et al. (Stegehake, Riese, et al. 2019). Adler summed up the state of the art of reactor modeling for heterogeneously catalyzed reactors with focus on continuum models including useful simplifications and catalyst deactivation focusing on the practitioner (Adler 2000b; Adler 2000a). The next section will focus on homogeneous continuum models since these models are used in this work. That includes the α_{w} and $\lambda(r)$ approach and the distinctive differences of both models.

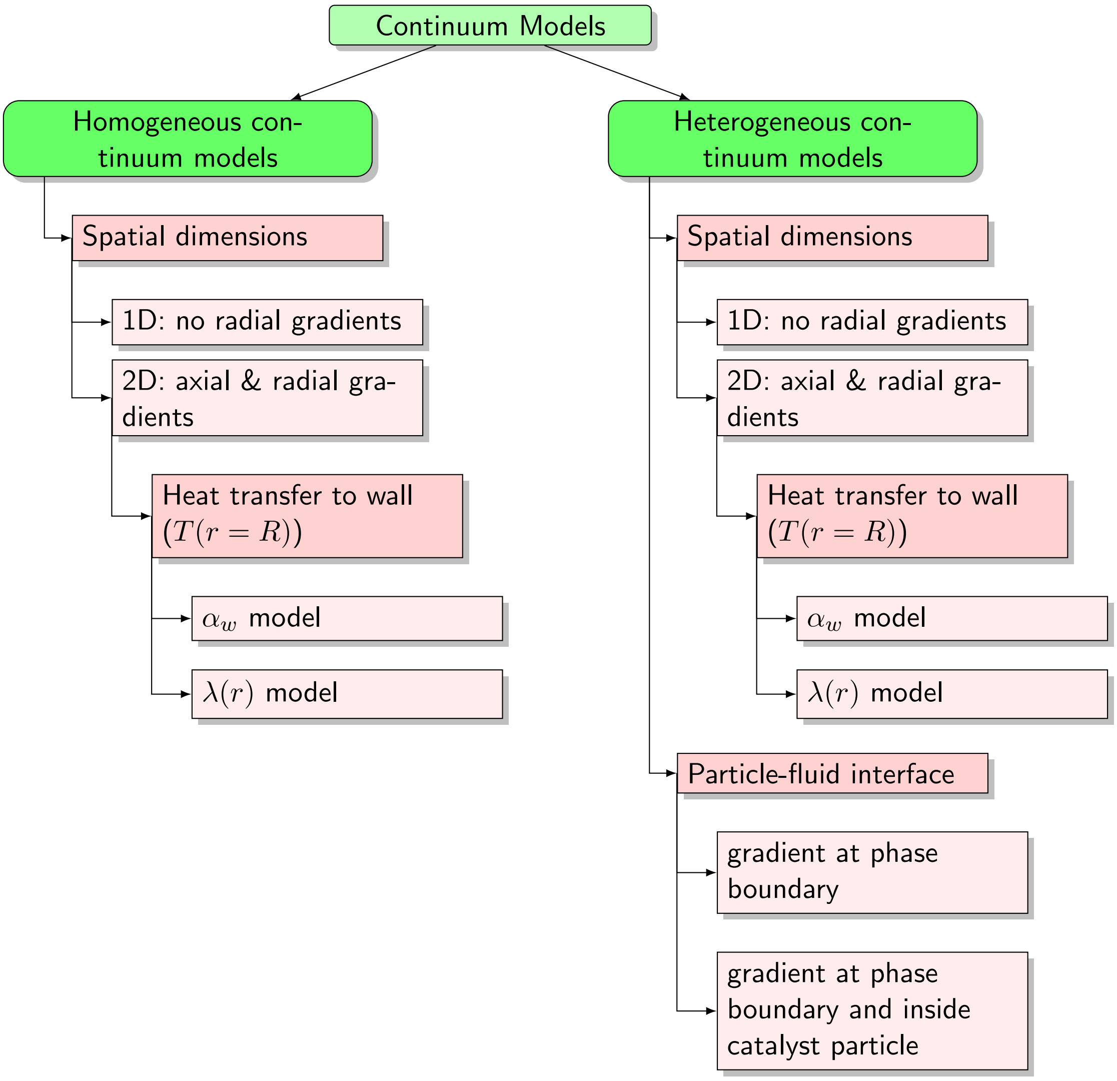
Continuum Models
Homogeneous continuum models
Spatial dimensions
1D: no radial gradients
2D: axial & radial gradients
Heat transfer to wall ($T(r = R)$)
α_w model
$\lambda(r)$ model
Heterogeneous continuum models
Spatial dimensions
1D: no radial gradients
2D: axial & radial gradients
Heat transfer to wall ($T(r = R)$)
α_w model
$\lambda(r)$ model
Particle-fluid interface
gradient at phase boundary
gradient at phase boundary and inside catalyst particle

Figure 2.10: Different continuum model approaches (Stegehake, Riese, et al. 2019).

Balance equations Continuum models are usually based on balance equation. The general equations do not depend on the form of the equipment used or the reaction and nature of the medium. By focusing on the phenomena that need to be described in order to model a reactor, the complexity can be reduced to the following aspects:

- Chemical reaction
- Transfer of mass
- Transfer of heat

- Transfer of momentum

Reaction rate equations will be covered in Section 2.3.2. This section deals with continuity, energy and momentum equations that are the basis of reactor modeling. The general form of these equations is presented in Eq. (2.11) for a mass balance in a volume element (Froment, Bischoff, and Wilde 2011).

$$\begin{aligned}\boxed{\text{Accumulation}} &= \boxed{\text{Incoming flows}}\\ &-\boxed{\text{Outgoing flows}}\\ &+\boxed{\text{Sources/Sinks}}\end{aligned} \tag{2.11}$$

If the control column consists of more than one phase, such an equation is needed for each of these phases. The accumulation of mass can be calculated as the sum of incoming and outgoing mass flows and sources and sinks in the considered volume element. Energy and momentum equations follow the same principle and are therefore not written down separately in this work. Most striking are the similarities of energy and mass balances. Incoming and outgoing flows of both mass and energy can be caused by convection. For mass balances, diffusion must also be considered. The analogy to mass diffusion in energy balances is conduction of heat. Sinks and sources for mass and energy in reactors are usually chemical reactions. In momentum balances, the sinks and sources can be caused by the influence of pressure or shear stress. In chemical reactor modeling, momentum balances typically consider only pressure drop and friction.
These general equations can be simplified according to the reactor type or operational conditions e.g. the accumulation is zero at steady state, which simplifies the equations. For an ideally mixed reactor type without any temperature or concentration gradients (Batch Reactor (BR), Continuous Stirred Tank Reactor (CSTR)) the whole reactor can be treated as the control volume, which simplifies the equations further in comparison to Plug Flow Tubular Reactors (PFTR) where infinitesimally small control volumes have to be considered. In that way balance equations of different complexity can result from the general balance equations.

Mass balance equation A general form of a mass balance equation for component i is given by

$$\underbrace{\frac{\partial c_i}{\partial t}}_{\text{Accumulation}} = \underbrace{-\nabla \cdot (c_i \mathbf{u})}_{\text{Convection}} \underbrace{-\nabla \cdot \mathbf{J}_i}_{\text{Divergence}} \underbrace{+R_i}_{\text{Reaction}} \quad , \quad R_i = \sum_j^M \nu_{i,j} r_j \tag{2.12}$$

The term $\mathbf{J}_i$ is the molar flux vector of the component i. For perfectly laminar flows, $\mathbf{J}_i$ results from the diffusivity. In packed beds additional mixing effects caused by the packing are considered in $\mathbf{J}_i$ as well. The total rate of change R_i of the component i describes the influence of all individual reaction rates r_j of the reaction j weighted by the stoichiometric factor $\nu_{i,j}$. Empirical equations for this can be found in literature (Hertwig et al. 2018). In heterogeneous systems, consisting of more then one phase a separate equation is needed for every phase. These phases are usually connected by additional terms that account for the mass transfer between the phases. In this work only homogeneous models are considered. Further details on modeling equations for heterogeneous models can be found elsewhere (Froment, Bischoff, and Wilde 2011; Stegehake, Riese, et al. 2019). Additional terms specifically for reactor modeling are added later on.

Energy balance equation The energy balance of a control volume can be described by

$$\sum_i^N M_i c_i c_{p,i}\Bigg(\underbrace{\frac{\partial T}{\partial t}}_{\text{Accumulation}} + \underbrace{\mathbf{u}\cdot\nabla T}_{\text{Convection}} \Bigg) = \underbrace{\sum_j^M (-\Delta H_j)\, r_j}_{\text{Reaction}} + \underbrace{\nabla\cdot(\lambda\nabla T)}_{\text{Conduction}} - \underbrace{\sum_i^N \mathbf{J}_i \nabla H_i}_{\text{Diffusion}} + \underbrace{\dot{Q}_{\text{rad}}}_{\text{Radiation}} \tag{2.13}$$

where M_i and $c_{p,i}$ are the molar mass and the specific heat of fluid i at constant pressure, respectively. Conduction is described by the thermal conductivity λ. The heat flux due to radiation $\dot{Q}_{\text{rad}}$ is usually neglected and only considered at very high temperatures. There are also approaches lumping together the radiation in an effective heat conduction term. Again, for more than one phase a specific equation for every phase is needed including a phase transfer term.

Momentum balance The momentum balance is described by the Navier-Stokes equation:

$$\underbrace{\frac{\partial}{\partial t}(\rho_f \mathbf{u})}_{\text{Change in time}} + \underbrace{\nabla\cdot(\rho_f \mathbf{uu})}_{\text{Convection}} = \underbrace{-\nabla p}_{\text{Pressure}} - \underbrace{\nabla\boldsymbol{\tau}}_{\text{Shear}} + \underbrace{\rho_f \mathbf{g}}_{\text{Gravity}} \tag{2.14}$$

Shear stress is specified by the shear stress tensor $\boldsymbol{\tau}$. The variable $\boldsymbol{g}$ defines the acceleration by gravity. Bird et al. describes the derivation of all balance equation in much more detail (Bird et al. 2007). The reader may be referred to their book for further information. To be able to solve these general equations for specific problems it is necessary to simplify them by taking various assumptions as described in the following sections. First the equations for a homogeneous 1D model will be discussed. After that the 2D models used in this work are introduced.

Homogeneous 1D models In homogeneous models of heterogeneous catalyzed reactors the influences fluid phase and the solid catalyst phase have to be distinguished in the equations. For that reason, porosity $\varepsilon = \frac{V_{\text{f}}}{V_{\text{R}}}$ is introduced that describes the ratio between the volume of void space, in this case usually filled with a fluid, V_{f} and the total volume of the reactor V_{R}. A mass balance for a fluid component i reads

$$\varepsilon\frac{\partial c_i}{\partial t} = \varepsilon D_{\text{ax},i}\frac{\partial^2 c_i}{\partial z^2} - \frac{\partial(u_0 c_i)}{\partial z} + \rho_{\text{bed}}(-R_i^{\text{m}}), \quad R_i^{\text{m}} = \sum_j^M \nu_{i,j} r_j^{\text{m}} \tag{2.15}$$

In this equation the total change rate R_i^{m} and the reaction rate $r_{i,j}^{\text{m}}$ are related to the catalyst mass, as indicated by the superscript m, which is in heterogeneous catalysis more convenient than relating it to the reactor volume. Volume-related and mass-related reaction rates can be converted into each other by

$$r_j\, V_{\text{R}} = r_j^{\text{m}}\, m_{\text{cat}} \tag{2.16}$$

$$r_j = \rho_{\text{bed}} r_j^{\text{m}} \tag{2.17}$$

with the bed density

$$\rho_{\text{bed}} = \frac{m_{\text{cat}}}{V_{\text{R}}}. \tag{2.18}$$

The mass diffusion is described in the 1D mass balance by the diffusion coefficient $D_{\mathrm{ax},i}$ for component i.
Eq. (2.15) can be simplified by assuming steady state and neglecting the influence of diffusion and then becomes

$$\frac{\partial(u_0 c_i)}{\partial z} = \frac{m_{\mathrm{cat}}}{V_{\mathrm{R}}} \sum_j^M \nu_{i,j} r_j^{\mathrm{m}} \tag{2.19}$$

The concentration can be replaced by $c_i = \frac{\dot{n}_i}{\dot{V}}$ with the assumption that $\dot{V}$ is constant. The superficial velocity can further be replaced by $u_0 = \frac{\dot{V}}{A}$, where A denotes the cross-sectional area of the reactor. The equation then reads

$$\frac{1}{A}\frac{\partial \dot{n}_i}{\partial z} = \frac{m_{\mathrm{cat}}}{V_{\mathrm{R}}} \sum_j^M \nu_{i,j} r_j^{\mathrm{m}} \tag{2.20}$$

Considering that the total reactor volume can be written as $V_{\mathrm{R}} = LA$ gives

$$\frac{\partial \dot{n}_i}{\partial z} = \frac{m_{\mathrm{cat}}}{L} \sum_j^M \nu_{i,j} r_j^{\mathrm{m}} \tag{2.21}$$

Eq. (2.21) is later on used to model the lab scale reactor in Chapters 3 and 4.

The energy balance has been modified similar to the mass balance and now reads

$$[\rho_p c_{p,p}(1-\varepsilon) + \rho_f c_{p,f}\varepsilon] \frac{\partial T}{\partial t} = \lambda_{\mathrm{ax}} \frac{\partial^2 T}{\partial z^2} - \rho_f u_0 c_{p,f} \frac{\partial T}{\partial z} - h\left(\frac{\partial A}{\partial V}(T - \bar{T}_{\mathrm{w}})\right) + \rho_{\mathrm{bed}} \sum_j^M r_j^{\mathrm{m}}(-\Delta H_{R,j}) \tag{2.22}$$

The contributions of the catalyst particles denoted with the subscript p and the fluid phase is marked by the subscript f. The parameter λ_{ax} describes the heat conductivity in axial direction. The radial direction is neglected in the 1D models. The heat transfer to the wall of the reactor is modeled in this simple model with a driving force approach, where the temperature difference between the temperature T inside the reactor and the mean temperature of the wall $\bar{T}_{\mathrm{w}}$ is the driving force and h is the heat transfer coefficient. The variable u_0 denotes the superficial velocity in the reactor. Further simplifications of the energy balance equations similar to the mass balance ((2.19) - (2.21)) are not presented here because, for reasons discussed later, the reactors modeled in 1D are assumed to be isothermal.

In this work, the moment balances were not explicitly solved for the 1D models and are therefore not described separately at this point.

Homogeneous 2D models By extension of the 1D models by a radial spatial variable, 2D models can be created. 2D models are in general more suitable to describe high exothermic reactions in cooled reactors due to the large influence of radial profiles in these applications.

The heat transfer from the catalyst bed to the reactor walls are of special importance. This heat transfer is influenced by increasing porosity and therefore higher flow velocities at the reactor walls. The most common α_w model and $\lambda(r)$ model are introduced in the following sections. The mass balance equations and heat balance equations are the same for both modeling approaches.
Based on the general formulation, the mass balance of the 2D homogeneous models is

$$\varepsilon\frac{\partial c_i}{\partial t} = -\varepsilon\frac{\partial(u_z c_i)}{\partial z} - \frac{1}{r}\varepsilon\frac{\partial(r u_r c_i)}{\partial r} + D^\mathrm{eff}_{\mathrm{ax},i}\frac{\partial^2 c_i}{\partial z^2} + \frac{1}{r}\left(D^\mathrm{eff}_{\mathrm{rad},i} r\frac{\partial^2 c_i}{\partial r^2}\right) + (1-\varepsilon)\rho_\mathrm{bed}\sum_j^M \nu_{i,j} r_j^\mathrm{m} \tag{2.23}$$

In Eq. (2.23) the velocity has been split into a radial component u_r and an axial component u_z. Similarly, the diffusion coefficients have been split into a radial diffusion coefficient $D^\mathrm{eff}_{\mathrm{rad},i}$ and an axial diffusion coefficient $D^\mathrm{eff}_{\mathrm{ax},i}$. The energy balance for the 2D model reads

$$\begin{aligned}&(\varepsilon\rho_f c_{p,f} + (1-\varepsilon)\rho_p c_{p,p})\frac{\partial T}{\partial t} = \\ &-\varepsilon u_z\rho_f c_{p,f}\frac{\partial T}{\partial z} - \frac{1}{r}\varepsilon u_r\rho_f c_{p,f}\frac{\partial(rT)}{\partial r} + \lambda^\mathrm{eff}_\mathrm{ax}\frac{\partial^2 T}{\partial z^2} + \frac{1}{r}\left(\lambda^\mathrm{eff}_\mathrm{rad} r\frac{\partial^2 T}{\partial r^2}\right) + (1-\varepsilon)\rho_\mathrm{bed}\sum_j^M(-\Delta H_{R,j}) r_j^\mathrm{m}\end{aligned} \tag{2.24}$$

The heat conductivities have been also separated in an axial part and a radial part denoted with $\lambda^\mathrm{eff}_\mathrm{ax}$ and $\lambda^\mathrm{eff}_\mathrm{rad}$, respectively. In Eq. (2.23) and (2.24) conductivity coefficients and diffusion coefficients are effective parameters, indicated by the superscript eff. The effective diffusion coefficients also account for dispersion effects caused by the catalyst bed and the effective heat conductivities take the conductivity of the catalyst bed, the fluid and disturbances by the flow into account. For 2D modeling the momentum balance

$$\rho_f\frac{\partial u_0}{\partial t} = -\nabla p + \nabla(\varepsilon\boldsymbol{\tau}) + \frac{\rho_f}{\varepsilon}\nabla u_0^2 + f \tag{2.25}$$

has also been solved. To obtain Eq. (2.25) the fundamental balance equation (2.14) has been modified to account for the momentum change due to the flow through the pores of the catalyst packing and the flow around the particles (Chandrasekhara and Vortmeyer 1979; Ene 2004; Brinkman 1949). Details on the momentum balance equation are given in the Appendix A.1.

As mentioned before, the mass transfer inside the reactor and the heat transfer inside the reactor and especially to the reactor walls is of special importance in 2D modeling approaches. The next paragraphs will shortly summarize the commonly used $\lambda(r)$ and α_w models and will also address there strengths and weaknesses. Both models have been used over the course of this project.

The $\lambda(r)$ model The $\lambda(r)$ model considers radial profiles of porosity. This porosity profile influences the velocity and temperature profiles as illustrated in Fig. 2.11. Due to these detailed velocity and porosity profiles, the temperature profile in the continuum can be described continuously up to the reactor wall, without temperature jumps. Different modeling approaches for the porosity profile and the heat transfer at the wall have been described in literature. An overview of these approaches is given by Stegehake et al.

(Stegehake, Riese, et al. 2019). The modeling in this work follows the procedure described by Tsotsas in the VDI Heat Atlas (Tsotsas 2010; VDI e. V. 2010). All necessary equations are explained in Appendix A.2.1.

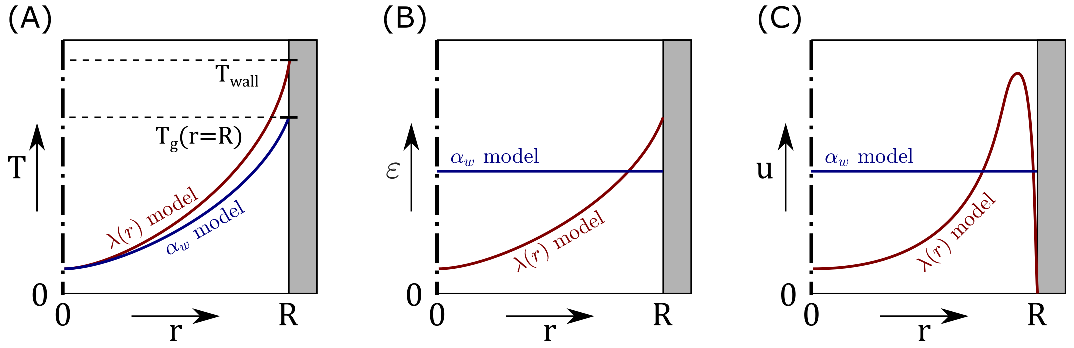

Figure 2.11: Differences of the α_w and the $\lambda(r)$ modeling approaches: (A) Temperature profiles; (B) Porosity profile; (C) Velocity profile.

Compared to other modeling approaches, this model is very complex and detailed, but has a wide range of validity. In some cases, there is a lack of reliable experimental data. The approach was critically evaluated in detail by Stegehake et al. (Stegehake, Grünewald, et al. 2018).

The α_w model The α_w model considers in comparison to the $\lambda(r)$ model a mean porosity $\bar{\varepsilon}$ over the whole radius of the reactor (see Fig. 2.11). Regarding mass transfer parameters, the equation for the axial dispersion coefficient remains unchanged in comparison to the $\lambda(r)$ model (Eq. (A.6)). Instead of a porosity function, the mean porosity $\bar{\varepsilon}$ is used in the equation.

The model is based on the observation that a temperature profile similar to the velocity profile is formed near the wall of the pipe. In the α_w model it is assumed that in a turbulent flow a temperature boundary layer forms at the wall in which the temperature changes from the wall temperature T_w to the temperature of the fluid T_f as shown in Fig. 2.12 (Böckh and Wetzel 2015).

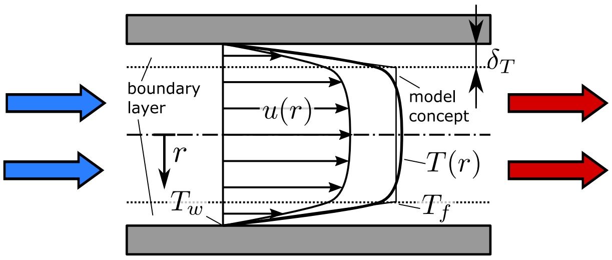

Figure 2.12: Modeling assumptions of the α_w model.

Knowing the width of the boundary layer, the heat transport coefficient α_w can be approximated by

$$\alpha_{\mathrm{w}} \approx \frac{\lambda_f}{\delta_T} \tag{2.26}$$

In most of the cases it is not possible to measure the thin temperature boundary layer. An analytically derivation of δ_T is not possible in turbulent flows and therefore has to be empirically determined on the basis of experiments. To avoid extensive measurements α_{w} is usually determined by empirical correlations that are based on characteristic numbers (Martin and Nilles 1993). Further details on the equations and correlations used in the α_{w} model are given in the Appendix A.2.2.

The heat transport coefficient α_{w} describes the heat transfer between the tube wall and the inner part of the reactor. The driving force is the difference between the temperature of the reactor wall T_{w} and the temperature T_f of the continuum inside the reactor at the wall. The width of the boundary layer δ_T is neglected. This creates a discontinuity in the temperature field between the core and the reactor wall, which is an artificial third-order boundary condition in modeling (see Tab. 2.2). The simplified view in the form of a temperature jump at the reactor wall represents an inherent weakness of the model structure. Due to this discontinuity, it is only possible to a limited extent to represent reality with the model. This weakness is especially important for small tube diameters and strongly exothermic reactions. Nevertheless, the model is often used in the field due to its simple mathematical structure and has proven to be useful in different applications.

Boundary Conditions To be able to solve the modeling equations numerically for the different reactor concepts, it is necessary to define boundary conditions. The different reactor concepts that are investigated in this work are illustrated in Fig. 2.13. The different boundary conditions are indicated by number from ① to ⑤. Position ① describes the reactor inlets, position ② the reactor outlets, position ③ the center line of the axial symmetric tubular reactor. The walls of the reactor are either indicated by ④ or by ⑤. Position ④ specifies non-permeable, non-porous reactor walls whereas position ⑤ specifies the porous membrane walls.

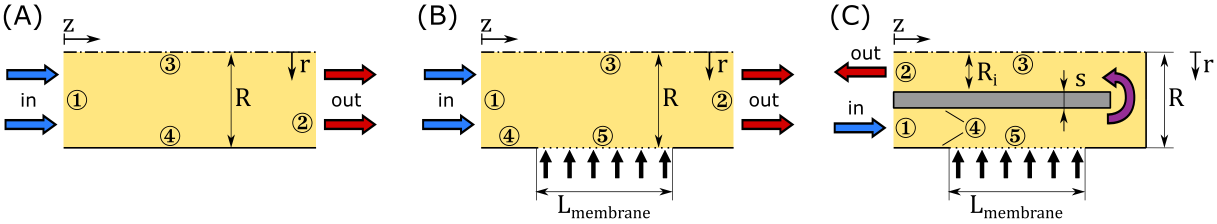

Figure 2.13: Boundary conditions for different reactor concepts: (A) Fixed Bed reactor (FBR), (B) Packed Bed Membrane Reactor (PBMR), (C) integrated Packed Bed Membrane Reactor (PBMRint).

The mathematical formulation of these boundary conditions are given in Tab. 2.2. The boundary conditions are of different mathematical complexity. At position ① a Dirichlet boundary condition is implemented (1^{st} order boundary condition) that defines a constant value (e.g. $c_i = c_i^{\mathrm{in}}$). The same type of boundary condition is used for solving the momentum balance at position ④ (no-slip boundary condition) (Deuflhard and Weiser 2020).

Table 2.2: Boundary conditions for different modeling approaches in reactor modeling: (A) Boundary condition for α_w model; (B) Boundary conditions for the $\lambda(r)$ model.

Boundary conditions	Mass balance	Energy balance	Momentum balance
①	$c_i = c_i^\mathrm{in}$	$T = T^\mathrm{in}$	$0 = -p^\mathrm{in}\bar{n}$
②	$\bar{n}D_i^\mathrm{eff}\nabla c_i = 0$	$\bar{n}\lambda^\mathrm{eff}\nabla T = 0$	$(-p(I) + \boldsymbol{\tau})\bar{n} = -p_0\bar{n}$
③	$\bar{n}(D_i^\mathrm{eff}\nabla c_i - c_i u_0) = 0$	$\bar{n}(\lambda^\mathrm{eff}\nabla T - (\rho c_p)_f T u_0) = 0$	$-\bar{n}u_0 = 0$
④	$\bar{n}(D_i^\mathrm{eff}\nabla c_i) = 0$	(A): $\bar{n}\lambda^\mathrm{eff}\nabla T = \alpha_w(T - T_w)$ (B): $T = T_w$	$u_0 = 0$
⑤	$\bar{n}(D_i^\mathrm{eff}\nabla c_i - c_i u_0) = n u_0 c_i^\mathrm{in}$	(A): $\bar{n}\lambda^\mathrm{eff}\nabla T = \alpha_w(T - T_w)$ (B): $T = T_w$	$u_{0,z} = 0,$ $u_{0,r} = \frac{\dot{V}_{ss}}{A_\mathrm{membrane}}$

At position ② and ⑤ the Danckwerts boundary condition is used (Danckwerts 1953). The α_w model requires for the energy balance at positions ④ and ⑤ a Robin boundary condition (3^{rd} order boundary condition). Using the λ_w model changes the heat balance boundary condition at position ④ and ⑤ to a Dirichlet boundary condition ($T = T_w$).

To be able to solve both energy and mass balances it is necessary to be able to describe the reaction kinetics depending on temperature and the concentration of the reactants. Reaction kinetics are the link between the mass and energy balances. The next section aims to introduce the most common ways to model reaction kinetics in a comprehensive way with special emphasis on reaction kinetics of the ODH reaction and the reaction network present when combining ODH and TDH.

2.3.2 Reaction Kinetics

Chemical reaction kinetics are a crucial part of chemical reaction engineering and the essential key for reactor and process development and optimization, respectively. They express the dependencies between the reaction conditions (temperature, concentration, pressure, etc.) and the rate in which a reactant is consumed or produced under these conditions. Generally mechanistic and empirical kinetic models can be distinguished. A mechanistic model represents all concepts regarding the nature, sequence and rate of different elementary steps leading to an appropriate mathematical rate expression for the reaction considered. A systematic procedure for setting up a mechanistic model is for example described by Helfferich (Helfferich 2004). A deep knowledge of all steps involved is necessary for mechanistic models. The synthesis of these models can be supported by methods in computational quantum chemistry like Density Function Theory (DFT) (Carrero et al. 2014). Since the determination of molecular mechanisms is still difficult, different conclusions about molecular mechanisms can be drawn from the same results.
Empirical kinetic models on the other hand are functional dependencies under certain experimental conditions based on a specific set of experimental data. The validity of these models is generally limited to the experimental conditions in which the experiments have been performed. For both approaches, kinetic experiments are still crucial in identifying intermediates, nature of reaction routes (consecutive/parallel) or rate determining steps.

They are a valuable starting point for the elucidation of the molecular mechanism. The models mainly used to describe the ODH and TDH of light alkanes are

1. Eley-Rideal model
2. Langmuir-Hinshelwood model
3. Mars-van Krevelen model
4. Power Law model

Model 1 - 3 consider the molecular mechanism. Model 4 is usually used for empiric description of the reaction rate. Further details on these models are given in the following paragraphs. The different models are explained using the following, simple model reaction:

$$\mathrm{A} + \mathrm{B} \xrightarrow{k} \mathrm{C} \tag{2.27}$$

It is assumed that the reactants and products of the example reaction are present in gaseous form. Therefore, partial pressure is used instead of concentrations in the rate laws. This is in accordance with the dehydrogenation of propane, in which the reactants are also present in the gaseous phase.

Eley-Rideal Model The Eley-Rideal model (Eley and Rideal 1941; Rideal 1939) assumes the adsorption of reactant A (Eq. (2.28)) and a consecutive reaction of the adsorbed species with the gaseous component B (Eq. (2.29):

$$\mathrm{A_g} \overset{K_\mathrm{A}}{\rightleftharpoons} \mathrm{A_{ads}} \tag{2.28}$$

$$\mathrm{A_{ads}} + \mathrm{B_g} \longrightarrow \mathrm{C_g} \tag{2.29}$$

Considering Lanngmuirs approach for adsorption gives

$$r = \frac{kK_\mathrm{A}p_\mathrm{A}}{1 + K_\mathrm{A}p_\mathrm{A}} \tag{2.30}$$

for the overall reaction with the equilibrium constant K_A of the adsorption reaction (Eq. (2.28)) and the rate constant k of the overall reaction (Eq. (2.27)).

Langmuir-Hinshelwood Model The Langmuir-Hinshelwood model has been developed by Hinshelwood on the findings of Langmuir (Langmuir 1922; Hinshelwood 1929). It assumes the adsorption of A (Eq. (2.31)) as well as the adsorption of reactant B (Eq. (2.32). Both adsorbed species react and form the product C that also adsorbs at the catalyst (Eq. (2.33)).

$$\mathrm{A_g} \rightleftharpoons \mathrm{A_{ads}} \tag{2.31}$$

$$\mathrm{B_g} \rightleftharpoons \mathrm{B_{ads}} \tag{2.32}$$

$$\mathrm{A_{ads}} + \mathrm{B_{ads}} \longrightarrow \mathrm{C_{ads}} \rightleftharpoons \mathrm{C_g} \tag{2.33}$$

This approach can be varied by assuming different rate determining steps or adsorbing components.

Mars-van Krevelen Model and Redox Models The Mars-van Krevelen model (Mars and van Krevelen 1954) considers the variation in the oxidation state of the active catalyst. The models described so far focus on the reaction itself. Models based on this principle are also called Redox Models. The reduction step is illustrated in Eq. (2.34), where the catalyst is reduced and the hydrocarbon is selectively oxidized. In another oxidation step (Eq. (2.35)) the catalyst is re-oxidized.

$$\text{hydrocarbon} + \text{oxidized catalyst} \longrightarrow \text{products} + \text{reduced catalyst} \tag{2.34}$$

$$\text{oxygen} + \text{reduced catalyst} \longrightarrow \text{oxidized catalyst} \tag{2.35}$$

This approach is still widely used although there is criticism due to the thermodynamic inconsistency of the original approach (Vannice 2007). Steady state adsorption models can be seen as variants of the Mars-van Krevelen model (Grabowski 2006).

Power Law Model Deriving a mechanistic model can be difficult due to the complex nature of surface reactions and the lack of knowledge of elementary steps. A fast approach to describe the kinetic behavior is the power law approach

$$r = k p_{\mathrm{A}}^{\alpha} p_{\mathrm{B}}^{\beta} \tag{2.36}$$

where α and β represent the reaction order that usually have to be determined experimentally.

The power law model is advantageous due to its relative simplicity and ease of application. The mathematical effort for the use of the power law approach in complex reactor simulations is lower than for other approaches. It can be adapted to various types of reactions, both elementary and complex, offering a general framework for expressing reaction rates. However, due to its lack of mechanistic details on the reaction steps and intermediates, the power law model falls short in providing a deeper understanding of the underlying chemistry. Moreover, caution is necessary when extrapolating the model beyond the experimental data range, as the behavior of the reaction at extreme conditions might not adhere to the same trend observed within the experimental range.

All kinetic approaches presented can be combined to describe different reactions in a given reaction network. The equations presented here can vary according to other assumptions about rate determining steps or adsorption behavior. More details on the approaches including the detailed derivations can be found in textbooks and are not given in detail in this work.

The temperature dependency of reaction kinetics can be modeled using an Arrhenius approach (Arrhenius 1889a; Arrhenius 1889b; Laidler 1984) that relates the rate constant

k_j of reaction j to the activation energy $E_{A,j}$ and the temperature T by

$$k_j = k_{0,j} \exp\left(\frac{-E_{A,j}}{RT}\right) \tag{2.37}$$

with the universal gas constant R and the pre-exponential factor $k_{0,j}$ for reaction j. Due to the strong correlation between the parameters in the Arrhenius equation, it is the parameters are very difficult to fit numerically to experimental data. For this reason, different temperature-centered approaches are discussed, which have already been applied to similar problems (Schwaab and Pinto 2007). One of these approaches (Eq. (2.39) - (2.40)) is also used in this work and follows from the integration of the differential form of the Arrhenius approach.

$$k_j = \exp\left[a + B\left(\frac{T - T_{\mathrm{ref}}}{T}\right)\right] \tag{2.38}$$

$$A_j = \ln\left(k_0\right) - \frac{E_A}{RT_{\mathrm{ref}}} \tag{2.39}$$

$$B_j = \frac{E_A}{RT_{\mathrm{ref}}} \tag{2.40}$$

In this form, instead of parameters $k_{0,j}$ and $E_{A,j}$, parameters A_j and B_j are fitted to the experimental data and a reference temperature T_{ref} has to be defined.

Reaction network and reaction kinetics of ODH and TDH An overview about kinetic approaches describing the ODH is given by Grabowski (Grabowski 2006). A critical review that also considers DFT calculations is given by Carrero et al. (Carrero et al. 2014). Literature mainly agrees on the Mars-van Krevelen model to describe the ODH reaction on vanadia catalysts best. Side reactions that are considered during ODH are often partial and total oxidation reactions of the reactant propane as shown in Eq. (2.41) and (2.42)

$$\mathrm{C_3H_8} + 5\,\mathrm{O_2} \longrightarrow 3\,\mathrm{CO_2} + 4\,\mathrm{H_2O} \tag{2.41}$$

$$\mathrm{C_3H_8} + 3.5\,\mathrm{O_2} \longrightarrow 3\,\mathrm{CO} + 4\,\mathrm{H_2O} \tag{2.42}$$

Due to the higher reactivity of unsaturated alkenes, it is also likely that the product propene oxidates to CO or CO_2 as illustrated in Eq. (2.43) and (2.44).

$$\mathrm{C_3H_6} + 4.5\,\mathrm{O_2} \longrightarrow 3\,\mathrm{CO_2} + 3\,\mathrm{H_2O} \tag{2.43}$$

$$\mathrm{C_3H_6} + 3\,\mathrm{O_2} \longrightarrow 3\,\mathrm{CO} + 3\,\mathrm{H_2O} \tag{2.44}$$

Kinetic investigations on the TDH of propane mainly focus on Pt and Pt-Sn catalysts, since they are known to show the best performance for this reaction (see Section 2.1.2, Tab. 2.1). Common side reactions that are also considered with TDH reactions are cracking and coking reactions. The kinetic models mainly describe the TDH with Langmuir-Hinshelwood approaches of different complexity (Sui et al. 2014; Lobera et al. 2008; Sheintuch, Liron, et al. 2016).

In this thesis, the focus is on the combination of ODH and TDH in one apparatus. The experimental studies aim at an investigation of a large operating range, therefore the inclusion of all relevant side reactions in the reaction network applied is of particular importance. Kinetic studies that consider TDH and ODH reactions in one network are scarce in literature, although it is known that both reactions can occur, for example, on VO_x catalyst, depending on the oxidation state of the catalyst, as already described in Section 2.1.3 (Xiong et al. 2019; Carrero et al. 2014). When TDH and ODH are performed in one reaction volume, the Water Gas Shift (WGS) reaction has to be considered, especially at higher temperatures (Eq. (2.45)).

$$CO + H_2O \underset{\text{RWGS}}{\overset{\text{WGS}}{\rightleftharpoons}} CO_2 + H_2 \tag{2.45}$$

The WGS is limited by a chemical equilibrium. Depending on the reaction conditions, the Reverse Water Gas Shift Reaction (RWGS) can proceed.

A network consisting of ODH, TDH, Water gas shift reaction (WGS), total oxidation of propane to CO_2 and partial oxidation of propene to CO has been introduced by Liebner (Liebner 2003) and used by Hamel et al. (Hamel, Wolff, Subramaniam, et al. 2011). Kinetic parameters of the WGS/RWGS reaction has been taken from literature (Hou and Hughes 2001). Considering oxidation of the reactant C_3H_8 is based on the findings by Chen et al., who detected a direct, primary combustion of C_3H_8 to CO_2 and CO as shown in Eq. (2.41) and (2.42), respectively. This is in contrast to the observation that a significant direct oxidation of propane cannot be monitored according to other sources (Carrero et al. 2014; Dinse et al. 2009).

After reviewing the available literature, the network shown in Fig. 2.14 was chosen for further analyses in this work.

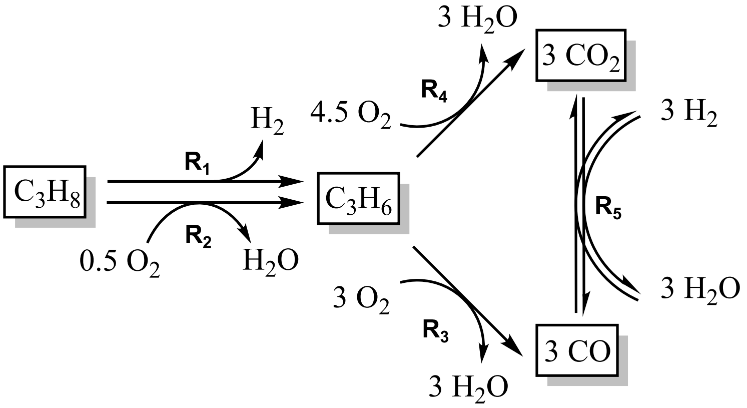

Figure 2.14: Reaction network of the combined TDH and ODH of propane.

Oxidation reactions of the product propane have been neglected according to Carrero et al. In comparison to the network of Liebner and Hamel et al., the total oxidation of propene was added to account for the CO_2 that has been detected in experiments. Coking reactions are not included in the network of main and side reactions because the time constants of these phenomena differ by orders of magnitude. Modeling approaches for coking and deactivation behavior are introduced in the next sections.

2.3.3 Coke Formation and Catalyst Deactivation

Catalyst coking is a known problem in catalysis and has a direct influence on reactor design. Typical time scales of catalyst deactivation can range between years, e.g. for three way catalysts in automotive applications, to seconds, e.g. in fluidized catalytic cracking (FCC). Typical reactor types for different deactivation times are presented in Tab. 2.3 (J. Moulijn et al. 2001).

Table 2.3: Influence of the time scale of deactivation on reactor design.

Typical reactor type	Time scale of deactivation
Fixed bed reactor (FBR), no regeneration	years
FBR, regeneration while offline	↓
Moving bed reactor	
Fluidized bed reactor	
Entrained flow reactor (riser, continuous regeneration)	seconds

Since deactivation is a general problem, simulation of this phenomenon is important for reactor design. The characteristics of the different deactivation mechanisms, e.g. sintering, poisoning etc. are not discussed here. Textbooks and review articles can give an overview about the specific details on that categorization (Argyle and Bartholomew 2015; Levenspiel 1999). In this work only fouling, which means the deposition of unwanted material on the catalyst surface is discussed, since this is the only mechanism relevant for the reaction network investigated in this work.

First approaches to kinetic modeling of coking and deactivation Generally, the modeling approaches for deactivation can be categorized into phenomenological and mechanistic approaches. Phenomenological approaches date back to the 1940s, where Voorhies related the coke content and activity of a catalyst to its time on stream (Voorhies 1945). Early mechanistic modeling approaches for deactivation, related the activity of a catalyst to a certain reactant or product. Eq. (2.46) describes a reaction where a reactant A reacts to a desired product R and a coke precursor P as a side product of the same reaction. The downward arrow implies that this component deposits on the catalyst surface, blocking the active catalytic centers and is therefore responsible for the deactivation of the catalyst.

$$\mathrm{A} \longrightarrow \mathrm{R} + \mathrm{P}\downarrow \tag{2.46}$$

The coke precursor can also be formed in a parallel reaction as shown in Eq. (2.47)

$$\begin{tikzcd} & \mathrm{R} \\ \mathrm{A} \arrow[ur] \arrow[dr] & \\ & \mathrm{P}\downarrow \end{tikzcd} \tag{2.47}$$

Another option is the formation of the coke precursor in a series reaction:

$$\mathrm{A} \longrightarrow \mathrm{R} \longrightarrow \mathrm{P}\downarrow \tag{2.48}$$

Deactivation due to contamination in the feed stream is also possible. That behavior is known as side-by-side deactivation:

$$\begin{aligned} &\mathrm{A} \longrightarrow \mathrm{R} \\ &\mathrm{P} \longrightarrow \mathrm{P}\downarrow \end{aligned} \tag{2.49}$$

The catalyst activity itself is commonly integrated in the mass balance equations in reactor modeling by a catalyst activity coefficient

$$a_j(t) = \frac{r_j(t)}{r_{j,0}} \tag{2.50}$$

that relates the reaction rate $r_j(t)$ at a certain time t to the reaction rate of the fresh catalyst $r_{j,0}$. This also indicates that the catalyst deactivation does not influence all reactions in a reaction network to the same extent. A *selective* deactivation of single reactions can be caused by different active centers at the catalyst surface that are not equally prone to coke deposition. If all reactions are similarly effected by deactivation, the deactivation is *unselective*. The activity factor itself is modeled with an additional balance equation

$$-\frac{da_j}{dt} = k_\mathrm{d} c_i^m a^d \tag{2.51}$$

similar to the other mass balances. In this equation m describes the concentration dependency and d the order of deactivation. For the different coking mechanisms according to Eq. (2.46) - (2.49) the component i might vary. Thus

$$i = \begin{cases} \mathrm{A} & \text{for parallel deactivation} \\ \mathrm{R} & \text{for series deactivation} \\ \mathrm{P} & \text{for side by side deactivation} \end{cases} \tag{2.52}$$

If the deactivation is independent from concentration of reactants or products the exponent m becomes zero and thereby eliminates the concentration dependent term from Eq. (2.51). A combination of these mechanisms is thinkable and can be expressed by altering the equations above. This basic approach relates the deactivation behavior to gas phase concentrations. Several extensions and modifications of this simple model have been presented in literature. Reiff and Kittrell modified the approach to relate the activity to a active site balance. This bears the advantage of better interpretability (Reiff and Kittrell 1980). Carberry presents an approach to describe both sintering and fouling by modifiying the presented equations (Carberry 2001). An advantage of these models is their mathematical simplicity, which makes them suitable for applications where computational time is a bottleneck e.g. in detailed 2D simulation (see Section 4.2).

Coke dependent approaches Besides a direct correlation of deactivation to concentration of the precursor and, after integration of Eq. 2.51, to time on stream it is common to relate the deactivation behavior to the coke content on the catalyst. To do so, it is necessary to be able to describe the coke build-up ($c_\mathrm{coke} = f(c, T)$) and then relate the catalyst activity to the coke deposited on the catalyst surface ($a = f(c_\mathrm{coke})$). Several examples for this approach can be found in literature (Froment and Bischoff 1961; Dumez and Froment 1976; Nam and Kittrell 1984). The deposition of coke in these approaches is usually connected to the coke precursor and follows equation similar to eq (2.51). The connection between coke content and activity is then often described by an empirical equation (Dumez and Froment 1976), e.g.

$$a_j = \exp\left(-\zeta_j c_{\mathrm{coke}}\right) \tag{2.53}$$

$$a_j = \frac{1}{1 + \zeta_j c_{\mathrm{coke}}} \tag{2.54}$$

$$a_j = \frac{1}{\left(1 + \zeta_j c_{\mathrm{coke}}\right)^2} \tag{2.55}$$

An alternative to describe the coke build-up on catalysts was introduced by Nam and Kittrell by taking monolayer and multilayer coke into account (Monolayer Multilayer Coke Growth Model - MMCGM) (Nam and Kittrell 1984). This approach assumes that the coke build-up on the surface of a catalyst can be divided into a monolayer c_{m}, that grows directly on the catalysts surface and a multilayer c_{M}, that is deposited on the primary monolayer. Due to the limited surface area of the catalyst the monolayer growth is limited to the maximum monolayer capacity c_{max}. The total amount of coke is given by

$$c_{\mathrm{coke}} = c_{\mathrm{m}} + c_{\mathrm{M}} \tag{2.56}$$

as the sum of monolayer and multilayer. The coking rate is defined as

$$r_{\mathrm{coke}} = \frac{dc_{\mathrm{coke}}}{dt} = \frac{dc_{\mathrm{m}}}{dt} + \frac{dc_{\mathrm{M}}}{dt} \tag{2.57}$$

and describes the change of the monolayer and the mulitlayer coke over time. The monolayer coking rate can be described by

$$r_{\mathrm{m}} = \frac{dc_{\mathrm{m}}}{dt} = k_{\mathrm{m}}\left(c_{\mathrm{max}} - c_{\mathrm{m}}\right)^h \tag{2.58}$$

where h describes the reaction order of the monolayer coke growth. The rate expression for the multilayer is

$$r_{\mathrm{M}} = \frac{dc_{\mathrm{M}}}{dt} = k_{\mathrm{M}} c_{\mathrm{m}}^n \left(c_{\mathrm{max}} - c_{\mathrm{m}}\right)^m \tag{2.59}$$

with reaction orders m and n of the multilayer coke growth, respectively. Variation of the reaction orders creates a variety of different rate equations and therefore modeling approaches. Different reaction orders were tested in literature to describe the coke growth on different catalysts (Gascón et al. 2003). The MMCGM has frequently been used in the field of propane dehydrogenation e.g. to describe coke build-up on Pt-Sn/Al_2O_3 or Pt/Al_2O_3 catalysts (Lobera et al. 2008; Barghi et al. 2014; van Sint Annaland, Kuipers, et al. 2001). Sokolov et al. introduced an additional term that takes into account that lattice oxygen is desorbed in reductive environments (Sokolov, Bychkov, et al. 2015). Barghi et al. included sintering in a deactivation model based on the MMCGM (Barghi et al. 2014). In the work of Brencio et al. the MMCGM was used to describe the coking behavior of a Pd-based membrane in propane dehydrogenation (Brencio, Gough, et al. 2022).

Phenomenological approaches In addition to the mechanistic approaches mentioned above, phenomenological approaches are used as well. An approach by Janssens is based on the idea that the amount of active catalyst decreases temporally as a function of conversion of the reactor (Janssens 2009). A loss in active catalyst mass is equivalent to a shortening of the catalyst bed as illustrated in Fig. 2.15.

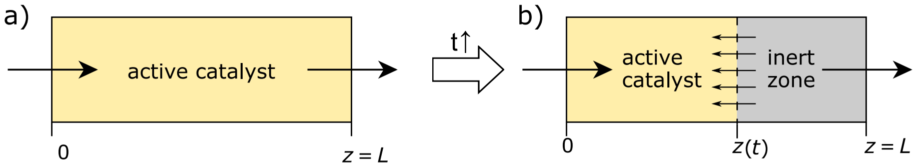

Figure 2.15: Schematic representation of the decrease of the catalyst length as modeled by the Janssens approach.

This can be mathematically expressed by

$$\frac{dm_{\mathrm{cat}}}{dt} = a^{\mathrm{J}} X \tag{2.60}$$

where a^{J} presents the activity parameter of this specific approach, which is not identical with the activity coefficients introduced in Eq. (2.50). By introducing the weight hourly space velocity $WHSV = \frac{m_{\mathrm{cat}}}{\dot{V}}$ and with the assumption of a constant volumetric flow rate Eq. (2.60) can be rearranged to

$$\frac{d\,WHSV}{dt} = -a_{\mathrm{V}}^{\mathrm{J}} X, \qquad a_{\mathrm{V}}^{\mathrm{J}} = \frac{a^{\mathrm{J}}}{\dot{V}} \tag{2.61}$$

which shows, that a shortening of the catalyst bed is equivalent to change in WHSV, meaning an increase in volumetric flow or gas velocity, respectively. Expressing the mass of active catalyst with the catalyst bed density ($m_{\mathrm{cat}} = A\rho_{\mathrm{bed}} z$) allows to rearrange Eq. (2.61) to

$$\rho_{\mathrm{bed}} A \frac{dz}{dt} = -a^{\mathrm{J}} X \Leftrightarrow \frac{dz}{dt} = a_{\mathrm{D}}^{\mathrm{J}} X, \qquad a_{\mathrm{D}}^{\mathrm{J}} = \frac{a^{\mathrm{J}}}{\rho_{\mathrm{bed}} A} \tag{2.62}$$

This reveals that the original approach is equivalent to a gradual shortening of the catalyst bed. Combining Eq. (2.62) with the 1D-PFTR balance equation (Eq. (2.21)) results

$$\frac{d\dot{n}_i}{dt} = \frac{d\dot{n}_i}{dz}\frac{dz}{dt} = -a_{\mathrm{D}}^{\mathrm{J}} X \frac{m_{\mathrm{cat}}}{L} \sum_j \nu_{i,j} r_j^{\mathrm{m}} \tag{2.63}$$

Several examples for deactivation modeling based on this approach can be found in literature (Lee et al. 2019; Juan S. Martinez-Espin et al. 2017). Most of them are related to methanol to olefin (MTO) or methanol to hydrocarbon (MTH) reactions, since the original publication of Janssens used the approach in this field of research (Janssens 2009; Janssens et al. 2013). Olsbye et al. presented the Janssens approach in a review paper in the context of other approaches to modeling catalyst deactivation in MTO processes (Olsbye et al. 2015).

Pore modeling approaches Another method of describing catalyst deactivation is modeling based on the pore structure. All modeling approaches discussed so far do not consider in any form the pore properties of the catalyst. Since pore models are long established and nowadays more detailed modeling can be performed due to increased computational power, this category of models will also be briefly addressed here. Many pore network models can distinguish between a direct poisoning or blockage of an active catalyst site that has no influence on the surrounding active catalyst mass and a blockage of pores that cuts off a higher number of active sites from being reached by the fluid phase (Fig. 2.16). This effect can only be addressed phenomenologically by the deactivation models described before.

As early as in the 1980s, the first pore models have been described in literature. Tsakalis compared a "single pore model" and a "bundle of pores model" for the description of catalyst deactivation by site poisoning and pore blockage (Tsakalis 1984). The effect of catalyst size, average pore size and pore size distribution on deactivation behavior has been investigated theoretically. The goal was to develop an algebraic expression to predict values for the above mentioned parameters for best overall performance and catalyst activity. Later on Sahimi developed a model using percolation theory[2] that takes the interconncetivity of the pores (topology) into account (Sahimi 1985). The catalyst was described as a random 3D network. It has been shown that more interconnected pore structures are more resistant to catalyst deactivation by pore blockage, which was not possible to investigate by previous models. These models have been further refined, deficiencies of the models have been reduced and it has been used for first computer based simulations (Arbabi and Sahimi 1991a; Arbabi and Sahimi 1991b). Based on these 3D models it is possible to optimize the catalysts properties with respect to catalyst deactivation (Keil and Rieckmann 1994).

2D and 3D pore network modeling of the deactivation behavior has also already been used in the field of propane dehydrogenation. Ye et al. first studied the modeling and later the optimization of the pore network of a Pt-Sn catalyst for propane dehydrogenation (G. Ye, H. Wang, Duan, et al. 2019; G. Ye, H. Wang, Zhou, et al. 2019).

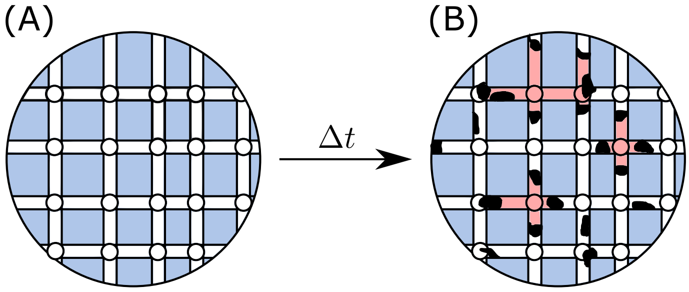

Figure 2.16: Schematic representation of a porous catalyst particle (A) Particle without coking (B) Coked particle with pore blockage; 🟦: matrix material of catalyst particle, 🟥: blocked pores not connected to the fluid phase, ■: coke deposits.

2.3.4 Catalyst Regeneration

Since catalyst coking is in many cases an unavoidable phenomenon, it is necessary to regenerate the catalyst in a lot of industrial applications, including TDH processes (see Section 2.1.2). Catalyst regeneration is usually achieved by gasification of the deposited coke. Several gases with gasification reaction rates of different orders of magnitude can be used. The following order of reactivity regarding the regeneration reaction has been found (Argyle and Bartholomew 2015):

---

[2] For more details on percolation theory see Zhdanov 1993

$$O_2 > H_2O > H_2 \tag{2.64}$$

Most commonly, coke is combusted using oxygen because it is abundantly available in the air. To control the reaction rates, it can be beneficial to dilute the air with an inert gas to avoid hotspots. Another control variable during regeneration is temperature. Power law kinetics of the form

$$r_{\text{reg}} = \frac{dm_{\text{coke}}}{dt} = k_{\text{reg}} m_{\text{coke}}^{\alpha_{\text{reg}}} x_{\text{O}_2}^{\beta_{\text{reg}}} \tag{2.65}$$

can be utilized to model coke regeneration by gasification with oxygen. The parameters α and β are the reaction orders in terms of coke content and the molar fraction of oxygen respectively. The kinetic constant k_{reg} includes the temperature dependency and can be expressed by an Arrhenius equation as introduced in Section 2.3.2.
Power law approaches to model coke burning kinetics based on TGA measurements are widely used in industry and research (Aguayo, Gayubo, Atutxa, et al. 1999; Kern and Jess 2005; Sørensen 2017). The results of these analyses can be used to design regenerators or regeneration strategies for fixed bed reactors (Kelling et al. 2012; Jiang et al. 2017).

In order to account for the complex structure of coke, several types of coke can be distinguished for the modeling of the regeneration process. A separate power law approach can be used to describe the burn-up kinetics of each coke species. For example, in a Pt-Sn-K/Al_2O_3 catalyst used for the dehydrogenation of C_{10} to C_{13} parafines, Luo distinguishes between three different coke species, each of which is deposited at different locations on the catalyst (Luo et al. 2015). Sørensen observed that seven lumped coke families are necessary to describe the regeneration of a catalyst from an MTG pilot plant (Sørensen 2017). The different coke families or species differed in the kinetic parameters of the power law approach. To account for the structural properties of the catalyst, Kern and Jess combined the power law approach to regeneration with a description of mass transfer limitations using the Thiele modulus (Kern and Jess 2005).

A problem in estimating regeneration kinetics is the fact that coke depositions change their structure and their composition over time, a phenomenon known as coke aging (Aguayo, Gayubo, Ereña, et al. 2003; Royo, Ibarra, et al. 1994). This can lead to difficulties in the reliable description of the kinetics of coke combustion. Differences in the behavior of the coke during regeneration can occur after different pretreatments but can also be observed in different parts of the reactor (Sørensen 2017; Royo, Perdices, et al. 1996).

In addition to the widely used power law approach, a number of other approaches can be found in literature, mainly in the area of evaluation of TGA measurements. These originate from the description of degradation processes, for example, in the decomposition of polymers (Mamleev, Bourbigot, et al. 2000; Mamleev and Bourbigot 2005; Koleva et al. 2008). Ochoa et al. use them to describe the combustion-regeneration kinetics of coked FCC catalyst (Ochoa et al. 2017). The approaches represent different rate-determining steps during the combustion process. These can be, for example, reaction kinetics, surface area of the reducing spherical body, diffusion, or nucleation and growth of the nuclei. Practical applications of the approaches, for example in the context of reactor design, are not common.

In most examples that can be found in literature, regeneration is implemented in continuum reactor models. The advances in pore models offer the possibility to study regeneration on a pore size level in analogy to coking of pore networks. This approach was used by Liu et al., who studied the deactivation of catalysts in the Claus process by condensation of sulfur in the pores. Therefore the phase change of sulfur in the pores from gaseous to liquid phase and the subsequent phase change back to gaseous phase during regeneration was implemented (Liu et al. 2020). Examples for the oxidation of coke deposits in pore networks are not known to the author.

2.4 Interim Conclusion

This chapter of the thesis aimed to present the theoretical foundations that contribute to the further understanding of the work. First, current commercial processes for propane production were discussed (Section 2.1). The advantages and disadvantages of the processes were presented and the difficulties and challenges encountered in these processes were identified. Currently used catalysts and process alternatives under research were presented, compared and discussed. Research gaps became clear and will be addressed as part of this thesis. Thereupon, the area of process intensification was addressed in detail and common approaches to process intensification that are currently being researched were elaborated (Section 2.2). A classification of the approaches to process intensification used in this work was carried out. Special emphasis was put on membrane reactor concepts (Section 2.2.1) and heat integration (Section 2.2.2), since these concepts are utilized in this thesis. Latest developments in these fields have been shown. In the following part, the basics of modeling were presented (Section 2.3). Different modeling approaches and their specific fields of application were explained, with the focus on homogeneous continuum models (Section 2.3.1), which are applied in the context of this work. For this purpose, all necessary equations were introduced, which will be referred to in the next chapters. This covered the modeling of the reactors including reaction kinetics (Section 2.3.2), deactivation (Section 2.3.3) and regeneration (Section 2.3.4).

It has become clear, that TDH processes suffer from specific disadvantages. The most striking and largely unavoidable disadvantages is catalyst coking, which significantly influences the designs of commercially established TDH processes (see Section 2.1). A largely unused alternative to TDH is ODH that is not limited by a chemical equilibrium and does not show significant coking. A major disadvantage is the limited selectivity due to side reactions. A combination of TDH and ODH in one apparatus has not been investigated yet. This promising combination can benefit from different measures of process intensification, namely membrane dosing, heat integration and periodic operation. A thorough understanding of the reaction kinetics, including coking and regeneration, is required for a comprehensive study of different reactor setups combining both reactions in one apparatus. The kinetic model has to be based on a wide range of experiments. Relying on such a model, detailed simulation studies can be performed before a scale-up to pilot scale is possible. These experimental and theoretical investigations will be carried out in the next chapters.

First, the reaction kinetics for the main and side reactions, coking, regeneration and deactivation are parametrized in Chapter 3. With this detailed model, it is then possible to optimize the process and evaluate complex integrated reactor concepts as described in Chapter 4. These integrated reactor concepts are assessed experimentally in Chapter 5.

3 Experimental Investigation and Parameter Estimation

All models are wrong, but some are useful.

GEORGE BOX[1]

In this chapter the kinetic models necessary to model the reaction system are parametrized. In Section 3.1 the main and side reactions of the reaction network shown in Fig. 2.14 are parametrized based on experiments in a lab scale FBR. The deactivation and regeneration behavior is studied in Section 3.2. That section is largely based on measurements in a setup for thermogravimetric analysis (TGA). The connection between catalyst deactivation and coke build-up on the catalyst surface is investigated in Section 3.3.

Goal of this chapter is to establish models that can be used in Chapter 4 to optimize the overall production process and model different integrated reactor setups.

3.1 Kinetics of Main and Side Reactions

For the parametrization of the kinetic model, lab scale experiments in a quartz glass fixed bed reactor were conducted. The inner diameter (ID) of the reactor was 6 mm. The temperature range was varied between 350 °C and 600 °C. Weight hourly space velocities (WHSV) of 100, 200 and 400 $\mathrm{kg\,s\,m^{-3}}$ were applied. The mass of the catalyst used for these experiments was either 1.5 g or 0.75 g which results in a bed length of around 6 cm or 3 cm, respectively. A variation of the catalyst mass was necessary due to the limitations of the experimental setup, mainly the ranges of the mass flow controllers (MFCs). The quartz glass tube was heated by an electric oven and the temperature in the middle of the catalyst bed was measured with a thermocouple. The temperature of the oven was controlled according to the temperature in the middle of the catalyst bed to assure constant temperatures during the measurements. For safety reasons, the propane and the oxygen concentration were varied between 0% and the lower explosion limit of around 1 % (Steen 2009). Experiments without oxygen were performed up to a maximum propane concentration of 5 %. All gas flows were controlled by MFCs. The composition of the gas flows at the reactor inlet and at the reactor outlet were analyzed by GC measurements (Agilent Technologies 7890B GC System).

---

[1] Box 1979; Box 1976.

For all experiments in this study a VO_x catalyst was used (Hamel, Tóta, et al. 2008; Hamel, Wolff, Subramaniam, et al. 2011; Klose 2004). The catalyst was prepared via impregnation of γ-Al_2O_3 spheres (diameter: 1 mm, specific area: $168\,\mathrm{m^2\,g^{-1}}$) with vanadyl acetylacetonate in acetone. The impregnated catalyst was washed, dried and calcinated. The vanadium content of the catalyst was 1.4 % and its specific area $158\,\mathrm{m^2\,g^{-1}}$ (BET).

To estimate the kinetic parameters the 1D plug flow model

$$\frac{d\dot{n}_i}{dz} = \frac{m_{\mathrm{cat}}}{L} \sum_{j=1}^{M} \nu_{i,j} r_{j,m} \tag{3.1}$$

was implemented in MATLAB to describe the reactor. Steady state as well as isobar and isothermal conditions were assumed. A detailed derivation of this reactor model can be found in Section 2.3.1 (Eq.(2.15) - (2.21))

The lsqnonlin function[2] of MATLAB was used for optimizing the kinetic parameters Γ_{kin} by minimizing the objective function

$$OF_{\mathrm{kin}} = \min_{\Gamma_{\mathrm{kin}}} RSS = \sum_{l=1}^{N_{\mathrm{exp,kin}}} \left[K_l^{\mathrm{exp}} - K_l^{\mathrm{sim}}(\Gamma_{\mathrm{kin}})\right]^2 \tag{3.2}$$

where $N_{\mathrm{exp,kin}}$ is the absolute number of all conducted experiments ($N_{\mathrm{exp,kin}} = 269$) and K are the experimentally measured (subscript: exp) or simulated (subscript: sim) key performance parameters of the reactor. That includes the propane conversion $X_{C_3H_8}$ that is defined by

$$X_{C_3H_8} = \frac{\dot{n}_{C_3H_8}^{\mathrm{in}} - \dot{n}_{C_3H_8}(z = L)}{\dot{n}_{C_3H_8}^{\mathrm{in}}} \tag{3.3}$$

and propene selectivity $S_{C_3H_6}$, CO_2 selectivity S_{CO_2} and CO selectivity S_{CO}. The conversion is calculated based on the molar flow at the reactor inlet $\dot{n}_{C_3H_8}^{\mathrm{in}}$ and the molar flow of propane at the reactor outlet at length L, denoted with $\dot{n}_{C_3H_8}(z = L)$. The selectivity in this contribution is defined using the number of carbon atoms of the respective product in relation to the number of carbon atoms of all products. The general equation reads

$$S_K = \frac{|\nu_{\mathrm{carbon},K}| c_K}{\sum_{prod} \nu_{\mathrm{carbon},prod} c_{prod}} \tag{3.4}$$

where $\nu_{\mathrm{carbon},K}$ is the number of carbon atoms of component K and $\nu_{\mathrm{carbon},prod}$ the number of carbon atoms in a product species. See Appendix B.5, Eq. B.27 - B.29 for the definitions for the separate components.

As described in Section 2.3.2, various kinetic approaches are available to describe the reaction network consisting of ODH and TDH. These are usually based on mechanistic considerations (e.g. Mars-van Krevelen approach, Eley-Rideal approach). In preliminary investigations, it was found that a description using a power law approach provides a good agreement of the experimental values with the modeling. An additional advantage is that this approach is mathematically less complex than mechanistic approaches and therefore easy to integrate into numerical simulations. Keeping in mind the future application in large-scale simulations (Chapter 4), this approach was chosen to describe the kinetics of the main and side reactions. That results in the following equations:

---

[2] Nonlinear least-squares solver based on Levenberg-Marquardt and trust-region-reflective methods. For further information see MATLAB Documantation:
https://de.mathworks.com/help/optim/ug/lsqnonlin.html

$$r_1 = k_1 p_{\mathrm{C_3H_8}}^{\alpha_1} \tag{3.5}$$

$$r_2 = k_2 p_{\mathrm{C_3H_8}}^{\alpha_2} p_{\mathrm{O_2}}^{\beta_1} \tag{3.6}$$

$$r_3 = k_3 p_{\mathrm{C_3H_8}}^{\alpha_3} p_{\mathrm{O_2}}^{\beta_2} \tag{3.7}$$

$$r_4 = k_4 p_{\mathrm{C_3H_8}}^{\alpha_4} p_{\mathrm{O_2}}^{\beta_3} \tag{3.8}$$

Variable p_i represents the partial pressure of component i, α_j is the reaction order with respect to propane and propene and β_j is the reaction order of oxygen. This power law approach was extended by a rate law for the WGS from literature (Hou and Hughes 2001):

$$r_5 = k_5 p_{\mathrm{H_2}} p_{\mathrm{CO_2}} \left(1 - \frac{p_{\mathrm{H_2O}} p_{\mathrm{CO}}}{\frac{1}{K_{\mathrm{WGS}}} p_{\mathrm{H_2}} p_{\mathrm{CO_2}}}\right) \tag{3.9}$$

where K_{WGS} represents the equilibrium constant of the water–gas shift reaction. The temperature dependency of this model was described by a reparametrized Arrhenius approach (Eq. (2.39) - (2.40), $T_{\mathrm{ref}} = 450\,°\mathrm{C}$).

During the parameter estimation process it was found that the influence of the water–gas shift reaction in the reaction network is negligible. Therefore, it is reasonable to simplify the network and to remove the reaction rates of the WGS from the network. Fig. 3.1 reveals the parity plot of the optimized parameters and the experimental data and shows that the simulated data are in good agreement with the experimental data. The optimized kinetic parameters are summarized in Tab. 3.1. Activation energies $E_{A,j}$ and collision factors $k_{0,j}$ listed in the table result from directly estimated parameters A_j and B_j from the reparametrized Arrhenius equations. These directly optimized parameters and their corresponding 95 % confidence intervals are presented in Appendix B.1, Tab. B.1. The small reaction order of oxygen of the ODH reaction has to be noted. This is consistent with results from the literature and suggests that catalyst reoxidation is not the rate-determining step (Bottino, Capannelli, Comite, et al. 2003; K. Chen et al. 2000; Dinse et al. 2009).

The derived kinetic equations are able to describe the reaction network over a wide range of temperatures, oxygen, and propane concentrations. However, deactivation effects are not considered yet. It is well-known that under oxygen lean conditions catalysts tend to deactivate over time due to coking. These coke deposits are responsible for a loss of catalyst activity. The next section will present the results of coking experiments and mechanistic mathematical modeling to describe this phenomenon.

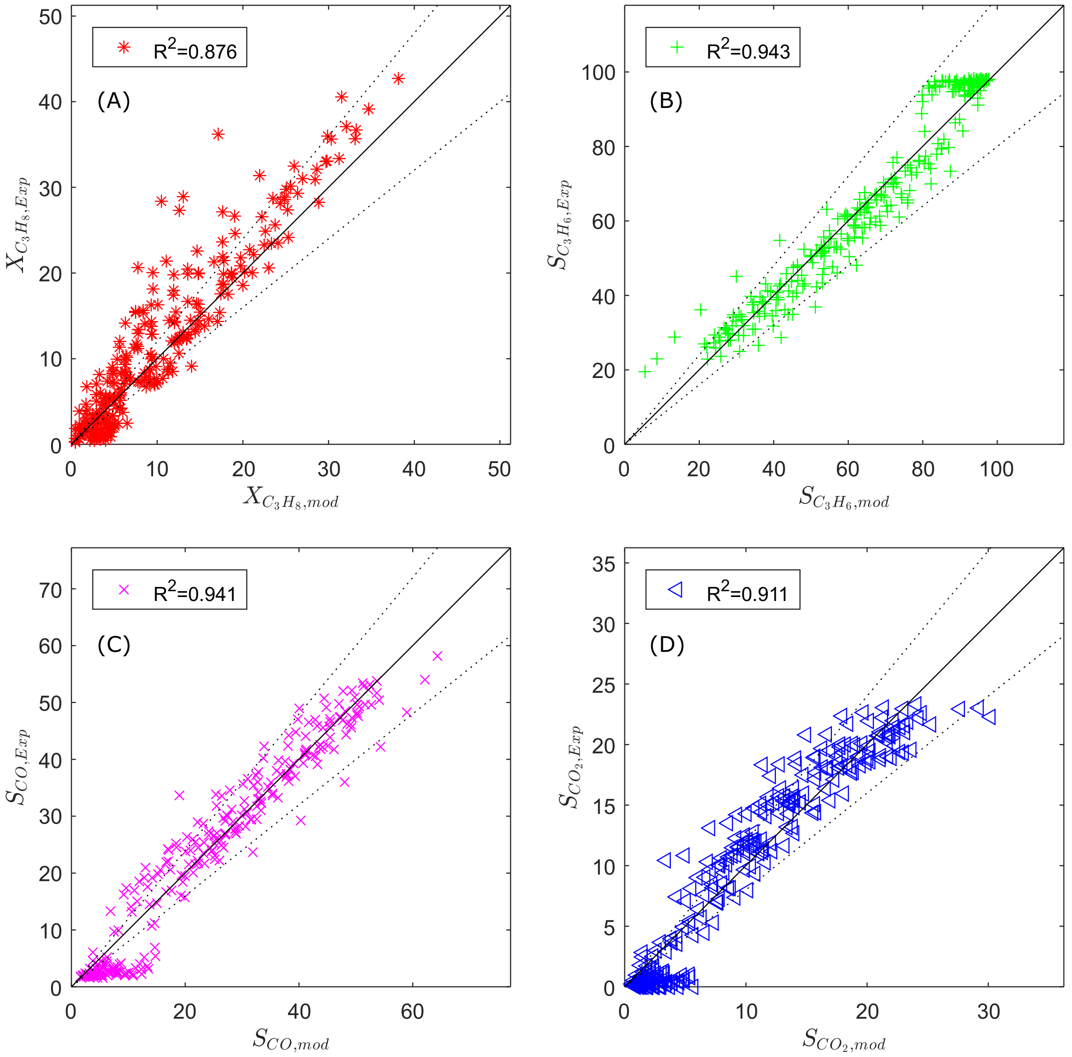

Figure 3.1: Parity plots for the estimated kinetic model: (A) conversion of propane; (B) selectivity of propene; (C) selectivity of CO; (D) selectivity of CO_2.

Table 3.1: Optimized kinetic parameters of the reaction network.

Parameter	Opt. Value	Unit
$k_{0,1}$	2.151	$\mathrm{mol\,kg^{-1}\,s^{-1}\,Pa^{-(\alpha_i+\beta_i)}}$
$k_{0,2}$	0.044	$\mathrm{mol\,kg^{-1}\,s^{-1}\,Pa^{-(\alpha_i+\beta_i)}}$
$k_{0,3}$	0.064	$\mathrm{mol\,kg^{-1}\,s^{-1}\,Pa^{-(\alpha_i+\beta_i)}}$
$k_{0,4}$	0.283	$\mathrm{mol\,kg^{-1}\,s^{-1}\,Pa^{-(\alpha_i+\beta_i)}}$
$E_{\mathrm{A},1}$	94.977	kJ/mol
$E_{\mathrm{A},2}$	80.909	kJ/mol
$E_{\mathrm{A},3}$	70.148	kJ/mol
$E_{\mathrm{A},4}$	70.813	kJ/mol
α_1	0.500	–
α_2	1.130	–
α_3	0.814	–
α_4	0.725	–
β_2	1.051×10^{-4}	–
β_3	0.212	–
β_4	0.170	–

3.2 Coke Formation and Catalyst Regeneration

Several industrial processes suffer from catalyst deactivation of different intensity (see Section 2.3.3). Strategies to deal with this phenomenon vary depending e.g. on the time scale of deactivation, deactivation mechanism and catalyst stability. In propane dehydrogenation reactions the deactivation of the catalyst largely results from coke deposition on the catalyst surface. The coke deposits are usually burnt off the catalyst with oxygen from air, since it is readily available in the atmosphere. In many industrial processes, production and regeneration phases alternate in order to ensure high catalyst activity on average as illustrated in Fig. 3.2 (e.g. Catofin process, see Section 2.1.2). To be able to optimize these processes it is important to be able to model catalyst coking and regeneration in order to estimate optimal production times and regeneration time to maximize space-time yields.

In this section the $\mathrm{VO_x}$ catalyst for propane dehydrogenation, which has already been characterized in terms of main and side reactions in the previous section (Section 3.1) is studied in terms of coking (Section 3.2.1) and regeneration behavior (Section 3.2.2) on lab scale. The derived models are later on validated by imitating the industrial process of consecutive production and regeneration phases in the lab setup (Section 3.2.3).

Coking and regeneration experiments have been conducted in a TGA setup (Netzsch STA 445 F5 Jupiter) that allows deactivating the catalyst at constant temperature in a defined gas atmosphere adjusted by three MFCs. The TGA is coupled with a Micro GC for a fast online analysis of gas compositions (Agilent 490 Micro GC, Channel 1: 10 m Molsieve 5 Å, Channel 2: 10 m PPU; Detectors: TCD).

3.2.1 Coke Formation

The WHSV during the coking experiments was set to $400\,\mathrm{kg\,s\,m^{-3}}$ and the overall gas flow was set to $100\,\mathrm{mL\,min^{-1}}$. The resulting mass of the catalyst sample was 666 mg. Propene and propane diluted in nitrogen were used as feed gases for coking experiments. The concentration of hydrocarbons was varied between 1, 3 and 5 %. A coking experiment started with evacuating the setup twice and flushing it with nitrogen to assure an inert atmosphere. The sample was then heated up to reaction temperature and after an equilibration time of 15 min the hydrocarbon mixture was introduced to the system. The deactivation time was 7 h. An overview of all experiments used for parameter estimation is given in Tab. 3.2. Over the whole course of the experiment the concentration of the gases at the outlet of the TGA setup were monitored by online GC measurements.

Preliminary experiments showed that experiments with temperatures between 575 °C and 650 °C offer a reasonable deactivation behavior at simultaneously high reactor performance. The temperature was varied in steps of 25 K within these limits between the experiments. The mass change and catalyst temperature were recorded by the TGA during the experiments.

A comparison between the coking behavior of the catalyst at different temperatures and between propane and propene feeds is illustrated in Fig. 3.3 (A). Propene is more reactive than propane, therefore propene is characterized as the dominant coke precursor in accordance with literature (Argyle and Bartholomew 2015). For both reactants the coke build-up is faster at higher temperatures (Fig. 3.3 (A)). Fig. 3.3 (B) shows that the coking rate increases with increasing propane concentration and also more significantly for increasing propene concentration.

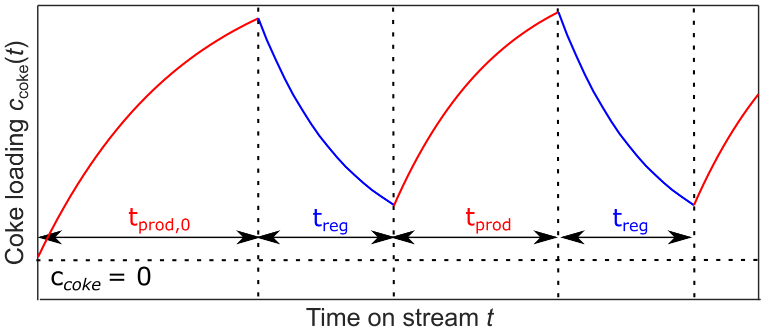

Figure 3.2: Schematic production cycle including consecutive production and regeneration cycles.

Table 3.2: Data set for kinetic analysis of the deactivation kinetics of the catalyst (PA: propane; PE propene; ✓: tested; ✗: not tested).

Temperature	575 °C	600 °C	625 °C	650 °C
Feed gas	PA/PE	PA/PE	PA/PE	PA/PE
1 %	✓/ ✓	✓/ ✓	✓/ ✓	✓/ ✓
3 %	✓/ ✓	✓/ ✓	✓/ ✓	✗ / ✓
5 %	✓/ ✓	✓/ ✓	✓/ ✓	✓/ ✓

Furthermore, it is possible to observe a decrease in sample mass at the beginning of the measurement. Directly after starting the measurement the catalyst loses weight (see Fig. 3.4). This behavior depends on the temperature and was described in detail by Sokolov et al. for other VO_x catalysts (Sokolov, Bychkov, et al. 2015). The reason for this counter intuitive mass loss is the desorption of water and the partial reduction of the vanadium oxide of the catalyst since lattice oxygen is consumed during the dehydrogenation reaction. The analytical methods used do not allow to distinguish between mass loss due to desorption and mass loss due to partial oxidation. This behavior can therefore only be described phenomenologically. It cannot be observed for measurements with propene because the rapid increase in mass due to coking compared to propane overlays these effects. In Fig. 3.4 it is also visible that the sampling of the GC caused defined but neglectable disturbances, which did not affect the quality of the measured data.

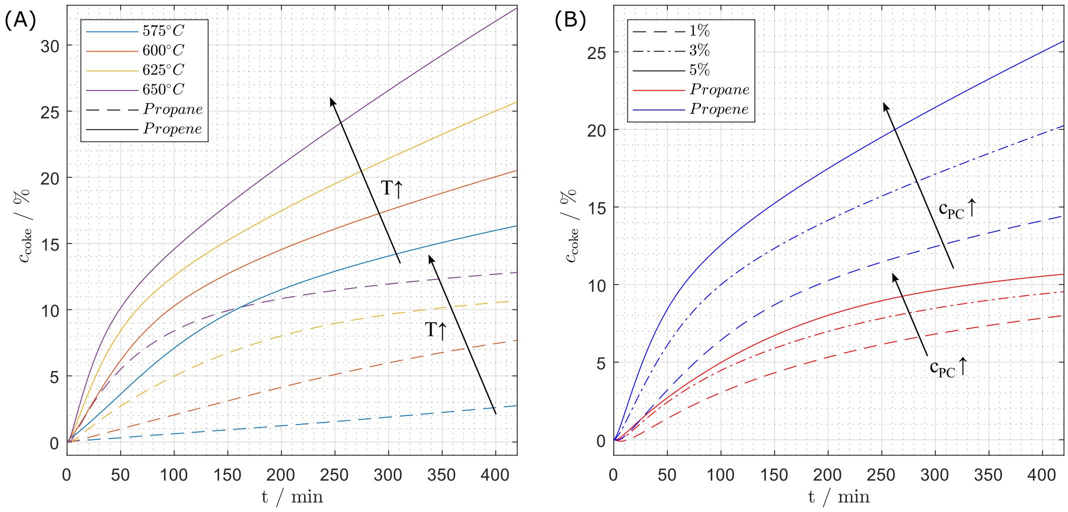

Figure 3.3: Comparison of the coking behavior of the catalyst using different precursors at (A) different temperatures and a concentration of 5 % of propane or propene respectively and (B) a temperature of 625 °C and varying hydrocarbon precursor (PC) concentrations.

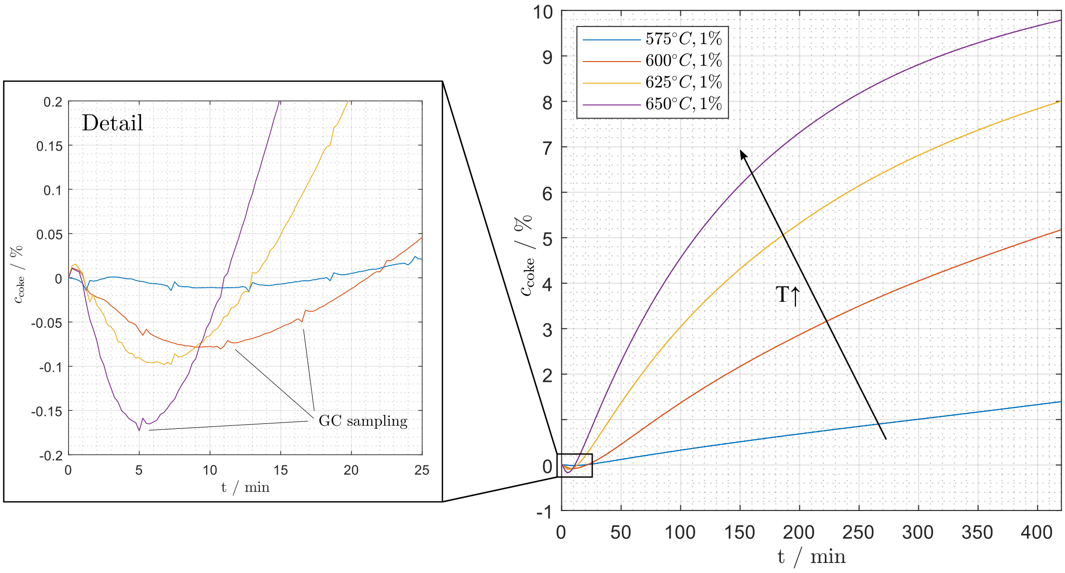

Figure 3.4: Mass change during deactivation at different temperatures and 1 % propane.

To be able to evaluate the catalyst performance over time it is inevitable to describe the catalyst coking by a mathematical model. In this contribution the multilayer-monolayer coke growth model (MMCGM) was used (see Section 2.3.3, Eq. (2.56) - (2.59)). It is assumed that the total amount of coke that is built up on the catalyst surface is either formed as a monolayer (c_{m}) or as a multilayer (c_{M}). The total amount of coke is described as the addition of both terms (Eq. (2.56), (2.57)). The coking rate of the monolayer can be described by

$$r_{\text{m}} = \frac{dc_{\text{m}}}{dt} = k_{\text{m}} \left(c_{\text{max}} - c_{\text{m}}\right)^h \tag{3.10}$$

and of the multilayer by

$$r_{\text{M}} = \frac{dc_{\text{M}}}{dt} = k_{\text{M}} c_{\text{m}}^n \left(c_{\text{max}} - c_{\text{m}}\right)^m \tag{3.11}$$

as described in Section 2.3.3 in detail. The rate constants of the monolayer and multilayer coke growth k_{m} and k_{M} are given by a standard Arrhenius approach (Eq. (2.37) , $j \in \{m, M\}$). Different reaction orders were tested in literature to describe the coke growth on different catalysts (Gascón et al. 2003). Tab. 3.3 summarizes the different reaction orders that lead to different forms of the MMCGM that were tested in this work. Besides the forms known from literature (A1, B1, D1) an additional approach using a free parameter for the reaction order h of the monolayer was developed (C1).

Table 3.3: Reaction orders of different MMCGM approaches.

	Parameter		
	h	n	m
(A1)	1	0	0
(B1)	2	0	0
(C1)[a]	h	0	0
(D1)	1	1	0

[a] Reaction order h is treated as an additional free parameter during parameter estimation.

Eq. (3.12) - (3.15) illustrate the integrated forms of the MMCGM approaches:

$$\text{(A1)}: \quad c_{\text{coke}} = c_{\text{max}} \left(1 - \exp(-k_{\text{m}}\, t)\right) + k_{\text{m}}\, t \tag{3.12}$$

$$\text{(B1)}: \quad c_{\text{coke}} = \frac{k_{\text{m}}\, t\, c_{\text{max}}^2}{k_{\text{m}}\, t\, c_{\text{max}} + 1} + k_{\text{M}}\, t \tag{3.13}$$

$$\text{(C1)}: \quad c_{\text{coke}} = c_{\text{max}} - \left((h-1)\, k_{\text{m}}\, t + c_{\text{max}}^{1-h})\right)^{\frac{1}{1-h}} + k_{\text{M}}\, t \tag{3.14}$$

$$\text{(D1)}: \quad c_{\text{coke}} = c_{\text{max}} \left(1 - \exp(-k_{\text{m}}\, t)\right) \left[\frac{k_{\text{m}} - k_{\text{M}}}{k_{\text{m}}}\right] + k_{\text{M}}\, c_{\text{max}}\, t \tag{3.15}$$

Extension of the model by concentration of precursor Since these forms do not take the concentration of the coke precursor c_{PC} into account, the monolayer terms of the models (A1), (B1), (C1) and (D1) were extended by the concentration of the precursor c_{PC} and an exponent l:

$$\frac{dc_{\text{m}}}{dt} = k_{\text{m}} c_{\text{PC}}^{l} \left(c_{\text{max}} - c_{\text{m}}\right)^{h} \tag{3.16}$$

The integrated rate laws following from this new developed extended approach are listed in Eq. (3.17) - (3.20).

$$\text{(A2)}: \quad c_{\text{coke}} = c_{\text{max}} \left(1 - \exp(-k_{\text{m}}\, c_{\text{PC}}^{l}\, t)\right) + k_{\text{m}}\, t \tag{3.17}$$

$$\text{(B2)}: \quad c_{\text{coke}} = \frac{k_{\text{m}}\, c_{\text{PC}}^{l}\, t\, c_{\text{max}}^2}{k_{\text{m}}\, c_{\text{PC}}^{l}\, t\, c_{\text{max}} + 1} + k_{\text{M}}\, t \tag{3.18}$$

$$\text{(C2)}: \quad c_{\text{coke}} = c_{\text{max}} - \left((h-1)\, k_{\text{m}}\, c_{\text{PC}}^{l}\, t + c_{\text{max}}^{1-h})\right)^{\frac{1}{1-h}} + k_{\text{M}}\, t \tag{3.19}$$

$$\text{(D2)}: \quad c_{\text{coke}} = c_{\text{max}} \left(1 - \exp(-k_{\text{m}}\, c_{\text{PC}}^{l}\, t)\right) \left[\frac{k_{\text{m}}\, c_{\text{PC}}^{l} - k_{\text{M}}}{k_{\text{m}}\, c_{\text{PC}}^{l}}\right] + k_{\text{M}}\, c_{\text{max}}\, t \tag{3.20}$$

For the kinetic analysis of the catalyst coking it was assumed that the TGA setup is perfectly mixed and that there are no concentration gradients in the catalyst sample tray. The coke precursor is therefore available in excess and the concentration of it is assumed to be constant (CSTR behavior).

In the following paragraphs the coking behavior of the catalyst using propene in the feed gas mixture is studied. Later on propane is used. The methodological approach remains the same.

Propene as coke precursor The models (A2), (B2), (C2) and (D2) were fitted to the experiments that were using propene as the coke precursor in the feed gas mixture. The models (A1), (B1), (C1) and (D1) are not considered as they cannot reflect the influence of the feed gas concentration. To estimate the parameters based on the experimental results, MATLAB's lsqnonlin solver was used to minimize the objective function

$$OF_{\text{deact}} = \min_{\Gamma_{\text{deact}}} RSS = \sum_{l=1}^{N_{\text{exp,deact}}} \left[c_{\text{coke},l}^{\text{exp}} - c_{\text{coke},l}^{\text{sim}}(\Gamma_{\text{deact}}) \right]^2 . \tag{3.21}$$

The kinetic parameters of the deactivation models are summarized by Γ_{deact}.

Fig. 3.5 compares the experimental results with the different modeling approaches. The models are not able to describe the curvature of the curve at the beginning of the measurements especially at low temperatures and low concentrations of propane. At higher temperatures and high concentrations, the experiments reveal a linear increase in mass at the end of the deactivation time. The linear multilayer term of the models should be able to describe this behavior. It is clearly visible that model (A2) describes the coking behavior not as precise as the other models. Thus, model (A2) is not suitable as a coking model. To find the most reasonable model, different measures describing the quality were used in the following.

A frequently used parameter of validity of a model is the coefficient of determination R^2, which is inadequate for nonlinear regressions (Spiess and Neumeyer 2010). An alternative parameter that can be derived from information theory is the Akaike Information Criterion (AIC), which can be adapted for least squares parameter estimations (Burnham and Anderson 2004; Akaike 1978). AIC includes the number of model parameters p as well as the residual sum of squares (RSS) and can therefore be used to avoid over-parametrization. For the comparison of different models, it is for reasons of clarity useful to calculate Akaike weights ($w(AIC)$) based on the AIC values. These values can be interpreted as the weight of evidence of the model to describe the underlying mechanism among the set of models analyzed. For more information and a detailed derivation see Appendix B.2. It has to be noted that the AIC is usually only used for independent experimental data, due to the strong correlation of the data. Nevertheless, it is exploited as a measure for qualitative comparison in this work. The results of the different evaluation criteria are summed up in Tab. 3.4. Model (C2) is, according to the evaluation criteria, able to describe the experimental data best since it shows the lowest value of the RSS and has the highest Akaike weight regardless of its additional parameter in comparison to the other models tested.

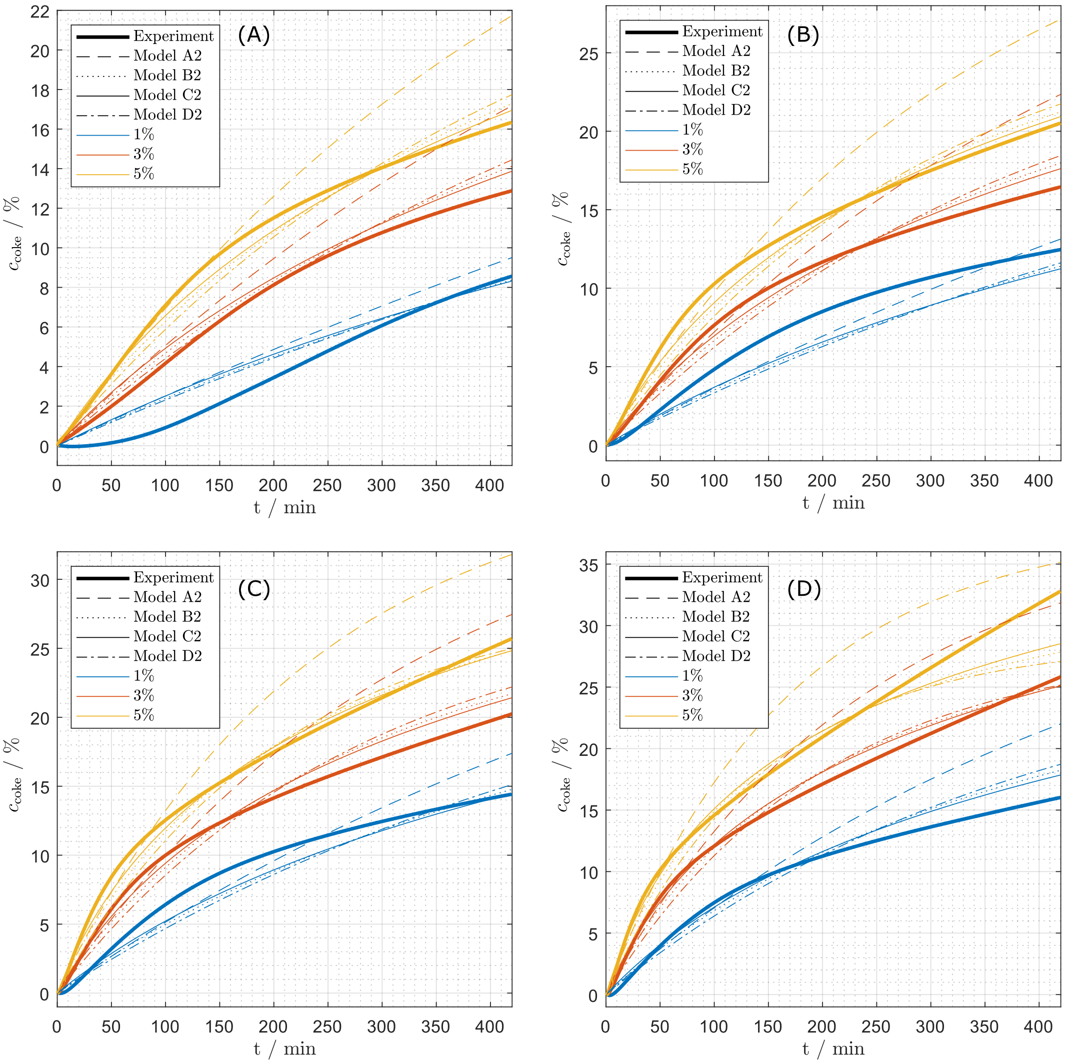

Figure 3.5: Mass change during coking experiments at different propene concentrations (1 %, 3 %, 5 %) at (A) 575 °C, (B) 600 °C, (C) 625 °C and (D) 650 °C for the models (A2), (B2), (C2) and (D2).

Table 3.4: Information criteria and comparison of the models (A2), (B2), (C2) and (D2) for deactivation experiments using propene.

	(A2)	(B2)	(C2)	(D2)
RSS_{opt}	31 483	22 259	17 241	31 483
p	6	6	7	6
AIC	66 210	59 220	54 072	66 210
$w(AIC)$	0 %	0 %	100 %	0 %

Model reduction and extension with desorption term Based on model (C2) different modifications, extensions as well as reductions were tested to achieve a better agreement with the measured data. To study the influence of the multilayer term on the overall mass change, a model consisting only of the monolayer term (Model (C3), Eq. (3.22)) was examined. To be able to describe the mass loss due to desorption at the beginning of the measurements the models (C2) and (C3) were extended by a desorption term (Eq. (3.23) and (3.24)) (Sokolov, Bychkov, et al. 2015). The adsorption term is not depending on temperature, meaning that k_{des} is a constant value for all measurements. A temperature depended desorption term was also tested in preliminary parameter estimations but did not offer any advantages.

$$\text{(C3)}: \qquad c_{\mathrm{coke}} = c_{\max} - \left((h-1)\,k_{\mathrm{m}}\,c_{\mathrm{PC}}^{l}\,t + c_{\max}^{1-h}\right)^{\frac{1}{1-h}} \tag{3.22}$$

$$\text{(C4)}: \qquad c_{\mathrm{coke}} = c_{\max} - \left((h-1)\,k_{\mathrm{m}}\,c_{\mathrm{PC}}^{l}\,t + c_{\max}^{1-h}\right)^{\frac{1}{1-h}} + k_{\mathrm{M}}\,t - c_0\,(1-\exp(-k_{\mathrm{des}}\,t)) \tag{3.23}$$

$$\text{(C5)}: \qquad c_{\mathrm{coke}} = c_{\max} - \left((h-1)\,k_{\mathrm{m}}\,c_{\mathrm{PC}}^{l}\,t + c_{\max}^{1-h}\right)^{\frac{1}{1-h}} - c_0\,(1-\exp(-k_{\mathrm{des}}\,t)) \tag{3.24}$$

Models (C2), (C3), (C4) and (C5) were fitted to the experimental data. The resulting modeled mass changes of the fresh catalyst are summarized in Fig. 3.6. The plots of the fitted and experimental data reveal no visible differences between the models. The residual sum of squares for the optimized models RSS_{opt} show only minor differences among the models (Tab. 3.5). Since the Akaike weight of model (C3) is the highest, this model was finally chosen for describing the coking behavior of the catalyst using propene in the feed gas mixture. The analysis exposes that the multilayer term is not necessary to describe the coking behavior for the experimental conditions tested with the $\mathrm{VO_x}$ catalyst and can be neglected for the mathematical modeling of these experiments. The desorption term studied in model (C4) and (C5) has no significant influence on the goodness of fit and can also be disregarded.

Consequently, the reduced model consisting only of a monolayer term (model (C3)) is sufficient to describe the mass changes in the experiments. It has to be stressed that the prediction quality of this model decreases for low concentrations and low temperatures. The optimized parameters of the selected model are shown in Tab. 3.6. For the estimation

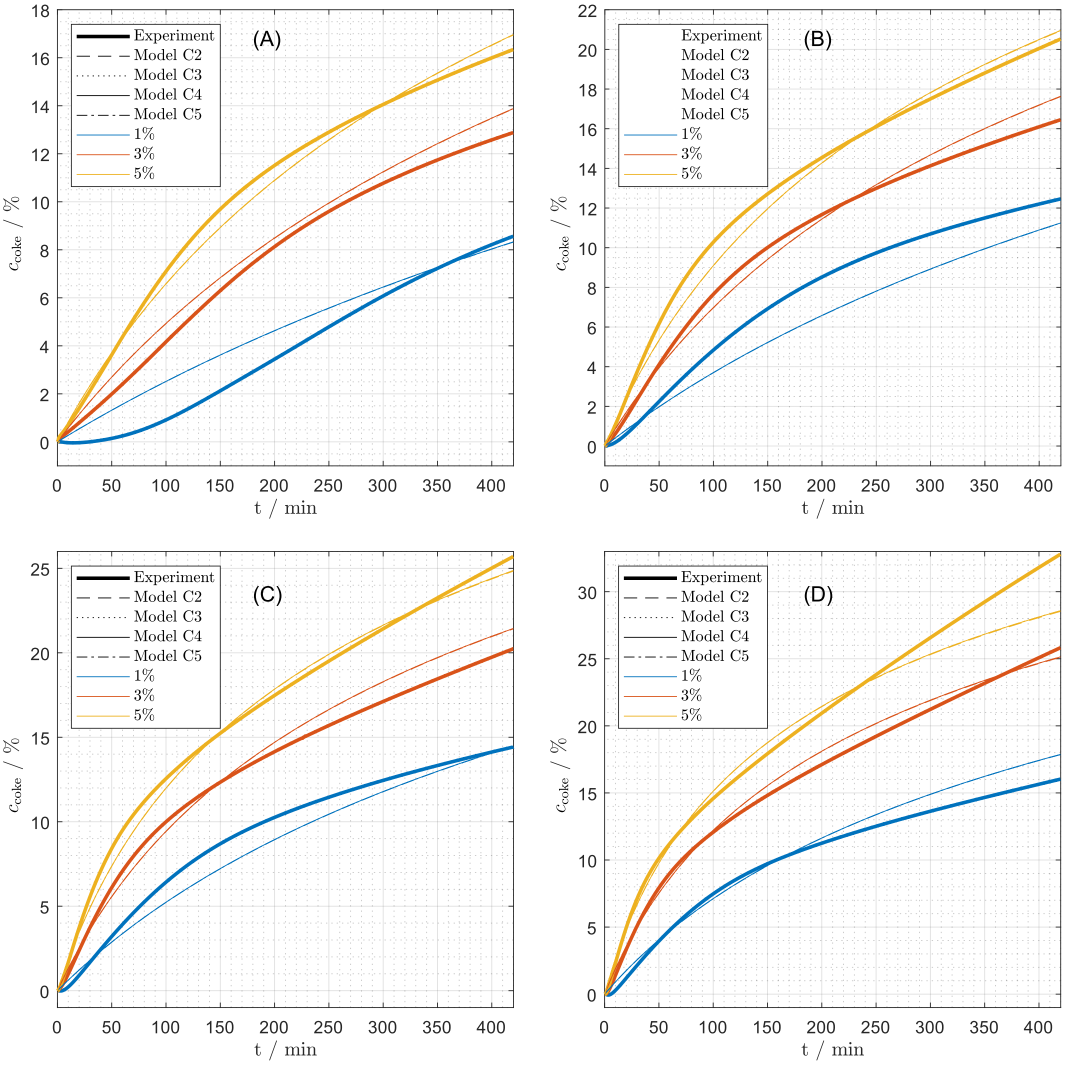

Figure 3.6: Mass change during coking experiments at different propene concentrations (1 %, 3 %, 5 %) at (A) 575 °C, (B) 600 °C, (C) 625 °C and (D) 650 °C for the models (C2), (C3), C4) and (C5).

Table 3.5: Information criteria and comparison of the models (C2), (C3), (C4) and (C5) for deactivation using propene.

	(C2)	(C3)	(C4)	(C5)
RSS_{opt}	17 240.8	17 164.9	17 166.9	17 166.7
p	7	5	9	7
AIC	54 072	53 979	53 990	53 985
$w(AIC)$	0 %	95.19 %	0.52 %	4.29 %

Table 3.6: Optimized parameters of model C3 to describe the coking behavior of the VO_x catalyst.

Parameter	Opt. Value	Confidence Intervals		Unit
$c_{\max}$	87.06	−0.45 %	+0.82 %	% $\left(\frac{\text{kg}_{\text{coke}}}{\text{kg}_{\text{cat}}} \times 100\right)$
l	0.7	−0.3 %	+0.3 %	-
k_0	9.52×10^7	−33.21 %	+11.26 %	$(\text{kg}_{\text{coke}}\,\text{kg}_{\text{cat}}^{-1}\,\text{min}^{-1})^{1-h}$
E_A	106397	−0.13 %	+0.12 %	$\text{J}\,\text{mol}^{-1}$
h	6.401	−0.38 %	+1.27 %	-

of confidence intervals (CI) a bootstrapping algorithm (Carpenter and Bithell 2000; Gentle 2009; Chernick 2008) was used (see Appendix B.3).

Propane as coke precursor Besides the fact that propene has been identified as the coke precursor, experiments using propane in the feed gas have also been conducted. This allows to simulate complete production cycles in the TGA setup that have been used for model validation (Section 3.2.3). The parameter estimation was performed in the same way as discussed for propene. A comparison between the unmodified MMCGM models (A2), (B2), (C2), and (D2) is shown in Fig. 3.7.

By comparing the information criteria listed in Tab. 3.7, it becomes clear that model (C2) describes the deactivation with propane as a precursor best.

Table 3.7: Information criteria and comparison of the models (A2), (B2), (C2) and (D2) for the deactivation of VO_x catalyst with propane.

	A2	B2	C2	D2
RSS_{opt}	4889.5	5078.9	4783.5	4889.4
p	6	6	7	6
AIC	28 665	29 431	28 225	28 664
$w(AIC)$	0 %	0 %	100 %	0 %

As well as for the deactivation measurements with propene, the developed models (C3), (C4) and (C5) were compared to model (C2). The corresponding graphs are illustrated in Fig. 3.8. In comparison to the models for the deactivation experiments with propene (Fig. 3.6) there are visible differences between the models. Especially the models including a desorption term ((C4) and (C5)) fit the experimental data at low temperatures and low propane concentrations better than the models without desorption terms. These differences are also evident in the parameters summarized in Tab. 3.8. Model (C4) and (C5) show a lower RSS_{opt} value than the other models. Since model (C5) needs two parameters less than model (C4) it is to be preferred. Tab. 3.9 shows the optimal parameters of the model and the corresponding confidence intervals, estimated by a bootstrapping procedure. Details on the bootstrapping algorithm used are given in Appendix B.3.

Model (C5) does also not include a multilayer term. The difference between model (C3),

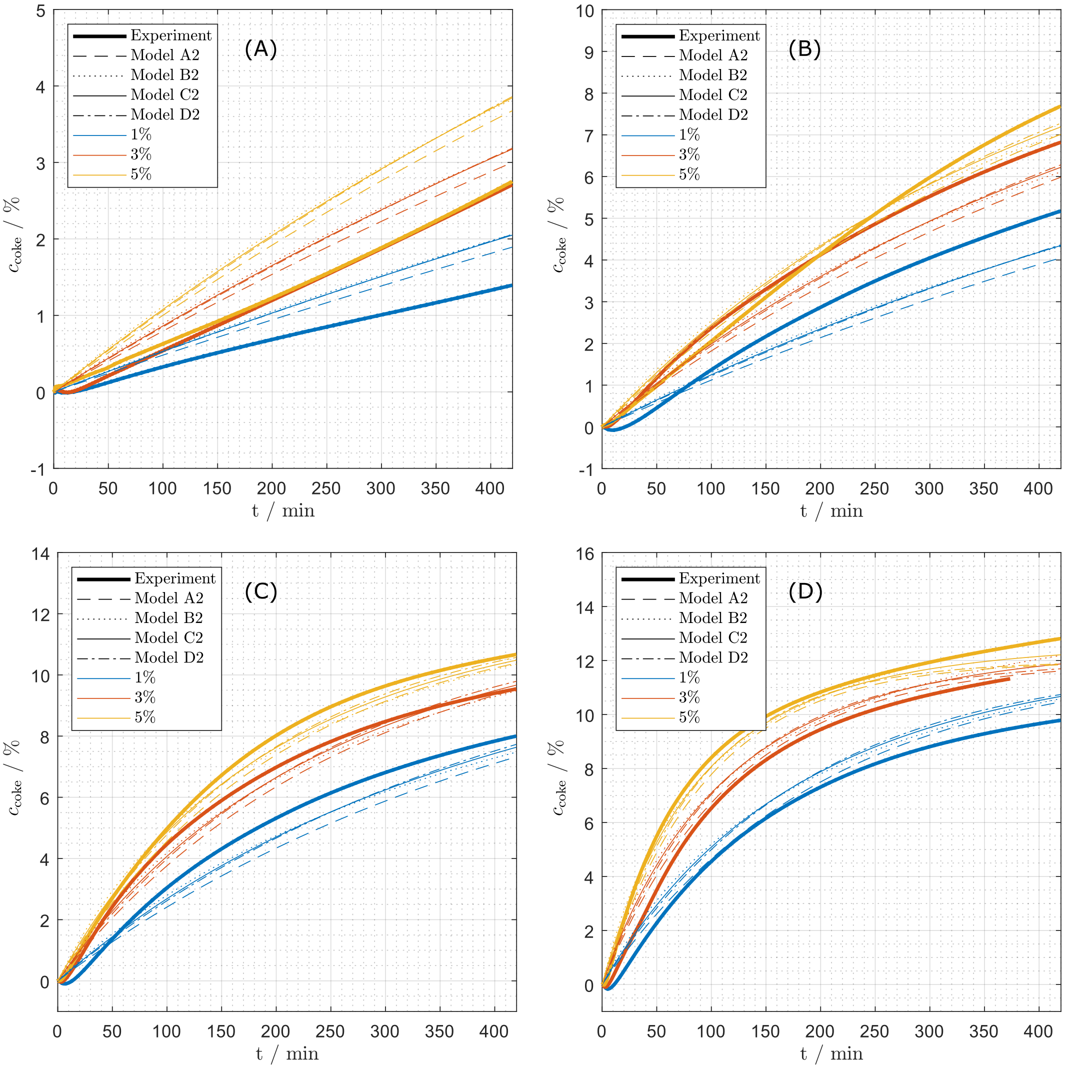

Figure 3.7: Mass change during coking experiments at different propane concentrations (1 %, 3 %, 5 %) at (A) 575 °C, (B) 600 °C, (C) 625 °C and (D) 650 °C for the models (A2), (B2), C2) and (D2) as used for coking from propene (Eq. (3.17) - (3.20)).

Table 3.8: Information criteria and comparison of the models (C2), (C3), (C4) and (C5) for deactivation using propane.

	C2	C3	C4	C5
RSS_{opt}	4783.5	5509.6	3631.6	3631.6
p	7	5	9	7
AIC	28 225	31 070	22 675	22 671
$w(AIC)$	0 %	0 %	11.92 %	88.08 %

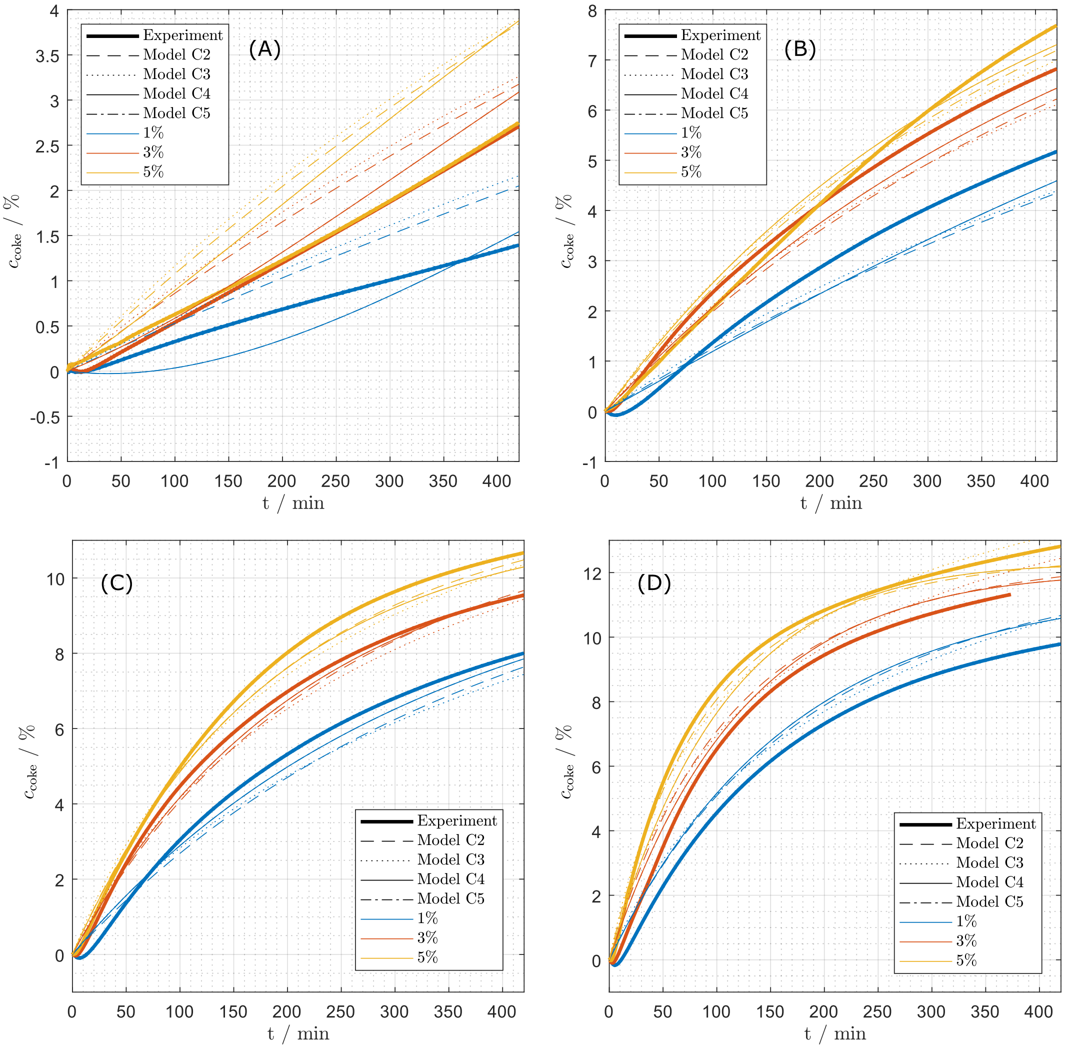

Figure 3.8: Mass change during coking experiments at different propane concentrations (1 %, 3 %, 5 %) at (A) 575 °C, (B) 600 °C, (C) 625 °C and (D) 650 °C for the models (C2), (C3), (C4) and (C5)) as used for coking from propene (Eq. (3.19), (3.22) - (3.24)).

Table 3.9: Optimized parameters of model C5 to describe the coking behavior of the VO_x catalyst using propane.

Parameter	Opt. Value	Confidence Intervals		Unit
c_{max}	17.695	$-1.54\,\%$	$+1.35\,\%$	% $\left(\frac{kg_{coke}}{kg_{cat}} \times 100\right)$
l	0.275	$-2.05\,\%$	$+1.55\,\%$	-
k_0	9.59×10^5	$-29.71\,\%$	$+33.72\,\%$	$(kg_{coke}\, kg_{cat}^{-1}\, min^{-1})^{1-h}$
E_A	139022	$-1.92\,\%$	$+1.35\,\%$	$J\, mol^{-1}$
h	1.106	$-2.79\,\%$	$+1.47\,\%$	-
k_{des}	3.22×10^{-3}	$-2.24\,\%$	$+4.09\,\%$	min^{-1}
c_0	5.994	$-4.47\,\%$	$+5.17\,\%$	% $\left(\frac{kg_{coke}}{kg_{cat}} \times 100\right)$

which was chosen for the deactivations using propene and model (C5) is the missing desorption term in model (C3). The desorption does not play a significant role in describing the deactivation using propene due to the fast coking which dominates in the experiments. It has to be noted that these results are valid for the deactivation times realized in this study. Especially for propane a linear mass change at the end of the measurements for high temperatures can be observed, which leads to the conclusion that a linear multilayer term is suitable to describe the coking behavior for longer deactivation times (Gascón et al. 2003; Lobera et al. 2008). This is an indicator that the systematic model reduction disregards a multilayer term that would be reasonable from a mechanistic point of view. A different experimental basis may lead to another model describing the coking of the catalyst. In this section, a simple mathematical model was developed and validated to describe the coking behavior of the VO_x catalyst under a wide range of deactivation conditions. The models describe the mass change of the catalyst in good agreement with experimental data in a temperature range relevant for industrial processes. Keeping the total industrial production cycle in mind (see Fig. 3.2), a description of the regeneration of the catalyst is still necessary. A mathematical model for the regeneration of the catalyst with oxygen is developed in the next section.

3.2.2 Catalyst Regeneration

Subsequent regeneration of the inactivated catalyst is accomplished by gasifying the coke. Various gases can be used for this purpose. The reactivity of these gases and therefore the gasification rates vary by orders of magnitudes (see Section 2.3.4) (Argyle and Bartholomew 2015). Many cyclic processes, as illustrated in Fig. 3.2, utilize oxygen for regeneration of coked catalysts which has the advantage of the availability in air and reasonable regeneration rates at moderate temperatures. In this contribution oxygen diluted in nitrogen was used.

To study the regeneration step, at first the catalyst was deactivated in long-term experiments utilizing the described fixed bed reactor also employed for the kinetic experiments ($ID = 6\,\mathrm{mm}$, see Section 3.1). Samples of the deactivated catalyst were later used for the regeneration experiments. The catalyst bed was divided into three segments (Fig. 3.9), 0.5 g catalyst each, separated by quartz glass wool. The samples that were used for the regeneration experiments were deactivated at two different conditions which are given in detail in Tab. 3.10

Table 3.10: Deactivation conditions of the samples used in regeneration experiments.

	Deactivation Condition 1	Deactivation Condition 2
Temperature	600 °C	500 °C
Propane concentration	5 %	1 %, 3 %, 5 %
Oxygen concentration	0 %	0 %
Deactivation time	48 h	96 h
$WHSV$	$400\,\mathrm{kg\,s\,m^{-3}}$	$400\,\mathrm{kg\,s\,m^{-3}}$
Tested segment	1,2,3	3

The first deactivation condition consists of a 48 h deactivation period at 600 °C, 5 % propane and a WHSV of $400\,\mathrm{kg\,s\,m^{-3}}$. At deactivation condition 1 samples of all three segments of the catalyst bed were used for regeneration experiments in the TGA (Fig. 3.9). The second deactivation condition includes a 96 h time period at 500 °C. The propane concentration was varied between 1, 3 and 5 %. Since the build-up of coke on the catalyst is less severe at deactivation condition 2, only the third segment of the catalyst bed was analyzed, due to the higher coke concentration in this part of the reactor compared to the other segment closer to the reactor inlet (Fig. 3.10). The regeneration time was adjusted to the regeneration conditions. Low regeneration temperatures and low oxygen concentrations demand longer regeneration times because of their effect on the kinetics of the regeneration that will be discussed in this section. The same TGA setup described above that was used for the deactivation experiments was also applied for the regeneration experiments (Netzsch STA 445 F5 Jupiter). The standard sample size in regeneration experiments was 80 mg. Before starting a regeneration measurement, the TGA setup was evacuated and flushed with nitrogen twice to ensure an inert environment. After heating up the TGA to a starting temperature of 100 °C the sample was heated up to the desired regeneration temperature with $20\,\mathrm{K\,min^{-1}}$. After an equilibration period of 15 min the oxygen was introduced to the system and the mass change was recorded by the TGA until the end of the regeneration time. The whole experiment was monitored simultaneously

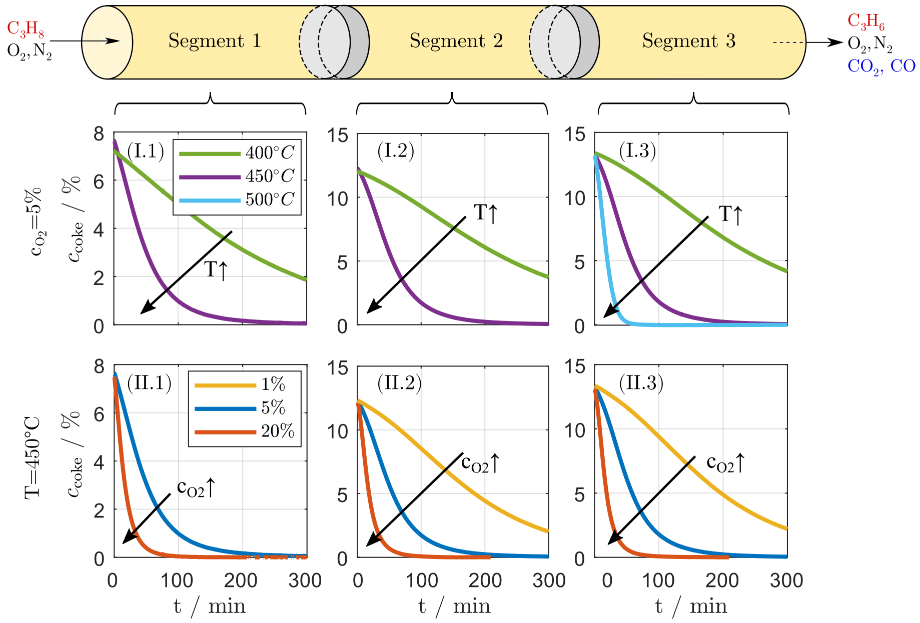

Figure 3.9: Regeneration behavior for samples from different catalyst segments in the lab scale fixed bed reactor at (I) constant oxygen concentration and (II) constant temperature and varied oxygen concentration for catalyst deactivated at deactivation condition 1.

by Micro GC measurements. Tab. 3.11 summarizes all experiments that were used for the parameter estimation of the regeneration model (Eq. (2.65)).

Table 3.11: Deactivation conditions of the samples used in regeneration experiments.

		Activation Condition				
		$T_{reg} = 450\,°C$ $c_{reg} = 5\,\%$	$T_{reg} = 450\,°C$ $c_{reg} = 20\,\%$	$T_{reg} = 400\,°C$ $c_{reg} = 5\,\%$	$T_{reg} = 450\,°C$ $c_{reg} = 1\,\%$	$T_{reg} = 500\,°C$ $c_{reg} = 5\,\%$
Deact. cond. 1	Segment 1	✓	✓	✓	✗	✗
	Segment 2	✓	✓	✓	✓	✗
	Segment 3	✓	✓	✓	✓	✓
Deact. cond. 2	$c_{C_3H_8,deact} = 1\,\%$	✓	✓	✓	✓	✓
	$c_{C_3H_8,deact} = 3\,\%$	✓	✓	✓	✓	✓
	$c_{C_3H_8,deact} = 5\,\%$	✓	✓	✓	✓	✓

Table 3.12: Regeneration times for different regeneration conditions.

	1 %	5 %	20 %
400 °C	-	24.5 h	-
450 °C	18.5 h	6.5 h	3 h
500 °C	-	2.5 h	-

Fig. 3.9 and 3.10 show the mass changes during the regeneration experiments. It becomes obvious that a higher temperature leads to a faster regeneration (Fig. 3.9 I.1 - I.3 and

Fig. 3.10 I.1 - I.3). With increasing oxygen concentrations, the coke burning rate also increases significantly (Fig. 3.9 II.1 - II.3 and Fig. 3.10 II.1 - II.3). Comparison of the different segments of the catalyst bed reveals that more coke is deposited at the end of the catalyst bed in segment 3. (Fig. 3.9). That supports the assumption that propene is the precursor for coking, since the propene concentration increases along the reactor length. At deactivation condition 1 (Tab. 3.11) the coke loading in the first catalyst segment 1 was only 7.4 % (Fig. 3.9 I.1, II.1) whereas the coke loading at the last segment 3 was 13.3 % (Fig. 3.9 I.3, II.3). A significant difference between the coke loading of the catalyst deactivated at the different conditions is also observable. With 13.3 % coke loading in the third segment the catalyst deactivated at condition 1 (Tab. 3.11) shows much more coking than the catalyst deactivated at condition 2 (1.7 %). This is the effect of the elevated temperature of 600 °C at coking condition 1.

For the kinetic analysis of the regeneration behavior it was assumed that the TGA is perfectly mixed (CSTR behavior) and the oxygen is in high excess similar to the experiments for studying the deactivation behavior. For that reason, it can be assumed that the oxygen concentration is constant in the apparatus. The temperature dependency of the reaction rate constant was expressed with the Arrhenius equation (Eq. (2.37)). To describe the complex kinetics of the regeneration the power law approach introduced in Section 3.2.2 (Eq. (2.65)) was applied.

Power law approaches to model coke burning kinetics based on TGA measurements are widely used in industry and research (Aguayo, Gayubo, Atutxa, et al. 1999; Kern and Jess 2005; Sørensen 2017). The results of these analyses can be used to design regenerators or regeneration strategies for fixed bed reactors (Kelling et al. 2012; Jiang et al. 2017). A problem in estimating regeneration kinetics is the fact that coke depositions change their structure and their composition over time, a phenomenon known as coke aging. This can lead to difficulties in describing reliable coke burning kinetics. Differences in the behavior of the coke during regeneration can occur after different pretreatments but can also be observed in different parts of the reactor (Sørensen 2017; Royo, Perdices, et al. 1996). The aim of this section is to develop a simplified kinetic model of the complex coke burning kinetics and to check whether these difficulties occur in the considered reaction system. For that reason it was ensured that samples of a wide variety of coking experiments are used for the parameter estimation of the regeneration kinetics.

The kinetic parameters have been estimated similar to the parameter estimation of the coking kinetics (see Eq. (3.21)) and the main reaction network (see Eq. (3.2)) by using the lsqnonlin routine in MATLAB with the objective function

$$OF_{\mathrm{reg}} = \min_{\Gamma_{\mathrm{reg}}} RSS = \sum_{l=1}^{N_{\mathrm{exp,reg}}} \left[c_{\mathrm{coke},l}^{\mathrm{exp}} - c_{\mathrm{coke},l}^{\mathrm{sim}}(\Gamma_{\mathrm{reg}}) \right]^2 \tag{3.25}$$

where Γ_{reg} describes the kinetic parameters of the regeneration.

The coke content c_{coke} is given in % (mass of coke per mass of fresh catalyst), in analogy to the deactivation experiments to make it possible to combine deactivation and regeneration models. x_{O_2} denotes the volume fraction of oxygen. The optimized parameters of the power law kinetics (Eq. (2.65)) are listed in Tab. 3.13. The activation energy of 120 kJ mol^{-1} and the preexponential factor of 1.62×10^8 % min^{-1} are in the range of acti-

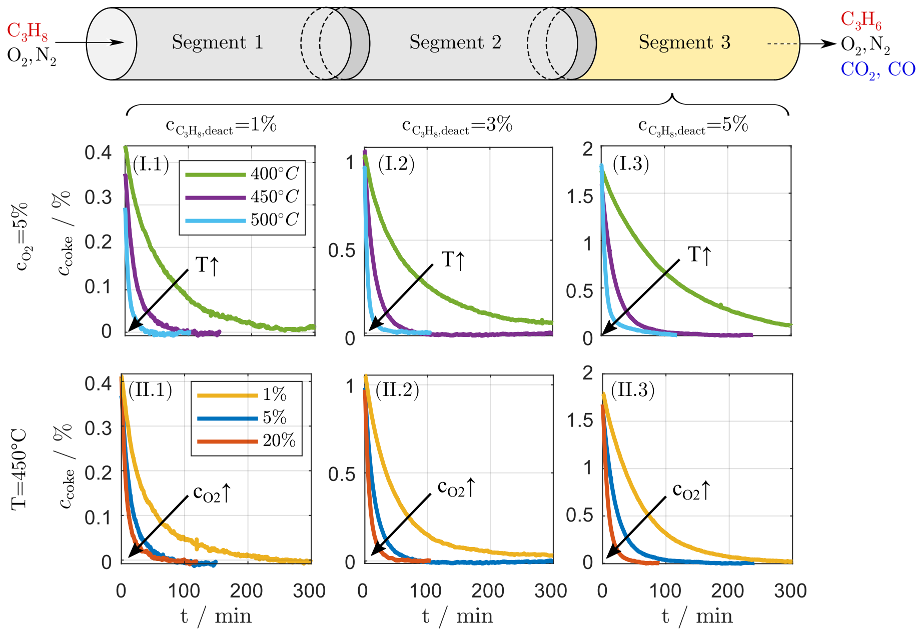

Figure 3.10: Regeneration behavior for samples from catalyst bed segment 3 in the lab scale fixed bed reactor at (I) constant oxygen concentration and (II) constant temperature and varied oxygen concentration for catalyst deactivated at deactivation condition 2.

vation energies reported for dehydrogenation catalysts (Luo et al. 2015). This is especially notable because the model in this contribution is not strictly mechanistic and can be seen as a simplification that lumps together the regeneration kinetics of different coke species that are supposed to be deposited at the different parts of the catalyst (support, active sites, etc.) Fig. 3.11 illustrates experimental and simulated values of mass loss during the regeneration. The simulated mass loss during the regeneration is in good agreement with the experimental data for all experimental conditions covered. The simulated values reach a fully regenerated state earlier than the experimental values. Both deactivation conditions are fitted with a good precision. Fig. 3.12 A compares the regeneration for different segments of the catalyst. The model is able to predict the mass loss for all segments with the same quality. Fig. 3.12 B shows a comparison between samples deactivated with different propane concentrations. The different deactivation conditions have no influence on the goodness of the fit. Consequently, it can be stated that the model is able to describe the regeneration behavior for samples deactivated at different temperatures, over different times and at different propane concentrations with a good agreement and can be used for further model-based investigations and process optimization.

The aim of this section was the experimental and model-based investigation of the coking and regeneration of a VO_x catalyst during the thermal and oxidative dehydrogenation of propane. An empirical power law model was able to describe the kinetic network and kinetics of propane dehydrogenation (ODH + TDH) with good agreement in a wide range of experimental conditions. Propene was identified as the main precursor for coke formation. Coking kinetics were quantified to allow to describe the coke growth during long-term production cycles. These kinetics were modeled using multilayer-monolayer coke growth models of different complexity. Approaches from literature were extended to describe the influence of the precursor concentrations. A systematic model discrimination

Table 3.13: Optimized parameters for the regeneration model (Eq. (2.65)).

Parameter	Value	Unit
α_{reg}	0.5517	[-]
β_{reg}	0.6859	[-]
$E_{\mathrm{A,reg}}$	120 928	$\mathrm{J\,mol^{-1}}$
$k_{0,\mathrm{reg}}$	6 987 955	$\%\,\mathrm{min^{-1}}$

was applied to find the most suitable model. Gasification of the coke deposits was described by a power law approach. It was shown that the corresponding model enables to describe the regeneration behavior regardless of the position of the coke in the reactor and the coking conditions.

Although the power law model agrees well with the experimental values, it is a very simplified model of the regeneration. An inaccuracy is caused by the division of the catalyst into three sections during coking. The coarse local subdivision would not allow to reveal strong gradients in the coke distribution along the reactor. Furthermore, a constant temperature and constant concentration profiles have been assumed for the modeling. In general, moving temperature fronts can be observed in chemical reactors during production operation as well as during regeneration (Eigenberger et al. 2007; Kelling et al. 2012). Changing concentration and coke profiles over the radius of the catalyst particle have also been demonstrated in modeling and experiments and cannot be observed with the chosen experimental setup (Kern and Jess 2005; Sosna et al. 2020). The design of the experiments (low oxygen concentrations, good mixing of the reactor interior) attempted to minimize this effect as much as possible. Nevertheless, in situ measurement methods for both temperature and concentration along the length of the catalyst bed of a tubular reactor would provide a gain in additional information for a more detailed description of coking and regeneration kinetics.

Another unwanted influence on the results may be the removal of the sample from the laboratory tubular reactor and transfer to the TGA. With longer time intervals between coking and subsequent regeneration, a change in the coke structure may occur (coke aging). A desorption of gaseous species during sample preparation for external regeneration tests is also very likely. In the validation tests in the next section deactivation and regeneration phases are carried out in one apparatus without taking out the sample. That procedure eliminates this error.

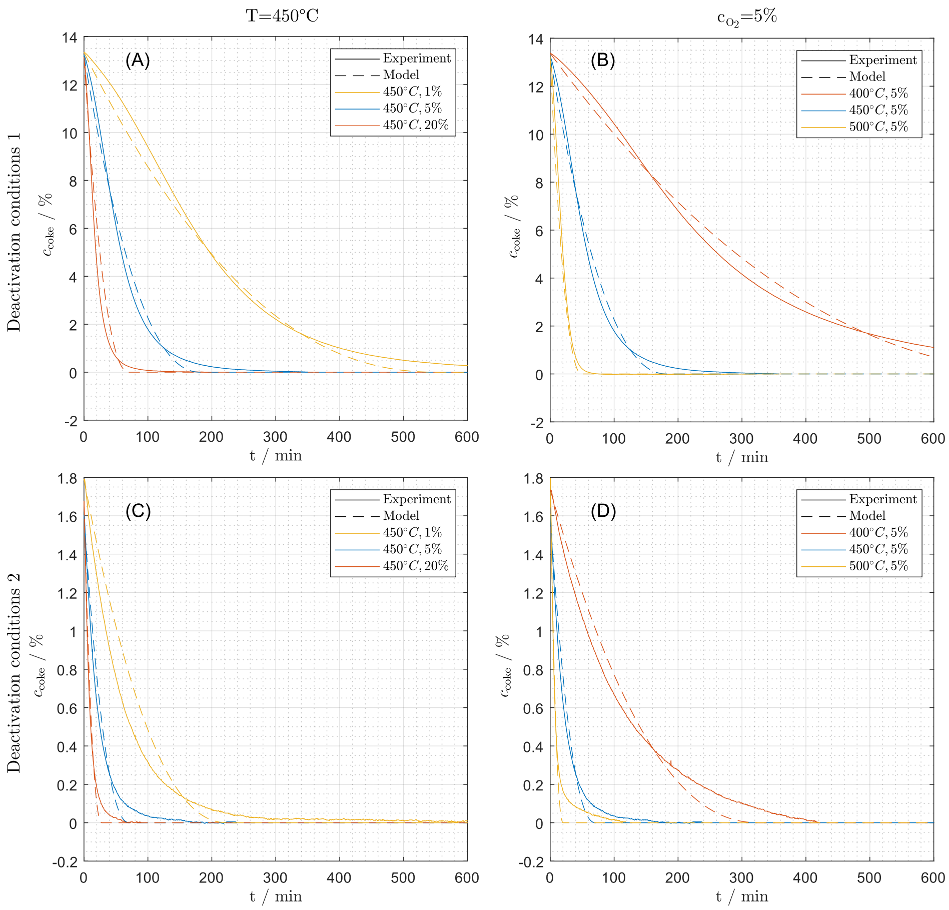

Figure 3.11: Comparison between the simulation and the experimental mass changes during regeneration for (A) deactivation condition 1 at varying oxygen concentration (1 %, 5 %, 20 %), (B) deactivation condition 1 at different temperatures (400 °C, 450 °C, 500 °C), (C) deactivation condition 2 at different oxygen concentrations, (D) deactivation condition 2 at different temperatures.

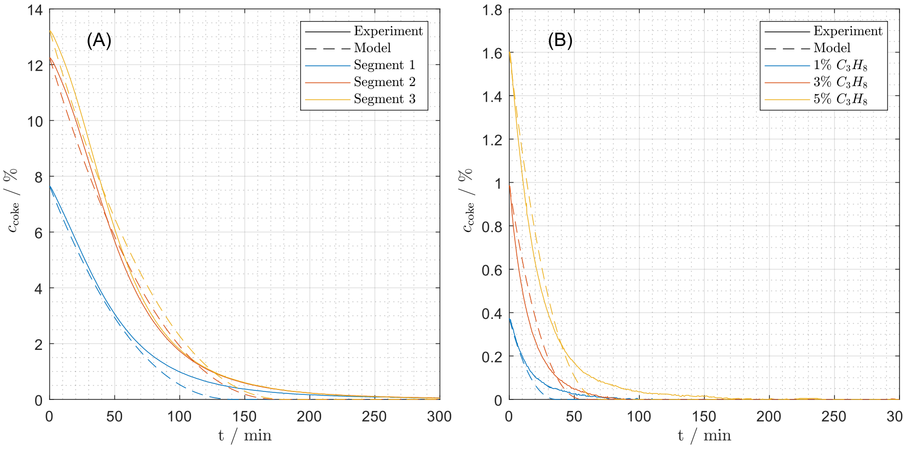

Figure 3.12: (A) Comparison of the regeneration of different segments of the catalyst packing deactivated at deactivation condition 1, (B) influence of propane concentration (1 %, 5 %, 20 %) on coke loading in segment 3 (deact. condition 2).

3.2.3 Model Validation

For validation of the parametrized kinetic models for catalyst deactivation and reactivation, different, sequential periodic experiments using the TGA coupled with an online Micro GC setup were conducted. All periodic experiments consisted of three deactivation phases followed by regeneration phases as schematically illustrated in Fig. 3.2. The periodic operation was used to verify the validity of the mathematical models and to check the stability of the catalyst and reproducibility under periodic operation. Propane diluted in N_2 was used during the deactivation phase as a simplified industrial feed (Won et al. 2009).

Three different periodic experiments were conducted for this study. Either the deactivation phase or the regeneration phase was varied between the experiments. The deactivation phases were performed at 625 °C for 120 min. Regeneration phases were performed at lower temperatures of 450 °C and 500 °C to avoid structural changes of the catalyst by local hotspots. This was considered to make sure that similar experiments can be performed in pilot and industrial scale equipment where local hotspots play an important role. The regeneration time in all experiments was 60 min.

The concentration of oxygen was varied between 5 % and 20 %. For an overview of the experimental conditions of all three periodic experiments see Tab. 3.14.

Table 3.14: Experimental conditions of the deactivation and regeneration phase of the periodic experiments.

Exp.	Deactivation				Regeneration			
	T_{deact}	t_{deact}	$\dot{V}_{\mathrm{C_3H_8,deact}}$	$c_{\mathrm{C_3H_8,deact}}$	T_{reg}	t_{reg}	$\dot{V}_{\mathrm{O_2,reg}}$	$c_{\mathrm{O_2,reg}}$
(1)	625 °C	120 min	5 mL min^{-1}	5 %	500 °C	60 min	24 mL min^{-1}	5 %
(2)	625 °C	120 min	1 mL min^{-1}	1 %	500 °C	60 min	24 mL min^{-1}	5 %
(3)	625 °C	120 min	1 mL min^{-1}	1 %	150 °C	60 min	95 mL min^{-1}	20 %

Between the individual sequences during the periodic operation it is necessary to cool down the instrument from the deactivation temperature to the regeneration temperature and vice versa. The time required was also used to purge the unit from the reaction gases to avoid the formation of explosive gas mixtures.

The deactivation sequences started with evacuating and flushing the TGA twice with nitrogen. The sample was then heated up to the deactivation temperature with a heating rate of 20 K min^{-1}. After 15 min of equilibration the coking was started by introducing the intended amount of propane to the gas flow. After 120 min the gas composition was changed to nitrogen only and the instrument cooled down to 500 °C or 450 °C with a cooling rate of 12.5 K min^{-1}. The cooling procedure takes 10 min or 14 min, respectively. In preliminary experiments it was verified that a 10 min time span for cooling is sufficient to flush out propane to be able to safely introduce oxygen without operating within the explosion limits. The regeneration sequence started by introducing the selected oxygen concentration to the system at a temperature of 500 °C or 450 °C, respectively. After 60 min the gas composition was changed to nitrogen and the setup was heated up to

625 °C with $12.5\,\mathrm{K\,min^{-1}}$ to reach deactivation temperature and to reject all oxygen from the system. Throughout the experiments, the composition of the gases at the outlet of the TGA were monitored using Micro GC. Mass and temperature changes were recorded by the TGA system itself. For an overview of the periodic experiments see Fig. 3.13 and Fig. B.3 and B.4 in Appendix B.4.

Mass changes of the sample and measured temperature during the periodic experiments (1) (see Tab. 3.14) are shown in Fig. 3.13 A. At the beginning of the experiment, the sample was heated up to reaction temperature. During this initial heat up phase a significant mass loss due to desorption can be observed. After the equilibration phase, propane was introduced to the system. An additional small mass loss is observable at the beginning of the deactivation phase. This result is consistent with the observations of the deactivation experiments described above. After that, the mass of the sample increased due to coke build-up until the deactivation phase was ended. Fig. 3.13 C illustrates the change in the product gas composition during the deactivation phase. Since the TGA setup is not able to switch to the regeneration gas mixture during the measurement automatically, the operator had to change settings at the experimental setup manually which causes disturbances in the TGA signal as well as in the temperature signal directly after the deactivation phase. A drop in temperature was unavoidable so that the setup had to be heated up to the regeneration temperature after changing the settings. In Fig. 3.13 B the measured oxygen concentration at the outlet of the experimental setup and the inlet concentration are presented. At the beginning of the regeneration phase, the concentration of the inlet flow differs from the concentration of the outlet flow due to the consumption of oxygen during the regeneration. Simultaneously, a spike in the concentrations of the product gases of the regeneration (CO, CO_2, Fig. 3.13 C) was detected. The concentration of CO_2 is at every point significantly higher than the concentration of CO, which indicates that enough oxygen for a total oxidation of coke is provided. Over the course of the regeneration phase the oxygen concentration at the outlet converged to the inlet concentration. The decreasing product gas concentrations imply that the gasification reactions are completed at the end of the regeneration phase, as can be seen in the mass signal, too. Similar figures for the periodic experiments (2) and (3) can be found in Appendix B.4. A trend that is observable in all periodic experiments is a shift of the sample mass. This decreasing trend can be explained by the intervention of the operator during the experiments. Switching between the deactivation and regeneration phases was not possible in fully automated mode, so manual switching was necessary. For this reason, continuous measurement of the mass was not possible and the individual measurements had to be subsequently combined. Mass changes during the switch-over could not be recorded, which probably contributes to the downward trend in the measurements.

Considering all results, the periodic experiments indicate a good long-term stability of the catalyst. Deactivation as well as regeneration phases are reproducible. The reproducibility of the regeneration phase is also shown in Fig. 3.14 where the product gas concentration and the oxygen concentrations of the different regeneration phases are depicted.

The concentration curves of CO and CO_2 were also used to calculate the amount of carbon that was gasified. These calculations are compared to the mass loss recorded by the TGA in Tab. 3.15. The calculated carbon mass is generally in accordance with the TGA measurements but overestimates the mass loss. The source of this difference is unclear. Coking of the inner parts of the TGA oven itself cannot be excluded.

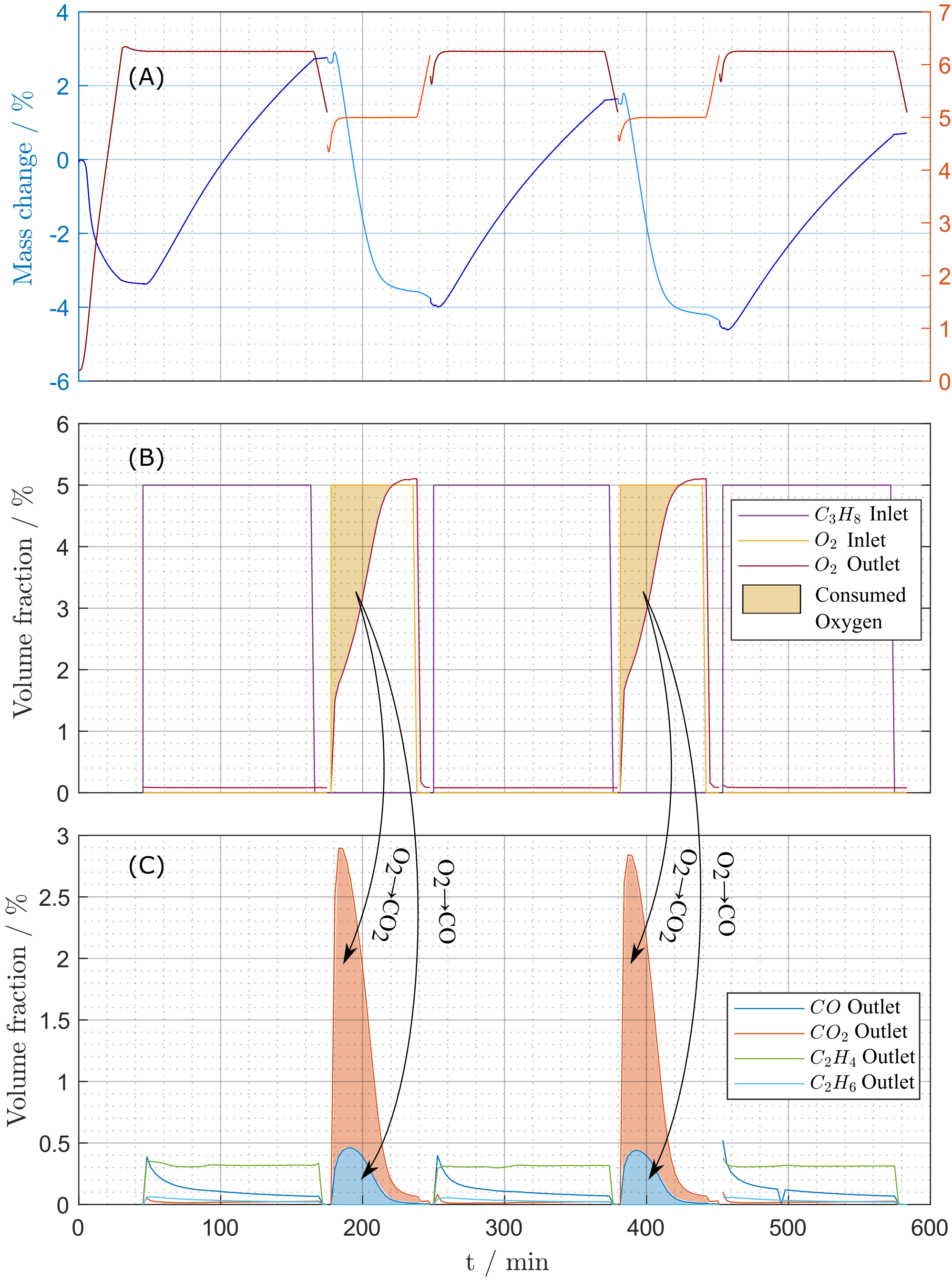

Figure 3.13: Measurements during periodic experiments: (A) mass changes (TGA) and temperature, (B) oxygen and propane concentrations, (C) CO, CO_2, ethene and ethane concentrations for periodic experiment (1).

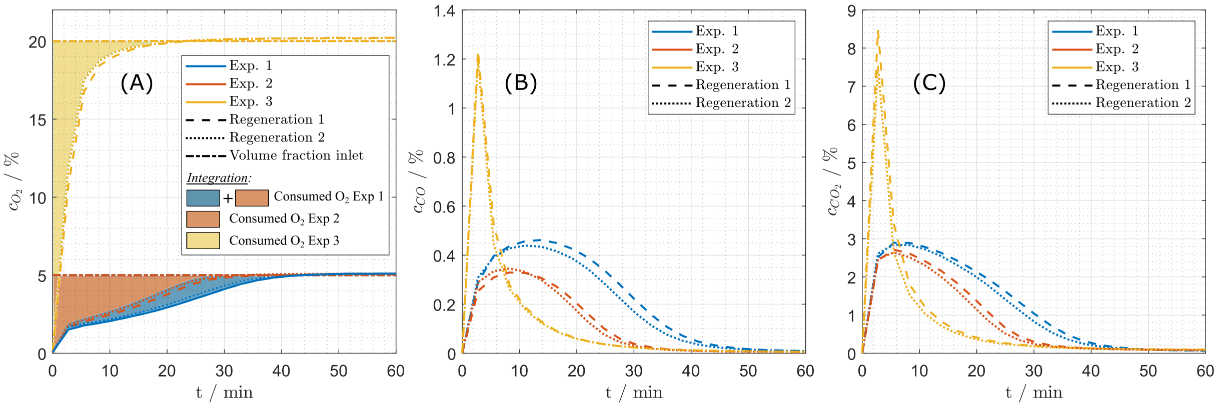

Figure 3.14: Comparison of measured concentrations during all regeneration phases: (A) oxygen, (B) CO, (C) CO_2 (for experimental conditions see Tab. 3.14).

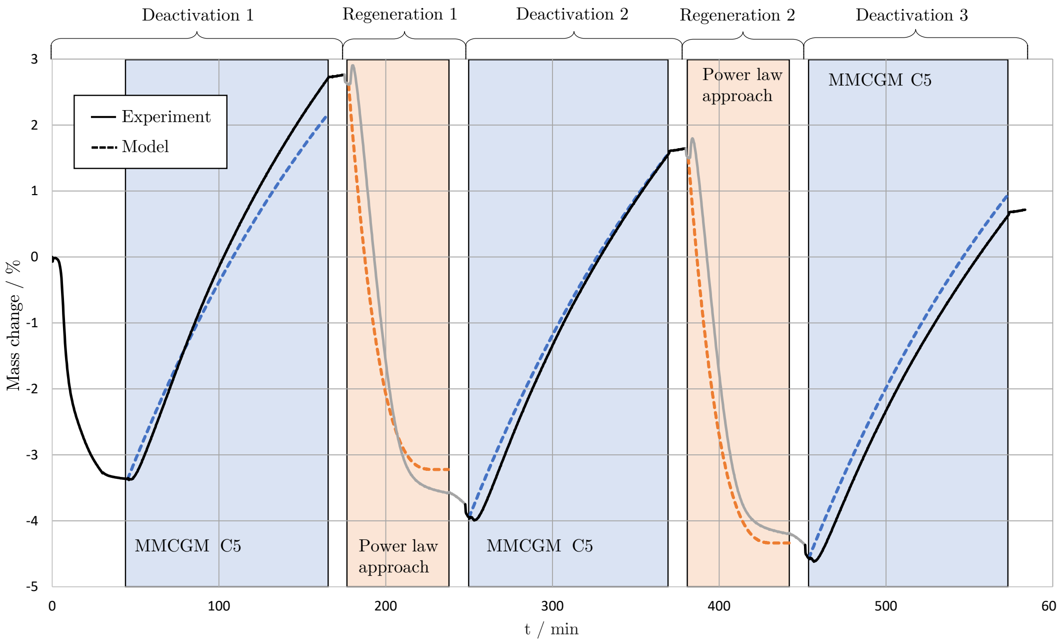

Figure 3.15: Experimental (TGA) and simulated mass changes during periodic experiment 1 (for experimental conditions see Tab. 3.14).

Table 3.15: Comparison between gasified carbon and mass loss recorded by the TGA (for experimental conditions see Tab. 3.14).

Analytics	Parameter	Exp 1		Exp 2		Exp 3	
		Reg 1	Reg 2	Reg 1	Reg 2	Reg 1	Reg 2
GC	Mass carbon (combustion products) in mg	43.41	40.49	30.25	28.19	30.16	26.43
TGA	Total mass change in mg	42.07	39.29	27.27	25.55	28.44	25.11
GC/TGA	Deviation carbon content: GC vs. TGA	3.18 %	3.06 %	10.93 %	10.33 %	6.05 %	5.24 %

Finally, to verify the models of deactivation and regeneration a simulation of the periodic experiments was conducted. Model C5 (Eq. (3.24)) was used to simulate the deactivation phase and the power law approach (Eq. (2.65)) was used to simulate the regeneration phase with the parameters given in Tab. 3.9 and 3.13. The results are shown in Fig. 3.15. Due to the manual changes between the regeneration and deactivation phase an ideal behavior cannot be observed in the periodic experiments performed. For that reason, calculated mass changes were normalized to the actual mass at the beginning of the respective phase in Fig. 3.15 and a good agreement of the experimental and the simulated data can be recognized.

The purpose of the experiments presented here is the validation of the kinetics of regeneration and coking. The test conditions reproduce a production process consisting of a production phase with simultaneous deactivation and a subsequent regeneration phase. However, it should be noted that the experimental set-up is an ideally mixed reactor system for the experimental investigation of kinetics. Industrial processes usually use other reactor types (see Section 2.1.2). The design of the experiments should ensure the greatest possible transferability of the kinetic data. Nevertheless, in tubular reactor types, phenomena occur that cannot be represented by systems with CSTR behavior (e.g. reaction fronts, strong local hotspots). For this reason, verification of the results by means of simulations and subsequent pilot experiments is essential for the transfer of the results.

One missing link and subject of the next section is the exploration of the connection between coking and activity loss.

3.3 Catalyst Deactivation - Model-based Description of the Activity Loss of the Catalyst

After developing a mathematical model to describe the coking and regeneration behavior of the catalyst (Fig. 3.16 B), the aim of this section is to establish models to describe the deactivation of the catalyst (Fig. 3.16 A). Deactivation describes the decrease in catalyst activity over time on stream. Approaches of different complexity are available and will be used in this section. An overview on these approaches is given in Section 2.3.3. All approaches to model the deactivation have been parametrized using the long term experiments which are described in Section 3.3.1. In Section 3.3.2 a phenomenological approach will be parametrized. This approach is based on findings of Janssens (Janssens 2009). Section 3.3.3 uses the insights on catalyst coking that have been established in Section 3.2.1 to develop a deactivation approach that connects the coking behavior with the loss of catalyst activity. The most elementary approach utilized in this work is a time dependent approach that is described in Section 3.3.4.

The goal of the section is to provide models of different complexity that are used in Chapter 4 for simulation and process optimization.

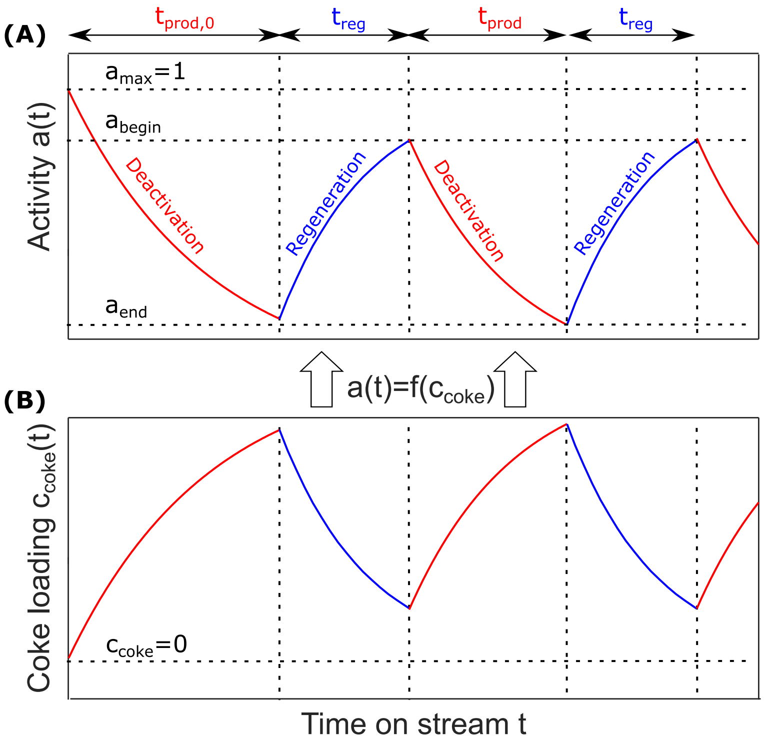
(A)
$t_{prod,0}$
t_{reg}
t_{prod}
t_{reg}
Activity a(t)
$a_{max}=1$
a_{begin}
a_{end}
Deactivation
Regeneration
Deactivation
Regeneration
$a(t)=f(c_{coke})$
(B)
Coke loading $c_{coke}(t)$
$c_{coke}=0$
Time on stream t

Figure 3.16: Schematic representation of (A) catalyst activity and (B) coke loading over time on stream for a production cycle consisting of alternating production and regeneration phases.

3.3.1 Experimental Results

To provide a basis for the model parametrization, lab scale experiments in a quartz glass reactor have been conducted. The same experimental setup as in described in Section 3 was used. The propane concentration at all experiments was 1 %. The temperature was varied between 550 °C and 600 °C. Oxygen concentrations during the experiments have been varied between 0 % and 0.75 %. At higher oxygen percentages no deactivation was visible. A weight hourly space velocity ($WHSV$) of 400 $\mathrm{kg\,s\,m^{-3}}$ was applied. The mass of the catalyst used for these experiments was 1.5 g which results in a bed length of around 6 cm. All experimental conditions are summarized in Tab. 3.16.

Table 3.16: Experimental conditions of long-term deactivation experiments (48 h) conducted in a lab scale PFTR ($x_{\mathrm{C_3H_8,in}} = 1\,\%$, $WHSV = 400\,\mathrm{kg\,s\,m^{-3}}$.

Experiment	T in °C	$x_{\mathrm{O_2,in}}$ in %
(1)	550	0.75
(2)	600	0
(3)	550	0.125
(4)	600	0.125
(5)	550	0.25
(6)	600	0.25
(7)	550	0.5
(8)	600	0.5

For easier comparison of the results and for later fitting of the kinetic parameters, conversion and selectivity over time were determined for all experiments according to the definitions presented in Eq. (3.3) and Eq. (3.4). The experiments show that the operational parameters have a significant influence on the deactivation rate of the catalyst. Fig. 3.17 reveals, that an operation of the reactor without any oxygen and at a temperature of 600 °C leads to a severe drop in conversion (Exp. (2)) whereas at 500 °C and an oxygen concentration of 0.75 % the conversion does not decrease (Exp. (1)). At both temperatures the selectivity of the main product propene and the side products CO_2 and CO do not decrease. With constant selectivity the yields of the different components follow the shape of the conversion curve and decrease in the experiments at 600 °C and without oxygen. The yield in presence of oxygen does not decrease. The results of all deactivation experiments performed can be found in Appendix B.5, Fig. B.5 - B.7.

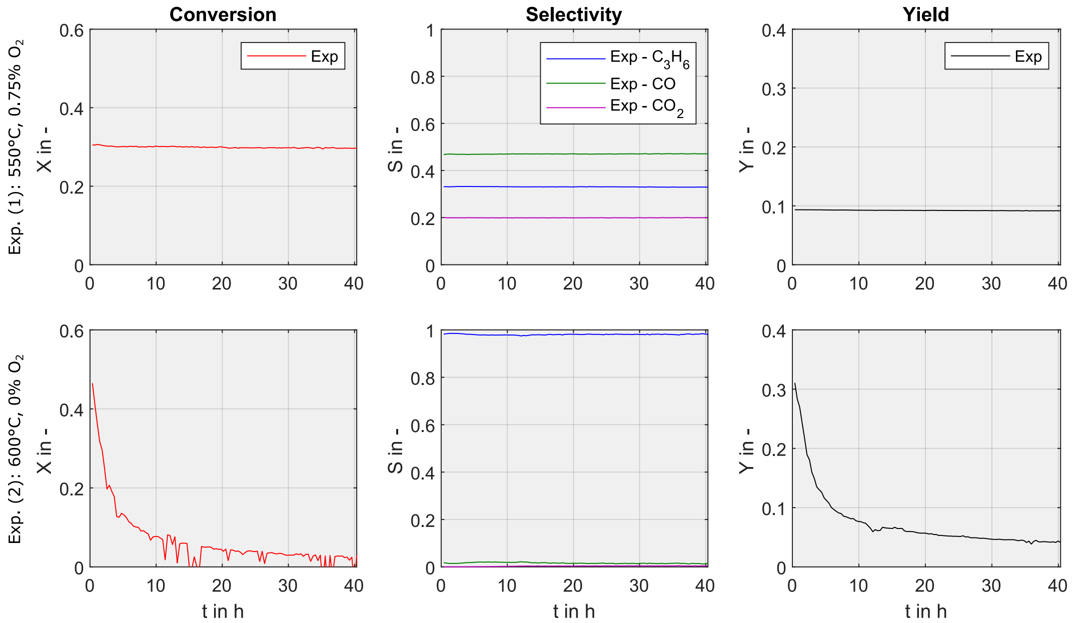

Figure 3.17: Experimental results for experiment (1): $T_{\mathrm{prod}} = 550\,°\mathrm{C}$, $x_{\mathrm{O_2,in}} = 0.75\,\%$, $x_{\mathrm{C_3H_8,in}} = 1\,\%$; and (2): $T_{\mathrm{prod}} = 600\,°\mathrm{C}$, $x_{\mathrm{O_2,in}} = 0\,\%$, $x_{\mathrm{C_3H_8,in}} = 1\,\%$.

3.3.2 Phenomenological Approach for Deactivation

Based on the experimental results, phenomenological models were fitted and model parameters were estimated. The phenomenological approach is based on the findings of Janssens as described in Section 2.3.3. Janssens dedicated the loss of activity in an MTO reactor to the loss of active catalyst (Eq. (2.60)), which is equivalent to shortening of the catalyst bed (Eq. (2.62)). To further generalize the approach in this work, the term $-a_{\mathrm{D}}^{\mathrm{J}} X$ of Eq. (2.62) that describes the shortening of the catalyst bed proportional to conversion has been replaced by an arbitrary function of the conversion X which gives

$$\frac{dz}{dt} = f(X) \tag{3.26}$$

Combining this generalized approach with the mass balance equation leads to

$$\frac{\dot{n}_K}{dt} = \frac{d\dot{n}_K}{dz}\frac{dz}{dt} = f(X)\frac{m_{\mathrm{cat}}}{L}\sum_j \nu_{K,j} r_j^{\mathrm{cat}} \tag{3.27}$$

For the arbitrary function $f(X)$ three different approaches J1 – J3 (Eq. (3.28) - (3.30)) have been chosen in this work.

$$\text{J1:}\quad f(X) = a^{\mathrm{J}}_{\mathrm{D},0}\exp\left(-\frac{E_{\mathrm{D}}}{RT}\right)X \tag{3.28}$$

$$\text{J2:}\quad f(X) = a^{\mathrm{J}}_{\mathrm{D},0}\exp\left(-\frac{E_{\mathrm{D}}}{RT}\right)X^{\gamma} \tag{3.29}$$

$$\text{J3:}\quad f(X) = a^{\mathrm{J}}_{\mathrm{D},10}\exp\left(-\frac{E_{\mathrm{D},1}}{RT}\right)X^{\gamma_1}x_{\mathrm{C_3H_8,in}} + a^{\mathrm{J}}_{\mathrm{D},20}\exp\left(-\frac{E_{\mathrm{D},2}}{RT}\right)\left(X^0 - X\right)^{\gamma_2}x_{\mathrm{O_2,in}} \tag{3.30}$$

The temperature dependence of the approaches has been realized with an Arrhenius-like approach for the constants a_{D}.

$$a^{\mathrm{J}}_{\mathrm{D}} = a^{\mathrm{J}}_{\mathrm{D},0}\exp\left(-\frac{E_{\mathrm{D}}}{RT}\right) \tag{3.31}$$

Model J1 is similar to the original approach introduced by Janssens. In model J2 an exponent γ is added to offer an additional free parameter. The models J1 and J2 both converge to a catalyst activity of zero over time. To account for a residual activity of the catalyst bed, model J3 has been developed. From experiments, it is known that the residual activity of the catalyst bed is higher when a higher inlet concentration of oxygen is used. This trend continues until a point is reached where no deactivation is visible (see Fig. 3.17, Exp. 1). That behavior is described by the additional activation term in model J3. To describe more extensive data sets containing more than one propane concentration, the deactivation term in model J3 was multiplied by the inlet concentration of propane. For parametrization of the models the objective function

$$OF = \sum_{i=1}^{N_{\mathrm{Exp}}}\sum_{j=1}^{N_{t_{\mathrm{point}}}}\left(\hat{y}^{\mathrm{Sim}}_{j,i} - \hat{y}^{\mathrm{Exp}}_{j,i}\right)^2 \tag{3.32}$$

was minimized. The variables $\hat{y}$ describe performance parameters normalized by the maximum value according to Eq. (3.33).

$$\hat{y}_{j,i} = \frac{y_{j,i}}{\max(y_i)} \tag{3.33}$$

$$Y \in \left\{S_{\mathrm{C_3H_6}}, S_{\mathrm{CO}}, S_{\mathrm{CO_2}}, X_{\mathrm{C_3H_8}}\right\}, \qquad y_{j,i} = Y_{j,i} \tag{3.34}$$

The reason for this normalization of the parameters becomes apparent in Fig. 3.18 and is indicated by the difference in conversion ΔX that represents a discrepancy between experimental and simulated evaluation variables at time t^0_{deak}. This difference arises from the already determined steady-state model, which, like any mathematical description of reality, exhibits some deviation from measured values. Fitting of the deactivation kinetics to the absolute values obtained from the experiment would therefore lead to an incorrectly simulated deactivation behavior because of the systematic deviation due to the pre-determined kinetics of the main and side reactions. Therefore, the goal is not to minimize the difference between the absolute values of the simulation and the experiments, but to obtain a kinetic model that describes the deactivation behavior i.e. the curvature of the graph. This can be achieved by scaling the values of both simulation and experiment to the maximum value of the respective time series.

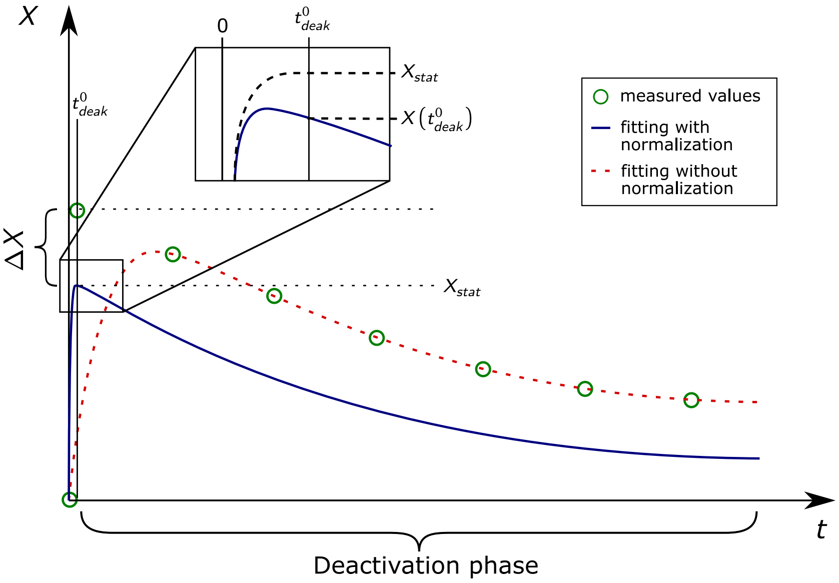

Figure 3.18: Problems with modeling deactivation.

In reality, the deactivation processes start together with the beginning of the experiment. However, this initial condition is difficult to combine with the approaches used in this work. To reduce mathematical complexity, it is assumed for modeling purposes that deactivation starts from a previously calculated steady state. This assumption is justified if the deactivation is significantly slower than the start-up to steady state, which is the case in this example. For the phenomenological approaches, the steady state was calculated by solving the steady state balance expressed in Eq. (2.21).

Another discrepancy between model and reality is shown in the magnification in Fig. 3.18. Here, an offset can be seen between the simulated conversion without deactivation and with deactivation at t^0_{deak}. However, this difference is so small in the present work that the assumption $X_{\text{stat}}(t^0_{\text{deakt}}) = X(t^0_{\text{deak}})$ is justified. Consequently, the modeling process considers the start of deactivation to be at the time of the first measurement point of the experiment.

$$t^{0,(j)}_{\text{deakt}} = t^{(j)}_1 \tag{3.35}$$

This fitting methodology has also been used for the other deactivation modeling approaches in this work (see Section 3.3.3 and 3.3.4). The approaches J1 – J3 described the deactivation behavior with different precision. The models J1 and J2 were not able to describe the curvature of the measured data as depicted in Appendix B.5 Fig. B.5 - B.7. A comparison of the models J1 – J3 is given in Tab. 3.17.

Table 3.17: Evaluation parameters for the model discrimination of the different models based on Janssens approach.

Model	SSQ	N_{par}	AIC	w in %
J1	115.33	3	-2.04×10^3	0
J2	107.43	4	-2.29×10^3	0
J3	6.97	7	-11.91×10^3	100

According to the Akaike information criterion (AIC) J3 fits the experimental data best regardless of the higher number of free parameters. The optimized model parameters for model J3 are summarized in Tab. 3.18.

Table 3.18: Optimized model parameters and confidence intervals of model J3 (Eq. (3.30)).

Parameter	Opt. Value	Unit	Confidence interval in %
$E_{\text{D},1}$	69.8067	kJ mol^{-1}	$\pm 2.2036 \times 10^{-7}$
$a_{\text{D},10}$	291.0634	m s^{-1}	$\pm 4.9581 \times 10^{-6}$
$E_{\text{D},2}$	76.608	kJ mol^{-1}	$\pm 2.5024 \times 10^{-6}$
$a_{\text{D},20}$	128.5876	m s^{-1}	$\pm 4.5150 \times 10^{-6}$
γ_1	1.7637	-	$\pm 4.3200 \times 10^{-6}$
γ_2	0.0038	-	$\pm 9.7838 \times 10^{-4}$

Fig. 3.19 illustrates the agreement between the curvature of the experimental data and the fitted model J3.

A significant difference between the conversion at $t = 0\,\text{s}$ at experiment (1) stands out. This deviation can be traced back to the kinetic model for the main and side reactions derived in Section 3.1, which has been fitted to a wide range of experimental conditions ($WHSV = 100 - 400\,\text{kg s m}^{-3}$, $x_{\text{C}_3\text{H}_8} = 1\,\% - 5\,\%$, $T_{\text{prod}} = 350 - 650\,°\text{C}$). This large parameter space results in a bigger deviation between experiments and simulations for some specific experimental conditions. Generally, experiments without any oxygen at the reactor inlet are described with less accuracy. This underlines the importance of the scaling of the evaluation parameters according to Eq. (3.33) and (3.34). It was carried out to ensure that the simulations accurately describe the shape of the experimental curves despite the absolute differences. Finally, the parameter estimation shows that it is possible to describe the deactivation behavior with a phenomenological approach. The computational effort to make estimations based on these models is reasonable and the approach is feasible for reactions conducted in plug flow reactors. The main disadvantage is the lack of physio-chemical insights regarding coke loading and activity. It has to be mentioned, that the model used in this contribution could have been simplified for this specific experimental data set. The aim of this study was rather to introduce a versatile model structure than to tailor a model for the specific reaction network.

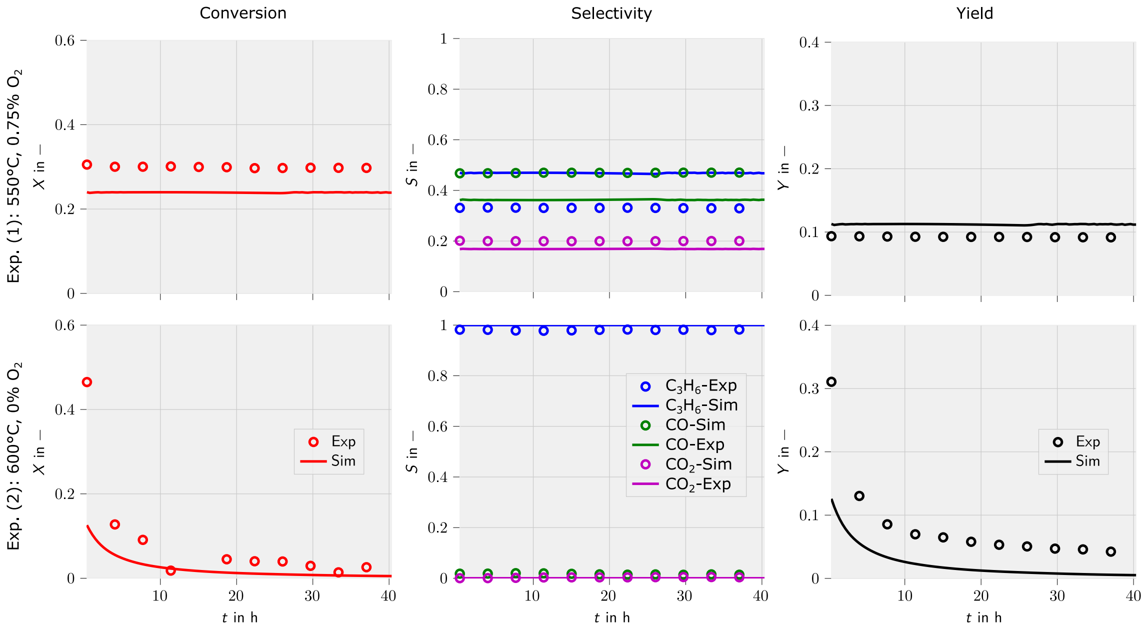

Figure 3.19: Comparison of experimental and simulated performance parameters (model J3) for experiment (1): $T_{\mathrm{prod}} = 550\,^{\circ}\mathrm{C}$, $x_{\mathrm{O_2,in}} = 0.75\,\%$, $x_{\mathrm{C_3H_8,in}}) = 1\,\%$; and (2): $T_{\mathrm{prod}} = 600\,^{\circ}\mathrm{C}$, $x_{\mathrm{O_2,in}} = 0\,\%$, $x_{\mathrm{C_3H_8,in}} = 1\,\%$.

3.3.3 Coke-Based Approach for Deactivation

Besides the phenomenological approach introduced by Janssens a more complex microkinetic model structure following a coke-based concept used by Dumez and Froment among others has been deployed. The model considers the coke build-up and connects the activity with the coke deposits on the catalyst as introduced in Section 2.3.3 (Eq. (2.53) - (2.55), Dumez and Froment 1976). For a more convenient presentation, the equations are denoted as DF1, DF2, and DF3 as shown in Eq. (3.36) - (3.39). Approach DF4 (Eq. (3.39)) represents an extension of the approaches from the literature. The exponents γ_j in the denominator of the equation was introduced as an additional free parameter in deviation from approach DF3.

$$\text{DF1:} \quad a_j = \exp\left(-\zeta_j c_{\mathrm{coke}}\right) \tag{3.36}$$

$$\text{DF2:} \quad a_j = \frac{1}{1 + \zeta_j c_{\mathrm{coke}}} \tag{3.37}$$

$$\text{DF3:} \quad a_j = \frac{1}{\left(1 + \zeta_j c_{\mathrm{coke}}\right)^2} \tag{3.38}$$

$$\text{DF4:} \quad a_j = \frac{1}{\left(1 + \zeta_j c_{\mathrm{coke}}\right)^{\gamma_j}} \tag{3.39}$$

As with the phenomenological approach, the fully developed concentration profiles from a simulation without deactivation influence were used as the starting point for fitting the deactivation kinetics. For that reason, Eq. (2.15) was used to simulate the reactor for a reaction time of 2 s, which is sufficient to develop steady state concentration profiles. The PDE has been solved with a Finite-Volume-Method. Therefore, the length of the reactor was divided into $N = 60$ segments. After discretization a conventional ODE solver (MATLAB: ode45) was used. Further details on discretization are given in Appendix B.7.1.

Deactivation of the catalyst was considered after the initial period. To describe the decay in activity, the deactivation coefficient introduced in Eq. (2.50) was utilized. This coefficient describes the catalyst activity as the ratio between the reaction rate of the fresh catalyst and the actual reaction rate during time on stream. The parameter estimation followed the the same procedure as described before for the phenomenological approach.

Parameters for all model structures have been estimated and have been compared using Akaikes Information Criterion (AIC), which allows a systematic model discrimination. The results of the model discrimination are summarized in Tab. 3.19.

Table 3.19: Evaluation parameters for the model discrimination of the different models based on Dumez and Froment.

	DF1	DF2	DF3	DF4
SSQ	20.8997	20.5492	20.4011	19.2062
N_{par}	3	3	3	6
AIC	-8.0479×10^3	-8.1074×10^3	-8.1329×10^3	-8.3393×10^3
w in %	0	0	0	100

The approach using model structure DF4 offers the smallest value for the residual sum of squares. Due to the additional parameters γ_j the model has six free parameters that can be adjusted to minimize the OF whereas the other models have only three. However, the strong improvement of the OF justifies these additional parameters, which is illustrated by the AIC values. The optimal parameters of model DF4 are presented in Tab. 3.20. Fig. 3.20 illustrates the average coke loading and the mean activities over time for the experiments (2), (4), (6) and (8) ($T = 600\,°\mathrm{C}$, $x_{\mathrm{C_3H_8,in}} = 1\,\%$).

Table 3.20: Optimized model parameters and confidence intervals for model DF4 (Eq. (3.39)).

Parameter	Value	Confidence intervals in %
ζ_1 in $\%^{-1}$	0.5396	$\pm 2.03 \times 10^{-3}$
ζ_2 in $\%^{-1}$	2.5923	$\pm 2.40 \times 10^{-3}$
ζ_3 in $\%^{-1}$	0.3464	$\pm 4.75 \times 10^{-3}$
γ_1 in $-$	0.9786	$\pm 2.14 \times 10^{-3}$
γ_2 in $-$	0.0869	$\pm 1.73 \times 10^{-2}$
γ_3 in $-$	0.2274	$\pm 4.89 \times 10^{-3}$

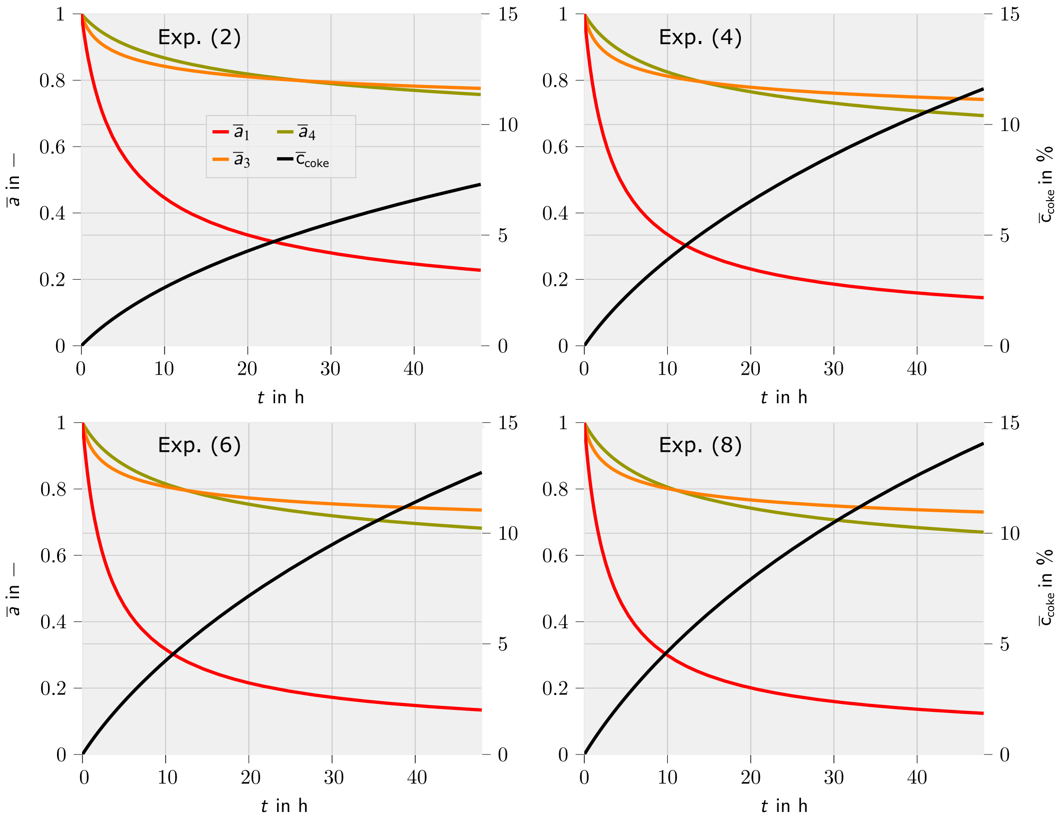

Figure 3.20: Simulated average coke and activity profiles (model DF4) under the conditions of experiments (2), (4) , (6) and (8); $T_{\mathrm{prod}} = 600\,^\circ\mathrm{C}$, $x_{\mathrm{C_3H_8,in}} = 1\,\%$,$x_{\mathrm{O_2,in}} = 0\,\%$, $0.125\,\%$, $0.25\,\%$ and $0.5\,\%$.

All values have been averaged over the length of the reactor. The graphs reveal a shortcoming of the modeling approach. According to Eq. (3.22) the coke build-up depends solely on the propene concentration. This leads to counter-intuitive coke profiles since the simulation predicts more coke build-up in oxygen rich conditions. This is in contrast to experimental results and experience in industry, where more oxygen leads to less severe coking of the catalyst and a more pronounced deactivation behavior is visible without oxygen. Based on these results, a functional relationship between overall propene concentration and catalyst coking seems to be an oversimplification. Thus, in the following section the model is modified to be able to describe the real coking behavior of the catalyst more precisely.

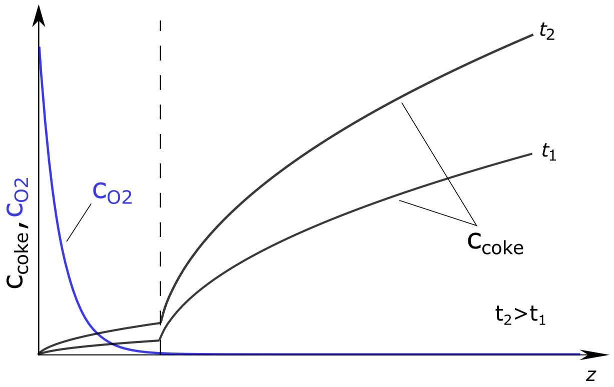

Figure 3.21: Schematic representation of coking profiles in a tubular reactor in a dehydrogenation experiment utilizing oxygen.

Qualitative description of the coke formation As presented in Fig. 3.21, only moderate coke formation is expected as long as oxygen is present in the reactor. To suppress unwanted consecutive reactions, the oxygen concentrations in the experiments and the simulations respectively have been kept relatively low. Under such condition oxygen will not penetrate to the end of the reactor. Parts of the reactor without oxygen show more coking than parts with oxygen. The current simple model structure does not represent this behavior properly. To improve the model, further attempts were made to link the coking process to the TDH reaction. In order to keep the original model structure, a distinction was made between propene produced in the TDH reaction and propene produced via ODH. This assumption is based on the fact that during ODH, coking is almost absent whereas in TDH the catalyst shows fast coking. This separation has to be reflected in the stochiometric matrix. A modified version of the stochiometric matrix is presented in Eq. (B.36) (Appendix B.7). Due to this modification, the kinetic equation for the coke forming reaction changes. For the following models, the coke formation is described by

$$c_{\mathrm{coke}} = c_{\mathrm{max}} - \left((h-1)\, k_{\mathrm{m}}\, c^{l}_{\mathrm{C_3H_6,TDH}}\, t + c_{\mathrm{max}}^{1-h} \right)^{\frac{1}{1-h}} \tag{3.40}$$

where $c_{\mathrm{C_3H_6,TDH}}$ describes the concentration of propene produced by the TDH reaction. Besides the coke forming reaction, other reactions do not distinguish between propene species. For that reason, weighting factors Φ_{TDH} and Φ_{ODH} (Eq. (3.41) – (3.42)) have been introduced. The subsequent reactions consume these pseudo species in two specific proportions.

$$\Phi_{\mathrm{TDH}} = \frac{x_{\mathrm{C_3H_6,TDH}}}{x_{\mathrm{C_3H_6,TDH}} + x_{\mathrm{C_3H_6,ODH}}} \tag{3.41}$$

$$\Phi_{\mathrm{ODH}} = \frac{x_{\mathrm{C_3H_6,ODH}}}{x_{\mathrm{C_3H_6,TDH}} + x_{\mathrm{C_3H_6,ODH}}} \tag{3.42}$$

To assure that mass balances are fulfilled, the weighting factors add up to 1 and the concentration of both pseudo propene species add up to the total amount of propene as presented by

$$1 = \Phi_{\mathrm{TDH}} + \Phi_{\mathrm{ODH}} \tag{3.43}$$

and

$$p_{\mathrm{C_3H_6}} = p_{\mathrm{C_3H_6,ODH}} + p_{\mathrm{C_3H_6,TDH}} \tag{3.44}$$

The reactions affected by these changes are the partial and the total oxidation of propene (R3, R4). After introducing the weighting factors, Eqs. (3.7) and (3.8) are modified and now read

$$r_3^{\mathrm{mod}} = k_3 \left(p_{\mathrm{C_3H_6,ODH}} + p_{\mathrm{C_3H_6,TDH}}\right)^{\alpha_3} p_{\mathrm{O_2}}^{\beta_3} \tag{3.45}$$

$$r_4^{\mathrm{mod}} = k_4 \left(p_{\mathrm{C_3H_6,ODH}} + p_{\mathrm{C_3H_6,TDH}}\right)^{\alpha_4} p_{\mathrm{O_2}}^{\beta_4} \tag{3.46}$$

In analogy to the analysis performed before, all model structures have been tested again to find the model that describes the measured data with the closest agreement. Modified models are denoted by DF1 TDH - DF4 TDH. The AIC values summarized in Tab. 3.21 show that model structure DF1 TDH yields better results than structure DF4 TDH, which was superior before the modification.

Table 3.21: Evaluation parameters for the model discrimination of the different models based on Dumez and Froment with modified propene species.

Parameter	DF1 TDH	DF2 TDH	DF3 TDH	DF4 TDH
SSQ	10.7	11.55	10.91	10.73
N_{par}	4	4	4	7
AIC	-10.4038×10^3	-10.1363×10^3	-10.3356×10^3	-10.3890×10^3
w in %	99.9397	0	0	0.0603

Resulting from the model structure, the number of free parameters has been reduced to 3, which are presented in Tab. 3.22. Fig. 3.22 illustrates the calculated coke and activity profiles of model DF1 TDH for the experiments (2), (4), (6) and (8) (Tab. 3.16).

Table 3.22: Optimized model parameters of model DF1 TDH with corresponding confidence intervals (Eq. (3.36)).

Parameter	DFT1 TDH	Confidence interval in %
ζ_1 in $\%^-1$	0.1868	$\pm 2.43 \times 10^{-3}$
ζ_2 in $\%^-1$	0.1505	$\pm 3.06 \times 10^{-3}$
ζ_3 in $\%^-1$	0.4867	$\pm 5.36 \times 10^{-4}$

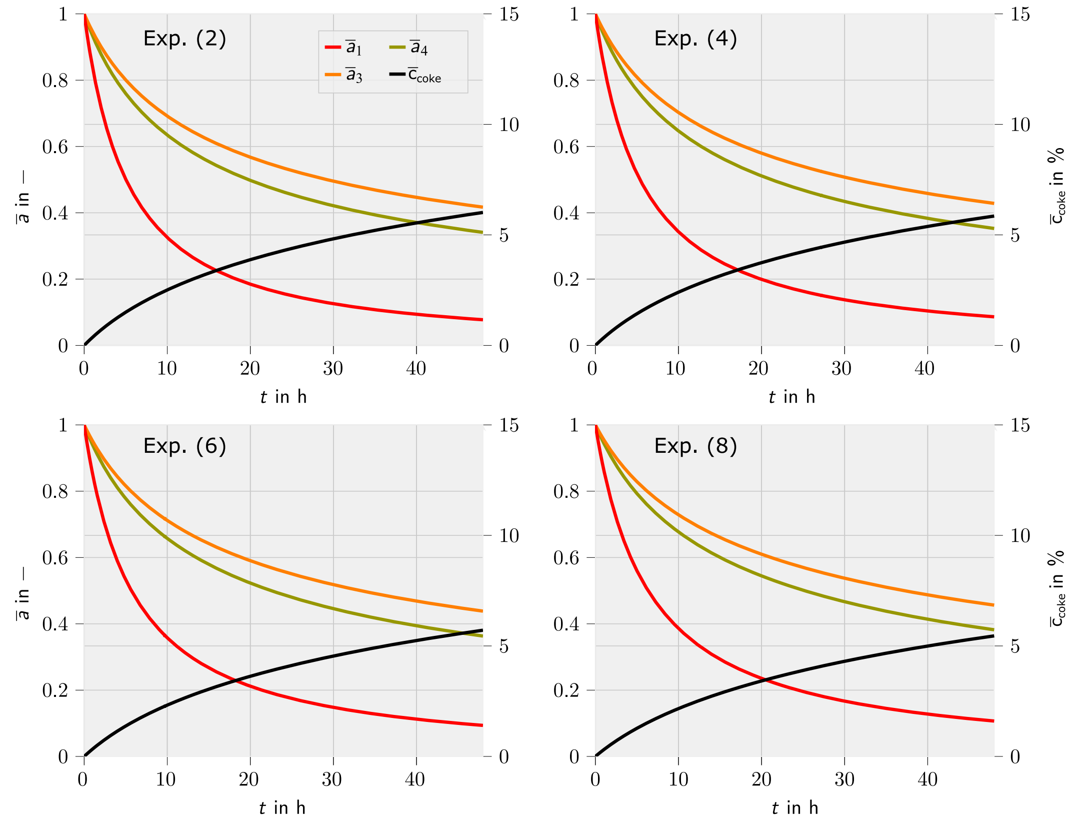

Figure 3.22: Simulated average coke and activity profiles (model DF1 TDH) under the conditions of experiments (2), (4) , (6) and (8) (see Table 3.16); $T_{\text{prod}} = 600\,°\text{C}$, $x_{\text{C}_3\text{H}_8,\text{in}} = 1\,\%$, $x_{\text{O}_2,\text{in}} = [0\,\%, 0.125\,\%, 0.25\,\%, 0.5\,\%]$.

In this model, the amount of coke decreases with increasing oxygen concentration, which is in agreement with the experiments. While the coking profiles exhibit a qualitative agreement with the experimental results, there is a noticeable discrepancy between the experimentally measured coke profiles and the simulated coking profiles. Model DF1 TDH underestimates the coke content on the catalyst. Due to these shortcomings, the rate constant of the coking kinetics k_0 has been adapted. In that way it was possible to maintain the original model structure that proved to fit the experimental data satisfyingly.

Quantitative description of coke formation As described in Section 3.2.2 the catalyst bed in the lab scale PFTR reactor used in the experiments can be separated into segments in order to determine coke loadings for the segments by using a TGA setup. For experiments (2), (4), (6) and (8), the coke loadings of the individual reactor segments have been measured and could be used to refine the model. The average coke loading of the 3 reactor segments has been measured according to the procedure explained in Section 3.1. Fig. 3.23 A illustrates the segmentation of the reactor with increasing coke depositions over reactor length caused by the increasing concentration of propene as coke precursor.

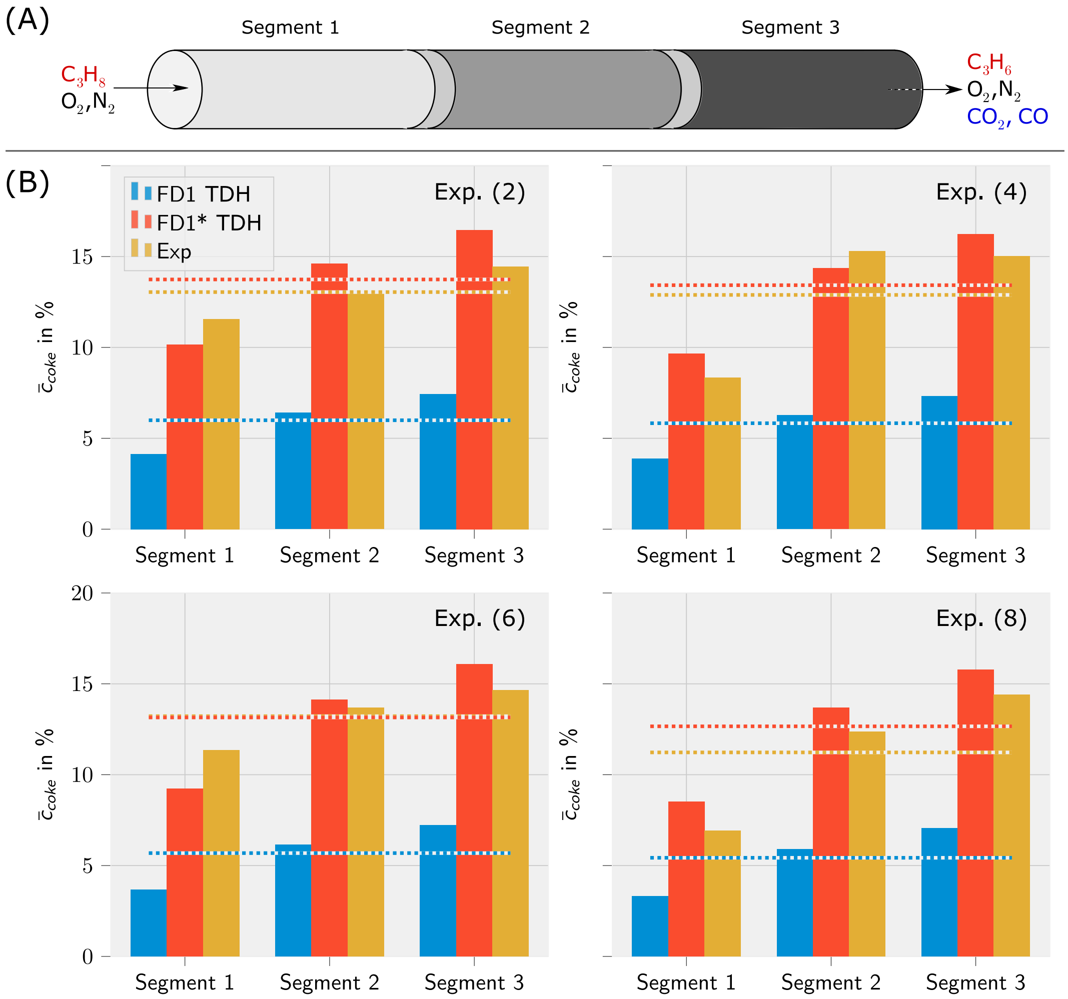

Figure 3.23: (A) Schematic of the segmented lab scale reactor; (B) Comparison of simulated and experimentally determined coke loadings in a segmented tubular reactor for the experiments (2), (4), (6) and (8) (see Table 3.16) with $T_{\mathrm{prod}} = 600\,°\mathrm{C}$, $x_{\mathrm{C_3H_8,in}} = 1\,\%$, $x_{\mathrm{O_2,in}} = [0\,\%, 0.125\,\%, 0.25\,\%, 0.5\,\%]$, dashed line: average coke loading over all three segments.

The coke loading as additional information allowed to extend the OF as presented in Eq. (3.47). A weighting factor of 100 is multiplied to the squared differences of the coke loading to enhance its effect on the objective function. This weighting factor is necessary to account for the larger number of values for the key parameters $\hat{y}_{i,j}^{\mathrm{Exp}}$ ($N_{\mathrm{Exp}} = 8$, $N_{t_{\mathrm{point}}} = 110$) in comparison to the lower number of values for the coke loading $c_{\mathrm{coke}}^{\mathrm{Exp}}$ ($N_{\mathrm{Exp,600}} = 4$).

$$OF = \sum_{i=1}^{N_{\mathrm{Exp}}} \sum_{j=1}^{N_{t_{\mathrm{point}}}} \left(\hat{y}_{j,i}^{\mathrm{Sim}} - \hat{y}_{j,i}^{\mathrm{Exp}}\right)^2 + 100 \sum_{n=1}^{N_{\mathrm{Exp,600}}} \left(\bar{c}_{\mathrm{coke},n}^{\mathrm{Sim}} - \bar{c}_{\mathrm{coke},n}^{\mathrm{Exp}}\right)^2 \tag{3.47}$$

The parameter estimation was conducted following the procedure described above. The set of fitting parameters was extended by the rate constant of coking, since coking was underestimated by the previous models. Fig. 3.23 B shows the measured coke loadings and the simulated values. The modified model including an adjusted rate constant of the coke build-up is denoted as DF1* TDH. The new model is able to describe the average coke loading and the development of coke deposition over length of the reactor for the experiments with good agreement. Fig. 3.24 reveals that the calculated performance parameters are in good agreement with the measured values.

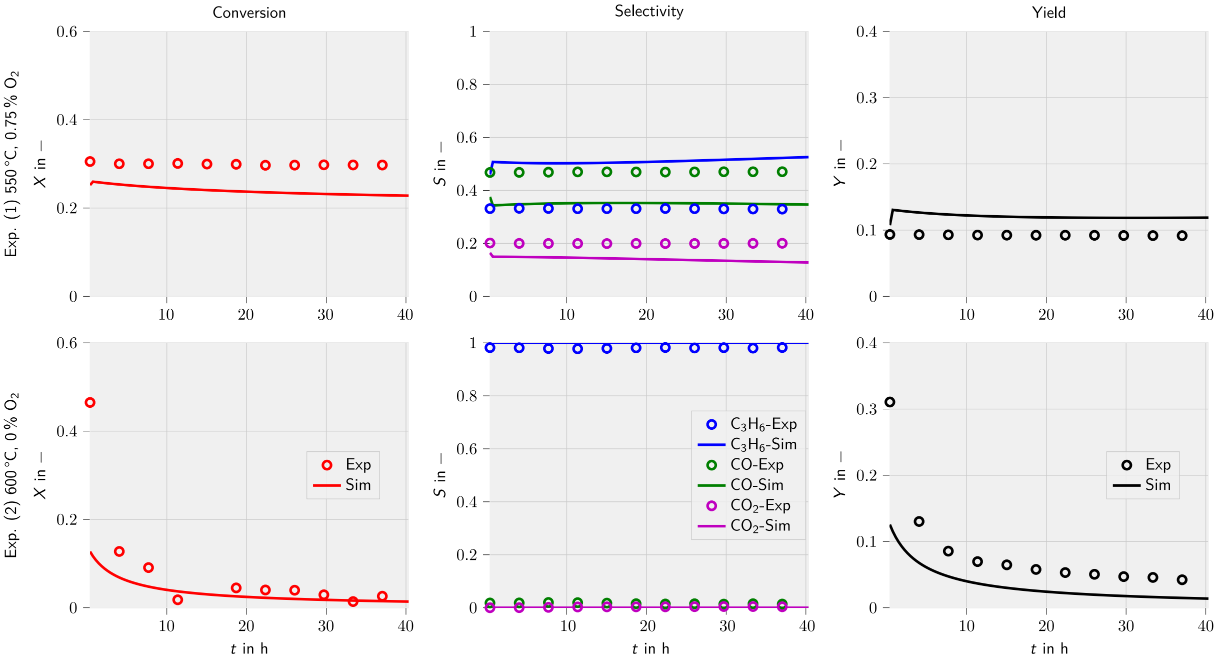

Figure 3.24: Comparison of experimental and simulated performance parameters (model DF1* TDH) for experiment (1): $T_{\mathrm{prod}} = 550\,°\mathrm{C}$, $x_{\mathrm{O_2,in}} = 0.75\,\%$, $x_{\mathrm{C_3H_8,in}} = 1\,\%$; and (2): $T_{\mathrm{prod}} = 600\,°\mathrm{C}$, $x_{\mathrm{O_2,in}} = 0\,\%$, $x_{\mathrm{C_3H_8,in}} = 1\,\%$.

The model parameters are given in Tab. 3.23. All values of ζ_i are remarkably smaller than in the previous models. This is caused by the adjusted rate constant of coking k_0 which leads to more coking in model DF1* TDH. To keep the activity loss the same, lower values of ζ_i are necessary.

Table 3.23: Optimized parameters of model DF1* TDH with corresponding confidence intervals.

Parameter	Opt. Value	Unit	Confidence interval in %
ζ_4	0.1119	$\%^{-1}$	0.0425
ζ_3	0.0471	$\%^{-1}$	0.0291
ζ_1	0.1837	$\%^{-1}$	0.0052
k_0	3.2657×10^{-6}	$(\mathrm{kg_{coke}\,kg_{cat}^{-1}\,min^{-1}})^{1-h}$	0.6111

To compare model DF1* TDH to model DF1 TDH, the OF described in Eq. (3.32) has been calculated with the performance parameters of model DF1* TDH. This provides a basis for comparing both models. The value of the OF for model DF1* TDH is 14.13 whereas for model DF1 TDH it is 10.70. That illustrates that the former model DF1 TDH without modified coking kinetics is more accurate in predicting the change in activity than the modified model. The reason is a trade off between the ability to predict performance parameters and coke content. The decline in precision in terms of performance parameters is acceptable, since a more accurate knowledge of the coke loading provides useful insights with respect to catalyst regeneration. Fig. 3.25 illustrates the advantage of the applied modeling approach. It is possible to calculate coke and activity profiles with temporal and spatial resolution.

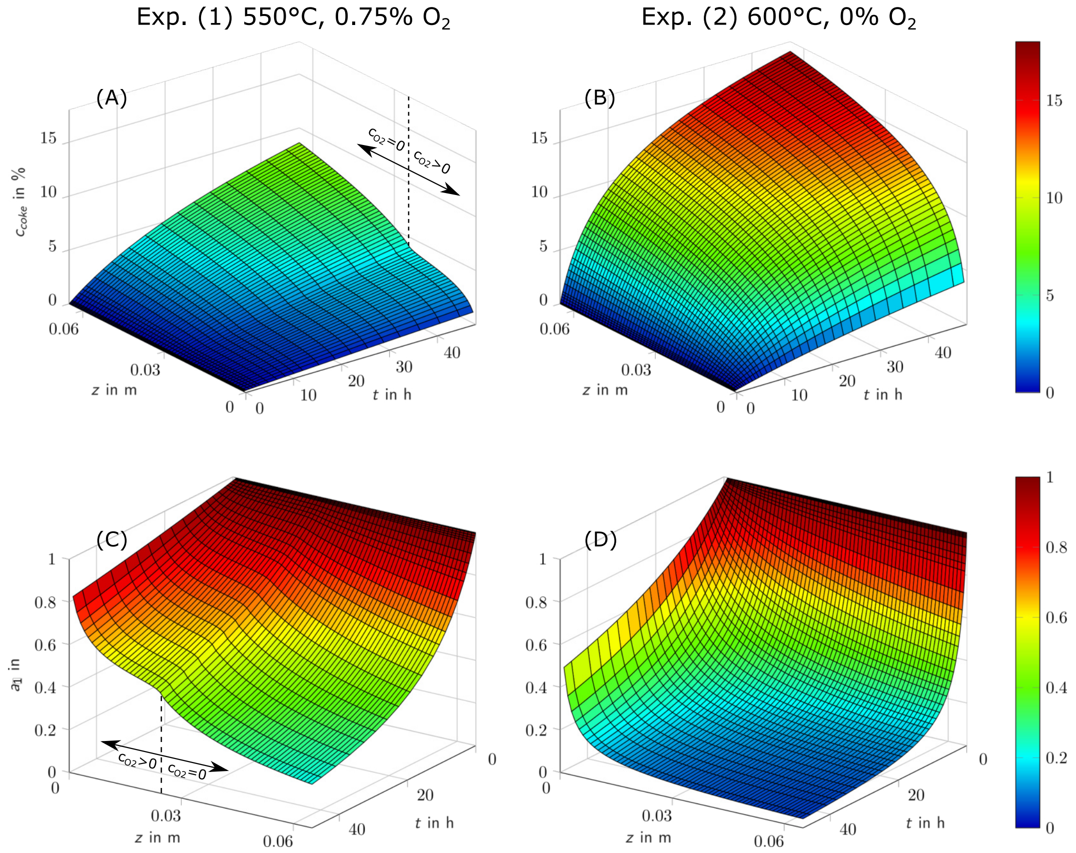

Figure 3.25: Spatially and temporally resolved coke profiles (A and B) and activity profiles (C and D) for experiment (1) and (2).

Fig. 3.25 presents the results for Exp. (1) and (2) and shows activity a_1, since it represents the decay in propene production. For the activities a_3 and a_4 see Fig. B.11 in Appendix B.7. A significant difference between the simulation results of Exp. (1) and (2) illustrated in Fig. 3.25 is the amount of coke deposited on the catalyst surface. At higher temperatures and without oxygen (Exp. (2), Fig. 3.25 B) the amount of coke is higher compared to lower temperatures and small amounts of oxygen (Exp. (1), Fig. 3.25 A). For Exp. (1) it is clearly visible where the oxygen is depleted in the reactor. After the oxygen has been completely consumed, there is a significant increase in coke formation (Fig. 3.25 A). This transition can also be observed in the activity curves (Fig. 3.25 C - D), where the activities decrease faster after all oxygen has been consumed. Due to the spatial resolution of the profiles it is possible to transfer the model to more complex reactor geometries. A 2D simulation is possible. The calculated coking profiles are used in the next section to simulate the regeneration phase of the reactor. This allows the simulation of both production and regeneration phases and a cyclic reactor operation. In that way, an optimization of the whole process is possible.

3.3.4 Time Dependent Approach for Catalyst Deactivation

Besides the phenomenological approach introduced in Section 3.3.2 and the coke-based approach presented in Section 3.3.3 a time dependent approach has been parametrized to describe the deactivation behavior of the catalyst. The theoretical foundations of this approach are discussed in Section 2.3.3. Similar to the coke dependent approach, the activity is defined as in Eq. (2.50) as a time dependent factor, which is multiplied to the reaction rates of the fresh catalyst. The activity coefficient itself is modeled with an additional balance equation (Eq. (2.51)) and depends on the concentration of the coke precursor and the activity. Propene has been identified to be the main coke precursor in this reaction. Nevertheless, for the sake of simplicity of the model, it was assumed that both propane and propene contribute to the coke formation on the catalyst surface. With this assumption Eq. (2.51) now reads

$$r_{\mathrm{deact}} = -a^n k_{\mathrm{d}} \left(x_{\mathrm{C_3H_8}} + x_{\mathrm{C_3H_6}} \right)^{a_{\mathrm{d}}} \tag{3.48}$$

To further simplify the equations, side products have been neglected. Due to the stoichiometry, the sum of propene and propane at every point in the reactor is equal to the inlet concentration of propane which leads to

$$r_{\mathrm{deact}} = -a^n k_{\mathrm{d}} x_{\mathrm{C_3H_8,in}}^{a_{\mathrm{d}}} \tag{3.49}$$

The experimental results revealed that oxygen in the reactor has a beneficial influence on catalyst deactivation. To account for this, the power law approach reading

$$r_{\mathrm{reg}} = +a^n k_{\mathrm{a}} x_{\mathrm{O_2,in}}^{b_{\mathrm{a}}} \tag{3.50}$$

has been used, which is analogous to the model for coke combustion (Eq. (2.65)) presented in Section 2.3.4. The deactivation term (Eq. (3.49)) and the regeneration term (Eq. (3.50)) have been combined to

$$\frac{da}{dt} = r_{\mathrm{a,deact,net}} = r_{\mathrm{a,deact}} + r_{\mathrm{a,reg}} = a^n \left(k_{\mathrm{a}} x_{\mathrm{O_2,in}}^{b_{\mathrm{a}}} - k_{\mathrm{d}} x_{\mathrm{C_3H_8,in}}^{a_{\mathrm{d}}} \right) \tag{3.51}$$

Integration of Eq. (3.51) leads to

$$a(t) = \left(\left(k_{\mathrm{a}} x_{\mathrm{O_2,in}}^{b_{\mathrm{a}}} - k_{\mathrm{d}} x_{\mathrm{C_3H_8,in}}^{a_{\mathrm{d}}} \right) t \left(1-n\right) + 1 \right)^{\frac{1}{1-n}} \tag{3.52}$$

To be able to determine optimized parameters for the deactivation model a parameter estimation has been performed. As an experimental basis Exp. (4), (6) and (8) have been used (see Tab. 3.16 for details). The reactor model was assumed to be isothermal, isobar and in steady state. On the basis of Eq. (3.1) and Eq. (2.50) this leads to the following 1D plug flow reactor model:

$$\frac{d\dot{n}_i}{dz} = \frac{m_{\mathrm{cat}}}{L} \sum_{j=1}^{M} \nu_{i,j} a_j(t) r_{j,m,0} \tag{3.53}$$

In contrast to the coke dependent approach it was assumed that all reactions are effected the same by catalyst activation.

$$\frac{d\dot{n}_i}{dz} = \frac{m_{\text{cat}}}{L} a(t) \sum_{j=1}^{M} \nu_{i,j} r_{j,m,0} \tag{3.54}$$

The lsqnonlin solver from Matlab was used to minimize the objective function

$$OF = \sum_{i=1}^{N_{\text{Exp}}} \sum_{j=1}^{N_{t_{\text{point}}}} \left(\hat{y}_{j,i}^{\text{Sim}} - \hat{y}_{j,i}^{\text{Exp}} \right)^2 \tag{3.55}$$

to determine optimized kinetic parameters of Eq. 3.51.

N_{Exp} represents the number of experiments ($N_{\text{Exp}} = 3$), $N_{t_{\text{point}}}$ is the number of measurements per experiments and ($N_{t_{\text{point}}} = 100$) and $\hat{y}_{j,i}$ are the experimentally (Exp) or simulative (Sim) investigated normalized performance parameters. The objective function describes the squared differences of the normalized performance parameters. For normalization the performance parameters are divided by the first value at the first time step t_1 at the beginning of the measurement:

$$\hat{y}_{j,i} = \frac{y_{j,i}}{y_{1,i}} \tag{3.56}$$

$$Y \in \left\{ S_{\text{C}_3\text{H}_6}, S_{\text{CO}}, S_{\text{CO}_2}, X_{\text{C}_3\text{H}_8} \right\}, \qquad y_{j,i} = Y_{j,i} \tag{3.57}$$

The performance parameters and the modeled values of the deactivation approach are presented in Fig. 3.26. It becomes clear, that even this very simple approach is able to describe the experimental values sufficiently. The optimized parameters are presented in Tab. 3.24.

Table 3.24: Optimized kinetic parameters of the time dependent deactivation model.

Parameter	Opt. Value	Confidence Intervals	Unit
k_d	9987.23	$\pm 9.77 \times 10^{-7}$	$(\text{h}\,\%^{a_\text{d}})^{-1}$
a_d	2.18	$\pm 1.1 \times 10^{-3}$	-
k_a	3.15	$\pm 6.02 \times 10^{-2}$	$(\text{h}\,\%^{b_\text{a}})^{-1}$
b_a	0.76	$\pm 9.49 \times 10^{-7}$	-
n	2.22	$\pm 3.2 \times 10^{-3}$	-

The time dependent approach presented in this section is the least complex modeling strategy studied in this work. The activity is not connected to the coke content built up on the catalyst surface that is the reason for the deactivation. It does not allow to give any insights about spatial distribution of activity inside the reactor. From coking experiments it is known that coking is more severe at the rear end of the reactor close to the outlet which indicates a more pronounced deactivation in these parts of the reactor. The catalyst activity described by the time dependent approach can therefore be interpreted as an integral activity of the overall reactor.

It has to be noted, that the experimental basis of this approach consists only of 3 experiments. The generality of the model and the possibility of extrapolation of the model

beyond the conditions of the experiments can be doubted. Nevertheless, the simple approach bears lots of advantages when it comes to complex simulations. Solving PDEs is especially demanding when the system of differential equations is stiff, which means for balance equations in reaction engineering that time constants are of different orders of magnitude (Strehmel et al. 2012). Since the main and side reactions in the reaction network (Fig. 2.14) are very fast compared to coking and thus deactivation, this system of equations can be considered as a stiff differential equation system. The time depending approach as introduced here can avoid difficulties in solving such a system by providing a simple algebraic equation for the catalyst activity.
The time dependent approach as presented in this section is later on used for 2D simulations of complex reactor configurations. Further simplifications are introduced in order to reduce the computational effort even more.

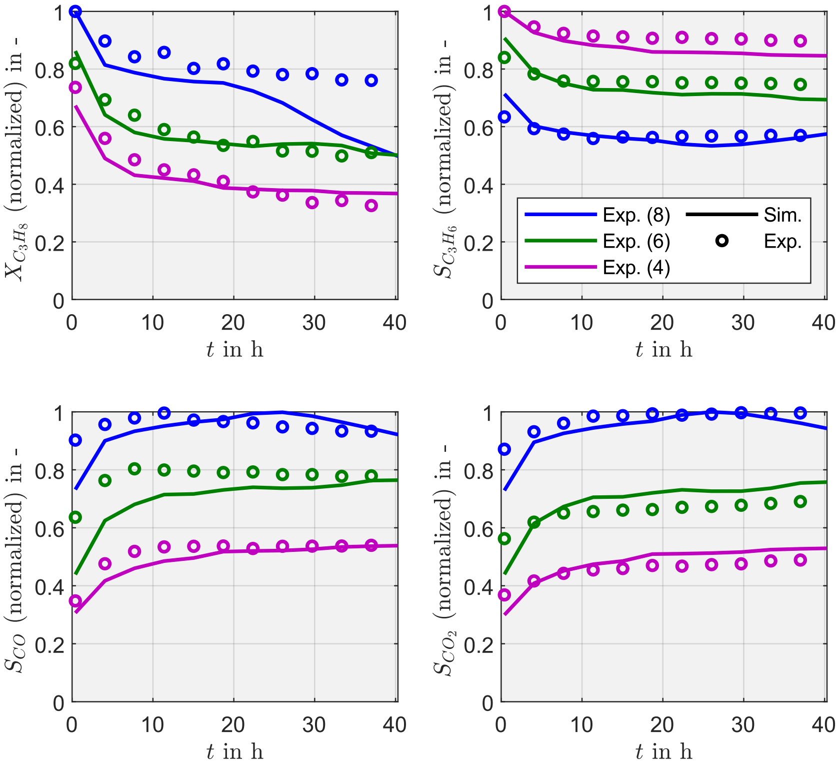

Figure 3.26: Measured and simulated performance parameters of the time dependent deactivation model.

3.4 Interim Conclusion

In Chapter 3 the experimental investigation and the successive parameter estimation of all aspects of the propane dehydrogenation process has been presented. In Section 3.1 the kinetics of the main and side reactions were determined based on experimental studies in a lab scale FBR. A power law approach proved to describe the kinetics with sufficient precision. The kinetics are able to describe the behavior of the catalyst in a broad range of experimental conditions. The kinetics of the main and side reactions are a prerequisite for the consecutive estimation of coking kinetics and regeneration kinetics presented in

Section 3.2. A TGA setup has been utilized for coking experiments that served as a basis for the parameter estimation of the coking kinetics (Section 3.2.1). For this purpose, the monolayer multilayer coke-growth model was specifically extended and adapted to the conditions in order to describe the coking kinetics as precisely as possible. A systematic model discrimination procedure has been used to identify the best fitting model. To determine the regeneration kinetics in Section 3.2.2, samples from long term coking experiments have systematically been regenerated in the TGA setup. Description of the regeneration kinetics has been achieved by using a power law approach. A model validation of coking and regeneration models has been also conducted in Section 3.2.3 with the TGA setup and verified the accordance of the models with the experimental data. Phenomena of importance in industrial processes that could not be observed by the experimental approach, such as the propagation of temperature fronts or intraparticle temperature and concentration profiles, were briefly discussed. The need for research in this area was addressed.

For the modeling of catalyst deactivation three different approaches of different levels of detail have been used in Section 3.3. All approaches offer different advantages and disadvantages in terms of level of detail and mathematical complexity. After illustrating the general trends with the help of the experimental results in Section 3.3.1 a phenomenological approach has been tested in Section 3.3.2 that was able to describe the deactivation behavior of an FBR. It was possible to show that, based on the models Janssens developed e.g. for MTO reactions, a transfer of the model structure to dehydrogenation reaction networks is possible. Knowledge of the coking behavior of the catalyst is not required for this approach and is not provided by the model. This means that it is not possible to evaluate the overall process, since regeneration cannot be simulated directly without knowledge about coke profiles. Its mathematical complexity is limited, but so is its applicability, since it is not applicable to reactor types other than FBRs. An extension of the approach to other reactor types is thinkable. The original approach from literature was extended and modified to take a residual activity of the catalyst into account connected to the amount of oxygen introduced to the reactor. This was successful without compromising the simple and efficient principle of the model structure.

Section 3.3.3 aimed to connect the coke loading on the catalyst to the catalyst activity. This model allows to describe the coke and catalyst activity distribution spatially and temporarily. An incorporation of the model into simulations of reactors of different geometrical complexity is possible. The coke-based approach is the most detailed deactivation approach tested in this work and offers unique advantages for the analysis of chemical processes.

Besides the aforementioned phenomenological approach and the coke-based approach, a time-dependent approach has been parametrized in Section 3.3.4. This approach incorporates an additional balance equation for the catalyst activity. The balance equation consists of a deactivation term, depending on the concentration of the coke precursor, and a regeneration term, considering the concentration of the oxygen introduced into the system. A direct connection between the coke concentration and catalyst activity has not been established. In the context of this work, the model can be seen as a compromise between the mathematical simplicity of the phenomenological approach and the detail of the coke-based approach.

The results of using these models to simulate the overall production process and different reactor concepts are described in Chapter 4. Optimization potentials have been identified and promising experimental conditions have been determined and used for scale-up to pilot scale in Chapter 5.

4 Simulation and Process Optimization

> If it's simple, it's always false. If it's not, it's unusable.
>
> Paul Valéry

In the previous chapters, all aspects of the selective dehydrogenation process of propane on a VO_x catalyst have been described by models of different levels of complexity. The aim of this chapter is to incorporate these models into reactor modeling.

Section 4.1 focuses on the modeling and optimization of the overall production process in a FBR consisting of production and regeneration phases. A combination of a 1D reactor model and a coke-based deactivation approach is used. This represents a process-level view. The reaction takes place in an ordinary FBR. An improvement should be achieved by selecting optimized process parameters, such as reactant concentrations and temperatures in the production and regeneration part of the process.

In Section 4.2 more complex innovative reactor concepts are modeled by a combination of 2D reactor models and a time-based deactivation approach to gain deeper insights into complex radial temperature and concentration profiles. Here, a possible improvement of the reactor performance results not, as in Section 4.1, on the process but on the reactor level. Section 4.2 is thus intended to provide insights for the subsequent experimental testing of these reactors on a pilot plant scale (Chapter 5).

4.1 1D Simulations: Optimization of the Overall Production Process

For the 1D simulation of the complete production cycle shown in Fig. 3.16, the models derived in the previous chapters were used. The main and secondary reactions can be described using the power law approach parametrized in Section 3.1. The modeling of the coke build-up follows the monolayer multilayer coke growth approach derived in Section 3.2.1 (Eq. 3.22). To describe the deactivation behavior as a function of the coke deposition on the catalyst, the model DF1*TDH was used (opt. parameters see Tab. 3.23 , Eq. 3.36). This was identified in a systematic model discrimination in Section 3.3.3 as the model that represented the experimental data best. In the parameter estimation, the quantitatively correct description of the coke formation on the catalyst was taken into account in addition to the activity curves. As shown in Fig. 3.16, the overall process consists of a production phase of length t_{prod} in which the catalyst deactivates due to coke deposition on the surface. The subsequent regeneration phase has a length of t_{reg}. Both phases of the process offer potential for process optimization through careful selection of temperatures, reactant concentrations and production and regeneration time. At first, different oxygen concentrations during production phase have been tested at $T_{\mathrm{prod}} = 500\,^{\circ}\mathrm{C}$ and $T_{\mathrm{prod}} = 600\,^{\circ}\mathrm{C}$ to find the most advantageous production conditions (see Fig. 4.1). The catalyst has been deactivated in a production phase of a certain length. Afterwards the complete activity has been restored by a regeneration phase at 500 °C and 1 % oxygen. The regeneration time was not fixed, but determined depending on the coke loading of the catalyst. In each case, the regeneration phase ended after the complete activity of the catalyst had been restored, i.e. after all coke deposits have been oxidized. Second, the regeneration conditions have been varied and the production conditions have been fixed (see Fig. 4.2). In order to avoid explosive mixtures of oxygen and residual reactants or reaction products, an additional 20 min purging phase, t_{purge}, was included in all simulations after the production and regeneration phases. This time can also be interpreted as the time needed to reduce the temperature from production level to regeneration level. The length of the purging phase was not varied in this contribution but has of course influence on the total process optimization. For analysis and evaluation of the total process including deactivation and regeneration, the space-time yield (STY) of the reactor has been calculated via

$$STY = \frac{\int_{t_{\mathrm{tot}}} \left(\dot{n}_{\mathrm{C_3H_6,out}} - \dot{n}_{\mathrm{C_3H_6,in}}\right) dt}{V_{\mathrm{R}} \left(t_{\mathrm{prod}} + t_{\mathrm{reg}} + t_{\mathrm{purge}}\right)} \tag{4.1}$$

This performance parameter includes the times for production as well as regeneration and purging. In that way it provides information about the productivity of the whole production cycle and is suitable to assess the performance of the overall production cycle. Fig. 4.1 sums up the results of the simulation under different production conditions and shows, that small amounts of oxygen during the production phase are beneficial for the reactor performance.

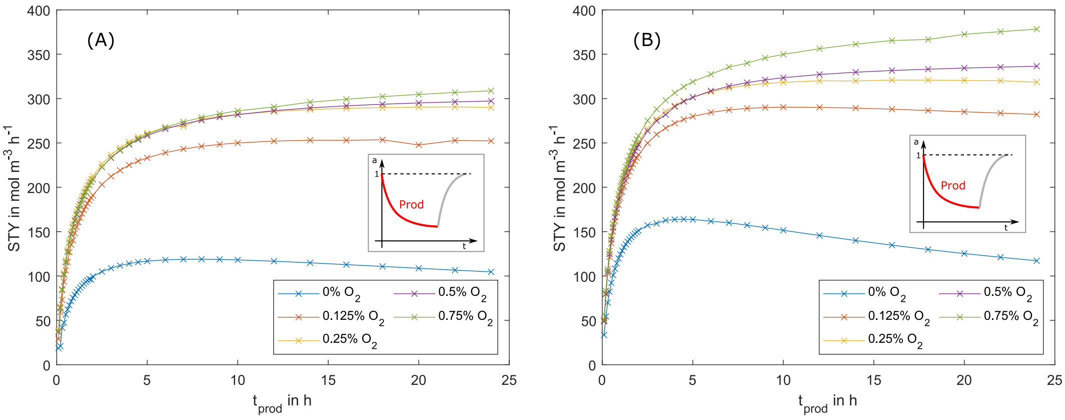

Figure 4.1: Space-time yield (STY) at different production times and varying oxygen concentrations during production at (A) $T_{\mathrm{prod}} = 550\,^{\circ}\mathrm{C}$ and (B) $T_{\mathrm{prod}} = 600\,^{\circ}\mathrm{C}$, considering full regeneration of the catalyst ($a = 1$) and 20 min purging time of the reactor after regeneration and production ($T_{\mathrm{reg}} = 500\,^{\circ}\mathrm{C}$, $x_{\mathrm{O_2,reg}} = 1\,\%$).

It is worth to mention that only some production conditions show a maximum in space-time yield. Without any oxygen present, the optimal production time at a production temperature of 550 °C is around 8 h. That results in a regeneration time of 1.67 h. The optimal production time at 600 °C is 4.5 h, which results in a regeneration time of 2.45 h. It is clearly visible that higher temperatures lead to more severe coking and therefore demand a more frequent catalyst regeneration. In addition to production times and production conditions, it is possible to further optimize the regeneration conditions (Fig. 4.2).

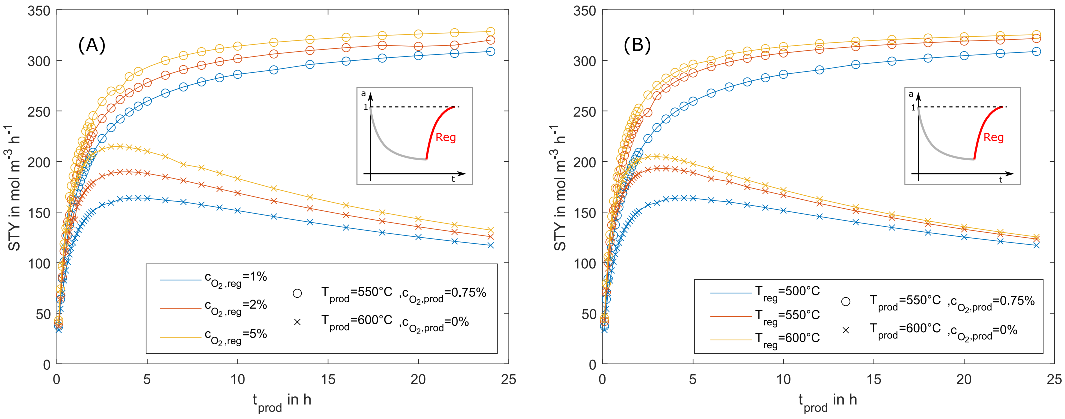

Figure 4.2: Space-time yield (STY) at different production times considering full regeneration of the catalyst ($t_{\mathrm{purge}} = 2 \times 20\,\mathrm{min}$): (A) Variation of oxygen concentrations during regeneration ($T_{\mathrm{reg}} = 500\,°\mathrm{C}$); (B) Variation of regeneration temperatures ($x_{\mathrm{O_2,reg}} = 1\,\%$).

To study the influence of regeneration temperature and oxygen concentration during regeneration both has been varied. The results reveal that higher oxygen concentrations and higher temperatures during regeneration increase the space-time yield. Whether it is suitable to choose a high temperature and a high oxygen concentration cannot be decided based on these calculations since enthalpies of reaction are not considered. For this reason, hotspots cannot be taken into account in the analysis. The development of hotspots at excessively high regeneration temperatures represents a limitation in real applications. On the other hand, a regeneration temperature close to the production temperature can reduce the time needed to cool down and heat up the reactor after the respective phase which can result in shorter purging phases.

Besides a complete catalyst regeneration, it could be more advantageous to regenerate the catalyst up to a certain activity level and start the next production phase with a partially coked catalyst in order to optimize the total process as illustrated in Fig. 4.3. The regeneration model leads to the conclusion that the reaction rate decreases with continued consumption of coke. In that way, burning the last bits of coke takes longer in comparison to regeneration of a strongly coked catalyst. To study the effect of partially regenerated catalyst, an optimization algorithm was applied to the simulations and optimal activities at the beginning and at the end of the reaction cycle have been estimated. Four complete production cycles including production and regeneration have been simulated. Optimized lower and upper boundaries have been calculated with respect to the averaged activity a_1 of the TDH reaction R1 (see Fig. 2.14). The activity a_1 has been averaged over the whole length of the reactor. The average space-time yield of cycle 2 to 4 has been considered for comparison because the simulations revealed, that the differences between the cycles 2 to 4 are insignificant (see Fig. B.12, Appendix B.8). The first cycle differs from all following cycles since it starts with fresh catalyst. All other cycles start with the activity

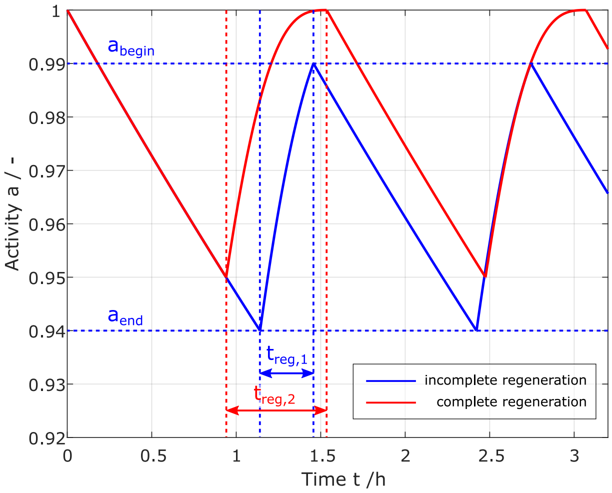

Figure 4.3: Example of the shortening of the regeneration time and the resulting shortening of the total cycle time.

and coke profiles of the previous cycle. The results of the optimization for a production temperature of 550 °C and an inlet concentration of 1 % propane during the production phase are presented in Fig. 4.4. The optimal points outperform the cases where complete regeneration of the catalyst was assumed. Fig. 4.5 gives further inside how the coke loading and the activity a_1 change over the course of the optimized process.

Fig. 4.5 A depicts the mean coke loading as well as the coke loading at the end of the reactor. As known from the experimental results (Fig. 3.23), the coke loading increases towards the end of the reactor, which results in a higher coke loading at the reactor outlet than in average. The average coke content of the catalyst shows no significant differences throughout the different production cycles but the coke content at the end of the reactor indicates that the profiles in the reactor differ between the first and the upcoming cycles. The same can be observed for the activity (Fig. 4.5 B). This is caused by the coke content that remains on the catalyst after the incomplete regeneration. More detailed information on the coking profiles is presented in Fig. 4.6 A, which presents the coke profiles in the reactor at the end of the production phase and at the end of the regeneration phase, respectively. The changes of the coke and activity profiles in the cycles 2, 3 and 4 do not differ significantly. In comparison to that, cycle 1 shows less coking at the end of the reactor. The effect of coke accumulation at the reactor outlet due to incomplete regeneration is clearly visible. The process optimization presented in this section is primarily intended to illustrate the potential of incomplete catalyst regeneration. Other aspects would go beyond the scope of the thesis and have therefore not been taken into account in detail. In the context of this work, the temperature was considered to be constant over the course of the individual process phases. Non-isothermal process control and input concentrations that vary over time in the course of the individual process phases represent further approaches for optimization.

In order to keep the computational effort low, the simulation of the entire process is based exclusively on 1D models. However, these are not suitable for the evaluation of more complex reactor models in which pronounced radial temperature and concentration profiles are to be expected. In order to be able to represent these, 2D simulations are

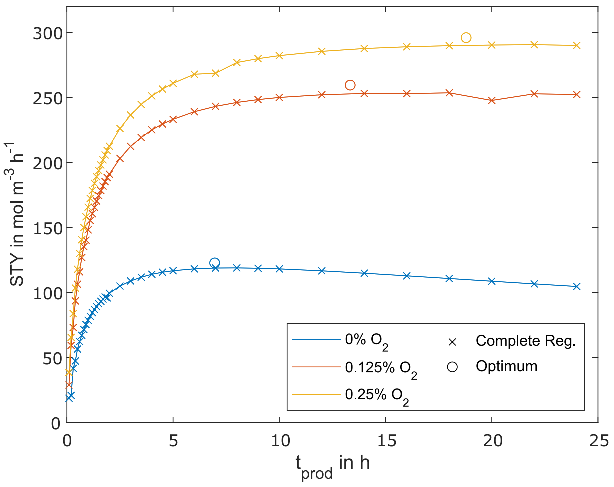

Figure 4.4: STY of production-deactivation cycles with complete regeneration (symbol: ×) compared to STY of optimized production-deactivation cycles with partial regeneration of the catalyst (symbol: ∘) at varying oxygen concentrations ($T_{\mathrm{prod}} = 550\,°\mathrm{C}$, $x_{\mathrm{C_3H_8,in}} = 1\,\%$, $T_{reg} = 500\,°\mathrm{C}$, $x_{\mathrm{O_2,reg}} = 1\,\%$).

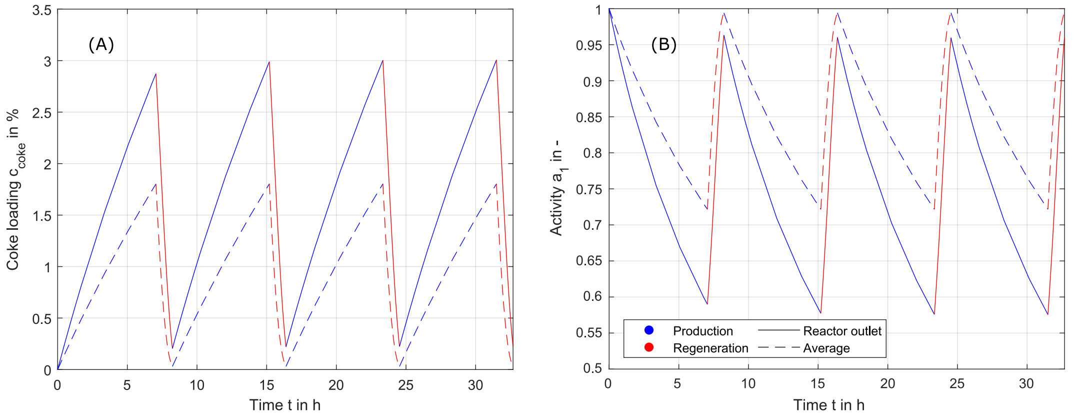

Figure 4.5: Predicted optimized production cycle consisting of four production and regeneration phases: (A): Average coke loading and coke loading at the reactor outlet; (B): Corresponding activity at the reactor outlet and averaged over the length of the reactor ($T_{\mathrm{prod}} = 550\,°\mathrm{C}$, $x_{\mathrm{C_3H_8,in}} = 1\,\%$, $x_{\mathrm{O_2,prod}} = 0\,\%$, $T_{\mathrm{reg}} = 500\,°\mathrm{C}$, $x_{\mathrm{O_2,reg}} = 1\,\%$).

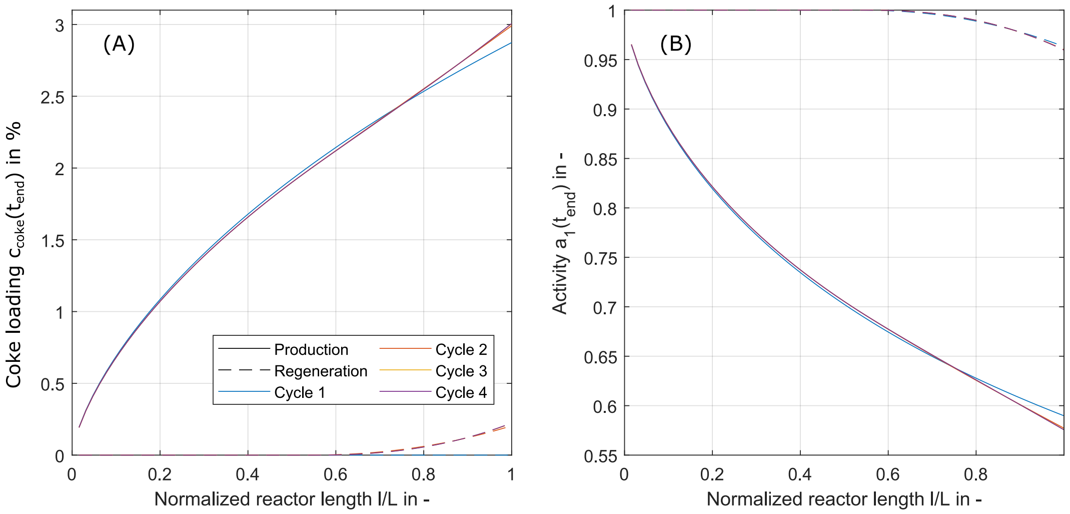

Figure 4.6: Predicted optimized production cycle consisting of four production and regeneration phases: (A): Coke loading at the end of the production cycle and at the end of the regeneration cycle; (B): Corresponding activity at the end of the production cycle and at the end of the regeneration cycle ($T_{\mathrm{prod}} = 550\,°\mathrm{C}$, $x_{\mathrm{C_3H_8,in}} = 1\,\%$, $x_{\mathrm{O_2,prod}} = 0\,\%$, $T_{\mathrm{reg}} = 500\,°\mathrm{C}$, $x_{\mathrm{O_2,reg}} = 1\,\%$).

used in the next section. Due to the higher computational complexity, these simulations are not as applicable for analyzing the overall process, so a systematic optimization of consecutive production and regeneration phases is not included in the next section.

4.2 2D Simulations

In the previous sections, only FBR reactors have been evaluated by 1D simulations. To be able to evaluate more complex reactor concepts, including membrane dosing concepts and heat integration, it is necessary to perform detailed 2D simulations. Especially in membrane reactors radial profiles are expected to have a major influence on reactor performance. With regard to an enlargement of the scale, radial concentration and temperature profiles gain further importance. In particular, temperature profiles are to be emphasized here. With detailed 2D simulations of various integrated reactors, this chapter is intended to bridge the gap to the experimental investigation of these reactor configurations on a pilot plant scale in Chapter 5.
In the first part (Section 4.2.1), different reactor concepts are introduced. After that, the 2D modeling procedure is explained in Section 4.2.2, followed by the results of steady state simulations (Section 4.2.3) and finally by results of transient simulation of the Integrated Packed Bed Membrane Reactor (PBMRint) (Section 4.2.4).

As explained in the preface, the results in this section are the outcome of an extensive collaboration with Jan Paul Walter, on whose work a large part of the results presented are based. Publications have already been published concerning both the steady state simulations and the transient simulations, providing prior documentation of the results (Walter, Brune, Seidel-Morgenstern, et al. 2021; Walter, Brune, Seidel–Morgenstern, et al. 2021).

4.2.1 Reactor Models

All 2D simulations presented have been conducted for geometries that have later been realized in pilot scale experiments (see Chapter 5). Objective of these simulations was to gain knowledge of the performance of these reactors and to evaluate whether more complex reactor concepts offer an advantage compared to conventional reactors. The geometry of these pilot scale reactor concepts is mainly determined by the ceramic membrane tube with an inner diameter $D = 0.021\,\mathrm{m}$ and a length $L = 0.35\,\mathrm{m}$. The permeable zone of this reactor tube is $L_{\mathrm{bed,ss}} = 0.104\,\mathrm{m}$ and defines the length of the catalyst bed. Further information on the experimental equipment and the membrane is given in Section 5. Fig. 4.8 illustrates the different reactor concepts schematically. Similar to the experiments in lab scale, a FBR has been simulated to gain information on the differences between the lab and pilot scale and as a reference case for the more sophisticated integrated reactor concepts. The dimensions are illustrated in Fig. 4.8 A. Closely related to the FBR is the Packed Bed Membrane Reactor (PBMR) also illustrated in Fig. 4.8 A. The only difference between these configurations is the dosing through the membrane wall, which has been exploited in case of the PBMR intending to increase selectivities as described in Section 2.2.1. For dosing via the membrane, the total volume flow must be divided into a fraction that flows through the membrane and a fraction that flows through the conventional reactor inlet (see Section 2.2.1, Eq. (2.10)). To assure comparability of the different reactor concepts, the overall volumetric flow without the influence of volume change due to reaction was the same for all reactor concepts, as illustrated in Fig. 4.7.

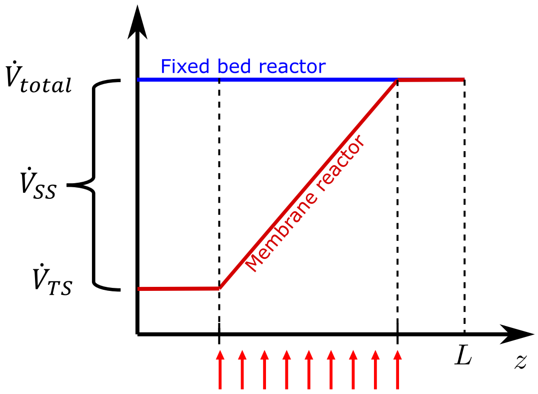

Figure 4.7: Schematic representation of the volume flow rates with and without membrane dosing without volume change due to reactions.

The ratio between the shell site flow $\dot{V}_{\mathrm{SS}}$ and the volumetric flow through the conventional reactor entrance at the beginning of the tube (tube side) $\dot{V}_{\mathrm{TS}}$ was for all simulations and experiments fixed to a value of $TS/SS = \frac{\dot{V}_{TS}}{\dot{V}_{SS}} = \frac{1}{8}$. This ensures a membrane flow high enough to avoid back permeation through the membrane in experiments. In all simulations and experiments the total amount of oxygen has been dosed via the membrane and the total amount of propane has been dosed via the tube side inlet. The porous membrane wall was modeled as an additional reactor inlet with a molar flux of

$$J_i = \frac{\dot{V}_{SS}}{A_{\mathrm{mem}}} c_{i,\mathrm{in,SS}} \tag{4.2}$$

which means that mass transfer through the membrane itself was not modeled separately. Details on the boundary conditions not only at the membrane walls are given in Tab. 2.2 in Section 2.3.1.

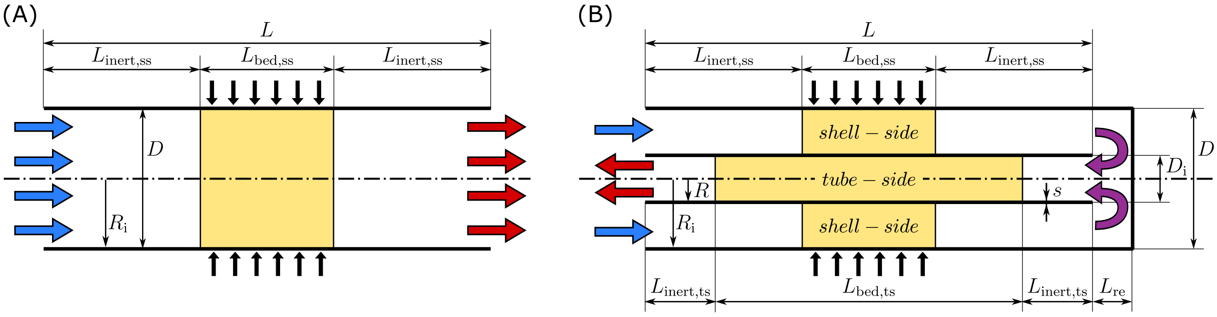
(A)
L
$L_{\mathrm{inert,ss}}$
$L_{\mathrm{bed,ss}}$
$L_{\mathrm{inert,ss}}$
D
R_{i}
(B)
L
$L_{\mathrm{inert,ss}}$
$L_{\mathrm{bed,ss}}$
$L_{\mathrm{inert,ss}}$
shell – side
tube – side
shell – side
R
R_{i}
s
D_{i}
D
$L_{\mathrm{inert,ts}}$
$L_{\mathrm{bed,ts}}$
$L_{\mathrm{inert,ts}}$
L_{re}

Figure 4.8: Geometric dimensions (A) of the PBMR and (B) of the PBMRint in pilot scale (For length specifications see Tab. 4.1).

Besides the PBMR, an integrated Packed Bed Membrane Reactor (PBMRint) was tested. This concept was developed to exploit the different reaction enthalpies of ODH and TDH in a heat integrated reactor concept. Besides the ceramic membrane tube of the FBR and PBMR an additional concentric steel tube was installed inside the membrane tube. The feed flow enters the reactor via the annular gap between the membrane tube and the steel tube and via the membrane similar to the PBMR concept. At the end of the reactor ($z = L$) the gas flow is redirected to the inner steel tube that includes an additional catalyst bed of a length of $L_{\mathrm{bed,ts}} = 0.24\,\mathrm{m}$. The gas flows through the inner tube in counter current manner to the flow in the annular gap and leaves the reactor at the same side where the tube side fraction of the gas flow enters it. In this more complex concept the reaction conditions have to be adjusted in a way that ensures that the exothermic ODH reaction ($\Delta_{\mathrm{R}}H = -118\,\mathrm{kJ\,mol^{-1}}$) is conducted in the annular gap with a total consumption of the dosed oxygen. The remaining propane is then converted to propene via endothermic TDH ($\Delta_{\mathrm{R}}H = 124\,\mathrm{kJ\,mol^{-1}}$) in the inner part of the reactor. The heat released by the exothermic ODH reaction in the annular gap is transferred by conduction to the inner part of the reactor where it is consumed by the endothermic TDH reaction. Thus, the presented concept represents an example of recuperative heat integration (see Section 2.2.2). Especially the suitability of the heat integration is going to be evaluated in this section.

The geometrical parameters of all reactor configurations are summarized in Tab. 4.1. Reaction conditions that are kept constant for the simulations presented here can be found in Tab. 4.2.

Table 4.1: Geometrical parameters of (A) FBR and PBMR and (B) PBMRint in lab scale.

Parameter	Value	Description
$L_{\mathrm{bed,ts}}$	0.24 m	Length of catalyst-bed of tube-side
$L_{\mathrm{inert,ts}}$	0.055 m	Length of inert zone of tube-side
D_{i}	0.0098 m	Inner diameter of inner tube
s	0.0015 m	Thickness of inner tube
$L_{\mathrm{bed,ss}}$	0.104 m	Length of catalyst-bed of shell-side
$L_{\mathrm{inert,ss}}$	0.123 m	Length of inert zone of shell-side
D	0.021 m	Inner diameter of membrane tube
L	0.35 m	length of membrane tube
L_{re}	0.01 m	Length of the reversal zone

Table 4.2: Reaction conditions of the 2D simulations.

Parameter	Value
T_{w}	600 °C
T_{in}	600 °C
$WHSV$	$400\,\mathrm{kg\,s\,m^{-3}}$
$m_{\mathrm{cat,ss}}$	0.017 kg
$x_{\mathrm{C_3H_8,in}}$	1 %

4.2.2 2D Modeling Procedure

Previous investigations showed that isothermal conditions can be assumed for laboratory-scale reactors, which simplifies the simulation. In addition, perfect mixing in the radial

direction could be assumed since the reactors have only a small diameter. These assumptions justify a 1D plug flow model for simulation, but they may not readily apply to larger reactors. Furthermore, the evaluation of membrane reactors requires 2D simulations due to radial flows caused by dosing through the porous reactor wall. For this reason, non-isothermal 2D models have to be used.
Comsol® Multiphysics 5.6 is applied to calculate axial, radial and temporal complex concentration, temperature and velocity fields simultaneously. The balance equations are derived in Section 2.3.1, where Eq. (2.23) represents the mass balance, Eq. (2.24) the energy balance and Eq. (2.25) the momentum balance that have been solved by the software.

As presented in Section 2.3.1, various models are available to describe the difficult heat and mass transfer, taking radial convection and dispersion of the dosed oxygen in homogeneous 2D models into account. For this work, the focus was on the α_w and the $\lambda(r)$ models. Based on the experimental data obtained in the laboratory scale FBR (see Section 3.1), both model approaches were systematically compared. For this purpose, based on the kinetic parameters estimated in the 1D model, 2D simulations of the laboratory reactor were performed using both model approaches. The comparison shows that the simulations based on the $\lambda(r)$ model show better agreement with the experimental data. For this reason, the more complex $\lambda(r)$ model is used for all further investigations (Walter, Brune, Seidel–Morgenstern, et al. 2021).

First simulations have been performed without considering coke build-up and regeneration (steady state simulation, Section 4.2.3). In later simulations coke build-up has been integrated in the steady state model by implementing the coking rate derived in Section 3.2.1 (transient simulation, Section 4.2.4).

Coke formation and regeneration Model C3 was used to model coke formation. This model is described by Eq. (3.10) or its integrated form, Eq. (3.22), with the optimized parameters presented in Tab. 3.6. It is based on the assumption that propene is the main coke precursor, which has been proven in Section 3.2.1 and is consent in literature. The coking kinetics are combined directly with the regeneration kinetics from Section 3.2.2. The regeneration rate is modeled with Eq. (2.65). Tab. 3.13 provides the optimized parameters. The net coking rate $r_\mathrm{coke,net}$ is therefore defined as

$$\frac{dc_\mathrm{coke}}{dt} = r_\mathrm{coke,net} = r_\mathrm{coke} - r_\mathrm{coke,reg} \tag{4.3}$$

The coke burning rate $r_\mathrm{coke,reg}$ depends on the concentration of oxygen, since oxygen is consumed during the gasification of coke. Therefore, the oxygen consumption due to coke combustion was included in the balance equations. To do so, the regeneration rate, which, like the coking rate, refers to the loading of the catalyst with coke in percent, must be converted as follows:

$$\frac{dc_{\mathrm{O}_2}}{dt} = r_\mathrm{reg} \frac{1}{100\,\%} \frac{1}{M_\mathrm{coke}} \frac{1}{(1-\varepsilon)\rho_\mathrm{bed}} \tag{4.4}$$

The molar mass of coke M_coke is assumed to be the molar mass of elemental carbon $M_\mathrm{coke} = M_\mathrm{C} = 12\,\mathrm{g\,mol^{-1}}$, since the exact composition of coke is not known.

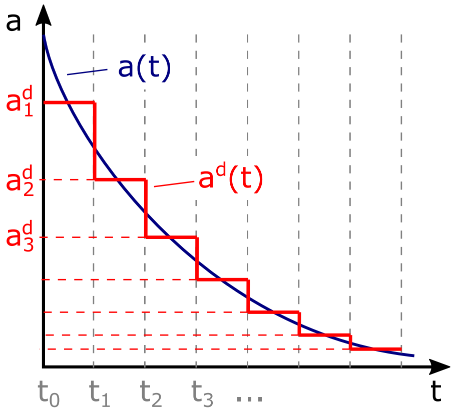

Figure 4.9: Principle of the discretization of the continuous activity $a(t)$ to discrete, averaged activity levels $a^{\mathrm{d}}(t)$.

Transient Reactor Modeling Considering Catalyst Activity To model deactivation in the transient 2D models, the time-dependent approach derived in Section 3.3.4 was used. Unlike the previous modeling approaches, there is no direct correlation between the coke build-up on the catalyst surface and the activity in this particular modeling strategy. Instead, the activity is solely determined by the time on stream. Nevertheless, there is a feedback between the activity and coke formation. As the catalyst's activity decreases, propene production also decreases, leading to a reduced formation of coke. Since the modeling of the complex interplay of membrane dosing, temperature, mass and momentum balances is already challenging, further simplifications regarding the modeling of the activity have been necessary. To be able to perform the transient simulations the activity function has been discretized as schematically illustrated in Fig. 4.9 (Janssens et al. 2013). It has been assumed that the activity decreases slowly. Therefore, the activity was considered to be constant within time intervals of $\Delta t = 1\,\mathrm{h}$ hour. The activity value in the middle of each time interval was assigned to every discrete time point within that interval:

$$a\left([t_i, \ldots, t_i + \Delta t]\right) = a(\bar{t}) \tag{4.5}$$

$$\bar{t} = t_i + \frac{\Delta t}{2}; \quad \Delta = 1\,\mathrm{h} \tag{4.6}$$

The differences between a more realistic continuous coupling and the simplified discrete coupling is illustrated in Fig. 4.10.

4.2.3 Steady State 2D Simulations

In order to perform a fundamental comparison of the different reactor concepts and to find the most promising reaction conditions for the different concepts, steady-state simulations of FBR, PBMR and PBMRint were performed. Fig. 4.12 presents concentration and temperature profiles for the PBMR (A) and a conventional FBR (B). In the oxygen concentration profiles the dosing through the membrane wall becomes apparent. The highest concentrations can be observed at the porous reactor wall of the PBMR. In the FBR the dosing together at the reactor inlet can be seen. The impact of oxygen distribution on reaction rates is exemplified by the propene concentration profiles. These profiles show

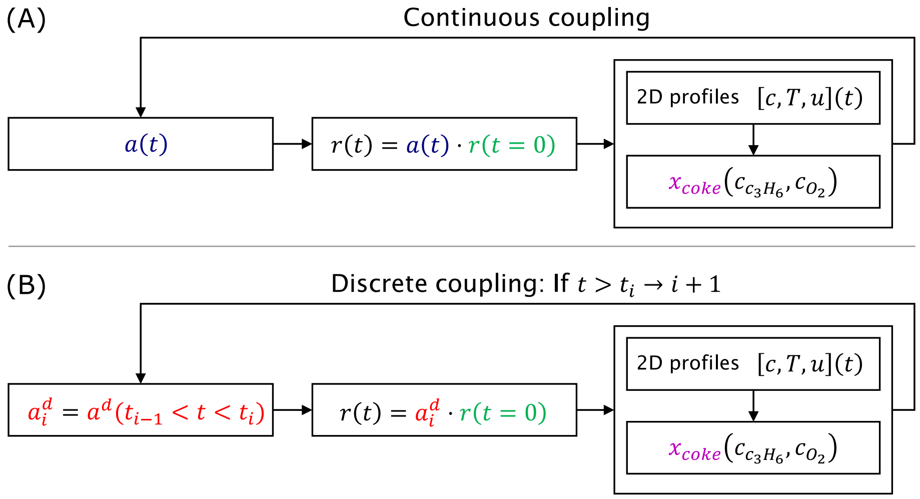
(A)
Continuous coupling
$a(t)$
$r(t) = a(t) \cdot r(t=0)$
2D profiles $[c, T, u](t)$
$x_{coke}(c_{C_3H_6}, c_{O_2})$
(B)
Discrete coupling: If $t > t_i \rightarrow i+1$
$a_i^d = a^d(t_{i-1} < t < t_i)$
$r(t) = a_i^d \cdot r(t=0)$
2D profiles $[c, T, u](t)$
$x_{coke}(c_{C_3H_6}, c_{O_2})$

Figure 4.10: Difference between (A) the principle of a continuous coupling of activity $a(t)$ and concentration and temperature profiles and (B) discrete coupling of a discretized activity a_i^{d} with concentration and temperature profiles.

that propene production in the FBR is mainly concentrated at the reactor inlet, where the highest propene concentration can be observed. The propene is then consumed in successive oxidation reactions to form CO and CO_2. The propene concentration decreases over the length of the reactor. In contrast, propene is formed over the whole length of the PBMR as illustrated in Fig. 4.12 (A). Comparing the oxygen and the propene profiles reveals that there is a reaction front visible where the oxygen concentration decreases to zero and the propene concentration is increasing. This reaction front is spread over the whole length of the reactor in the PBMR, but appears only at the beginning of the reactor in case of the FBR. The more distributed reaction front has also a large influence on the temperature fronts. While in the FBR the heat is generated close to the reactor inlet, in the PBMR the heat is released in a more distributed manner, as can be seen from the hotspot temperatures $\Delta T = T(z, r) - T_{\text{in}}$. In the FBR, a maximum hotspot temperature of $\Delta T_{\max} > 70\,°\text{C}$ is reached, whereas in the PBMR it stays around $16\,°\text{C}$. These high temperatures can promote unwanted side reactions like coking and cause irreversible damage of the catalyst. The high temperature gradients are also unwanted from a safety perspective as they can be associated with special stresses on the reactor.
Key performance parameters of the different reactor concepts are presented in Fig. 4.11. Conversion of propane, selectivity towards propene and the resulting yield of propene are presented for different oxygen inlet concentrations. The key performance parameters for all reactor concepts show a typical behavior for oxidation reactions suffering from consecutive side reactions. It can very often be observed that as the conversion increases, the selectivity decreases. In order to balance these two opposing trends, the yield is used as an evaluation parameter. It becomes apparent that the PBMR and the FBR deliver a similar selectivity at oxygen concentrations up to 0.75 %. The higher conversion of the PBMR in this concentration range results in a overall higher yield of the PBMR compared to the FBR at lower oxygen concentration. At higher concentrations of oxygen, the FBR shows higher conversions. The PBMR outperforms the FBR at oxygen concentrations over 1.5 % due to the lower selectivity of the FBR.

The PBMRint reveals a higher conversion for every oxygen concentration tested in the

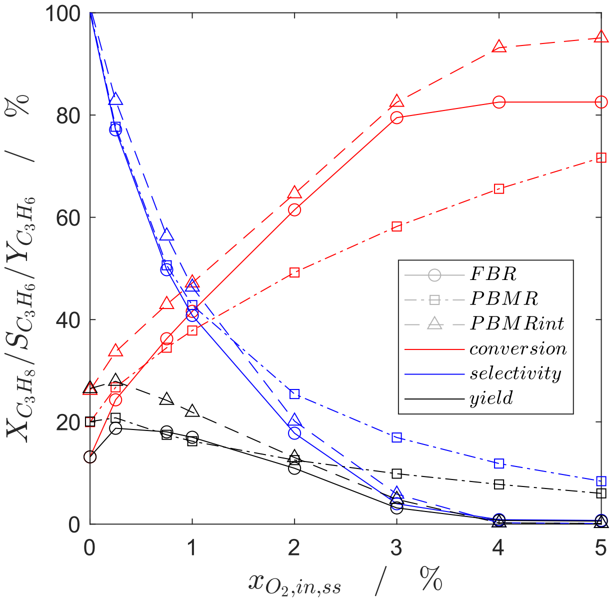

Figure 4.11: Conversion, selectivity, yield, of the FBR, PBMR and PBMRint for different oxygen inlet concentrations ($x_{\mathrm{C_3H_8,in}} = 1\,\%$; $x_{\mathrm{O_2,in}} = 0.25\,\%\ldots5\,\%$; $T_\mathrm{W} = T_\mathrm{in} = 600\,°\mathrm{C}$; $WHSV = 400\,\mathrm{kg\,s\,m^{-3}}$, figure adapted from Walter, Brune, Seidel-Morgenstern, et al. 2021).

simulations. At oxygen concentration above 1.5 % the selectivity of the PBMRint drops under the selectivity of the PBMR. This causes the yield of the PBMRint to decrease as well. Therefore, the PBMRint only shows better yields at oxygen inlet concentration below 2 % of oxygen. Fig. 4.13 shows the position of the hotspot in the PBMRint for different oxygen inlet concentrations. The position of the hotspot in the reactor moves away from the reactor inlet as the oxygen concentration increases. For concentrations of 0.25 %, 0.75 % and 1 % the hotspot is located in the shell side of the integrated reactor. For higher concentrations it moves to the tube side in flow direction. The concept of the PBMRint is to facilitate heat transfer from the annular gap to the inner tube. Thereby, the exothermic reaction in the outer tube can provide the necessary reaction enthalpy for the endothermic reaction in the inner tube. This principle is only fulfilled if the reaction hotspot is located in the shell side of the reactor, which is not the case for oxygen inlet concentrations of 2 % and 3 %. Fig. 4.13 illustrates that the reaction conditions in a complex reactor concept like the PBMRint have to be carefully adjusted in order to benefit from the higher complexity of the reactor setup. Details on the temperature profiles in the PBMRint with an oxygen inlet concentration of 1 % are illustrated in Fig. 4.14, which shows radially averaged temperatures. It can be seen that the hotspot is located towards the end of the catalyst bed on the shell side. On tube side there is also a local temperature maximum, which is caused by the heat transfer through the inner steel tube. A sudden increase in temperature at the beginning of the tube side (in the direction of flow) is noticeable. This is caused by the fact that the oxygen is not completely consumed in the shell side and reacts with the hydrocarbons present as soon as the catalyst bed of the tube side is reached. At this point, the tube side heats up the shell side. Once this oxygen is consumed, the temperature drops again and is later increased by the heat transfer. At the end of the tube side, the endothermic heat effect of the TDH becomes apparent as the temperature drops below the inlet temperature. It has to be noted that this heat integration effect is minimal due to the very diluted reaction system. A larger effect can be expected for industrial feeds operating above the upper explosion limit.

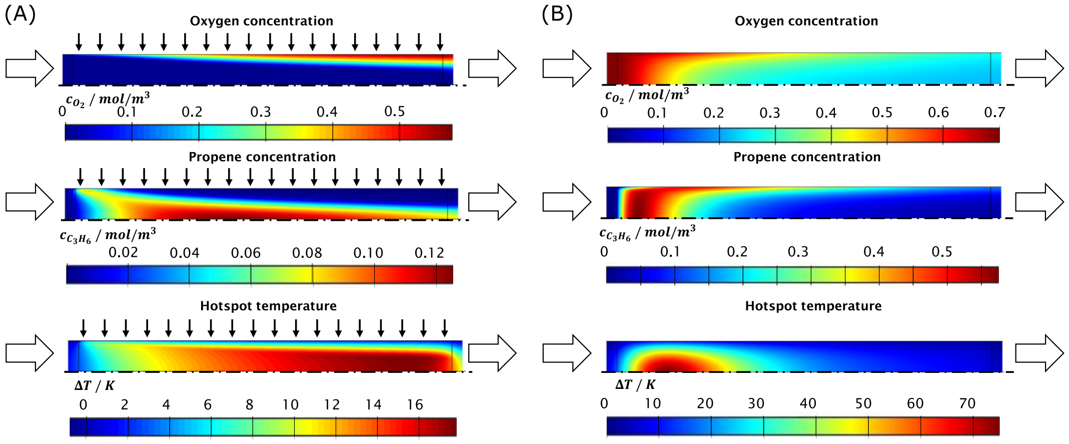

Figure 4.12: 2D concentration and temperature profiles for (A) PBMR and (B) FBR ($T_{\mathrm{wall}} = T_{\mathrm{in}} = 600\,°\mathrm{C}$, $c_{\mathrm{C_3H_8,in}} = 1\,\%$, $c_{\mathrm{O_2,in}} = 5\,\%$, $\dot{V}_{\mathrm{TS}} : \dot{V}_{\mathrm{SS}} = 1 : 8$, $WHSV = 400\,\mathrm{kg\,s\,m^{-3}}$).

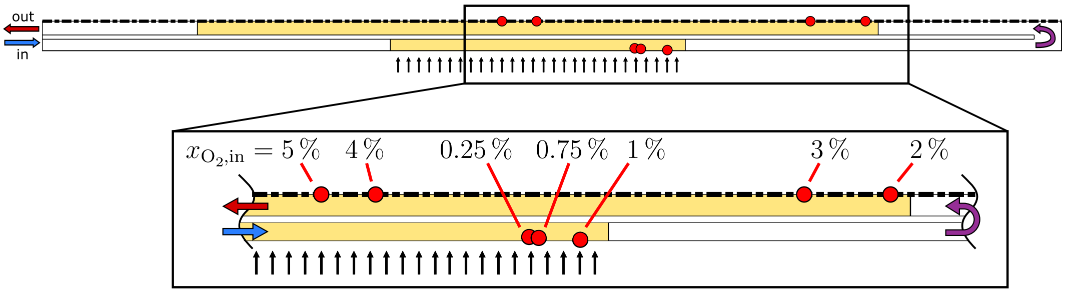

Figure 4.13: Steady state simulations of the PBMRint with different oxygen inlet concentrations ($T_{\mathrm{wall}} = T_{\mathrm{in}} = 600\,°\mathrm{C}$, $c_{\mathrm{C_3H_8,in}} = 1\,\%$, $\dot{V}_{\mathrm{TS}} : \dot{V}_{\mathrm{SS}} = 1 : 8$, $WHSV = 400\,\mathrm{kg\,s\,m^{-3}}$).

In summary, the simulations indicate that the process should be performed in oxygen lean conditions ($\frac{x_{\mathrm{C_3H_8,in}}}{x_{\mathrm{O_2,in}}} > 1$). The PBMRint shows a better performance than FBR and PBMR. So far, only steady state simulations have been performed. To be able to evaluate the complex PBMRint concept especially the deactivation and coking behavior has to be considered. Based on the experimental results from the previous chapters, it can be assumed that especially the catalyst in the inner steel tube will be affected by coking, since the oxygen is meant to be consumed when the gas flow enters the inner tube.

Further information on the scale-up of the process from lab scale to pilot scale, a comparison of 1D simulations (Matlab) and 2D simulations (Comsol Multiphysics) and a detailed study on different 2D modeling approaches (α_{w} vs. $\lambda(r)$, see Section 2.3.1) has been published by Walter et. al (Walter, Brune, Seidel–Morgenstern, et al. 2021; Walter, Brune, Seidel-Morgenstern, et al. 2021).

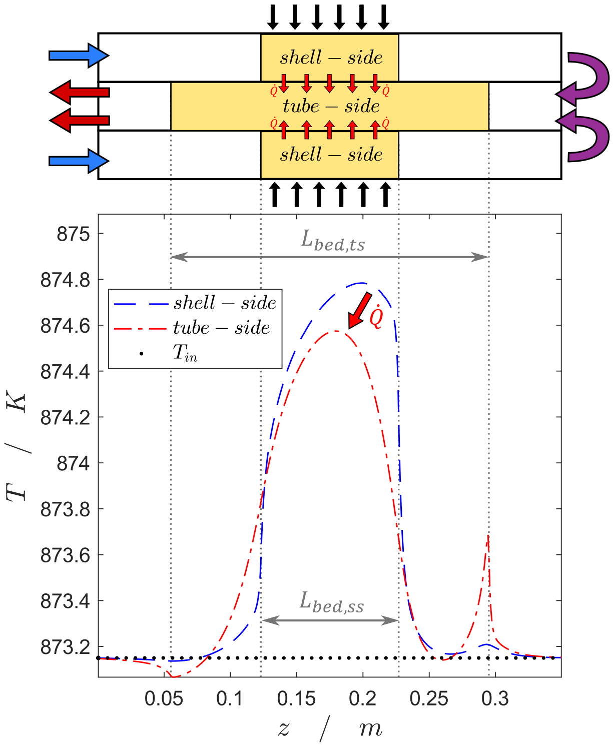

Figure 4.14: Radially averaged temperature profiles of the shell-side and the tube-side of the PBMRint along the axial coordinate ($T_{\mathrm{wall}} = T_{\mathrm{in}} = 600\,^{\circ}\mathrm{C}$, $c_{\mathrm{C_3H_8,in}} = 1\,\%$, $c_{\mathrm{O_2,in}} = 1\,\%$, $\dot{V}_{\mathrm{TS}} : \dot{V}_{\mathrm{SS}} = 1 : 8$, $WHSV = 400\,\mathrm{kg\,s\,m^{-3}}$).

4.2.4 Transient 2D Simulations

Transient simulations have only been conducted for the most promising PBMRint reactor setup with special emphasis on coke deposition. An oxygen concentration of 1 % has been chosen. As known from the steady state simulations, the hotspot for oxygen concentrations of 1 % is still on the shell side to ensure that the heat integration principle is still fulfilled. In addition, the highest possible oxygen concentration offers the greatest potential for heat integration because the exothermal ODH reaction is promoted. The other reaction conditions used in the simulations are similar to the steady state simulations ($T_{\mathrm{wall}} = T_{\mathrm{in}} = 600\,°\mathrm{C}$, $c_{\mathrm{C_3H_8,in}} = 1\,\%$, $\dot{V}_{\mathrm{TS}} : \dot{V}_{\mathrm{SS}} = 1 : 8$, $WHSV = 400\,\mathrm{kg\,s\,m^{-3}}$). The transient simulations have been conducted for a maximum time on stream of 20 h.

Fig. 4.15 illustrates the oxygen concentration in the PBMRint at $t = 1\,\mathrm{h}$, $t = 10\,\mathrm{h}$ and $t = 20\,\mathrm{h}$. At $t = 1\,\mathrm{h}$ the oxygen is consumed close to the wall. With increasing production time the oxygen penetrates further and further into the reactor and so does the reaction front, which is a direct effect of the catalyst deactivation.

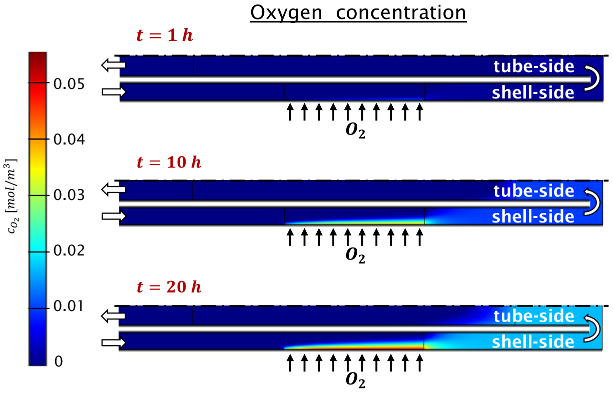

Figure 4.15: Calculated profile of the oxygen concentration in the PBMRint at 1 h, 10 h and 20 h ($T_{\mathrm{wall}} = T_{\mathrm{in}} = 600\,°\mathrm{C}$, $c_{\mathrm{C_3H_8,in}} = 1\,\%$, $c_{\mathrm{O_2,in}} = 1\,\%$, $\dot{V}_{\mathrm{TS}} : \dot{V}_{\mathrm{SS}} = 1 : 8$, $WHSV = 400\,\mathrm{kg\,s\,m^{-3}}$).

In Fig. 4.16, the propene concentration and the coke build-up are presented. The propene concentration at the reactor outlet and therefore the yield decreases due to the overall reactor deactivation (see Fig. 4.16 A). The highest propene concentration can be observed at the beginning of the shell side catalyst bed. This is caused by high propane concentrations. High concentrations are present because mixing with the nitrogen of the membrane stream has not yet occurred. Additionally, the oxygen that is dosed via the membrane wall does not reach the steel tube but is consumed before. Therefore, side reactions will not occur in this part of the reactor. The continuous dosing through the reactor wall pushes the produced propene inwards and contributes to the high propene concentrations. Fig. 4.16 B depicts the coke concentrations. It becomes clear that the coke build-up corresponds to the propene concentrations. Coke is mainly built up in regions of the reactor that are not reached by oxygen. In shell side parts of the reactor that show coking at $t = 10\,\mathrm{h}$, the coke loading has decreased at $t = 20\,\mathrm{h}$. The reason for this is that oxygen penetrates further into the reactor after the catalyst has been deactivated. It regenerates the previously coked parts of the reactor. The deactivation of the catalyst also causes penetration of oxygen into the tube side as illustrated in Fig. 4.15. The oxygen in the tube side reacts with propene in unwanted oxidation reactions to form CO and CO_2, but can also react with propane to form the desired product molecule propene.

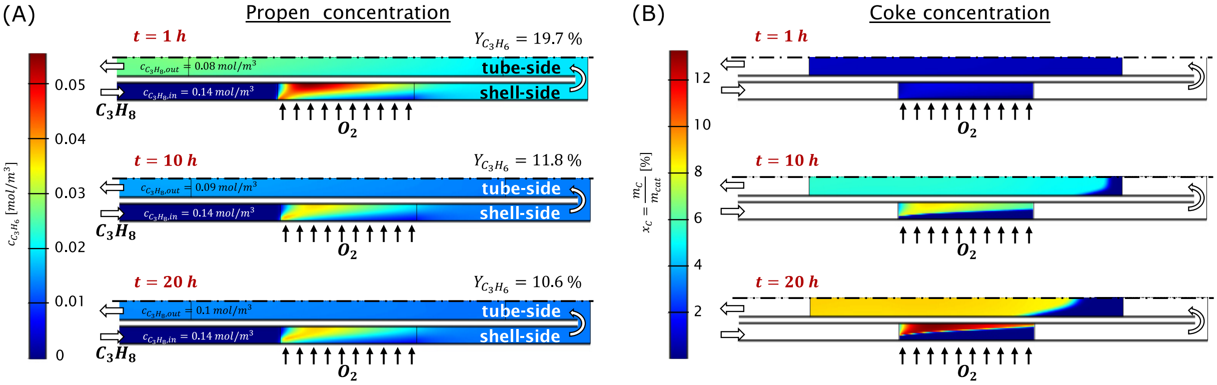

Figure 4.16: Calculated profiles of the propen and coke concentrations in the PBMRint at 1 h, 10 h and 20 h $T_{\text{wall}} = T_{\text{in}} = 600\,°\text{C}$, $c_{\text{C}_3\text{H}_8,\text{in}} = 1\,\%$, $c_{\text{O}_2,\text{in}} = 1\,\%$, $\dot{V}_{\text{TS}} : \dot{V}_{\text{SS}} = 1 : 8$, $WHSV = 400\,\text{kg}\,\text{s}\,\text{m}^{-3}$).

All of these reactions are exothermic and can cause a shift of the hotspot with time on stream. This shift is illustrated in Fig. 4.17. The shift of the hotspot from shell side to tube side can be observed between $t = 3.5\,\text{h}$ and $t = 4.5\,\text{h}$. With an hotspot on the tube side the heat integration principle is not fulfilled any more. As a consequence, the reactor has to be regenerated to bring the catalyst back to its initial activity. Fig. 4.18 shows the radially averaged temperatures on shell side and on tube side at $t = 19.5\,\text{h}$. It becomes apparent that at this time the heat is transferred from the tube side with a higher temperature to the slightly colder shell side.

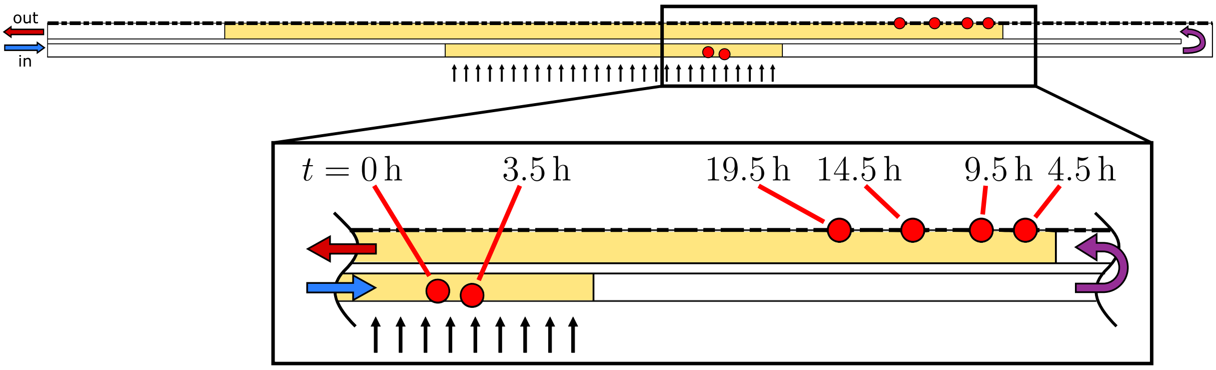

Figure 4.17: Location of the hotspot in the PBMRint in dependency of time on stream ($T_{\text{wall}} = T_{\text{in}} = 600\,°\text{C}$, $c_{\text{C}_3\text{H}_8,\text{in}} = 1\,\%$, $c_{\text{O}_2,\text{in}} = 1\,\%$, $\dot{V}_{\text{TS}} : \dot{V}_{\text{SS}} = 1 : 8$, $WHSV = 400\,\text{kg}\,\text{s}\,\text{m}^{-3}$).

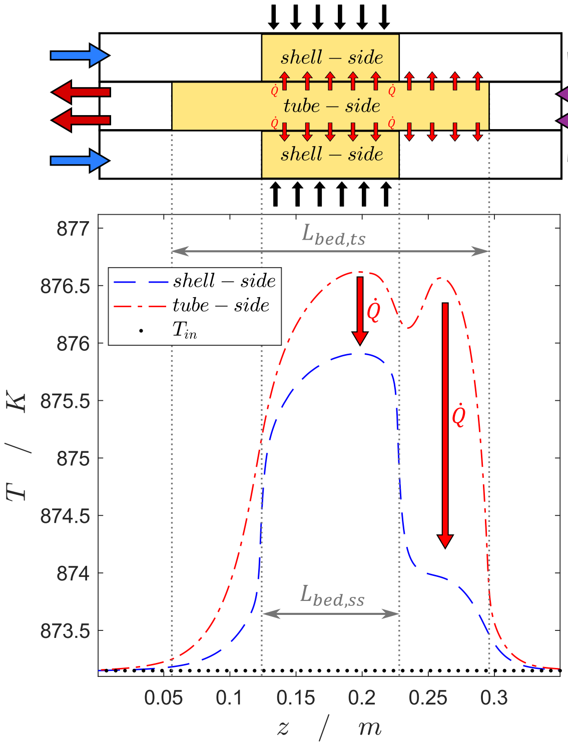

Figure 4.18: Radial averaged temperature profiles of the shell-side and the tube-side along the axial coordinate at $t = 19.5\,\text{h}$ ($T_{\text{wall}} = T_{\text{in}} = 600\,°\text{C}$, $c_{\text{C}_3\text{H}_8,\text{in}} = 1\,\%$, $c_{\text{O}_2,\text{in}} = 1\,\%$, $\dot{V}_{\text{TS}} : \dot{V}_{\text{SS}} = 1 : 8$, $\mathit{WHSV} = 400\,\text{kg}\,\text{s}\,\text{m}^{-3}$).

The deactivation characteristics of the PBMRint impact its performance parameters as illustrated in Fig. 4.19. The figure compares the yield development in the PBMRint for simulations with 0.25 % (A) and 0.75 % oxygen (B) along the length of the two catalyst beds. With increasing time on stream, the yield decreases for both reaction conditions. With 0.75 % oxygen the conversion of the reactor is higher compared to 0.25 % oxygen. Selectivity on the other hand is smaller due to side reactions. For the lower oxygen concentration of 0.25 %, the conversion is smaller. Since less oxygen is used, side reactions are suppressed to a larger extent and larger parts of the reactor are utilized for the TDH reaction. The disadvantage of reaction conditions with small amounts of oxygen is a more severe coke build-up in the reactor and faster deactivation. The faster deactivation can be observed in the simulation results in Fig. 4.19. After a time on stream of 3.5 h the yields are almost similar for both conditions.

This leads to a new optimization problem. For reaction conditions with less oxygen the PBMRint delivers better initial yields that drop fast, whereas with higher oxygen concentrations the deactivation is suppressed to a higher degree. This allows longer time on stream and less frequent regeneration of the reactor. The optimization task reveals similarities to the optimization already performed in the context of the 1D simulations (see Section 4.1). Due to the significant computational effort of this optimization task, it is beyond the scope of this work, but represents an interesting approach for future research.

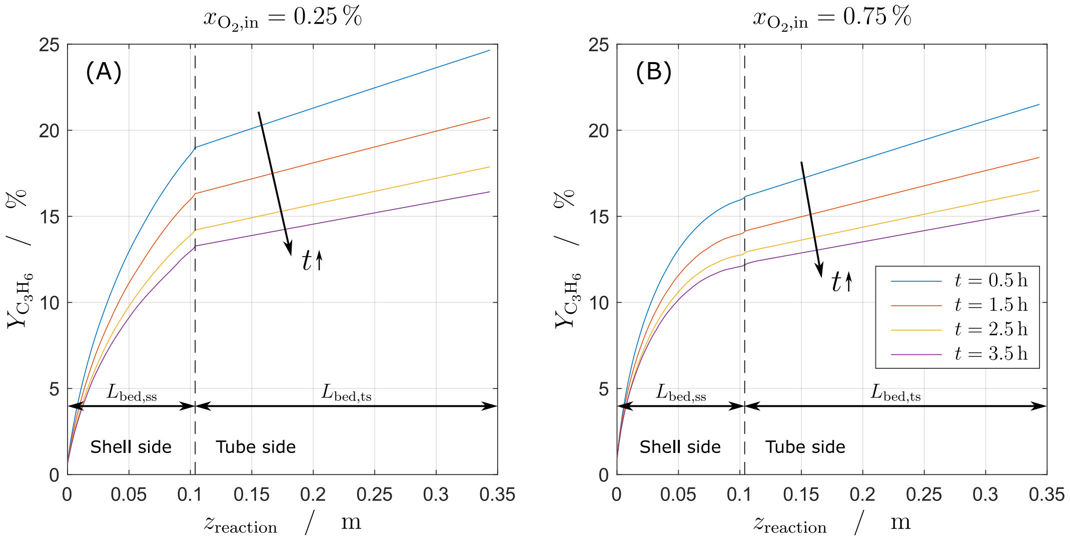

Figure 4.19: Simulated propene yield at different times on stream (0.5 h, 1.5 h, 2.5 h and 3.5 h) with an oxygen inlet concentration of (A) $c_{O_2,in} = 0.25\,\%$ and (B) $c_{O_2,in} = 0.75\,\%$ ($T_{wall} = T_{in} = 600\,°C$, $c_{C_3H_8,in} = 1\,\%$, $\dot{V}_{TS} : \dot{V}_{SS} = 1 : 8$, $WHSV = 400\,kg\,s\,m^{-3}$).

4.3 Interim Conclusion

In this chapter, simulation of various reactor concepts on different levels of detail have been presented. All simulations are based on the models derived in Section 2.3 and parametrized in Chapter 3. The simulations have been categorized into 1D simulations (Section 4.1) and 2D simulations (Section 4.2), which use different modeling approaches.

For 1D simulations, a coke-based deactivation approach has been used to perform simulation studies for reactors on lab scale. The simulations have been performed in Matlab. It was possible to model an overall production process consisting of production and regeneration phases. Optimization was achieved by optimizing the activity coefficients at the beginning and at the end of the production cycle, resulting in an incomplete regeneration of the catalyst. This strategy results in shorter regeneration times and a better space-time yield of the overall process. Consequently, this contribution provides models and parameters as a basis for the design and intensification of cyclically operating deactivation and regeneration processes involving catalyst coking.

The 2D simulations have been performed using Comsol Multiphysics to be able to model the complex geometries of the different reactor concepts at pilot scale. At first, the different reactor concepts have been described (Section 4.2.1) and the modeling procedure has been introduced (Section 4.2.2). Afterwards, steady state simulations have been used to compare a Fixed Bed Reactor (FBR), a Packed Bed Membrane Reactor (PBMR) and the new concept of an integrated Packed Bed Membrane Reactor (PBMRint) that allows heat integration in addition to membrane dosing (Section 4.2.3).

In steady state simulations, it was possible to determine reaction conditions in which the more complex reactor configurations have advantages in comparison to the conventional

FBR. The maximum yield for each type of reactor is achieved when the inlet concentration of $x_{\mathrm{O_2,in}}$ is 0.25 %, primarily due to the high selectivity at oxygen lean conditions. Under conditions of oxygen surplus, the PBMR demonstrates superior performance compared to both the PBMRint and the FBR. This can be attributed to high local oxygen concentration in the FBR and unreacted oxygen in the shell-side of the PBMRint. Regarding heat integration, the findings suggest that operating the PBMRint with an oxygen/propane inlet ratio of up to one is advantageous. Considering that higher oxygen concentrations lead to increased reaction rates and subsequently more heat released in the shell-side, an oxygen inlet concentration of 1 % is advantageous due to the intensified heat coupling in these conditions.

These reaction conditions have been the starting point for transient simulations including deactivation (Section 4.2.4). For deactivation, a simple time-based approach has been used. With increasing time on stream, a deeper penetration of oxygen into the reactor over time results in an undesired shift of the hotspot from the shell-side to the tube-side. At this point, the heat integration is not performed as intended. This transition of the hotspot location from the shell-side to the tube-side can be noticed between $t = 3.5\,\mathrm{h}$ and $t = 4.5\,\mathrm{h}$. Therefore, it is recommended to pause the production period after this time period and to reverse the flow direction for operando regeneration as tested in the next chapter.

The performance parameters of the PBMRint over time for different production conditions (see Fig. 4.19) revealed the need for a detailed optimization of consecutive cycles of production and regeneration phases due to the complex interplay between reactor performance and deactivation behavior. As a first step, the simulation of a consecutive regeneration phase of a PBMRint has already been performed and is presented in literature (Walter, Brune, Seidel-Morgenstern, et al. 2021).

In summary, the simulations performed represent a proof of concept for the PBMRint. Furthermore, valuable information on promising reaction conditions was obtained. Based on these results, experiments will be carried out on a pilot plant scale in Chapter 5. These will serve to experimentally validate the simulations and clarify any weaknesses and inaccuracies of the models. The complexity will be systematically increased from conventional tubular reactors to reactor cascades with and without membrane dosing and finally to the PBMRint.

5 Reactor Cascades and Integrated Reactor Concepts in Pilot Scale

In all previous chapters of this work, laboratory-scale experiments were carried out. These mainly served to gain knowledge about the reaction system and to parameterize models to describe it mathematically. In this way, various models with different levels of complexity could be developed and tested. These models were later used for process simulation. It was possible to evaluate simple fixed bed reactors as well as complicated reactor concepts and to determine reaction conditions for scale-up. This scale-up will be the subject of this chapter. In addition to the reactor concepts, periodic flow reversal will also be investigated as a possibility for operando regeneration of the catalyst bed.

The aim is to experimentally implement and evaluate the PBMRint presented in the last chapter as the innovative core of the entire thesis. The transfer from laboratory experiments to integrated reactor concepts on a pilot scale is to take place in several steps. First, the experimental pilot scale equipment will be introduced in Section 5.1. After that, pilot-scale experiments will be performed, with the aim of reproducing the laboratory experiments (Section 5.2). Then a reactor cascade with and without membrane assisted dosing will be investigated as a preliminary stage to integrated reactor concepts (Section 5.3). After that, the PBMRint will be realized and evaluated in pilot scale (Section 5.4). For all reactor concepts, it will be investigated whether periodic flow reversal has a beneficial effect on reactor performance.

5.1 Experimental Equipment and Operation Modes

5.1.1 Experimental Equipment

The core of the experimental setup is an asymmetric, porous, ceramic α-Al_2O_3 membrane tube (Fraunhofer IKTS, Fig. 5.1) with a length of 350 mm and an inner diameter of 21 mm. The membrane was vitrified at both ends. In the middle, a predefined permeable zone of 104 mm was maintained. Only this section was filled with active catalyst. The vitrified sections of the reactor were filled with inert material to ensure good mixing of the feed gases and heating of the gases in this area to the desired reaction temperature. The dimensions of the reactor correspond to those of the reactor simulated in Section 4.2 (see Fig. 4.8 and Tab. 4.1). The membrane is enclosed by a stainless steel outer tube. An engineering drawing of the reactor can be found in Appendix C.1, Fig. C.2. The stainless steel reactor is brought to reaction temperature by electric heating sleeves and is insulated by glass wool.

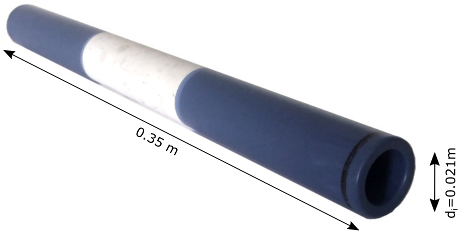

Figure 5.1: Asymmetric, porous, ceramic α-Al_2O_3 membrane tube (Fraunhofer IKTS).

The pilot scale test plant has been used in two different configurations as presented in a simplified Piping and Instrumentation Diagram (P&ID) in Fig. 5.2. In the first configuration, the setup consists of two reactors in series. These reactors can be used as FBR and PBMR reactors. In order to perform experiments in FBR configuration, fully vitrified membranes were available in addition to the partially vitrified membranes already described. The heat transport properties of fully vitrified and partially vitrified membranes do not change significantly. Thus, good comparability between PBMR and FBR experiments can be guaranteed. In the context of flow reversal, both reactors in the reactor cascade must be able to operate as PBMR and FBR. For this reason, fully vitrified membranes were used only to characterize the experimental plant. In the main tests, permeable membranes were used in both FBR and PBMR configuration.Gas flow samples were taken at the locations indicated in the P&ID. Similar to the setup used in the lab-scale experiments, samples were taken by redirecting a small portion of the gas flow to a GC.Due to the position of the sample lines it is possible to characterize the reactors separately.

For the PBMRint experiments the number of reactors was reduced to one as illustrated by Fig. 5.2 B. This is possible because the integrated reactor is designed in such a way that the amount of catalyst that was previously distributed between two reactors is now available in one integrated reactor. The inlet and the outlet of the reactor is now placed at the top due to the flow reversal to the inner stainless steel tube (see Fig. 4.8). Tab. 4.1 in Section 4.2.1 states the geometrical dimensions of the integrated reactor. An engineering drawing of the outer stainless steel housing can be found in Appendix C.1, Fig. C.4. The number of gas sampling positions had to be reduced due to the higher degree of integration.

Both setups were also equipped with pneumatic valves able to reverse the flow (V100a, V100b, V200 in Fig. 5.2). For a flow reversal, all three valves have to be switched at the same time. The components required to provide the gases are not shown in Fig. 5.2 B. Mass flow controllers are used to adjust the gas flows. These regulate the gas flow at room temperature. The gas flow is then heated in electrical preheaters to a temperature close to the reaction temperature. All piping downstream of the preheaters is heated by electrical pipe heat tracing to prevent heat loss and to bring the gases to reaction temperature. A detailed P&ID can be found in Appendix C.1, Fig. C.1 for the setup with the reactor cascade and in Fig. C.3 for the setup including the PBMRint. Fig. 5.3 gives an impression of the layout of the plant in the pilot plant.

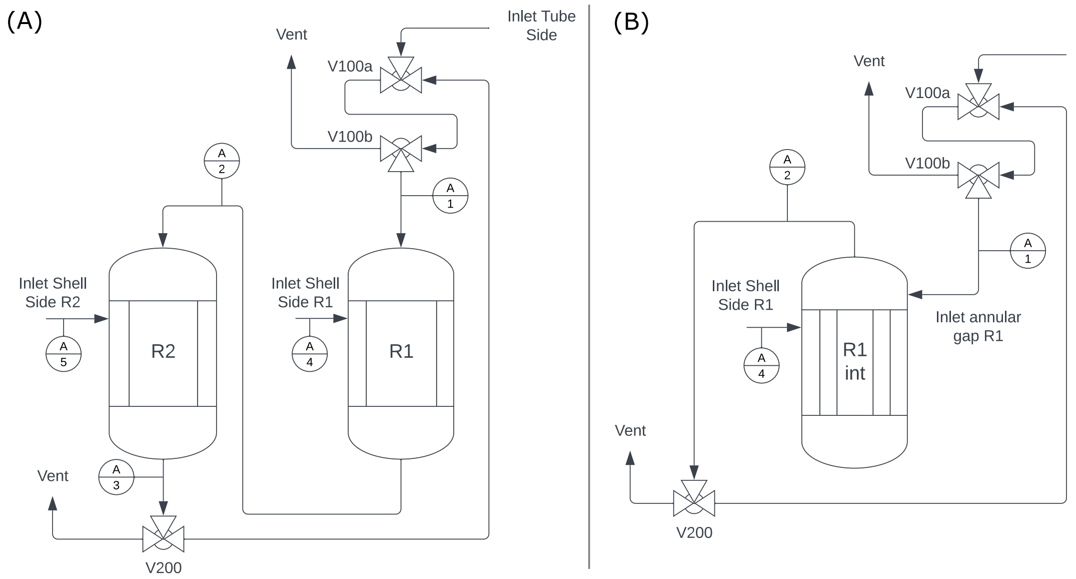
(A)
Vent
Inlet Tube Side
V100a
V100b
A 2
A 1
Inlet Shell Side R2
Inlet Shell Side R1
A 5
R2
A 4
R1
Vent
A 3
V200
(B)
Vent
V100a
V100b
A 2
A 1
Inlet Shell Side R1
Inlet annular gap R1
A 4
R1 int
Vent
V200

Figure 5.2: Simplified P&ID of the pilot plant setup: (A) Configuration used for FBR and PBMR experiments as cascade and single reactor, (B) Configuration used for PBMRint experiments.

Comparable test setups have already been used for other studies (Hamel, Tóta, et al. 2008; Hamel, Wolff, and Seidel-Morgenstern 2011; Brune, Wolff, et al. 2019).

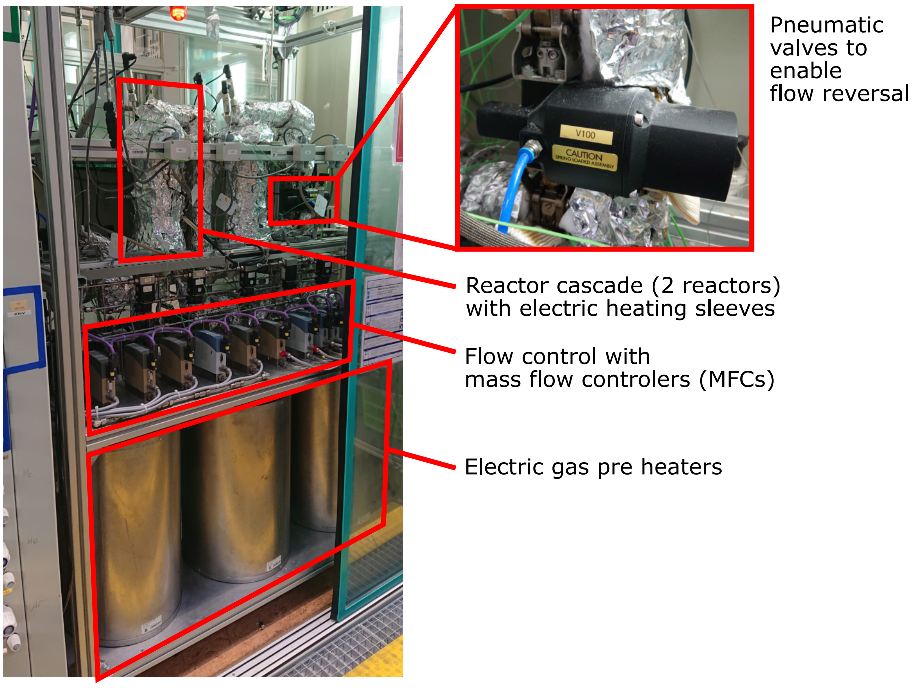
Pneumatic valves to enable flow reversal
Reactor cascade (2 reactors) with electric heating sleeves
Flow control with mass flow controlers (MFCs)
Electric gas pre heaters
V100
CAUTION

Figure 5.3: Experimental pilot scale setup for FBR and PBMR experiments in single reactor and cascade configuration with and without flow reversal.

5.1.2 Operation Modes

The pneumatic valves allow to operate the pilot plant in two different operation modes: Either with periodic flow reversal or without periodic flow reversal. The flow reversal is intended to achieve operando regeneration of the catalyst. Fig. 5.4 illustrates possible operation modes for a cascade of FBR (A, B) and for a cascade of a PBMR combined with a FBR (C, D). The idea of the concepts is to perform the ODH reaction mainly in the first reactor in the direction of flow and the TDH reaction in the second reactor. The dosing of oxygen is adjusted in a way that it is completely consumed in the ODH reactor. Since the TDH reaction benefits from higher temperatures the second reactor is heated to a higher temperature. Because catalyst coking and therefore deactivation is mainly happening in the parts of the reactor without oxygen, the reactor designated to the TDH reaction will show deactivation.
For operando regeneration, the flow is reversed after a certain production time (Fig. 5.4 B, D). By reversing the flow, oxygen and propane are now fed to the coked reactor that has been designated to the TDH reaction before. The introduction of oxygen into the reactor oxidizes the coke deposits on the catalyst surfaces in addition to the ODH reaction. The other reactor, that has formerly been used for ODH, is now performing the TDH reaction and is facing catalyst deactivation.
By flow reversal, the functions of the reactors are changed. Therefore, it is also reasonable to switch the temperatures of the reactors. This can be done in an intermediate purging phase between the separate phases.

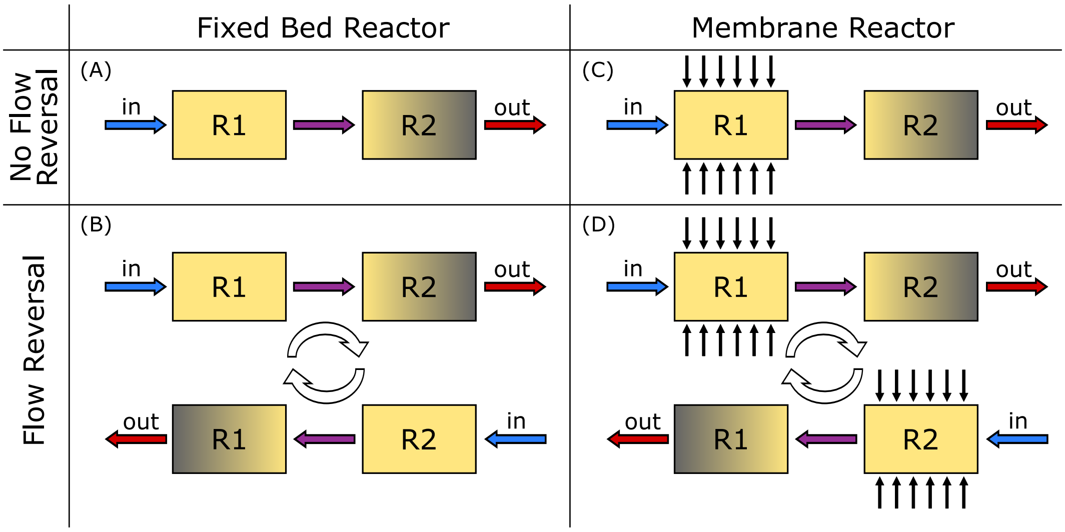

Figure 5.4: Different reactor setups and operation modes for a cascade of 2 fixed bed reactors ((A) and (B)) and membrane reactors ((C) and (D)) without flow reversal ((A) and (C)) and with flow reversal ((B) and (D)).

Fig. 5.5 illustrates the different production phases of a reactor cascade with flow reversal. In phase ① reactor 1 performs under oxygen rich conditions and is supposed to show little to no deactivation and the conversion is supposed to be constant. The conversion of reactor 2, which is designated to the TDH reaction, is supposed to decrease due to coking. During phase ②, the reactor setup is purged with nitrogen to prevent explosive mixtures.

Moreover, the gas flow is reversed, and the temperature of Reactor 1 is increased while that of Reactor 2 is decreased. The flow reversal is performed in the middle of phase ②. In phase ③ the functions of the reactors are switched and reactor 2 is supposed to perform the ODH with no loss in catalyst activity, whereas reactor 1 performs the TDH suffering from coking. Phase ④ is used to purge and switch temperatures and flow direction before the cycle can start again.

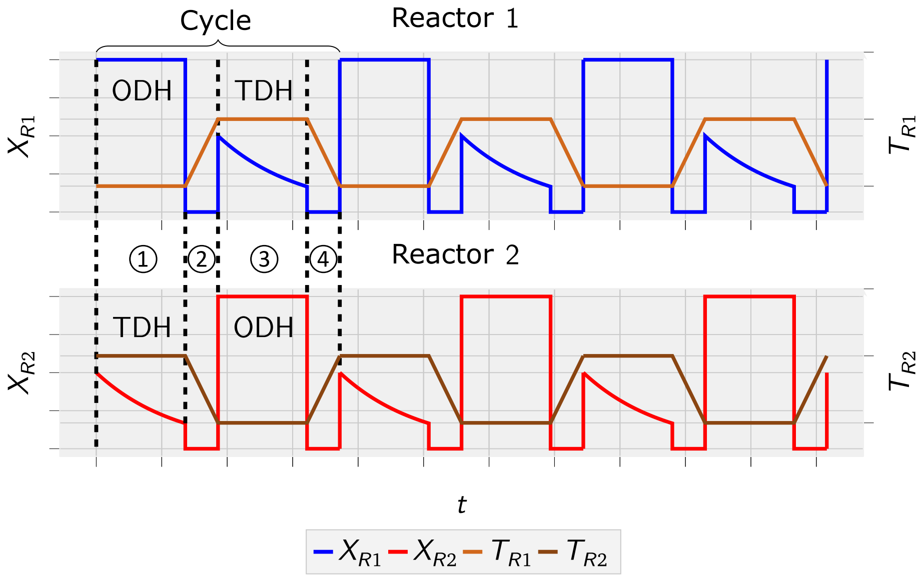

Figure 5.5: Schematic representation of the conversion and temperature in a reactor cascade performing consecutive cycles of ODH and TDH reactions.

Over the course of consecutive production cycles, both reactors in the reactor cascade are used as FBR and PBMR as shown in Fig. 5.6. The two operation modes are referred to as Fixed Bed Mode (Fig. 5.6 A) and Membrane Mode (Fig. 5.6 B). Only the first reactor in the flow direction has been operated in Membrane Mode as shown in Fig. 5.4 C and D. This is due to the intended comparability of the reactor cascade with the integrated reactor concept, since in the integrated reactor, for structural reasons, no gases can be dosed into the second catalyst bed via the reactor wall.

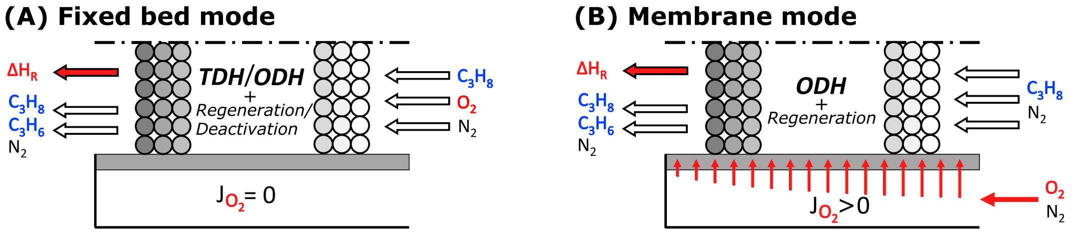

Figure 5.6: Illustration of the reactor used in (A) fixed bed mode and (B) membrane mode (adapted from (Brune, Wolff, et al. 2019)).

The principle of flow reversal has also been used with the PBMRint setup as illustrated in Fig. 5.7. In Phase 1 the gases enter the reactor via the annular gap (N_2, C_3H_8) and via the membrane wall (O_2, N_2). In this phase, the catalyst in the inner stainless steel tube will coke because of the TDH reaction. The annular gap will most likely show insignificant deactivation effects because of the oxygen dosage via the membrane wall. There is an analogy between this phase and the reactor cascade with a membrane reactor and a subsequent fixed bed reactor.

In phase 2 the flow is reversed and the gases enter the reactor via the inner stainless steel tube. Since it is not possible to dose any gases over the length of the reactor, all gases are fed together in co-feed mode. The catalyst in the inner steel tube is coked at this point. An operando regeneration parallel to the ODH reaction is expected. In this phase, the outer annular gap is dedicated to perform the TDH reaction and will show coking. When the performance of the reactor drops under a certain threshold the flow can be reversed again and the cycle starts over again. Similar to the reactor cascade, a purging phase has to be added after phase 1 and phase 2 to prevent explosive mixtures.

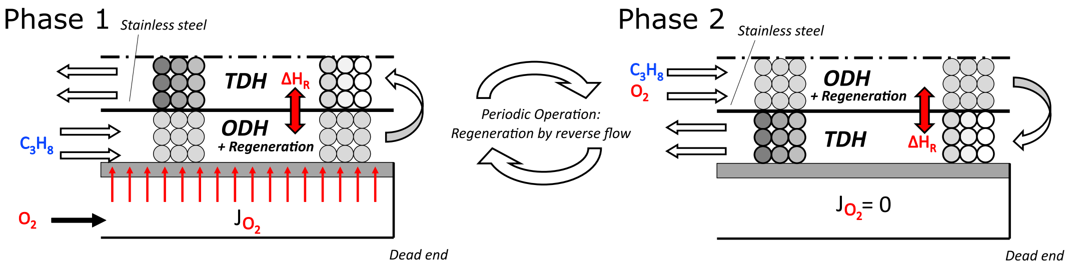

Figure 5.7: Illustration of the PBMRint operated in two phases with flow reversal to enable operando regeneration.

In the previous chapter, the pilot-scale experiments were already preceded by simulations in order to focus the experiments on promising reaction conditions and thus reduce the experimental effort. In Section 4.2.3, steady state simulations were performed. These focused on FBR and PBMR as single reactors with the goal of better understanding the inherent temperature and concentration profiles. A reactor cascade of FBR and PBMR as studied in this chapter was not explicitly simulated. Despite these differences, it can be determined from the simulations that low concentrations of oxygen are beneficial when operating the reactor cascade. This is also true for the PBMRint simulated in the same section. Based on this, low oxygen concentrations are a focus of the work in this experimental section. The results of the simulations are to be verified.

Section 4.2.4 deals specifically with the deactivation behavior of the PBMRint. A proof of concept for the PBMRint has already been achieved in the simulations. This is to be confirmed in the experiments.

To allow a comparison between calculated values and those measured in the pilot plant, the reactor cascade was simulated using 1D simulations. The results of these calculations are shown in Appendix C.2. Reference will be made to these simulation results throughout the chapter.

5.2 Scale-up and Comparison to Lab Scale Experiments

Before testing more complex reactor cascades, the pilot scale reactors have been tested separately to confirm that the reactor performance is equivalent to the lab scale reactors. Different degrees of freedom can be used to adjust the pilot plant settings. The results are very sensitive to the pipe trace heating temperature and the temperature of the preheaters. If temperatures anywhere in the plant are too high, wall reactions are thinkable. If temperatures are set too low, the wanted reaction temperature in the catalyst beds might not be reached.

Selected results of these experiments are illustrated in Fig. 5.8. The experiments show the same trends that have already been discussed in Section 3.3. In oxygen lean environments (Fig. 5.8, bottom row, $T_{\text{in}} = 600\,°\text{C}$, $x_{\text{O}_2\text{,in}} = 0\,\%$), the catalyst shows fast catalyst deactivation but offers a high selectivity towards propene. If oxygen is introduced to the system, the results are relatively stable over time, but the selectivity is significantly lower (Fig. 5.8, top row, $T_{\text{in}} = 500\,°\text{C}$, $x_{\text{O}_2\text{,in}} = 0.5\,\%$). Regardless of the effort that was taken to optimize the system, there are still differences between the results obtained with the lab scale equipment and the results obtained with the pilot plant.

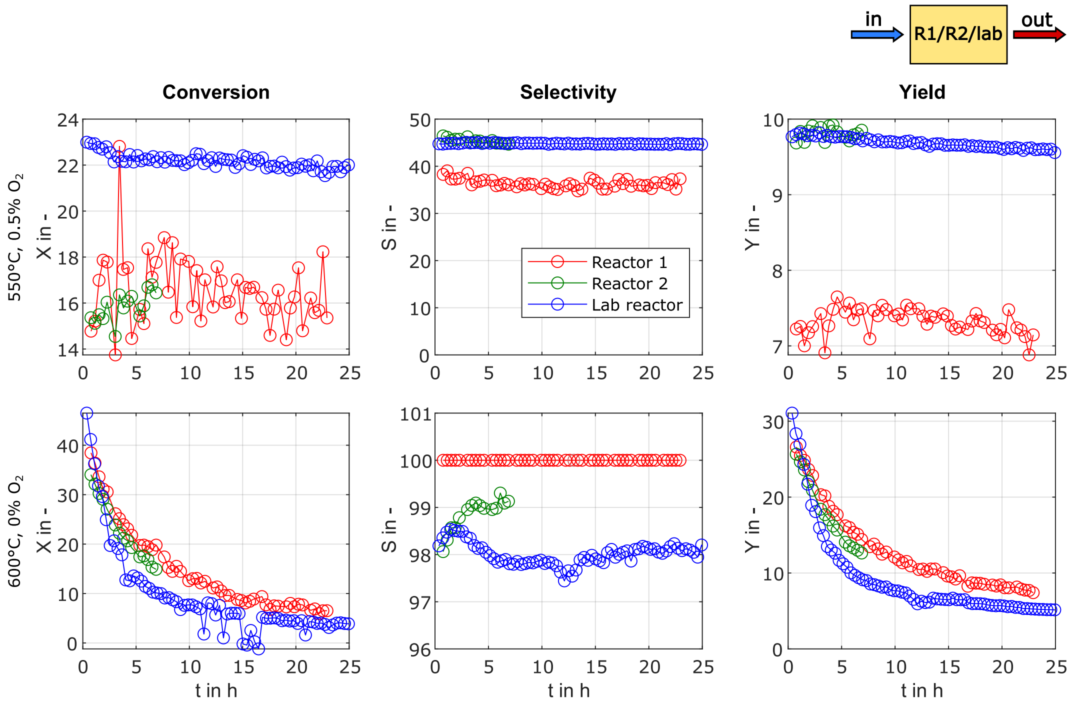

Figure 5.8: Comparison of the performance parameters of the lab scale reactors and the two reactors used in the pilot scale reactor cascade setup ($x_{\text{C}_3\text{H}_8\text{,in}} = 1\,\%$, $WHSV = 400\,\text{kg}\,\text{s}\,\text{m}^{-3}$ Top row: $T_{\text{in}} = 500\,°\text{C}$, $x_{\text{O}_2\text{,in}} = 0.5\,\%$; Bottom row: $T_{\text{in}} = 600\,°\text{C}$, $x_{\text{O}_2\text{,in}} = 0\,\%$).

For measurements without oxygen, it is noteworthy that the selectivity of the pilot-scale measurements is lower than that of the laboratory experiments. This is caused by small, untraceable leakages in the pilot plant setup that allow oxygen from air to get into the reactor. The unwanted oxygen intake is the reason for side reactions that lower the

selectivity. Besides that, the temperature profile in the system is not as homogeneous as in the lab scale experiments. The lower conversions at $t = 0\,\mathrm{h}$ indicate, that the temperature in the pilot plant reactor is lower on average. This is not detectable, since the number of thermocouples in the setup is limited to three (for details see Fig. C.1).
These results illustrate the higher complexity of the pilot plant setup in comparison to the lab scale reactor. After investigating the characteristics of the pilot plant setup, first experiments with a cascade of two reactors with different operation modes have been evaluated.

5.3 Fixed Bed Reactor Cascade With and Without Membranes

As an intermediate stage towards the PBMRint, the cascade of two reactors (FBR → PBMR) described in the previous section was evaluated experimentally. Such a cascade offers the advantage of a higher number of degrees of freedom compared to the fully integrated reactor concept. Although the cascade is integrated in terms of materials, it does not exhibit thermal integration. This means that individually optimized temperatures can be set for both reactors. It is known from preliminary studies that higher temperatures are advantageous for the TDH, while fewer side reactions are to be expected at lower temperatures for the ODH.
The performance of the reactor cascade was extensively tested both with and without oxygen dosing via the membrane. Tab. 5.1 exhibits the experiments performed with membrane dosing.

Table 5.1: Experimental matrix for the investigation of the membrane reactor cascade with dosing via the membrane with and without flow reversal (red: comparable to the measurements without membrane dosing; FR: with flow reversal; noFR: without flow reversal).

	Temperature $T_{\mathrm{R1}}/T_{\mathrm{R2}}$		
$x_{\mathrm{O_2}}$	550 °C/600 °C	575 °C/625 °C	600 °C/650 °C
0.125 %	noFR	noFR	-
0.25 %	FR/noFR	FR/noFR	-
0.5 %	FR/noFR	FR(+CO_2)/noFR(+CO_2)	FR/noFR
0.75 %	FR/noFR	FR/noFR	-
1 %	FR/noFR	FR/noFR	FR/noFR
1.25 %	FR/noFR	FR/noFR	-
2.5 %	FR/noFR	FR/noFR	-

Three different temperature levels have been compared. The difference between the reactor dedicated to ODH and the TDH reactor has always been $\Delta T = 50\,°\mathrm{C}$. The oxygen inlet concentrations have been varied between 0.125 % and 2.5 %. Most of the experiments have been performed both with flow reversal (Tab. 5.2: FR) and without flow reversal (noFR). Experiments without flow reversal have been conducted for 48 h.
To be able to evaluate the influence of the membrane dosing, it was necessary to perform experiments without membrane dosing. These experiments are listed in Tab. 5.2. The

experiments marked red in Tab. 5.1 and Tab. 5.2 are comparable, since measurements with and without membrane dosing have been performed for the same conditions.

Table 5.2: Experimental matrix for the investigation of the membrane reactor cascade without dosing via the membrane with and without flow reversal (red: comparable to the measurements with membrane dosing; FR: with flow reversal; noFR: without flow reversal).

	Temperature T_{R1}/T_{R2}	
x_{O_2}	550 °C/600 °C	575 °C/625 °C
0.5 %	FR/noFR	FR/noFR
0.75 %	FR/noFR	FR/noFR
1 %	FR	-
1.25 %	FR	-
2.5 %	FR/noFR	FR/noFR
5 %	FR	-

In this section the experimental results are presented beginning with a reactor cascade without membrane dosing and without cyclic flow reversal. The influence of temperature and the concentration of oxygen has been tested. The performance is then compared to the performance of the reactor cascade with periodic flow reversal. The evaluation of the reactor cascade with membrane dosing has been tested similarly by testing operation without flow reversal first and comparing it with cyclic operation afterwards (Section 5.3.1). After that, the membrane and fixed bed setups have been compared systematically. Dosing of CO_2 to utilize the RWGS reaction has also been considered and tested (Section 5.3.2). All these experiments allow to draw conclusions for the operation of the PBMRint, which has been studied in the next section (Section 5.4).

5.3.1 Fixed Bed Reactor Cascade With and Without Flow Reversal

FBR cascade: Without periodic flow reversal In Fig. 5.9 the results of a systematic variation of the oxygen concentration in the inlet flow of a FBR cascade are presented. By taking samples between the reactors, it was possible to evaluate the performance of both reactors separately. The top row illustrated the performance of the first reactor in the direction of flow and the bottom row shows the performance of the second reactor in the direction of flow. At this point, a general difficulty in the evaluation of the separate reactors has to be mentioned. Due to the different performance of the first reactor, it is very often difficult to compare the performances of the second reactor since the outlet flow of the first reactor is the inlet flow of the second reactor. The inlet flows of the second reactor are therefore generally not the same.

For the presented results, the reactors have been heated up to $T_{R1} = 575\,°C$ for the first reactor and to $T_{R2} = 625\,°C$ for the second reactor. Propane and oxygen were co-fed on the tube side of the reactor. The lower temperature of the first reactor was chosen to keep side reaction in the oxygen rich atmosphere reasonably low. The higher temperature in the second reactor was chosen to promote the endothermic TDH reaction. In this way, only the second reactor was supposed to show significant deactivation tendencies. The results confirm these assumptions. The conversions of the second reactor show a decrease for all oxygen concentrations tested. This indicates significant coking in that area. The first reactors on the other hand, reveal a relatively stable performance over the course of the experiment. The conversion in the first reactor increases with increasing oxygen concentration, whereas the selectivity towards propene decreases because of pronounced side reactions at higher oxygen concentrations. For the second reactor, negative selectivities of CO_2 can be obtained for all three oxygen concentrations considered. Since the selectivities are still calculated as described in Section 3.1, Eq. (3.4), negative selectivities indicate a consumption of CO_2 instead of a formation. This indicates that the RWGS reaction takes place and consumes H_2 formed in the TDH and CO_2 formed in side reactions to produce CO and water. This is also indicated by high CO selectivities. The previously used equations for selectivity relate the CO produced to the conversion of propane and propene alone and not to the alternative reaction pathway via CO_2. For this reason, the selectivities for CO appear disproportionately large and exceed 100 % in some measurements. To ensure comparability with all other considerations in this work, and since no distinction can be made between carbon sources in the formation of CO, this equation continues to be used to calculate selectivity. Overall, the results show that the intended principle of the reactor cascade with one reactor for ODH and one for TDH works.

Furthermore, it was observed that the RWGS reaction has a noticeable effect in pilot scale testing. This effect is not seen in laboratory scale experiments. Because the simulations are based on the laboratory results, they do not include the RWGS effects observed in pilot scale testing.

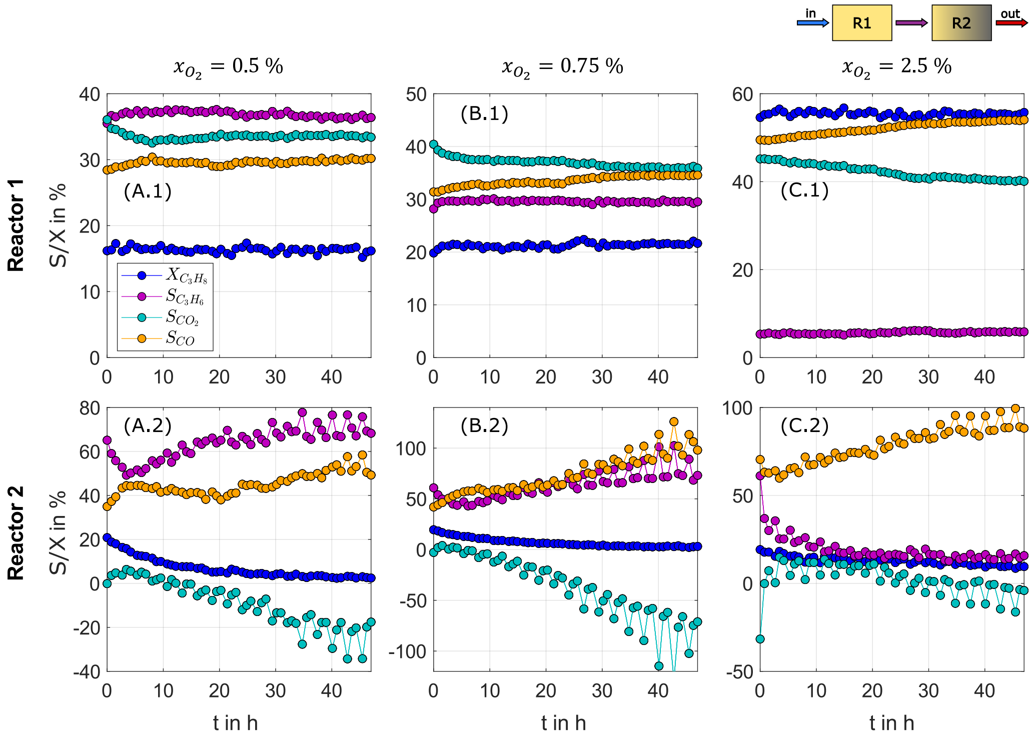

Figure 5.9: Selectivities and conversion of the separate reactors in a FBR cascade at different oxygen inlet concentrations (0.5 %, 0.75 % and 2.5 %) for Reactor 1 (A.1 - C.1) and Reactor 2 (A.2 - C.2) (T_1 = 575 °C, T_2 = 625 °C, $x_{C_3H_8,in}$ = 1 %, $WHSV$ = $400\,kg\,s\,m^{-3}$).

FBR cascade: With vs. without periodic flow reversal The comparison of reactor cascade operation with and without flow reversal is shown in Fig. 5.10. It reveals that a cyclic operation mode utilizing periodic flow reversal can outperform reactor operation without flow reversal. Measurements with 0.5 % oxygen in the feed stream show the best performance with long term yield fluctuating between 8 % and 10 % for the cyclic operation mode. The yield of the reactor cascade without flow reversal in comparison drops below 8 %. By keeping in mind that the cyclic operation mode eliminates the need for reactor down times for regeneration, it can be assumed that the cyclic operation pays off on long term. The results also draw the attention to the vastly different performance of the different reactors. In Fig. 5.10 A.2 it becomes clear that the conversion is significantly higher when the flow is reversed and the feed flow enters the second reactor first. This is only partially reflected in the yield because the yield does not increase to the same extent as the conversion. In both the yield and conversion, it is observable that the operando regeneration has a positive influence but does not bring back the catalyst to the same state it has been in at the beginning of the measurement. Overall, a decreasing trend over time can be seen for yield and conversion. Comparing A.1, A.2 and A.3 shows that the decrease in catalyst activity is mitigated at higher concentrations of oxygen.

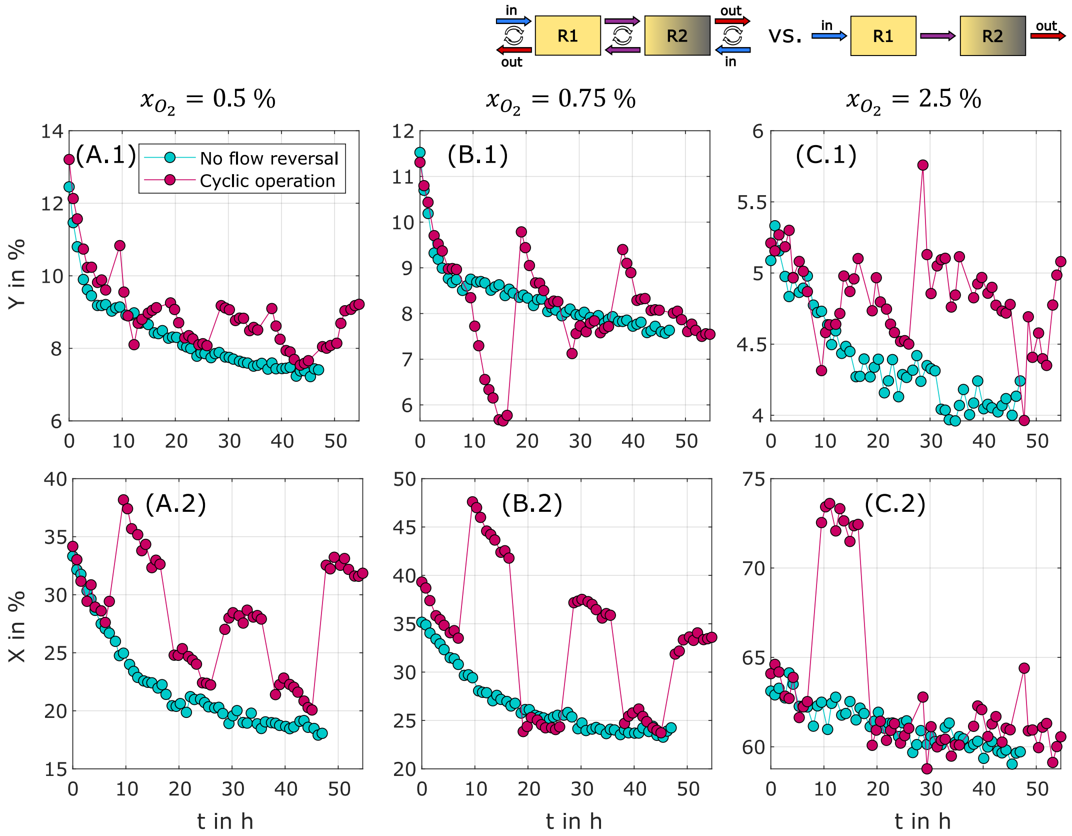

Figure 5.10: Yield (A.1 - C.1) and conversion (A.2 - C.2) of the entire FBR cascade at different oxygen inlet concentrations (0.5 %, 0.75 % and 2.5 %) (T_1 = 575 °C, T_2 = 625 °C, $x_{\mathrm{C_3H_8,in}} = 1\,\%$, $WHSV = 400\,\mathrm{kg\,s\,m^{-3}}$).

The same trends that have been illustrated here can also be observed for the measurements at other temperatures. For similar figures for $T_{\mathrm{R1}}/T_{\mathrm{R2}}$ = 550 °C/600 °C see Fig. C.8 and Fig. C.9 in Appendix C.3. In Fig. 5.5 the desired temperature changes and the associated trends in the conversions of the individual reactors were introduced. As Fig. 5.11 shows, despite the difficulties illustrated in Fig. C.9, it was possible to realize the desired change between the temperatures and the change in the flow direction. In principle, the experimental realization and the associated extensive modification of the test plant were successful. The deactivation tendencies can be clearly seen when TDH is carried out in the reactor (reactor 1: phase ③; reactor 2 phase ①) and slight regeneration of the catalyst is observable in the phases in which oxygen is supplied to the reactor (reactor 2: phase ③). The purge phases are sufficient to change the temperatures in the reactors.

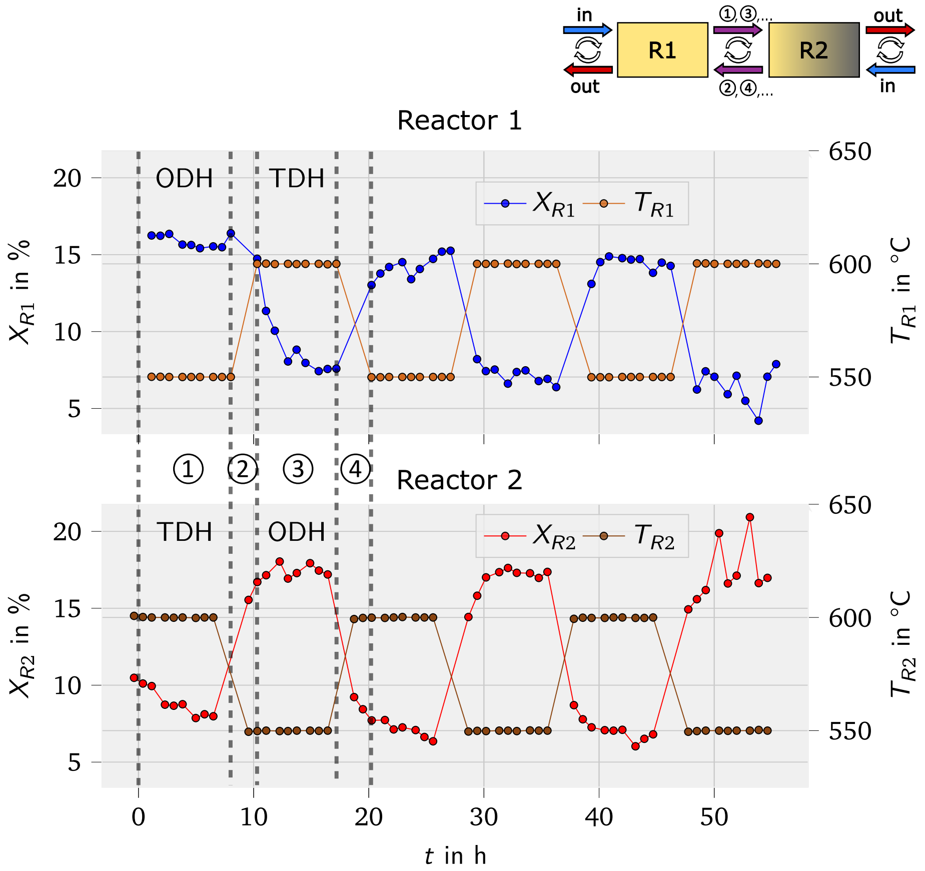

Figure 5.11: Temperature and conversion over time for the separate reactors in a FBR cascade for the different phases (① - ④) in the production cycle ($T_1 = 550\,°\mathrm{C}$, $T_2 = 600\,°\mathrm{C}$, $x_{\mathrm{C_3H_8,in}} = 1\,\%$, $x_{\mathrm{O_2,in}} = 0.5\,\%$, $WHSV = 400\,\mathrm{kg\,s\,m^{-3}}$).

FBR cascade: Influence of flow direction without periodic flow reversal The large differences in the performance of the reactor cascade depending on the flow direction led to experiments in which the cascade was studied with the flow reversed, but without a periodic change in flow direction. The results of these experiments are shown in Fig. 5.12. Reactor 1 (R1) in Fig. 5.12 (A) denotes the performance of the first reactor in the direction of flow, whereas Reactor 2 (R2) stands for the second reactor in the direction of flow. $MR1 \rightarrow MR2$ describes the flow direction before switching the valve and $MR2 \rightarrow MR1$ the flow direction after switching the valve, respectively. The single reactor performances in Fig. 5.12 (A) show that the conversion of propane ($X_{\mathrm{C_3H_8}}$) and the selectivity towards CO (S_{CO}) in R1 are higher for $MR2 \rightarrow MR1$. The selectivity towards $\mathrm{CO_2}$ ($S_{\mathrm{CO_2}}$) is lower.

This indicates a higher average temperature in R1 for $MR2 \rightarrow MR1$ ($\bar{T}_{\mathrm{R1,MR2\rightarrow MR1}} > \bar{T}_{\mathrm{R1,MR1\rightarrow MR2}}$).

The same trends can be observed in the comparison between Fig. C.8 ($T_{\mathrm{R1}}/T_{\mathrm{R2}} = 550\,°\mathrm{C}/600\,°\mathrm{C}$, Appendix C.3) and Fig. 5.9 ($T_{\mathrm{R1}}/T_{\mathrm{R2}} = 575\,°\mathrm{C}/625\,°\mathrm{C}$). In these measurements, a temperature difference on the FBR cascade was intentionally realized with the same flow direction. These identical trends suggest that there are significant temperature differences in the reactors at different flow directions. It should be noted that there are also temperature differences in the piping leading to the reactor when the flow is reversed. These differences can also have an influence on reactor performance by changing the gas temperatures prior to the reactor. Reactor 2 does also show significant differences in performance when reversing the flow. The most noticeable difference is that with flow reversal ($MR2 \rightarrow MR1$) there is greater selectivity towards CO than towards C_3H_6 and less RWGS reaction ($S_{\mathrm{CO_2}} > 0$). As mentioned before, a comparison between the second reactor in forward and reversed flow is not trivial because the inlet flows are not identical.

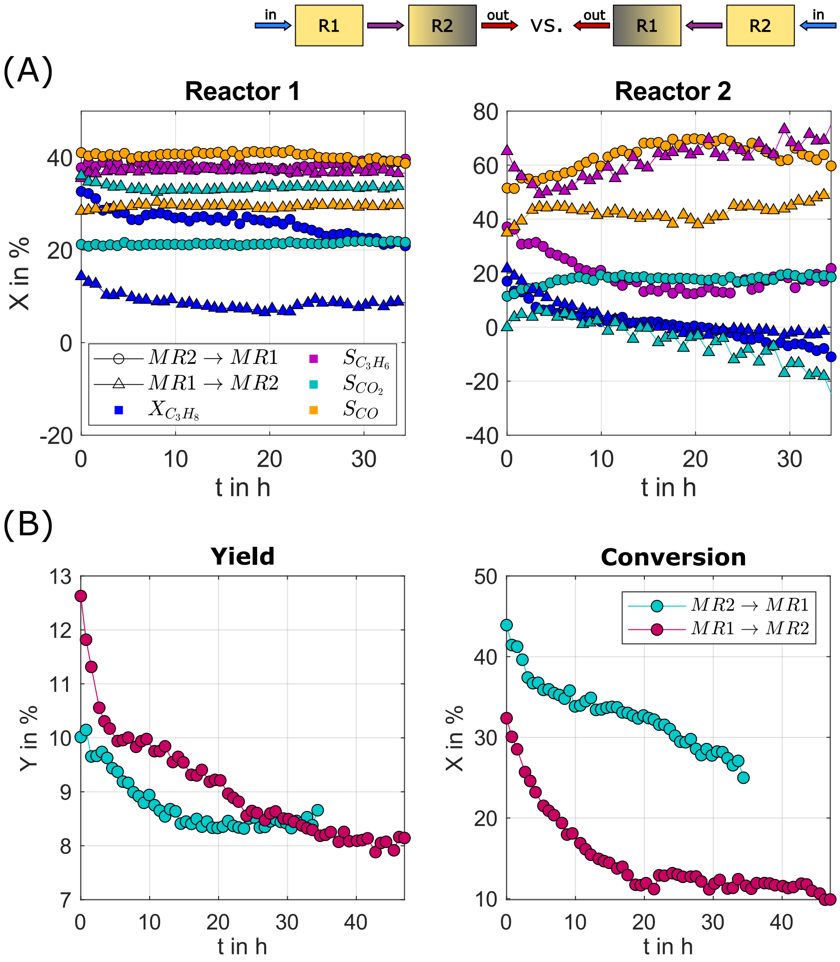

Figure 5.12: Performance parameter for the FBR reactor cascade operated in two different flow directions: (A) Selectivity and conversion of the reactors separately; (B) Yield and conversion of the entire reactor cascade ($T_1 = 575\,°\mathrm{C}$, $T_2 = 625\,°\mathrm{C}$, $x_{\mathrm{C_3H_8,in}} = 1\,\%$, $x_{\mathrm{O_2,in}} = 0.5\,\%$, $WHSV = 400\,\mathrm{kg\,s\,m^{-3}}$).

The overall yield of the reactor cascade (Fig. 5.12 B) of the reverse flow operation ($MR2 \rightarrow MR1$) is higher than for the forward flow ($MR1 \rightarrow MR2$), despite the fact that the conversion is lower.
In summary, the differences can be largely attributed to different temperature profiles in the reactors. This might also be caused by different pipe tracing temperatures. It has to be mentioned, that it is not trivial to measure these differences. The temperature of the electric heating sleeve of the reactor housing is controlled by a single thermocouple in the middle of the catalyst bed (see Appendix C.1, Fig. C.1). The temperature in the middle of the catalyst bed varies less than 1 °C over the course of the experiments. The differences are therefore to be located at the reactor inlets. The solid stainless steel housing also has a certain heat capacity, which leads to the formation of a profile towards the flanges, as these are not enclosed by the heating jacket.
Aware of these imperfections, the reactor cascade with membrane dosing was further investigated with the same experimental plant.

5.3.2 Membrane Reactor Cascade With and Without Flow Reversal

The membrane reactor cascade represents the next reactor concept on the way to a fully integrated PBMRint. In the reactor cascades tested, usually only the first reactor in direction of flow was used as a membrane reactor to mimic the PBMRint that is tested later. The difference of the membrane reactor cascade and the PBMRint is the additional degree of freedom due to the absence of heat integration. This allows to set the temperature of the second reactor individually. To investigate the membrane reactor cascade, first the oxygen concentration dosed via the membrane into the first reactor was systematically varied. This was followed by a variation of the temperature. Experiments with a FBR cascade presented in the section before indicated an influence of the RWGS reaction on reactor performance. For that reason, the influence of CO_2 dosage to induce the the RWGS reaction was also evaluated. Subsequently, a comparison of the reactor cascade with and without membrane dosing followed and an evaluation of the potential of cyclic operation with periodic flow reversal was performed.

PBMR cascade: Variation of oxygen concentrations Fig. 5.13 presents selectivities and conversion for the membrane reactor cascade for different oxygen concentrations. As already discussed in the results for the FBR cascade, the conversion in reactor 1 increases with increasing oxygen concentration, but the selectivity decreases. Likewise, the selectivity towards CO increases while the CO_2 selectivity remains constant. In the second reactor, it is noticeable that no more negative CO_2 selectivities are observed. Overall, it can be seen that even at low oxygen concentrations, only a little deactivation is noticed over time. This indicates the inflow of oxygen into the second reactor, which effectively prevents deactivation even at low concentrations. This oxygen input appears reasonable in the context of a continuous oxygen dosage over the entire length of Reactor 1. Oxygen dosed only at the end of the catalyst bed is not completely consumed in the first reactor due to the short residence time.
In addition, at high oxygen concentrations (Fig. 5.13, C.2), the consumption of propene in the second reactor can be observed, as indicated by the negative selectivities of propene. Accordingly, the propene produced in the first reactor is converted to the by-products

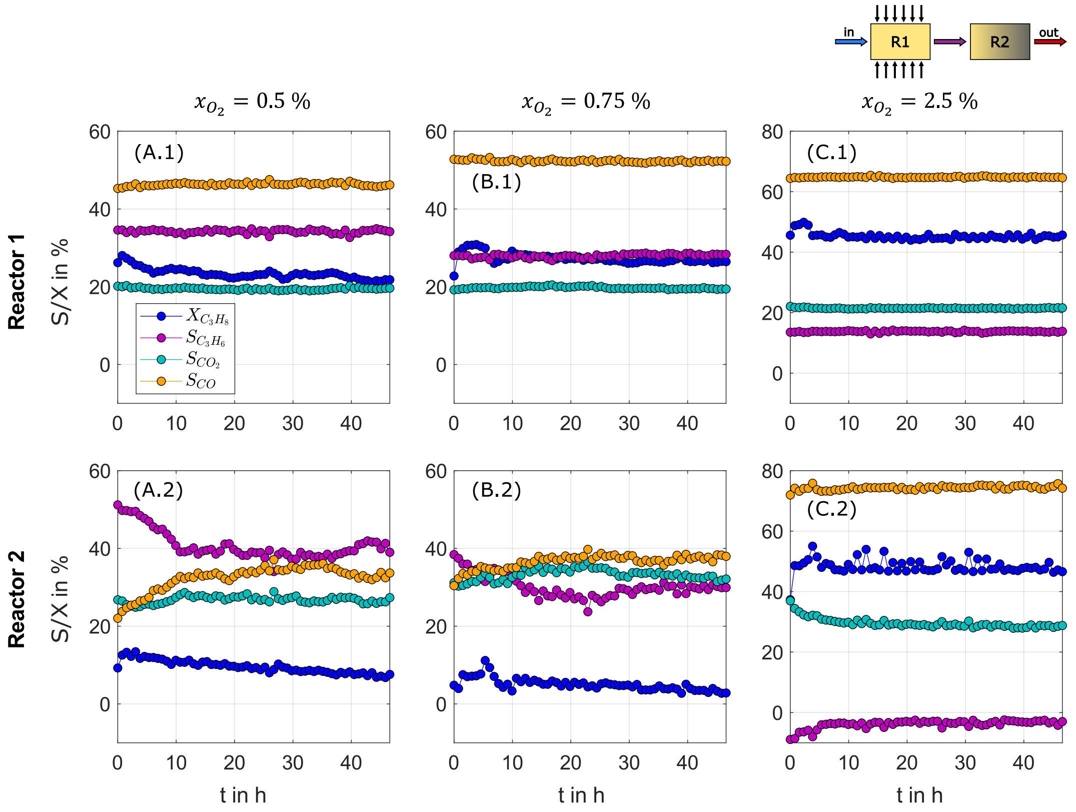

Figure 5.13: Selectivities and conversion of the separate reactors in a PBMR cascade at different oxygen inlet concentrations (0.5 %, 0.75 % and 2.5 %) for Reactor 1 (A.1 - C.1) and Reactor 2 (A.2 - C.2) ($T_1 = 550\,°\mathrm{C}$, $T_2 = 600\,°\mathrm{C}$, $x_{\mathrm{C_3H_8,in}} = 1\,\%$, $x_{\mathrm{O_2,in}} = 0.5\,\%$, $WHSV = 400\,\mathrm{kg\,s\,m^{-3}}$).

CO and CO_2. These side reactions are favored by the higher temperatures in the second reactor. This behavior shows that the tested reactor concept requires a precise adjustment of the reaction conditions and the input concentrations. The oxygen concentration must be adjusted so that as little oxygen as possible passes from the first reactor to the second to avoid side reactions.

A comparison of the membrane reactor with and without periodic flow reversal is given in Fig. 5.14. In opposite to the measurements without membrane dosing, significant drops in conversion after the flow reversals are visible (Fig. 5.14 A.2 - C.2). The reason for these drops of conversion is the reduced membrane dosing shortly after the flow reversal. There is a certain pressure drop through the membrane. Directly after switching the flow direction, the pressures on both sides of the membrane are equal and therefore no gas is pushed through the membrane. The pressure builds up over time by dosing gas to the shell side. Without a trans membrane flux of oxygen, the conversion in the reactor is much lower. Overall, the cyclic operation does not have an advantage compared to the operation without flow reversal. According to the yields, small oxygen concentrations have to be preferred. The optimal oxygen concentration among the tested concentrations for temperatures of $T_{\mathrm{R1}}/T_{\mathrm{R2}} = 550\,°\mathrm{C}/600\,°\mathrm{C}$ is $0.5\,\%$. This optimal oxygen concentration can vary at different temperatures e.g. at $T_{\mathrm{R1}}/T_{\mathrm{R2}} = 575\,°\mathrm{C}/625\,°\mathrm{C}$ the experiments reveal a better performance at $0.75\,\%$ (Fig. C.10 - C.11, Appendix C.3). Appendix C.2.2, Fig. C.6 (A) and Fig. C.7 show the 1D simulation results for varying oxygen concentrations at $T_{\mathrm{R1}}/T_{\mathrm{R2}} = 550\,°\mathrm{C}/600\,°\mathrm{C}$ and $T_{\mathrm{R1}}/T_{\mathrm{R2}} = 575\,°\mathrm{C}/625\,°\mathrm{C}$, respectively. For both temperature levels, the yield shows a decreasing trend for increasing oxygen concentrations and no temperature depended optimum at low oxygen concentrations like the pilot scale experiments. This confirms again that simplified, isothermal 1D simulations without considering radial profiles are not sufficient to represent the complex phenomena in the reactor at pilot plant scale.

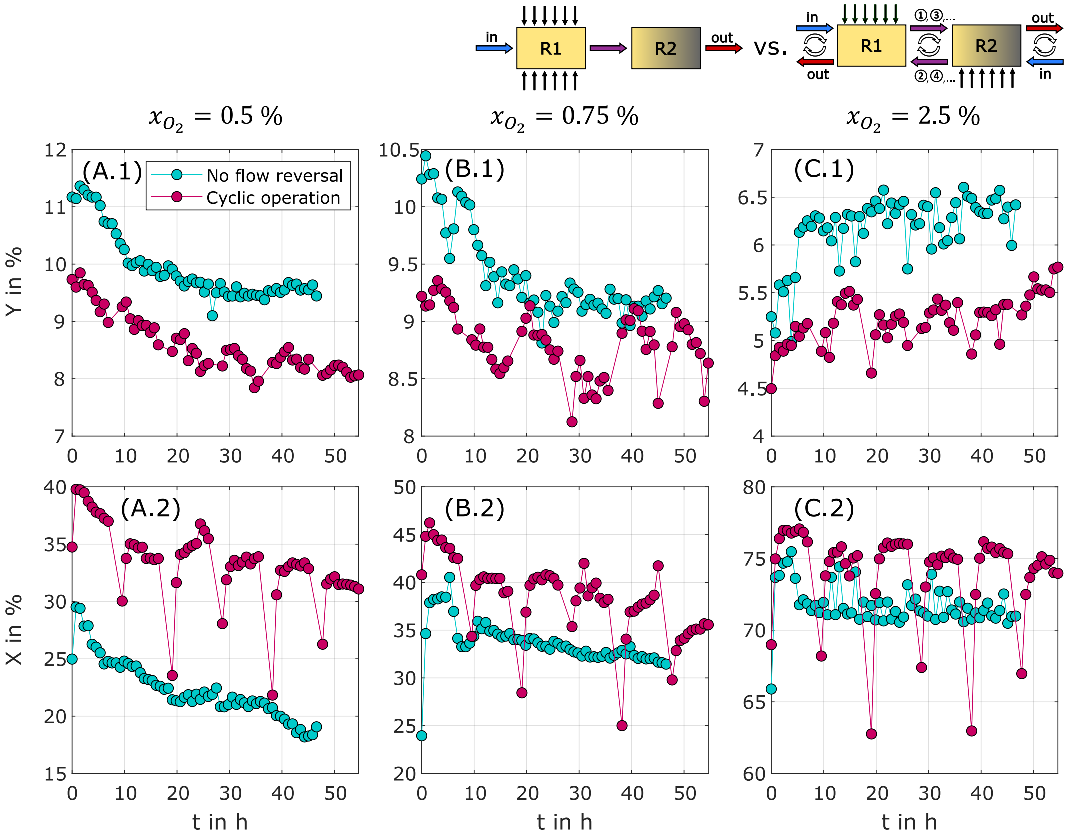

Figure 5.14: Yield (A.1 - C.1) and conversion (A.2 - C.2) of the entire PBMR cascade at different oxygen inlet concentrations (0.5 %, 0.75 % and 2.5 %) ($T_1 = 550\,°\mathrm{C}$, $T_2 = 600\,°\mathrm{C}$, $x_{\mathrm{C_3H_8,in}} = 1\,\%$, $WHSV = 400\,\mathrm{kg\,s\,m^{-3}}$).

PBMR cascade: Variation of temperatures Based on the results obtained by varying the oxygen input concentration, the effect of temperature was systematically investigated experimentally. The next figures present the results for measurements with 0.5 % oxygen at different temperature levels. This is the concentration at which the best yields were obtained. For the temperature variations, the temperature difference between the reactors was kept constant at $\Delta T = 50\,°\mathrm{C}$, and the temperatures in the single reactors have been increased in steps of 25 °C. Fig. 5.15 A.1, B.1 and C.1 reveal that the first reactor shows almost a similar performance at the different temperatures. The propene selectivity is increasing slightly, whereas the deactivation is more pronounced with increasing temperature. This is caused by the fact that the TDH preferentially proceeds with increasing temperature. The FBR cascade without membrane dosing shows larger performance differences with varying temperature (compare Fig. 5.9 and Fig. C.8, Appendix C.3). The influence of temperature on the second reactor in the membrane reactor cascade (Fig. 5.15 A.2, B.2 and C.2) is greater than on the first reactor. This result is not consistent with a simple consideration of the reaction rate constants of the kinetics. Increasing the temperature from 550 °C to 600 °C (T_{R1}) results in doubling the reaction rate constant of ODH. Similarly, the reaction rate constant of TDH doubles when the temperature is increased from 600 °C to 650 °C (T_{R2}). Accordingly, the effect of increasing temperature levels does not affect the reaction rate constants differently and does not explain the experimental measurements. The same result is obtained from the 1D steady state simulations presented in Appendix C.2.2 Fig. C.6 (B). The subtle difference in performance of the first rector and the bigger difference in the performance of the second reactor is not observable in 1D simulations. It becomes clear that sophisticated models and pilot-scale experiments are indispensable when investigating integrated reactor configurations, since the complex concentration and temperature profiles have to be considered.

The measurements also reveal the influence of temperature on the deactivation behavior of the reactor cascade. Only at $T_{\mathrm{R1}}/T_{\mathrm{R2}} = 550\,°\mathrm{C}/600\,°\mathrm{C}$ the second reactor shows a residual catalyst activity at the end of the measurement. At the higher temperatures the conversion drops to zero at the end of the measurements, which means that the second reactor does not contribute to the overall yield of the reactor cascade after a certain time on stream.

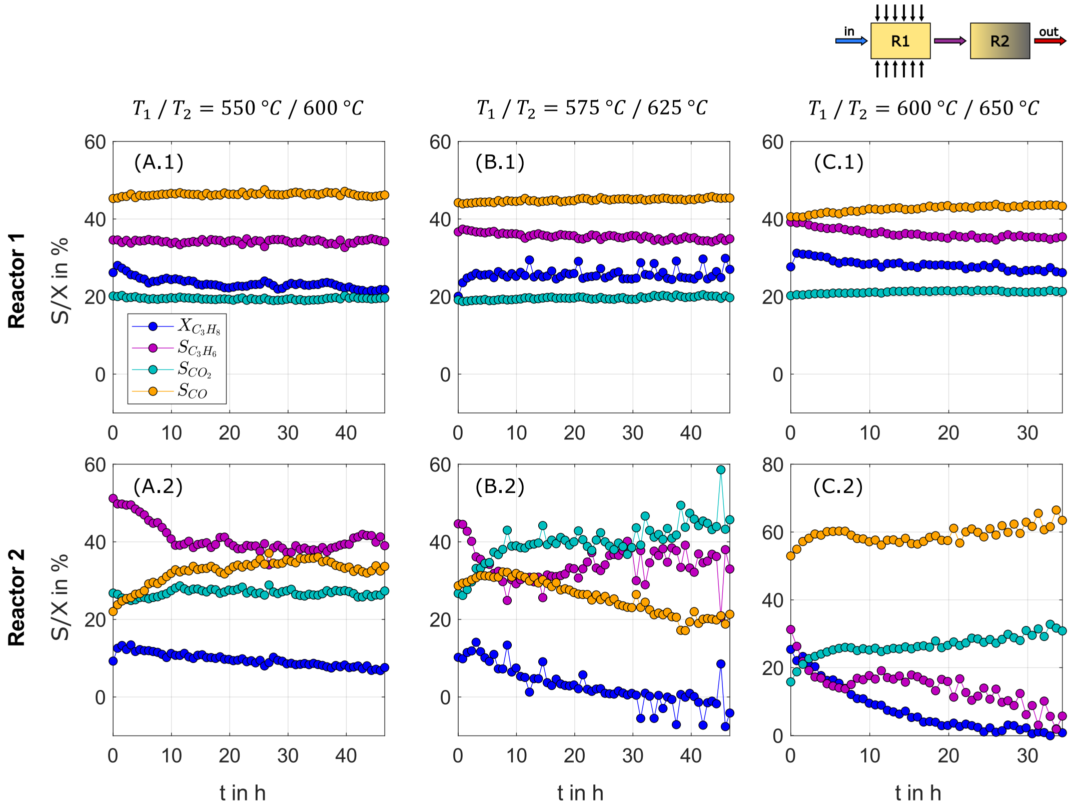

Figure 5.15: Selectivities and conversion of the separate reactors in a PBMR cascade at different reactor temperatures for Reactor 1 (A.1 - C.1) and Reactor 2 (A.2 - C.2) ($x_{\mathrm{C_3H_8,in}} = 1\,\%$, $x_{\mathrm{O_2,in}} = 0.5\,\%$, $WHSV = 400\,\mathrm{kg\,s\,m^{-3}}$).

Fig. 5.16 illustrates the yields and conversions of the reactor cascade as the temperatures are varied, showing that a new and interesting optimization problem arises here. At the elevated temperatures of $T_{\mathrm{R1}}/T_{\mathrm{R2}} = 575\,°\mathrm{C}/625\,°\mathrm{C}$ and $T_{\mathrm{R1}}/T_{\mathrm{R2}} = 600\,°\mathrm{C}/650\,°\mathrm{C}$, higher initial yields are measured at the beginning of the measurement. However, these decrease faster than at lower temperatures due to catalyst deactivation. Here, an optimization would have to determine whether longer production times at lower temperatures or shorter production times at higher temperatures with subsequent regeneration promise a higher space-time yield. This problem is comparable to the 1D optimization problem discussed in Section 4.1. The goal of this optimization was to determine optimized production and regeneration times while maximizing space-time yield. The simplifications of a 1D simulation are not feasible at this point due to the distinct radial temperature and concentration profiles. These have already been discussed in Section 4.2.3. For a rigorous optimization, 2D models capable of representing these profiles would have to be applied. The computational effort involved in an optimization based on 2D models is beyond the scope of this work and represents an interesting approach for future work.

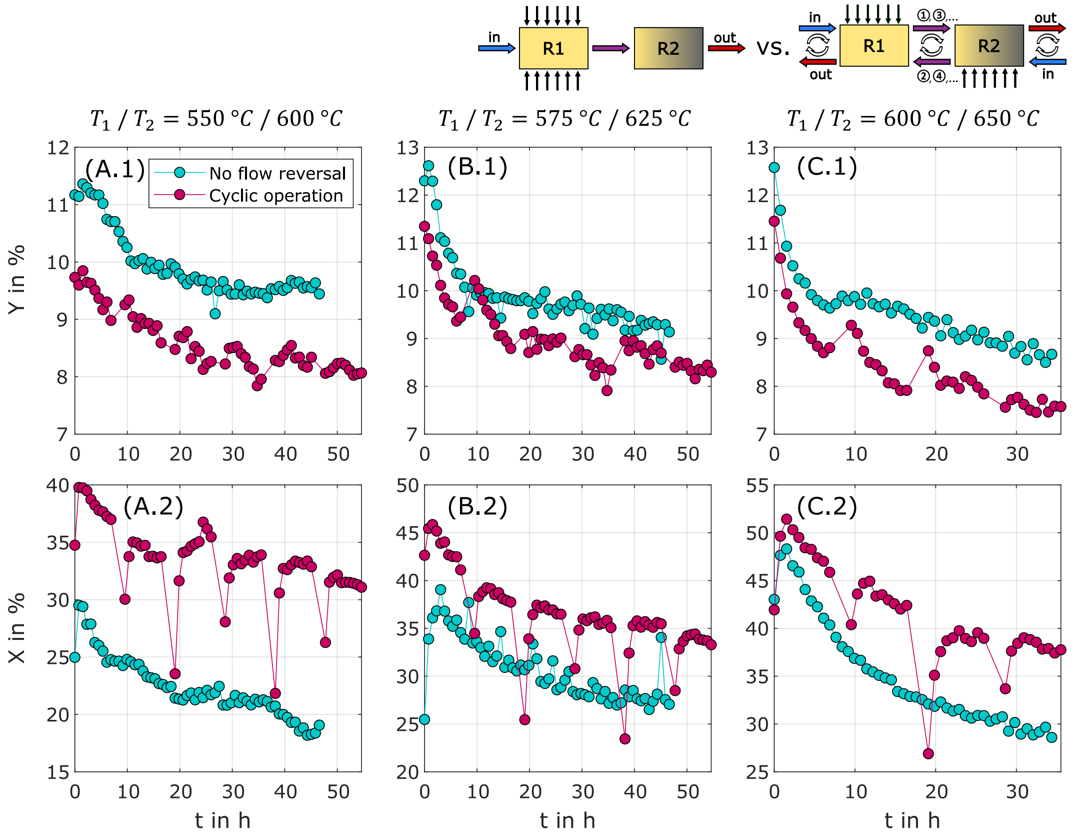

Figure 5.16: Yield (A.1 - C.1) and conversion (A.2 - C.2) of the entire PBMR cascade at different reactor temperatures ($x_{\mathrm{C_3H_8,in}} = 1\,\%$, $x_{\mathrm{O_2,in}} = 0.5\,\%$ $WHSV = 400\,\mathrm{kg\,s\,m^{-3}}$).

PBMR cascade: Influence of CO_2 dosing The experiments with the FBR reactor cascade, presented previously in Section 5.3.1, revealed that a RWGS reaction can occur in the second reactor of the cascade. This reaction helps to convert CO_2 stemming from side reactions into more valuable CO and, at the same time, shifts the chemical equilibrium of the TDH towards the product side. In contrast, no RWGS reaction was observed during the experiments with the membrane reactor cascade for reasons discussed before. So far, only the first reactor in the reactor cascade has been used for gas dosing. In that way, the reactor cascade can be interpreted as an intermediate step towards the PBMRint that also does not allow membrane dosing in the second catalyst bed. In order to enhance the RWGS reaction in the second reactor, some experiments were carried out in which CO_2 was additionally dosed into the second reactor via the membrane. The results of these experiments are presented in Fig. 5.17. Although the results in reactor 1 should be identical under the same conditions with and without CO_2 dosing, some differences in the results are visible (Fig. 5.17 A.1, B.1). These might be attributed to irreversible catalyst deactivation since the conditions in the first reactor should be comparable besides that. A long term irreversible deactivation was not observed in the lab scale experiments and might be attributed to hotspots appearing in scale-up. More significant are the differences in the performance of the second reactor (A.2, B.2). It is clearly visible that the selectivity towards CO is much higher if CO_2 is dosed through the membrane. Additionally, the CO_2 selectivity is negative at the beginning of the experiment which indicates, that CO_2 is consumed. An effect on the propene yield or propane conversion could not be detected as can be seen in Fig. 5.17 C.1 - D.2. The yields and conversions of the experiments without CO_2 are slightly higher than for the experiments with CO_2 dosing. The cause of these differences remains uncertain, as it is unclear whether they result from the introduction of additional CO_2 or if they stem from catalyst aging. Similar results were obtained by measurements at $T_{\mathrm{R1}}/T_{\mathrm{R2}} = 550\,^{\circ}\mathrm{C}/600\,^{\circ}\mathrm{C}$ which can be found in Appendix C.3, Fig. C.12. All in all, the dosing of CO_2 does not offer significant benefits regarding the TDH and the overall yield of the reactor cascade. Nonetheless, it might be an option to convert CO_2 from other sources to CO.

FBR cascade vs. PBMR cascade: Without periodic flow reversal After a detailed discussion of the membrane reactor cascade, the next step is to compare the performance of the membrane reactor cascade with the performance of the FBR cascade. A comparative plot of the performance parameters of membrane reactor cascade and fixed bed reactor cascade without flow reversal is shown in Fig. 5.18. It is evident that in the membrane reactor the selectivity to CO in the first reactor is much higher than in the fixed bed cascade, while the selectivity to CO_2 is lower. It is known from 2D simulations (Section 4.2.3, Fig. 4.12) that an elongated reaction front is formed in the membrane reactor, which provides uniformly low oxygen concentrations. It can be assumed that these low oxygen concentrations account for the incomplete oxidation to CO. At higher oxygen concentrations, such as those present in the fixed bed reactor, total oxidation of the propene occurs proportionally more often. It is surprising that the selectivity towards propene is similar in both reactor types at low oxygen concentrations (A.1, B.1). Higher selectivities are only visible at higher oxygen concentrations (C.1). The performance of the first reactor does also have an influence on the second reactor (A.2 - C.2), which is a similar FBR in both types of reactor cascade. The second reactor in the membrane reactor cascade does not show significant deactivation tendencies and no significant RWGS reaction as already discussed. Selectivities toward propene are higher in the second reactor in case of the FBR cascade due to the oxygen free atmosphere.

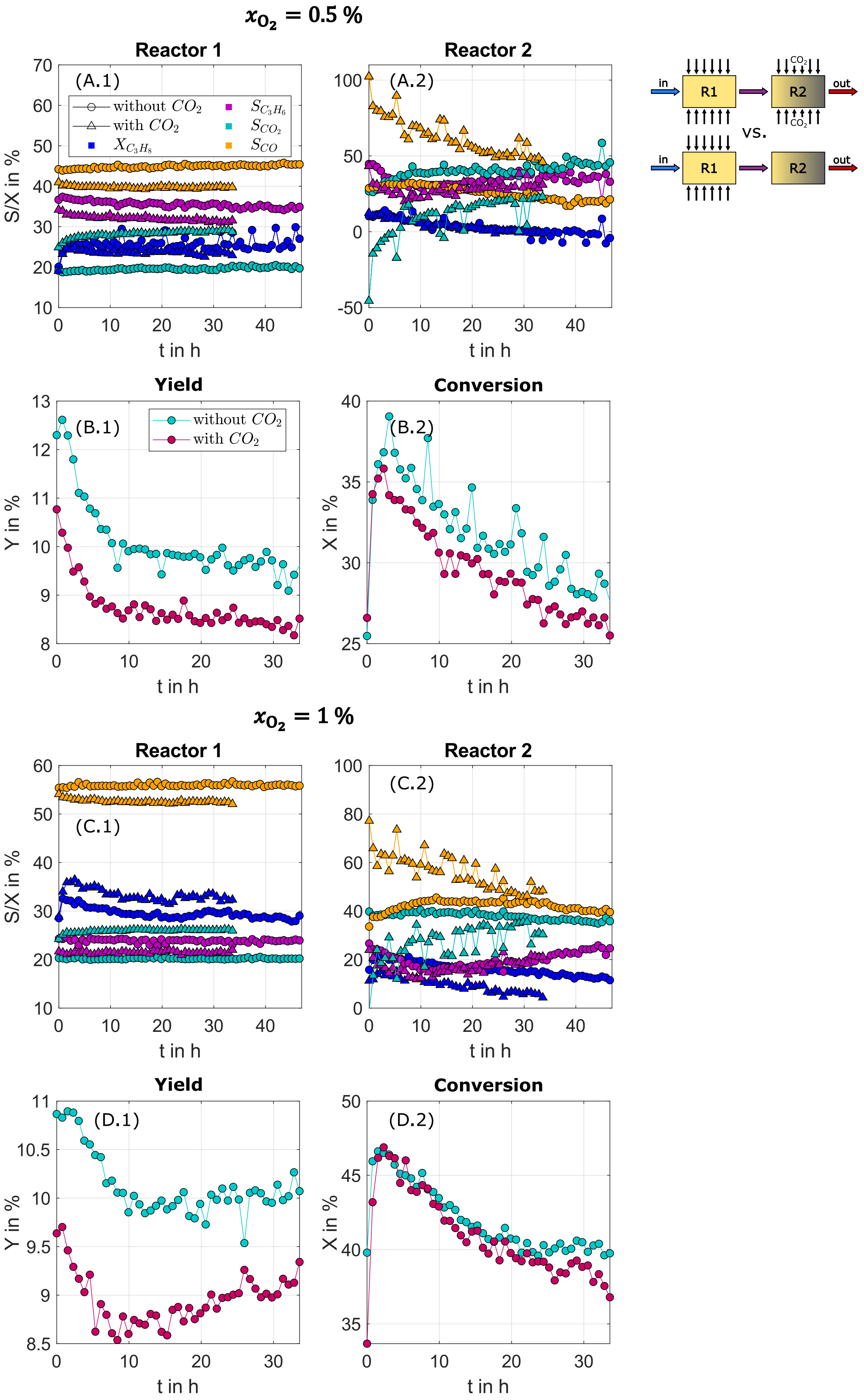

Figure 5.17: Comparison of measurements in PBMR cascade operation with and without additional dosing of CO_2 without flow reversal at different oxygen inlet concentrations ($T_1 = 575\,°C$, $T_2 = 625\,°C$, $x_{C_3H_8,in} = 1\,\%$, $x_{CO_2,in} = 2\,\%$).

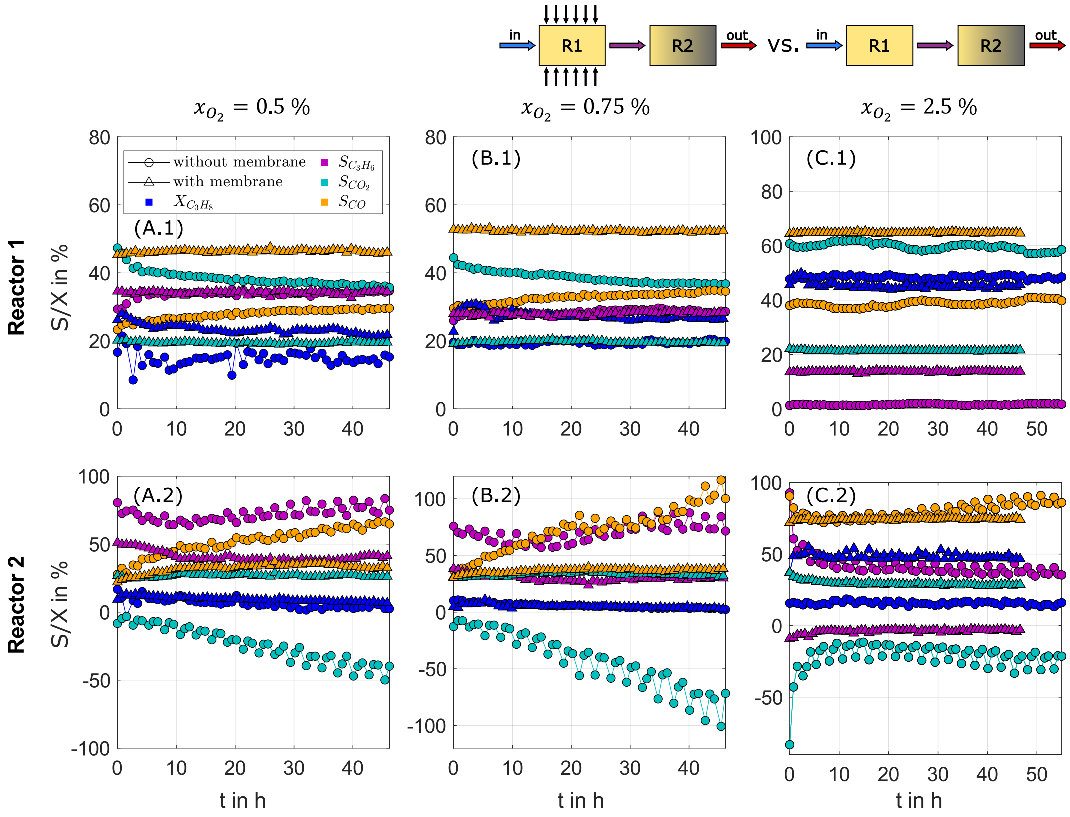

Figure 5.18: Selectivities and conversion of the separate reactors in a PBMR cascade (symbol: △) and a FBR cascade (symbol: ○) at different inlet oxygen concentrations for Reactor 1 (A.1 - C.1) and Reactor 2 (A.2 - C.2) (T_1 = 550 °C, T_2 = 600 °C, $x_{C_3H_8,in} = 1\,\%$, $x_{O_2,in} = 0.5\,\%$, $WHSV = 400\,kg\,s\,m^{-3}$).

Fig. 5.19 shows that the membrane reactor cascade outperforms the FBR cascade at all oxygen concentrations investigated. Both yields and conversions are higher. The difference in conversion increases with increasing oxygen concentration. In terms of yield, the differences are the biggest at low oxygen concentrations.

These trends are also evident at other temperatures. For a graphic representation of the results at $T_{R1}/T_{R2} = 575\,°C/625\,°C$, see Appendix C.3, Fig. C.18 - C.17.

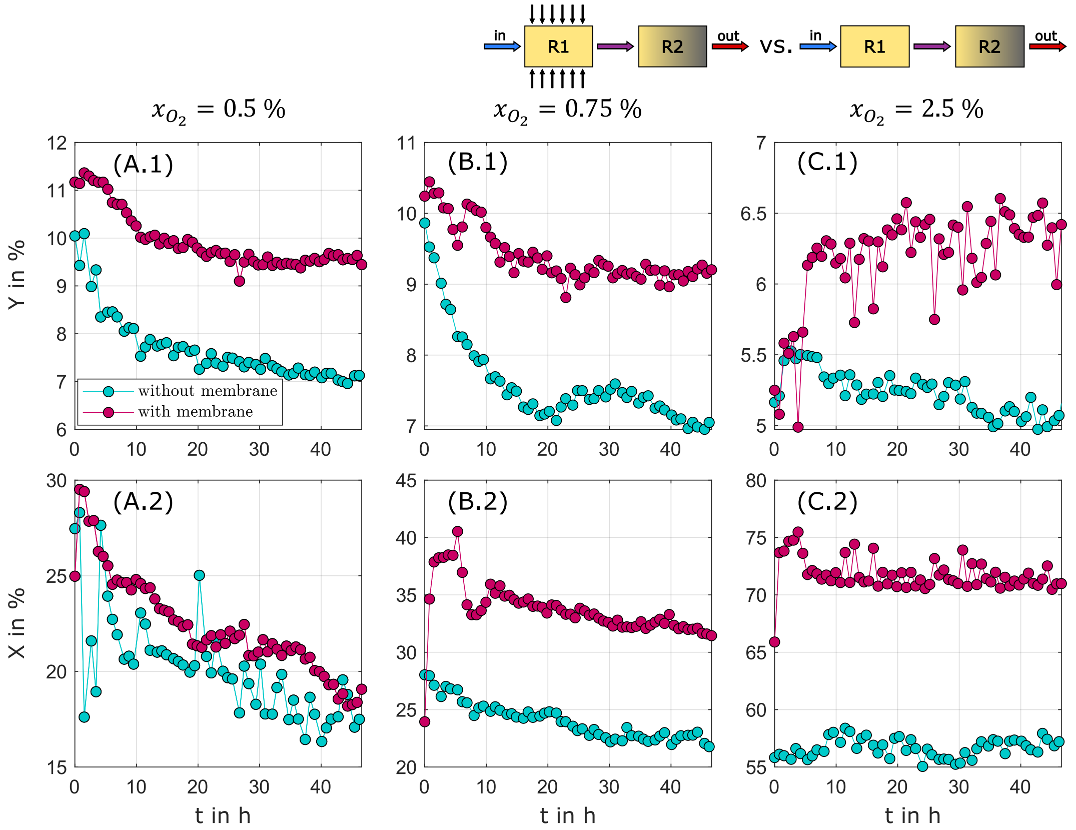

Figure 5.19: Yield (A.1 - C.1) and conversion (A.2 - C.2) of the entire reactor cascade in PBMR operation (with membrane) and in FBR operation (without membrane) at different oxygen inlet concentrations (0.5 %, 0.75 % and 2.5 %) ($T_1 = 550\,°\mathrm{C}$, $T_2 = 600\,°\mathrm{C}$, $x_{\mathrm{C_3H_8,in}} = 1\,\%$, $WHSV = 400\,\mathrm{kg\,s\,m^{-3}}$).

FBR cascade vs. PBMR cascade: With periodic flow reversal The performance parameters of the FBR cascade and the PBMR cascade with flow reversal are illustrated in Fig. 5.20. This figure underlines again how different the performances of the separate reactors in the cascade are. Differences between the reactors without membrane dosing are much more apparent. In Fig. 5.20 A.1 and B.1 it can be seen that during the TDH operation of reactor 1 (second reactor in direction of flow, phase ② and ④) the selectivity towards CO is very high. Reactor 2 does not exhibit this behavior during TDH operation (5.20 A.2 and B.2, phase ③ and ⑤), but a higher selectivity towards the desired product propene can be observed in these phases. Without the membrane dosing, the reactor with flow reversal shows a negative CO_2 selectivity only when the first reactor is used as the TDH reactor (A.1 and B.1, phase ② and ④). When Reactor 2 is in TDH mode, the aforementioned behavior cannot be observed. However, with the utilization of membrane dosing, the performance differences between the ODH and TDH phases and between the reactors are not as significant. This leads to a more homogeneous reactor performance, indicating a reduction in performance variability.

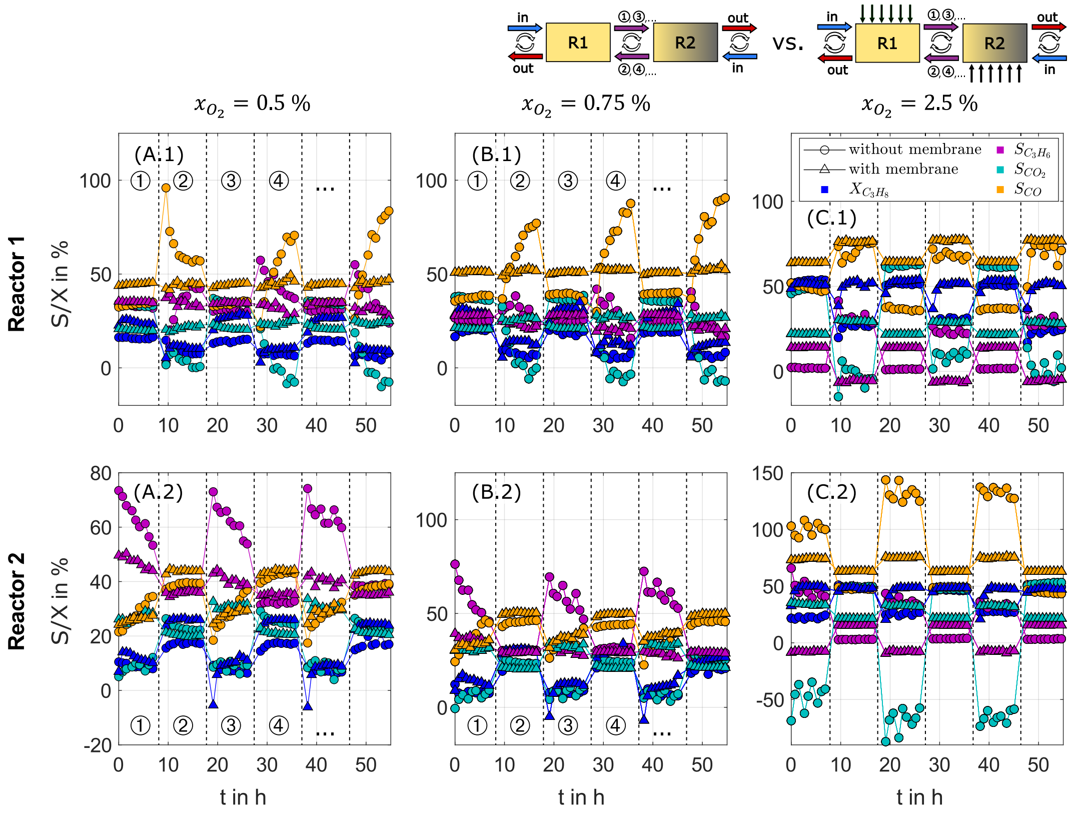

Figure 5.20: Selectivities and conversion of the separate reactors in a PBMR cascade (symbol: △) and a FBR cascade (symbol: ◯) at different inlet oxygen concentrations for Reactor 1 (A.1 - C.1) and Reactor 2 (A.2 - C.2) with periodic flow reversal ($T_1 = 550\,°\mathrm{C}$, $T_2 = 600\,°\mathrm{C}$, $x_{\mathrm{C_3H_8,in}} = 1\,\%$, $WHSV = 400\,\mathrm{kg\,s\,m^{-3}}$).

These large differences also have a direct effect on the overall performance of the reactor cascade. The jumps in the yield curve in Fig. 5.21 are much less pronounced in the case of membrane operation, especially at lower oxygen concentrations (Fig. 5.21 A.1 and B.1). The yields are on average also comparably high. The greater consistency in the production might have advantages in downstream processing. A similar yield at higher conversions (see Fig. 5.21 A.2 - C.2) results in another product spectrum. The PBMR cascade favors the production of CO, which is a valuable intermediate, due to larger areas with low oxygen concentrations that have already been shown in 2D simulations (see Section 4.2.3, Fig. 4.12). The formation of CO_2 is reduced. This might also affect the choice between membrane and FBR operation, since the separation processes have to be different and the valorization of side products have to be considered. The high conversions at low yields for an oxygen concentration of 2.5 % underline again the general trends that have already been discussed. These trends show that low oxygen concentrations are favorable for achieving efficient propene production. Oxygen concentrations of 0.5 % and 0.75 % deliver the best results. All in all, it can be summarized that reaction control using membrane dosing was successful and the trends of the simulation studies could be confirmed.

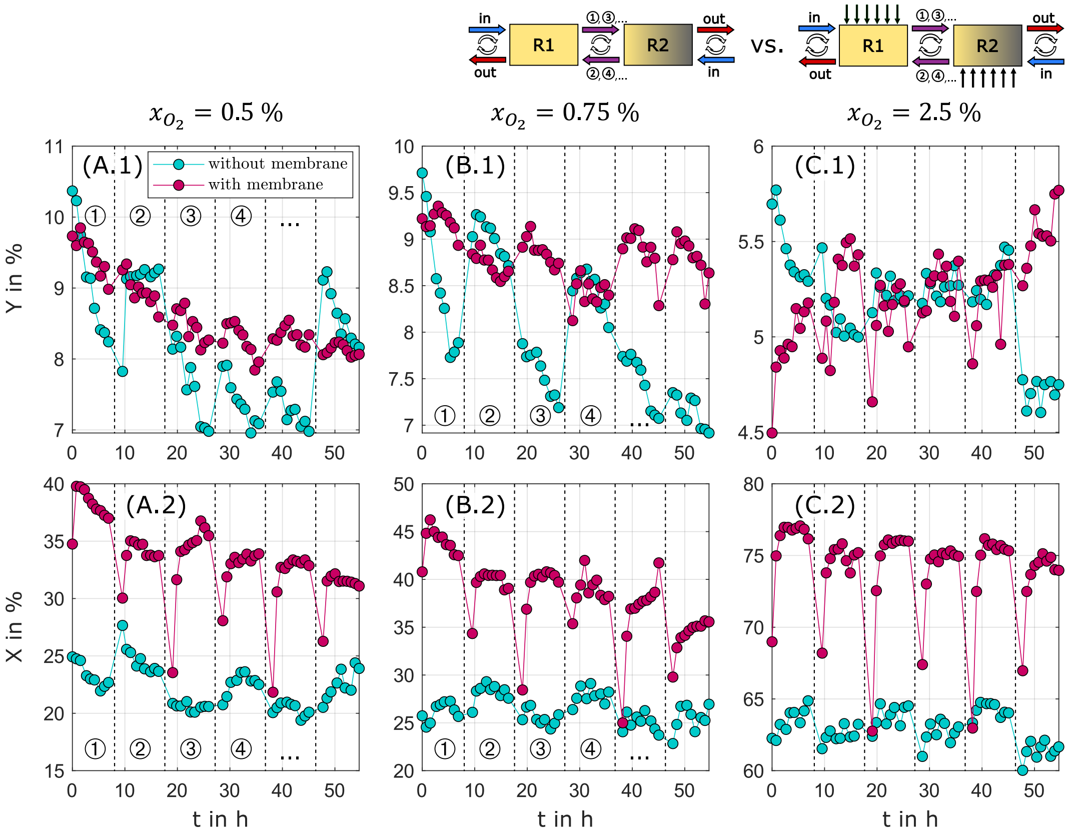

Figure 5.21: Yield (A.1 - C.1) and conversion (A.2 - C.2) of the entire reactor cascade in PBMR operation (with membrane) and in FBR operation (without membrane) at different oxygen inlet concentrations (0.5 %, 0.75 % and 2.5 %) with periodic flow reversal ($T_1 = 550\,°\mathrm{C}$, $T_2 = 600\,°\mathrm{C}$, $x_{\mathrm{C_3H_8,in}} = 1\,\%$, $WHSV = 400\,\mathrm{kg\,s\,m^{-3}}$).

After a detailed investigation of the reactor cascades, the next part of this work focuses on the PBMRint as a fully integrated reactor concept. The reactor cascades represent a preliminary stage for this, since with them a material but no thermal integration could be implemented. In the simulation studies, advantages of the PBMRint over the PBMR and the FBR in terms of performance parameters could already be demonstrated (see Section 4.2.3, Fig. 4.11). Compared to the PBMRint, the reactor cascade has the advantage that the temperatures of the individual reactors can be set separately. Due to the thermal integration, separate heating of the catalyst beds in the integrated reactor is not possible since the two catalyst beds are integrated in one apparatus. On the other hand, the integrated design offers the advantage that the energy released during exothermic ODH can be efficiently provided for TDH in the second catalyst bed. The feasibility of this principle for the PBMRint has also already been shown in simulations (see Section 4.2.3, Fig. 4.14). These simulation results are to be confirmed in the next section.

5.4 Integrated Membrane Reactor

The integrated membrane reactor has already been studied theoretically in Section 4.2, and the experimental equipment used as well as the operation mode have been discussed in Section 5.1.1 and 5.1.2, respectively. The experimental conditions have been kept similar to the conditions of the reactor cascade experiments to make a comparison possible. The propane concentration has always been set to 1 % and a $WHSV = 400\,\mathrm{kg\,s\,m^{-3}}$ has been kept. The oxygen concentration was varied between 1 % and 2 % and temperatures of 550 °C, 575 °C, 600 °C and 625 °C have been set. Furthermore, experiments with and without flow reversal were realized. An overview of the experiments is given in Tab. 5.3.

Table 5.3: Experimental matrix for the investigation of the PBMRint with and without flow reversal (FR: with flow reversal; noFR: without flow reversal).

	Temperature T			
x_{O_2}	550 °C	575 °C	600 °C	625 °C
0.5 %	FR/noFR	FR/noFR	FR/noFR	FR/noFR
1 %	FR/noFR	-	FR/noFR	-

Fig. 5.22 presents the selectivities (Fig. 5.22 A), yield (Fig. 5.22 B) and conversion (Fig. 5.22 C) of the PBMRint at T = 550 °C (A.1 - C.1) and T = 600 °C (A.2 - C.2) and an oxygen inlet concentration of 0.5 %. In the PBMRint it was not possible to take gas samples after the reactants passed the first catalyst bed in the annular gap. Therefore, the selectivities presented in Fig. 5.22 A.1 and A.2 are integral selectivities of the entire apparatus and not comparable to the selectivities of the separate reactors shown before. In Fig. 5.22 B.1 the different phases in periodic operation are indicated. In Phase ① and ③, the reactants are introduced into the annular gap as illustrated in Fig. 5.7 Phase 1. After passing the annular gap, the gas stream is redirected to pass the inner tube in counter current manner. This way of operating the PBMRint will be referred to as MBR operation, since gas penetrates through the membrane. In Phase ② and ④ the gas is introduced in the inner tube as presented in Fig. 5.7 Phase 2. In this direction of flow, it is not possible to dose gas along the length of the first catalyst bed. Operation in this flow direction will be referred to as FBR operation.

By evaluating the results, the significant differences in performance of the different phases become apparent. Fig. 5.22 A.1 and A.2 reveal that the selectivity towards propene decreases during FBR mode compared to MBR mode. This can be attributed to the co-feed of oxygen during FBR mode that results in high local oxygen concentrations and therefore enhanced side reactions. The selectivities towards CO and CO_2 increase in FBR mode for the same reasons. The conversion of propane decreases over time for experiments with and without flow reversal. There is a regeneration tendency during FBR operation in Phase ② and ④ indicated by increasing conversions. This does not offer an advantage for overall reactor performance, since the trans-membrane pressure drop needed for efficient dosing has to be built up in the next MBR operation phase. That results in a steep drop in conversion (Fig. 5.22 C.1, C.2, Phase ③). This behavior has already been observed in experiments with the PBMR cascade (see Fig. 5.21 A.2 - C.2). In opposite to the PBMR cascade, the PBMRint does not offer higher conversions in periodic operation with flow reversal than in operation without flow reversal (compare Fig. 5.16). Due to lower conversions and lower selectivities towards the wanted product propene, the yield in the FBR phases are not as high as during the MBR phases, as illustrated in Fig. 5.22 B.1 and B.2. In the yield graphs the regeneration tendencies during FBR operation in Phase ② and ④ are also visible. During the experiment, the yield of the PBMRint without flow reversal at $T = 600\,^\circ\mathrm{C}$ (Fig. 5.22 B.2) drops from 15 % to around 9 %, which is comparable to the yields in a PBMR cascade presented in Fig. 5.16. Therefore, the PBMRint does not offer a better performance in terms of yield compared to the PBMR cascade. An effect of the heat integration on the reactor performance cannot be proven with the help of the measurements. Similar results for experiments at $T = 575\,^\circ\mathrm{C}$ and $T = 625\,^\circ\mathrm{C}$ can be found in Appendix C.3, Fig. C.19.

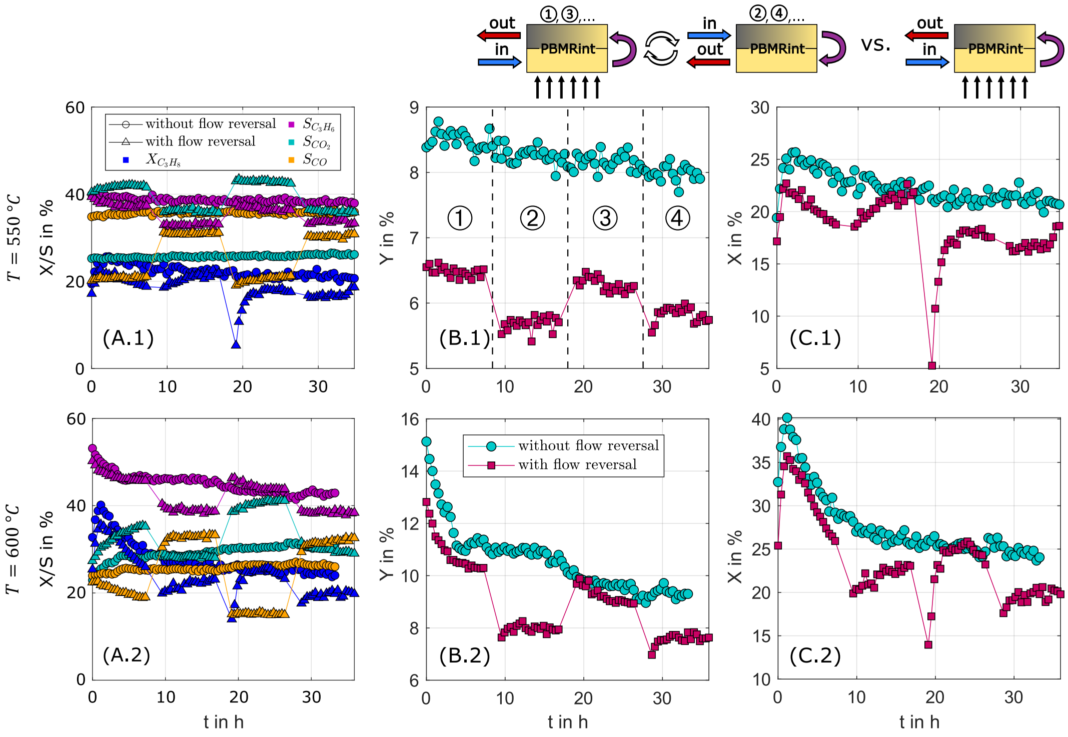

Figure 5.22: Selectivities (A.1, A.2), yield (B.1, B.2) and conversion (C.1, C.2) of the PBMRint at different reactor temperatures with and without periodic flow reversal ($x_{\mathrm{C_3H_8,in}} = 1\,\%$, $x_{\mathrm{O_2,in}} = 0.5\,\%$, $WHSV = 400\,\mathrm{kg\,s\,m^{-3}}$).

The results of experiments with a higher oxygen concentration of 1 % are presented in Fig. 5.23. Comparing the selectivites of the PBMRint at 0.5 % and 1 % reveals that much more side products and less propene is produced at higher oxygen concentrations. This result is in accordance with previous studies of the reactor cascades and 2D simulations (see Section 4.2.3, Fig. 4.11) and confirms that the PBMRint performs best a low oxygen concentrations. Even the greater consistency in yield due to less deactivation at higher oxygen concentrations cannot compensate for the disadvantage of low selectivities.

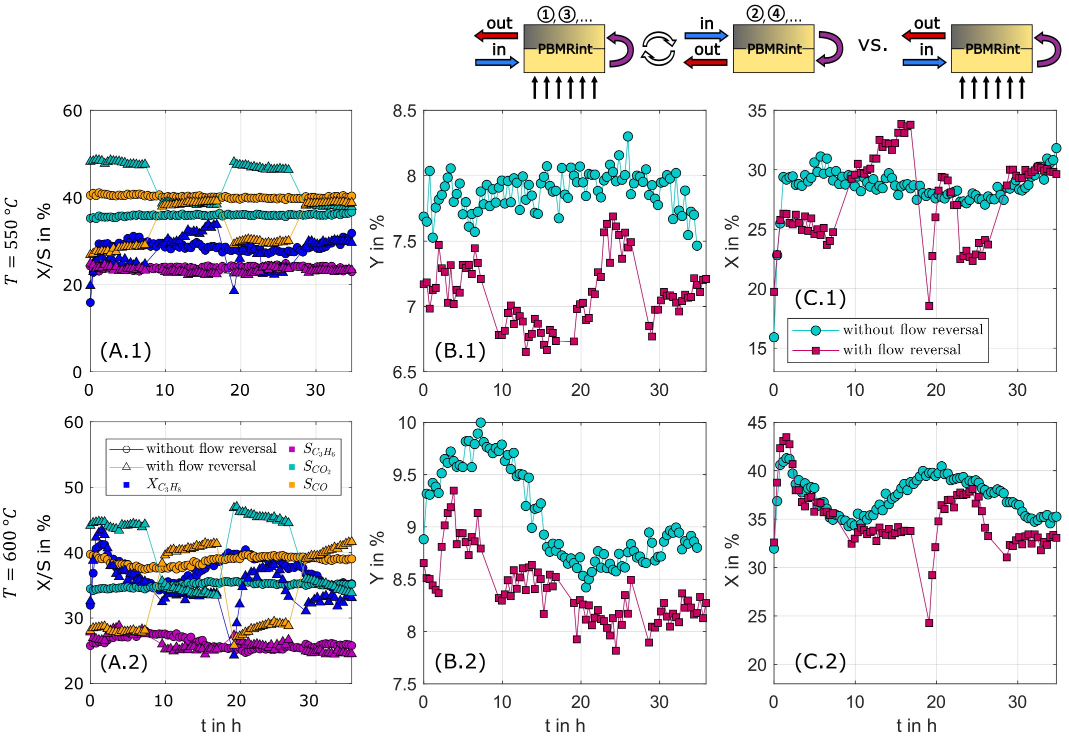

Figure 5.23: Selectivities (A.1, A.2), yield (B.1, B.2) and conversion (C.1, C.2) of the PBMRint at different reactor temperatures with and without periodic flow reversal ($x_{\mathrm{C_3H_8,in}} = 1\,\%$, $x_{\mathrm{O_2,in}} = 1\,\%$, $\mathit{WHSV} = 400\,\mathrm{kg\,s\,m^{-3}}$).

The 2D simulations in Section 4.2 assumed a constant temperature of the reactor walls and the inlet flows as boundary conditions. In the idealized simulations, the heat effect of the reactions influences the temperature in the reactor and leads to specific temperature profiles as shown in Fig. 4.14 and Fig. 4.18. Particularly on a semi-industrial scale, as in the experiments presented here, it can be assumed that the temperatures in the reactor deviate from this ideal behavior. A deviation in the inert zone before and after the catalyst zones is acceptable, since deviating temperatures there have no influence on the reaction and thus on the performance of the reactor. The inert inlet zone at the entrance to the reactor can accordingly be used to heat the reaction gases to the actual reaction temperature. In the reactive catalyst bed, the deviations from the target temperature should then be as small as possible.

In the experiments, the electric heating sleeves of the reactors are controlled by setting the temperature of a specific thermocouple to a certain value. The thermocouple in the annular gap has been chosen for that purpose. A PID controller is then able to hold this temperature by adjusting the temperature of the heating sleeve (see Appendix C.1, Fig. C.3). The temperature of the heating sleeve is usually hotter than the set point temperature due to heat losses to the environment. To minimize heat losses of the setup, the reactor and the piping are insulated with quartz wool as depicted in Fig. 5.3. Nevertheless, temperature loss cannot be avoided.

Since the heat losses cannot be quantified easily and are hard to predict, they have not been considered in the simulations of the PBMRint. The experiments showed that the assumptions of insignificant heat losses did not prove true. This has already been discussed in the previous paragraphs in context of the characterization of the single reactors and the performance of the reactor cascades. However, the deviation from the assumed temperatures in the PBMRint is the strongest.

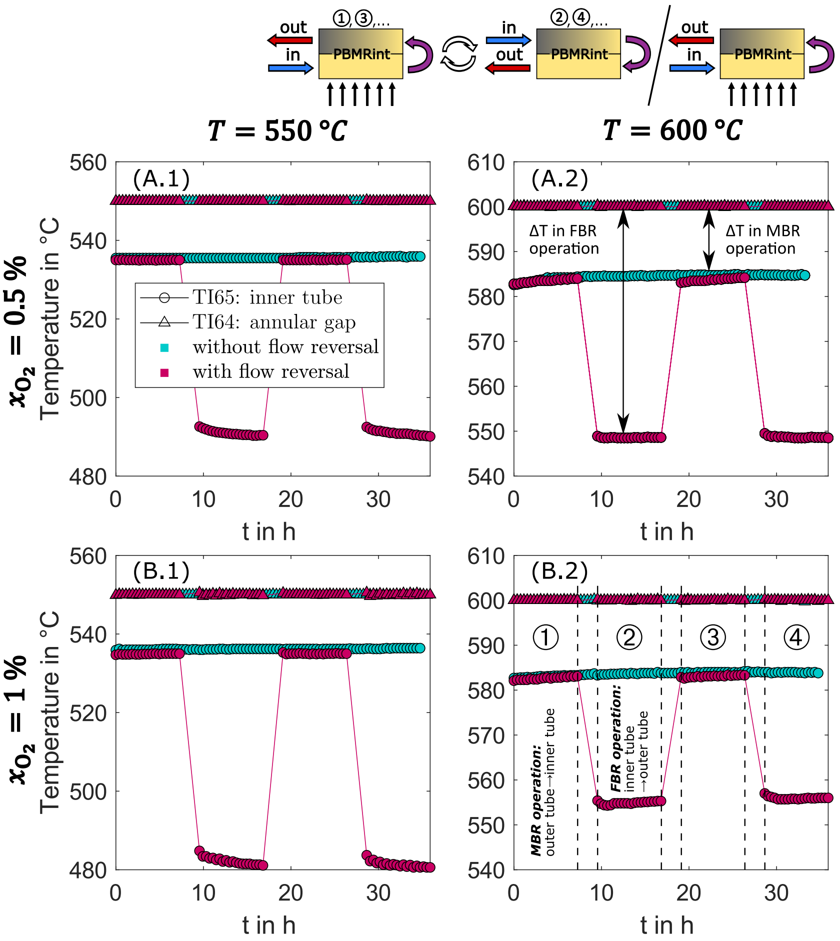

Figure 5.24: Temperature of the catalyst bed in the annular gap (TI65, symbol: △) and the inner tube (TI64, symbol ◯) over time during PBMRint measurements with and without flow reversal at set point temperatures of 550 °C (A.1, B.1) and 600 °C (A.2, B.2) and varying inlet oxygen concentrations of 0.5 % (A.1, A.2) and 1 % (B.1, B.2) ($x_{\mathrm{C_3H_8,in}} = 1\,\%$, $WHSV = 400\,\mathrm{kg\,s\,m^{-3}}$).

Fig. 5.24 shows the differences between the catalyst beds in the inner steel tube and the annular gap for measurements at temperatures of $T = 550\,°\mathrm{C}$ and $T = 600\,°\mathrm{C}$ for the measurements with 0.5 % and 1 % oxygen inlet concentration. The figure illustrates that the set point temperatures are kept constant in the annular gap (Thermocouple TI64) over the course of the entire experiment. For experiments without flow reversal, the temperatures in the inner tube (Thermocouple TI65) are also constant, but significantly lower than in the annular gap. The temperature differences vary between 7.6 °C at measurements with 1 % oxygen at 550 °C and 17.5 °C at measurements with 0.5 % oxygen at 625 °C. This means that the higher temperatures are measured in the annular gap dedicated to the ODH reaction and the lower temperatures are measured in the inner tube where the TDH is supposed to take place. This is in contrast to cascade experiments where the higher temperatures have been set in the TDH reactors to assure higher conversions. These large temperature differences can only be explained by temperature losses in the area of the reactor flange. In this area, the gas flow is redirected from the annular gap into the inner tube. The flanges themselves are not heated but are only insulated and, with their large heat capacity, represent a heat sink through which the heat of the gas flow is dissipated. Thus, the gas stream enters the inner tube with a lower temperature. This observation can likewise be made at 575 °C and 625 °C as shown in Appendix C.3, Fig. C.20. The temperature differences between the catalyst bed in the annular gap and the inner tube are also summarized in Fig. 5.25 for different experimental conditions.

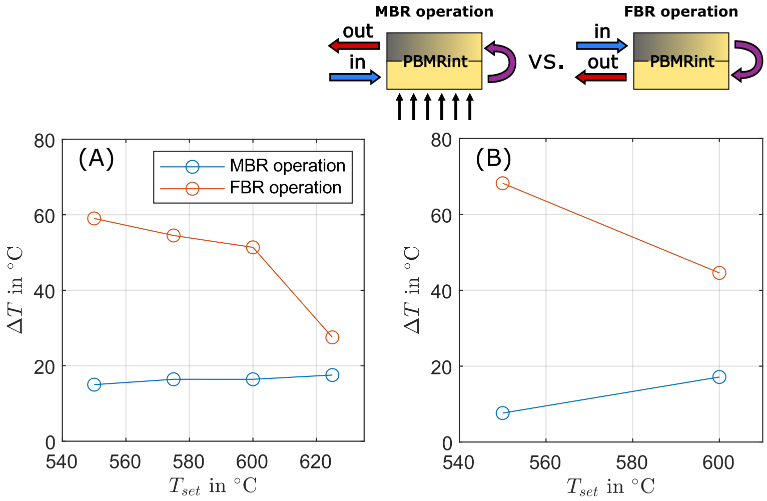

Figure 5.25: Temperature differences between the thermocouples in the catalyst bed in the annular gap and the inner tube for different set point temperatures and an oxygen inlet concentration of (A) 0.5 % and (B) 1 % ($x_{\mathrm{C_3H_8,in}} = 1\,\%$, $WHSV = 400\,\mathrm{kg\,s\,m^{-3}}$).

In periodic operation, the temperature of the catalyst bed in the inner tube drops significantly when switching to FBR operation (Fig. 5.24, Phase ② and ④). Similar to the MBR operation phases, the inner tube still operates at a lower temperature than the annular gap. In opposite to the FBR operation, the inner tube in this phase acts as the TDH reactor whereas the ODH is performed in the annular gap. Due to the flow reversal, the TDH part of the reactor has now a higher temperature than the ODH catalyst bed. Nevertheless, it has to be stated that the big temperature differences between annular gap and inner steel tube was not intended. This temperature difference can be as big as 68 °C in an experiment with 1 % oxygen and at 550 °C. The concept of heat transfer from the ODH catalyst bed to the TDH catalyst bed can therefore not be realized due to the uneven temperature distribution.

All in all, these large temperature differences contribute to the fact that it is not reasonable to compare the measurements at the pilot plant scale with the simulations (see Section 4.2) and the measurements with the reactor cascade.The performance of the PBMRint is comparable to the performance of the reactor cascade, using only one apparatus equipped with one heating sleeve instead of two reactors with separate heating in a row. The weaknesses in the temperature control of the PBMRint could be compensated by a different heating concept. It should be borne in mind that the temperature stability of the materials, especially the seals, must be taken into account.

5.5 Interim Conclusion

The goal of this chapter was to scale up the reaction to the pilot plant scale. In addition to the tubular reactors realized at laboratory scale, it was possible to implement the integrated reactor concepts previously investigated in simulations. There was also the possibility of an automated flow reversal during operation in order to study operando regeneration.

At the beginning of the chapter, the equipment available for this purpose was presented and the different operating modes were introduced (Section 5.1). This was followed by a systematic comparison between the laboratory reactor and the pilot plant reactors (Section 5.2). The pilot reactors were initially characterized as single reactors to ensure comparability between laboratory and pilot reactors. A discrepancy between the two pilot-scale reactors was identified. Careful adjustment of the pipe trace heaters minimized this difference.

Thereon, a cascade of two reactors was investigated (Section 5.3). Both reactors could be operated as fixed bed as well as membrane reactors. A two-stage process consisting of an ODH and a subsequent TDH reactor could be demonstrated. The effects known from simulations and laboratory scale studies could be observed in the reactors. By reversing the flow, an increase in production could be realized for selected operating points. In contrast to the laboratory experiments, the RWGS reaction could be observed in the pilot plant. The use of the membrane for spatially distributed reactant dosing also increased reactor performance. Due to better oxygen distribution, RWGS was suppressed in the membrane reactor.

Finally, the investigation of the PBMRint, which was fully integrated in terms of material and heat, was carried out (Section 5.4). After modifying the setup, deficiencies in the heating system were identified. Due to the heat integration, it is not possible to optimally adjust the temperature of the TDH area. Unexpectedly large heat losses further reduced the comparability with simulations and preliminary investigations.

Overall, all reactor concepts studied and suggested in simulations could be successfully realized. The positive effects of oxygen dosing are clear from the results. The successfully implemented flow reversal had a comparatively small influence on the results of the conducted experiments, but the potential could be illustrated. Weaknesses of the current experimental setup were identified. It became clear that the steel structure represents a comparatively large heat sink. Some of these problems could be avoided in a laboratory-scale membrane reactor, which would be easier to temper. Changing the heating concept of the pilot-scale reactor would be more challenging, as some seals are not approved for the reaction temperatures and the type of seals would have to be changed accordingly.

All experiments conducted in this work dealt with membrane reactors in distributor configuration. The advantages of these membrane reactors have been proven in the previous chapters. As elaborated in Section 2.2.1, it is known from literature that membrane reactors in extractor configuration can offer advantages by extracting hydrogen from the catalyst bed to overcome the chemical equilibrium of the TDH. The next chapter will present the characterization of selective Pd-Ag membranes as well as results of experiments in extraction configuration. From this, conclusions are drawn about the compatibility of the membrane with the catalyst selected in this work.

6 Membrane Reactors in Extractor Configuration

The focus of the previous chapters is clearly on the use of porous non-selective membranes for oxygen dosing. Conversion and yield can benefit from distributed dosing when ODH and TDH reactions are combined in one apparatus. Compared to other membrane materials, the ceramic membranes used in this work are robust, less costly to manufacture and therefore represent an interesting possibility for process intensification, especially against the background of an industrial application. The VO_x catalyst is of particular importance for this application because of its ability to catalyze both TDH and ODH reactions. Besides distributed dosing, today's membrane reactor research also focuses on using selective membranes to remove products and intermediates. Here, Pd-based H_2-selective membranes are of particular interest, as their high H_2 selectivity makes them suitable for a variety of processes (Fernandez, Helmi, Medrano, et al. 2017; Peters et al. 2016; Sheintuch and Nekhamkina 2018; Shelepova and Vedyagin 2020; Ricca et al. 2017).

A collaboration with the group of Prof. Fausto Gallucci at Eindhoven Technical University (TU/e) offered the opportunity to combine state-of-the-art Pd-based membranes with the VO_x catalyst used in previous chapters. The aim was to test the compatibility of catalyst and membrane and to evaluate the possibility of combining them in a reactor. In such a reactor the TDH reaction and simultaneous removal of H_2 to shift the chemical equilibrium of the TDH reaction can be performed. Furthermore, the experimental equipment at TU/e allowed a characterization of the catalyst beyond the parameter range that could be investigated at OVGU.

The first part of this chapter is therefore devoted to the description of the experimental setup (Section 6.1). This experimental setup was first used for a detailed characterization of the applied membrane. Afterwards, reaction tests were carried out without utilizing the membrane in order to obtain information about the reaction behavior at pressures greater than 1 bar (Section 6.2). Based on the results, a first estimation of the compatibility of catalyst and membrane can be made. The results of this assessment were later confirmed by reaction tests with membrane.

6.1 Experimental Setup and Membrane Characterization

The experimental setup used for all experiments presented in this section is illustrated in Fig. 6.1. It consists of a stainless steel reactor in an electrically heated oven. The gas flow is introduced at the bottom of the reactor through a porous metal filter. The gases on the permeate and retentate side can be analyzed by a Micro-GC (Global Analyzer Solutions CompactGC 4.0) or they can be sent directly to the vent. It is possible to by-pass the reactor to verify the composition of the inlet gas stream. The pressure in the reactor is regulated by a back pressure regulator to guarantee a trans-membrane partial pressure difference as a driving force for H_2 transfer from the retentate to the permeate side. Gas composition can be set by mass flow controllers. The mass flow controllers allowed for a maximum volumetric flow of 4 L/min.

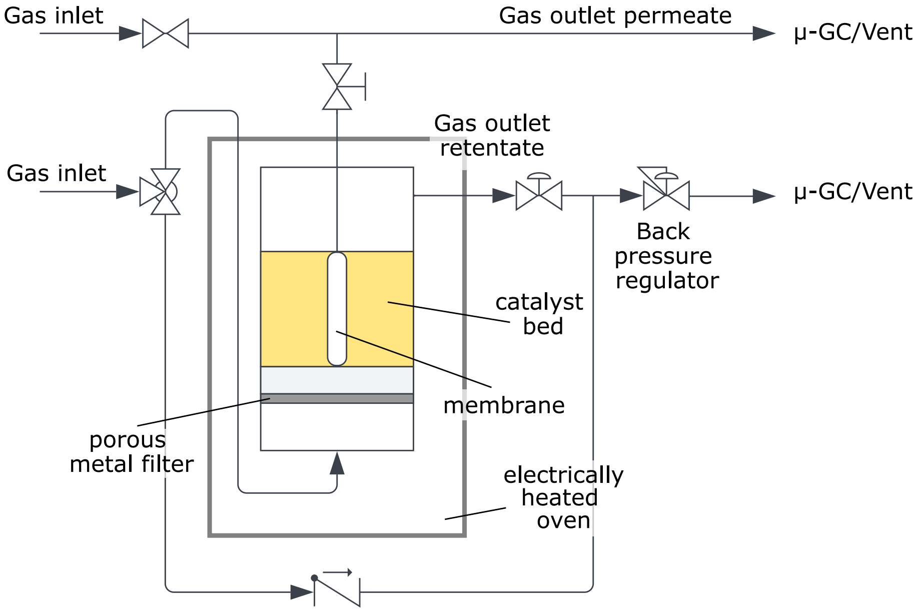

Figure 6.1: Sketch of the experimental setup used for membrane characterization and reaction tests.

Geometrical proportions of the reactor are given in Tab. 6.1.

Table 6.1: Geometric parameters of the experimental setup.

Length of membrane / length of catalyst bed	$L_{bed} = L_{mem} = 0.1\,\mathrm{m}$
Inner diameter of reactor	$D_i = 0.0427\,\mathrm{m}$
External diameter of membrane	$D_{mem} = 0.014\,\mathrm{m}$
Catalyst mass	$m_{cat} = 26.67\,\mathrm{g}$
Maximum volumetric flow of experimental setup	$\dot{V}_{max} = 4\,\mathrm{L/min}$

More detailed information about the setup is given by Brencio et al. (Brencio, Fontein, et al. 2022). The method used to prepare the membrane was described in detail by Arratibel (Arratibel et al. 2018). The membrane used in this study was prepared following the same procedure without the last step of the deposition of a protective ceramic layer. A graphite ferule was used to seal the membrane, as described by Fernandez (Fernandez, Helmi, Coenen, et al. 2015). Before permeation tests, the sealed membrane was tested for leakages by pressurizing with helium and an activation of the membrane inside the reactor was performed in H_2 at testing temperatures. For the membrane characterization experiments, the reactor was empty without a catalyst bed. The characterization tests have been performed with pure hydrogen. The permeate side flow of hydrogen that permeated through the membrane has been measured with a bubble flow meter at different temperatures and pressures. By knowing the geometrical proportions of the membrane a H_2 flux can be calculated. The membrane characterization follows the procedure described by Brencio et al. and a similar Pd-Ag membrane has been used (Brencio, Fontein, et al. 2022). Therefore, the results are expected to be similar. The H_2 flux J_{H_2} through a Pd membrane with a thickness δ of the selective layer can be described by Sievert's law (Helmi 2016), which reads

$$J_{H_2} = \frac{P}{\delta}\left(p^n_{H_2,\mathrm{ret}} - p^n_{H_2,\mathrm{perm}}\right) \tag{6.1}$$

where P describes the permeability coefficient of the membrane. Since the exact thickness of the membrane has not been determined, the permeability coefficient P and the membrane thickness δ are combined to give an effective permeability coefficient $P^{\mathrm{eff}} = \frac{P}{\delta}$. A detail description of the mechanistic steps involved in the hydrogen transfer can be found in literature (Gallucci et al. 2013; Lewis 1967). To model the hydrogen transfer in presence of mixtures, more sophisticated models are necessary to account for other phenomena, e.g., concentration polarization, which are not discussed in this work (Brencio, Fontein, et al. 2022). The temperature dependence can be described by an Arrhenius approach

$$P^{\mathrm{eff}} = P^{\mathrm{eff}}_0 exp\left(-\frac{E^{\mathrm{diss}}_A}{RT}\right) \tag{6.2}$$

From theoretical consideration it is known that the exponent n in Eq. 6.1 is 0.5. A deviation from this ideal exponent in reality indicates further relevant transport resistances in the boundary layer in addition to the dissociation of the H_2 molecules.

A parametrization of this equations has to be performed based on experimental results to determine the membrane characteristics. Details on the parametrization and the objective function are given in Appendix D.1. The optimized values of the model parameters and the optimized value of the objective function are presented in Tab. 6.2.

Table 6.2: Optimized parameters for Sievert's law.

Parameter	Opt. Value	Unit
P^{eff}_0	1.012×10^{-3}	$\mathrm{mol\,s^{-1}\,m^{-2}\,Pa^{-n}}$
E^{diss}_A	17.094	$\mathrm{kJ\,mol^{-1}}$
n	0.712	-
OF	0.999 972 5	-

In comparison with literature data, it is noticeable that the membrane tested within the scope of this work has slightly worse properties with respect to H_2 transport. According to the literature, a permeance of $1.56 \times 10^{-6}\,\mathrm{mol\,m^{-2}\,s^{-1}\,Pa^{-1}}$ was measured for an identical membrane at 500 °C and a pressure difference of 4 bar, whereas the membrane measured for this work only had a permeance of $1.375 \times 10^{-6}\,\mathrm{mol\,m^{-2}\,s^{-1}\,Pa^{-1}}$ under the same conditions. Literature reports an exponent of $n = 0.51$ for identical membranes, which is much closer to the theoretical value of $n = 0.5$ than the $n = 0.712$ determined with the measurements presented in this thesis (Brencio, Fontein, et al. 2022). The tested membrane, even at pressure differences below 1 bar, falls well within the window of reality for the use of membranes in industrial applications as defined by Weisz and depicted in Fig. 2.4 (Weisz 1982). The apparent activation energy is also higher than the directly comparable values in the literature, but is within the range of the common literature values ($5.47\,\mathrm{kJ\,mol^{-1}}$ - $20.48\,\mathrm{kJ\,mol^{-1}}$, Arratibel et al. 2018). The poorer performance of the measured membrane may be due to less careful conditioning of the membrane prior to characterization. A detailed investigation was neither possible nor necessary within the scope of this work.

6.2 Catalyst Characterization at Elevated Pressures and Reaction Tests With Membrane

The driving force for the transport of a substance through a membrane is the partial pressure difference of this substance (see Eq. (6.1)). To realize the pressure difference in a membrane reactor, the reaction on the retentate side of the membrane is carried out at elevated pressures. This contradicts the common practice that thermal dehydrogenation reactions are carried out at low pressures (see Tab. 2.1). The reason for this can be found in Le Chatelier's principle, which states that if the reaction increases the volume, the equilibrium shifts towards the smaller volume, i.e. to the product side. The reaction experiments without membrane were carried out at a total pressure of 1, 2 and 3 bar. The experimental conditions of the reaction experiments with membrane were based on the results of the previous experiments. Overall, an attempt was made to design the reaction conditions similar to those at OVGU. The maximum concentration of propane in the experiments in the laboratory reactor at OVGU was 5 % at $WHSV = 400\,\mathrm{kg\,s\,m^{-3}}$ (see Section 3.1). These low concentrations could not be achieved in the experimental setup at TU/e. The possibility to set the minimum concentrations depends on the smallest reliable settings of the hydrocarbon MFCs and the maximum total flow. For a total flow of 4 L/min, a minimum propane concentration of 11 % is feasible with the existing equipment at TU/e. This value is above the upper explosion limit and therefore represents a safe operating point. For a total flow rate of 4 L/min, the amount of catalyst to be used is 26.66 g. During the membrane tests, it should be ensured that the complete length of the membrane is surrounded by the catalyst bed. To achieve the volume required for this purpose, the catalyst was mixed with inert material of the same particle size. The procedure corresponds to the experiments in the pilot plant (see Section 5). This mixture of catalyst and inert material was used both for reaction experiments with and without membrane.

The results of these experiments are presented in Fig. 6.2 where (A) shows the conversion at an inlet propane concentration of 11 % and $WHSV = 400\,\mathrm{kg\,s\,m^{-3}}$ at different temperatures and pressures. The results indicate that the reaction benefits from elevated pressures and temperatures.

An important prerequisite for integrated reactors is that the operating windows of the various combined functions are compatible with each other. In the case of membrane reactors, this means that the reaction and separation function can be carried out in the same temperature and pressure range and that the selected membrane is compatible with the reaction medium. To avoid damage to the Pd-based membrane, a temperature of 500 °C was set as the maximum. From Fig. 6.2 (A) it can be seen that at this temperature there is only a conversion of about 6 % at a pressure difference of 3 bar. This corresponds to a hydrogen flux of $0.015\,\mathrm{L\,h^{-1}}$. With such small amounts of hydrogen, it can be assumed that no permeate flux can be measured when a membrane is used. To increase the amount of hydrogen in the reaction chamber, the $WHSV$ was increased to $600\,\mathrm{kg\,s\,m^{-3}}$

and $800\,\mathrm{kg\,s\,m^{-3}}$, respectively, in further experiments. This increases the residence time of the gases in the system, which should lead to higher conversions. The hydrocarbon concentration was also increased from 11 to 20 %. This is aimed at increasing the hydrogen flux at the reactor outlet and thus improving the utilization of the membrane. The results of these measurements are shown in Fig. 6.2 (B). A figure corresponding to Fig. 6.2, which shows the hydrogen fluxes at the tested conditions, can be found in Appendix D.2 Fig. D.2. An overview of all performed exeperiments is given in Tab. 6.3.

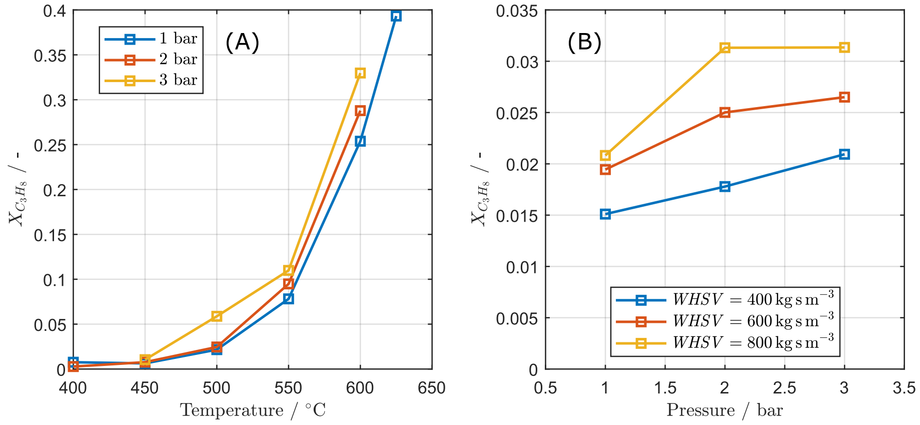

Figure 6.2: Propane conversion without membrane utilization at (A) varying pressure and temperature ($WHSV = 400\,\mathrm{kg\,s\,m^{-3}}$, $x_{\mathrm{C_3H_8,in}} = 11\,\%$) and (B) varying $WHSV$ and pressure ($x_{\mathrm{C_3H_8,in}} = 20\,\%$, $T = 500\,°\mathrm{C}$).

Table 6.3: Experimental matrix of reaction tests without membrane. Numbers indicate WHSV values ($400/600/800\,\mathrm{kg\,s\,m^{-3}}$). Colors indicate different propane inlet concentrations (Red: $x_{\mathrm{C_3H_8,in}} = 11\,\%$, Blue: $x_{\mathrm{C_3H_8,in}} = 20\,\%$).

	Pressure		
Temperature	1 bar	2 bar	3 bar
400 °C	400	400	-
450 °C	400	400	400
500 °C	400	400	400
	400/600/800	400/600/800	400/600/800
550 °C	400	400	400
600 °C	400	400	400
625 °C	400	-	-

Overall, it can be concluded from the measurements that a combination of the membrane available at TU/e with the $\mathrm{VO_x}$ catalyst used in this work does not appear very promising. At the temperatures that can be combined with the membrane, no sufficient conversions are achieved and thus hydrogen fluxes in the reaction space are too low. Nevertheless, reaction experiments were carried out with the membrane. A propane concentration of 20 % at a temperature of 500 °C and $WHSV = 400\,\mathrm{kg\,s\,m^{-3}}$ were chosen as most promising conditions. The same measurement was carried out twice (Exp. 1 and Exp. 2).

The course of these experiments is illustrated in Tab. 6.4. To allow mass transfer through the membrane, the shut-off valve on the permeate side was open during the entire measurement. Analogous to previous measurements, the input composition of the reaction gases was first controlled using a bypass (3 measurements). This was followed by GC measurements of the gas phase composition on the retentate side. After 3 measurements the analysis was switched to the permeate side and again after 3 measurements the retentate side was analyzed. During the retentate side measurements, the permeate flow was measured with a bubble flow meter. In the first experiment, the shut-off valve on the permeate side was closed at the end of the experiment for 5 additional measurements.

Table 6.4: Measuring procedure of the reaction tests including a membrane.

Step		No. Injection	
		Exp. 1	Exp. 2
1	Bypass	3	3
2	Retentate	3	3
3	Permeate	3	3
4	Retentate	6	3
5	Closed permeate side	5	-

In both experiments, it was not possible to detect a trans-membrane gas flow with the bubble flow meter. After shutting off the permeate side, there was no difference between the measured values on the retentate side. This confirms the assumptions from the previous experiments, which did not suggest any influence of the membrane at the tested conditions.

In addition to the GC measurements, further evaluation of the membrane performance during the reaction experiments was attempted. It is known from the literature that adsorption of gases on the surface of the membrane can occur and has an influence on the trans membrane hydrogen flux (Brencio, Gough, et al. 2022). Depending on the type of adsorbed gas, the surface species desorb in a nitrogen atmosphere or have to be removed from the surface oxidatively with the help of oxygen from air. Likewise, it is known that an oxygen-containing atmosphere can damage the membrane. To avoid dismantling the reactor, the catalyst was regenerated in the installed state during the experiments. The conditions for regeneration of the catalyst are sufficient for simultaneous regeneration of the membrane surface. Regeneration conditions of 450 °C and 7.5 % oxygen at a $WHSV$ of $400\,\mathrm{kg\,s\,m^{-3}}$ were chosen. The regeneration temperature is lower than the conditions chosen in the other experiments, but the oxygen concentration is slightly higher (compare Section 3.2.2). The level of oxygen concentration was again limited by the MFCs installed. A regeneration time of 5 min was chosen to be very short in order to protect the membrane.

To ensure that the membrane was in an undamaged state after installation, a measurement of the H_2 permeation was carried out directly after installation of the membrane and the catalyst. The measurements were performed analogously to the characterization measurements described in Section 6.1. The temperature was 500 °C throughout the experiments and the pressure difference was varied between 0.5 bar and 2.5 bar. Similar measurements were made after the regeneration phases. Immediately after the measurements, pressure variation was omitted and membrane flux versus time was recorded at a pressure difference of 2 bar. The results of these measurements are shown in Fig. 6.3.

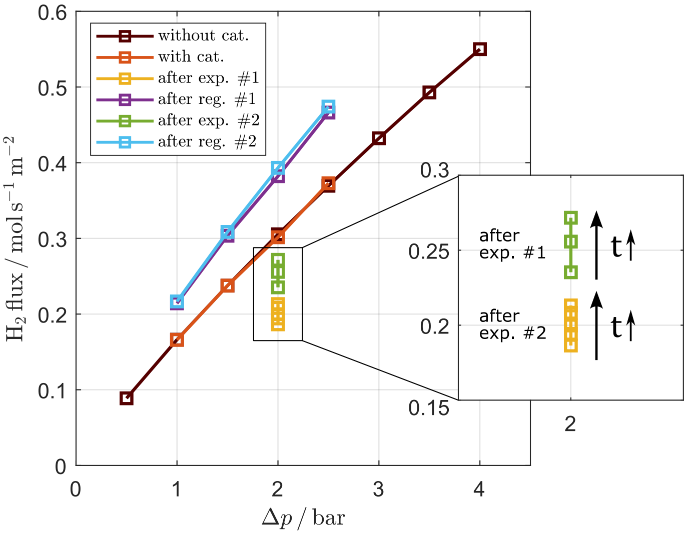

Figure 6.3: Influence of reaction and regeneration on membrane performance.

It is clear that after installation the membrane gave the same results as without catalyst. The higher membrane fluxes after the regeneration phases are striking. These are due either to damage caused by regeneration or to oxidation of residues from the production process. The small difference between the results after regeneration 1 and regeneration 2 points to the latter as one of the reasons. Directly after the reaction tests, it can be observed that the performance of the membrane improves with time. This behavior could also be noticed in literature for membranes of the same type (Brencio, Fontein, et al. 2022). This increase is attributed to the desorption of propane. Whether a complete recovery of the membrane without oxygen is possible was not tested within the scope of this work.

6.3 Interim Conclusion

The scope of this chapter was the systematic evaluation of the possibility of operating a membrane reactor in extractor mode with the VO_x catalyst developed for ODH reactions. For this reason, the properties of the Pd-Ag membrane provided by the TU/e were first systematically characterized. Using the experimental results, a successful parameter estimation was performed to model the transport of hydrogen from the retentate to the permeate side. These results also provided a benchmark against which the performance of the membrane could be assessed after the reaction experiments. Thereafter, the performance of the catalyst was tested at pressure ranges higher than 1 bar. Finally, the influence of the membrane on the reactor performance was experimentally validated.

Based on these results, it was concluded that the catalyst could not be reasonably combined with a Pd-based membrane in a membrane reactor in extractor operation. This is due to insufficient compatibility of membrane transport and reaction kinetics at relevant temperature and residence time. The temperature sensitivity of the membrane, which limits the operation of the reactor to 500 °C, has a particularly limiting effect. For the catalyst, it is known from Chapter 3 that the TDH reaction provides promising conversions not until the temperature exceeds 500 °C. With the catalyst used, it is not possible to achieve conversion rates at which hydrogen removal from the reaction chamber has a noticeably positive effect on reactor performance. The comparatively high sensitivity of the membrane also makes regeneration of the catalyst and membrane in the installed state difficult, since oxygen and excessively high temperatures can damage the membrane. It should be noted that catalysts specialized for TDH have already been developed and successfully combined with the membrane used here. However, these already show sufficient activity at temperatures of 500 °C. The effect of reaction conditions on the membrane performance was illustrated by measurements after reaction tests. Trends from literature have been reproduced.

7 Conclusion and Outlook

> I have yet to see any problem, however complicated, which when you looked at it the right way did not become still more complicated.
>
> POUL ANDERSON

This work evaluated the potential of integrated membrane reactors for the dehydrogenation of propane. To improve propane dehydrogenation, process intensification measures were applied. These included the implementation of membrane-based reactant dosing and heat integration by combining ODH and TDH in new, highly integrated reactor concepts. The project was systematically tackled by conducting lab-scale experiments (Chapter 3) to parametrize mathematical models to enable simulation of the overall process at different levels of detail. After that the process was scaled up from lab to pilot scale (Chapter 4 and Chapter 5). Every step will be summarized shortly in the following paragraphs.

Introduction The first chapter describes the environmental and political framework and illustrates the importance of the topic addressed. Against the background of the challenges posed by the climate crisis and the associated necessary changes towards a more ecological economy, the contribution that process intensification can make is outlined. Attention is drawn to the intended transferability of the methodological approach tested in this work to other processes that will gain importance in the future.

Theoretical Background This chapter presents the theoretical background of the thesis, including the state of the art in propane dehydrogenation and process intensification. Advantages and disadvantages of both ODH and TDH are discussed and a combination has been identified as promising. Current directions of research have been described. The importance of understanding the process in detail became clear. It is necessary to be able to mathematically model all aspects of the reaction system to be able to evaluate the potential of complex reactor systems. All necessary equations and different modeling approaches have been derived.

Experimental Investigation and Parameter Estimation To provide a basis for mathematical modeling, lab scale experiments in different experimental setups have been performed. A tubular reactor was used to study the main and side reactions. Power law kinetics proved to be sufficient for modeling. Coke growth and regeneration has been studied in a TGA setup. Different monolayer-multilayer-coke-growth modeling approaches have been tested systematically to describe coke growth and a power law approach described the regeneration kinetics in a broad range of experimental conditions. Three different approaches were used for modeling the deactivation behavior (phenomenological approach, coke dependent approach, time dependent approach). The models differ in the level of detail and are therefore suitable for different applications. Special emphasis was placed on systematic model discrimination to establish a methodology that can be applied to other processes.

Simulation and Process Optimization The parametrized models have been used in simulations of different complexity to study different aspects of the process. Basic 1D models have been used to evaluate the overall reaction regeneration cycle of a tubular reactor in periodical operation. The potential of rigorous optimization of the overall process was illustrated. Special emphasis was put on the incomplete regeneration as a measure to increase overall space-time yield. In more complex 2D models the benefits of integrated reactor concepts have been proved. The PBMRint setup offers advantages compared to the conventional PBMR and FBR reactors with respect to the developing concentration and temperature fields. Beneficial reaction conditions for scale-up have been identified at low oxygen concentrations. It has been shown that 2D models are necessary to be able to understand the complex temperature and concentration profiles inside integrated reactors with internal refeeding in periodic operation. It was possible to implement the kinetic models successfully to provide a deeper understanding and to identify suitable operation conditions for the experimental validation including scale-up.

Reactor Cascades and Integrated Reactor Concepts in Pilot Scale Based on the experimental results and simulations of the previous chapters a scale-up to pilot scale has been performed. A systematic comparison between laboratory and pilot scale reactors was conducted and adjustments were made to minimize discrepancies. After the validation of the single reactors, a step-by-step approach was used, starting with a less complex reactor cascade. The complexity was systematically increased and the number of degrees of freedom reduced until a fully material- and heat-integrated PBMRint was experimentally evaluated.

In a cascade of two reactors, the effects observed aligned with those known from simulations and laboratory-scale studies. Flow reversal and membrane reactant dosing increased reactor performance. The investigation of the fully integrated PBMRint revealed deficiencies in the heating system and heat losses impacting the comparability with simulations. A better performance of integrated reactor concepts has been shown under certain conditions. Overall, the reactor concepts proposed in simulations were successfully realized. Difficulties in the complex experimental setup have been identified.

Membrane Reactors in Extractor Configuration In addition to the focus on membrane distributors, membrane reactors in extractor operation were also investigated in cooperation with TU/e. Properties of the Pd-Ag membrane were characterized, enabling successful parameter estimation for hydrogen transport modeling. The catalyst was tested under conditions that are typical for the operation of a membrane reactor in extraction mode. Based on the findings, it was concluded that combining the VO_x catalyst with a Pd-Ag membrane in an extractor-mode membrane reactor is not feasible. Incompatibility between membrane transport and reaction kinetics at relevant temperature and residence time, especially the temperature sensitivity of the membrane posed limitations. Measurements after reaction tests confirmed the influence of reaction conditions on membrane performance, consistent with trends from the literature. The results illustrate the challenge of catalyst-membrane compatibility and the need for research on a compatible catalyst.

7.1 Outlook

During the work on this thesis, different research needs became apparent at every level of investigation, which are beyond the scope of this project but could serve as starting points for future analyses. The investigation of phenomena with short time constants could be considered in more detail in future studies. To gain more comprehensive insights, measurement techniques with higher temporal and spatial resolution could be employed. Such methods would greatly enhance the information obtained from individual experiments and facilitate more precise modeling of these rapid phenomena. It is worth mentioning the use of fiber-optic temperature measurement methods (Froggatt and Moore 1998; Kreger et al. 2006) which have proven valuable in estimating kinetic parameters (Bremer 2020).

The implementation of microkinetics in 2D models is still a major challenge, as illustrated in this thesis. Often, simplifications are employed. The approach of a multi-scale modeling is subject of current research and would be interesting especially against the light of the knowledge gained in this work (Wehinger et al. 2022).

During scale-up, the particular challenges of pilot tests became clear, especially with regard to the temperature control of the apparatus, which could be remedied by other heating concepts. With regard to the investigations with membrane extractors, the question arises whether a combination of extraction and distribution membranes in one apparatus represents a possibility for further reactor concepts. A two-stage process should be considered. To be able to realize such a concept, closer attention has to be payed to the development of a suitable catalyst (Grant et al. 2018).

7.2 Concluding Remarks

The methodology developed in this work, along with the established reactor setups, hold the potential for future application in other reaction systems relevant to energy transition and circular economy.

As membranes continue to evolve for use in membrane reactors, it is likely that they will become increasingly interesting for industrial application in the future. The evolution of membranes over the last 20 years is well illustrated by a comparison of Fig. 2.4 with the analogous figure published by van de Graaf (van de Graaf et al. 1999). Thus, currently used and developed membranes are increasingly meeting the requirements at the process level.

Catalyst deactivation will remain a challenge in future processes based on biological raw materials (Lange 2015; He et al. 2022; Alaba et al. 2016) or on recycled feedstocks (Daligaux et al. 2021; López et al. 2011; S. Dong et al. 2023). The methodology described in this work for the systematic modeling and evaluation of these processes can therefore contribute to their improvement and help to lead the chemical industry to more sustainability and a more efficient use of resources.

This work shows that the interplay of theory, experiments and simulations as the pillars of science are strong, interdependent tools to investigate complex reaction networks and reactor setups. Possible benefits of process intensification can only be exploited by using all these tools together.

Bibliography

Adler, R. (2000a). “Stand der Simulation von heterogen–gaskatalytischen Reaktionsabläufen in Festbettrohrreaktoren — Teil 1”. In: *Chemie Ingenieur Technik* 72.6, pp. 555–564.

— (2000b). “Stand der Simulation von heterogen-gaskatalytischen Reaktionsabläufen in Festbettrohrreaktoren — Teil 2”. In: *Chemie Ingenieur Technik* 72.7, pp. 688–699.

Agar, D. W. (1999). “Multifunctional reactors. Old preconceptions and new dimensions”. In: *Chemical Engineering Science* 54.10, pp. 1299–1305.

Agar, D. W. and W. Ruppel (1988). “Multifunktionale Reaktoren für die heterogene Katalyse”. In: *Chemie Ingenieur Technik* 60.10, pp. 731–741.

Aguayo, A. T., A. G. Gayubo, J. Ereña, et al. (2003). “Coke Aging and Its Incidence on Catalyst Regeneration”. In: *Industrial & Engineering Chemistry Research* 42.17, pp. 3914–3921.

Aguayo, A. T., A. G. Gayubo, A. Atutxa, et al. (1999). “Regeneration of a catalyst based on a SAPO-34 used in the transformation of methanol into olefins”. In: *Journal of Chemical Technology & Biotechnology* 74.11, pp. 1082–1088.

AIChE (1995). *Guidelines for chemical reactivity evaluation and application to process design*. New York, NY: Center for Chemical Process Safety of the American Institute of Chemical Engineers. 210 pp.

Akaike, H. (1978). “A Bayesian analysis of the minimum AIC procedure”. Annals of the Institute of Statistical Mathematics, 30(1), 9-14. In.

Alaba, P. A. et al. (2016). “Insight into catalyst deactivation mechanism and suppression techniques in thermocatalytic deoxygenation of bio-oil over zeolites”. In: *Reviews in Chemical Engineering* 32.1.

Amghizar, I. et al. (2017). “New Trends in Olefin Production”. In: *Engineering* 3.2, pp. 171–178.

Anastas, P. and N. Eghbali (2010). “Green chemistry: principles and practice”. In: *Chemical Society Reviews* 39.1, pp. 301–312.

Ansari, M. B. and S.-E. Park (2012). “Carbon dioxide utilization as a soft oxidant and promoter in catalysis”. In: *Energy & Environmental Science* 5.11, p. 9419.

Arbabi, S. and M. Sahimi (1991a). “Computer simulations of catalyst deactivation—I. Model formulation and validation”. In: *Chemical Engineering Science* 46.7, pp. 1739–1747.

— (1991b). “Computer simulations of catalyst deactivation—II. The effect of morphological, transport and kinetic parameters on the performance of the catalyst”. In: *Chemical Engineering Science* 46.7, pp. 1749–1755.

Argyle, M. and C. Bartholomew (2015). “Heterogeneous Catalyst Deactivation and Regeneration. A Review”. In: *Catalysts* 5.1, pp. 145–269.

Arratibel, A. et al. (2018). “Development of Pd-based double-skinned membranes for hydrogen production in fluidized bed membrane reactors”. In: *Journal of Membrane Science* 550, pp. 536–544.

Arrhenius, S. (1889a). “Über die Dissociationswärme und den Einfluss der Temperatur auf den Dissociationsgrad der Elektrolyte”. In: *Zeitschrift für Physikalische Chemie* 4U.1, pp. 96–116.

— (1889b). “Über die Reaktionsgeschwindigkeit bei der Inversion von Rohrzucker durch Säuren”. In: *Zeitschrift für Physikalische Chemie* 4U.1, pp. 226–248.

Atanga, M. A. et al. (2018). “Oxidative dehydrogenation of propane to propylene with carbon dioxide”. In: *Applied Catalysis B: Environmental* 220, pp. 429–445.

Baerns, M. (2013). *Technische Chemie.* 2., erw. Aufl. Weinheim: Wiley-VCH. XXVI, 736 S.

Barghi, B., M. Fattahi, and F. Khorasheh (2014). “The Modeling of Kinetics and Catalyst Deactivation in Propane Dehydrogenation Over Pt-Sn/Al 2 O 3 in Presence of Water as an Oxygenated Additive”. In: *Petroleum Science and Technology* 32.10, pp. 1139–1149.

BASF SE, ed. (July 15, 2020). *thyssenkrupp and BASF sign joint development agreement on STAR process® dehydrogenation technology.* Ludwigshafen.

BASF SE and SABIC, Linde, eds. (Sept. 1, 2022). *BASF, SABIC and Linde start construction of the world’s first demonstration plant for large-scale electrically heated steam cracker furnaces.* Ludwigshafen.

BASF SE and thyssenkrupp Industrial Solutions AG, eds. (Apr. 26, 2022). *BASF and thyssenkrupp Uhde optimize STAR process®dehydrogenation technology and demonstrate significant sustainability benefits.* Dortmund and Ludwigshafen.

Beer, M. M. de et al. (2015). “Intensification of convective heat transfer in a stator-rotor-stator spinning disc reactor”. In: *AIChE Journal* 61.7, pp. 2307–2318.

Bey, O. and G. Eigenberger (1997). “Fluid flow through catalyst filled tubes”. In: *Chemical Engineering Science* 52.8, pp. 1365–1376.

Bhasin, M. et al. (2001). “Dehydrogenation and oxydehydrogenation of paraffins to olefins”. In: *Applied Catalysis A: General* 221.1-2, pp. 397–419.

Bird, R. B., W. E. Stewart, and E. N. Lightfoot (2007). *Transport phenomena.* Revised second edition. New York et al.: John Wiley & Sons Inc. 905 pp.

Blanks, R. F., T. S. Wittrig, and D. A. Peterson (1990). “Bidirectional adiabatic synthesis gas generator”. In: *Chemical Engineering Science* 45.8, pp. 2407–2413.

Böckh, P. and T. Wetzel (2015). *Wärmeübertragung. Grundlagen und Praxis.* 6. Aufl. 2015. Berlin, Heidelberg: Springer Berlin Heidelberg. 337 pp.

Boreskov, G. K. and Y. S. Matros (1983). “Unsteady-State Performance of Heterogeneous Catalytic Reactions”. In: *Catalysis Reviews* 25.4, pp. 551–590.

Bortolotto, L. and R. Dittmeyer (2010). “Direct hydroxylation of benzene to phenol in a novel microstructured membrane reactor with distributed dosing of hydrogen and oxygen”. In: *Separation and Purification Technology* 73.1, pp. 51–58.

Bottino, A., G. Capannelli, and A. Comite (2002). “Catalytic membrane reactors for the oxidehydrogenation of propane. Experimental and modelling study”. In: *Journal of Membrane Science* 197.1-2, pp. 75–88.

Bottino, A., G. Capannelli, A. Comite, et al. (2003). “Kinetic investigations on the oxidehydrogenation of propane over vanadium supported on γ-Al2O3”. In: *Chemical Engineering Journal* 94.1, pp. 11–18.

Boudart, M. (1997). “Surface Time Yield of Membrane Reactors”. In: *Cattech* 2, p. 94.

Box, G. E. P. (1976). “Science and Statistics”. In: *Journal of the American Statistical Association* 71.356, pp. 791–799.

— (1979). “Robustness in the Strategy of Scientific Model Building”. In: *Robustness in statistics. Proceedings of a workshop, held at Army Research Office, Weiss Building,* *April 11 - 12, 1978*. Ed. by R. L. Launer. Academic Press rapid manuscript reproduction. New York: Academic Press, pp. 201–236.

Bremer, J. (2020). *Advanced operating strategies for non-isothermal fixed-bed reactors exemplified for CO 2 methanation.* In collab. with Universitäts- Und Landesbibliothek Sachsen-Anhalt et al. Universitäts- und Landesbibliothek Sachsen-Anhalt.

Brencio, C., F. Fontein, et al. (2022). "Pd-based membranes performance under hydrocarbon exposure for propane dehydrogenation processes: Experimental and modeling". In: *International Journal of Hydrogen Energy* 47.21, pp. 11369–11384.

Brencio, C., R. Gough, et al. (2022). "Kinetic model for Pd-based membranes coking/deactivation in propane dehydrogenation processes". In: *Chemical Engineering Journal*, p. 139125.

Brinkman, H. C. (1949). "A calculation of the viscous force exerted by a flowing fluid on a dense swarm of particles". In: *Flow, Turbulence and Combustion* 1.1.

Brune, A., A. Geschke, et al. (2021). "Modeling and Simulation of Catalyst Deactivation and Regeneration Cycles for Propane Dehydrogenation - Comparison of Different Modeling Approaches". In: *Chemical Engineering and Processing: Process Intensification*, p. 108689.

Brune, A., A. Seidel-Morgenstern, and C. Hamel (2020). "Analysis and Model-Based Description of the Total Process of Periodic Deactivation and Regeneration of a VOx Catalyst for Selective Dehydrogenation of Propane". In: *Catalysts* 10.12, p. 1374.

Brune, A., T. Wolff, et al. (2019). "Analysis of Membrane Reactors for Integrated Coupling of Oxidative and Thermal Dehydrogenation of Propane". In: *Chemie Ingenieur Technik* 56.2, p. 251.

Bundesministerium für Umwelt, Naturschutz, Bau und Reaktorsicherheit, ed. (2016). *Klimaschutzplan 2050. Klimaschutzpolitische Grundsätze und Ziele der Bundesregierung.* Version 1. Berlin: Bundesministerium für Umwelt, Naturschutz, Bau und Reaktorsicherheit.

Bunimovich, G. and H. Sapoundjiev (2013). "Periodic Flow Reversal". In: *Periodic Operation of Chemical Reactors*. Elsevier, pp. 495–542.

Burnham, K. P. and D. R. Anderson (2004). *Model Selection and Multimodel Inference.* New York, NY: Springer New York.

Carberry, J. J. (2001). *Chemical and catalytic reaction engineering.* Dover ed., (slightly corr.) Mineola, NY: Dover Publications. 642 pp.

Caro, J. (2016a). "Contactor-Type Catalytic Membrane Reactor". In: *Encyclopedia of Membranes*. Ed. by E. Drioli and L. Giorno. Vol. 49. Berlin, Heidelberg and s.l.: Springer Berlin Heidelberg, pp. 445–446.

— (2016b). "Membrane Distributor". In: *Encyclopedia of Membranes*. Ed. by E. Drioli and L. Giorno. Living Reference Work. Berlin and Heidelberg: Springer Berlin Heidelberg, pp. 1–2.

Caro, J. et al. (2007). "Catalytic Membrane Reactors for Partial Oxidation Using Perovskite Hollow Fiber Membranes and for Partial Hydrogenation Using a Catalytic Membrane Contactor". In: *Industrial & Engineering Chemistry Research* 46.8, pp. 2286–2294.

Carpenter, J. and J. Bithell (2000). "Bootstrap confidence intervals: when, which, what? A practical guide for medical statisticians". In: *Statistics in Medicine* 19.9, pp. 1141–1164.

Carrero, C. A. et al. (2014). "Critical Literature Review of the Kinetics for the Oxidative Dehydrogenation of Propane over Well-Defined Supported Vanadium Oxide Catalysts". In: *ACS Catalysis* 4.10, pp. 3357–3380.

Cavani, F., N. Ballarini, and A. Cericola (2007). “Oxidative dehydrogenation of ethane and propane. How far from commercial implementation?” In: *Catalysis Today* 127.1-4, pp. 113–131.

Chandrasekhara, B. C. and D. Vortmeyer (1979). “Flow model for velocity distribution in fixed porous beds under isothermal conditions”. In: *Wärme- und Stoffübertragung* 12.2, pp. 105–111.

Chaudhuri, A. et al. (2022). “Transesterification of Triglycerides in a Rotor–Stator Spinning Disc Reactor: Scale-Up and Solid Handling”. In: *Industrial & Engineering Chemistry Research* 61.20, pp. 6831–6844.

Chen, K., A. T. Bell, and E. Iglesia (2000). “Kinetics and Mechanism of Oxidative Dehydrogenation of Propane on Vanadium, Molybdenum, and Tungsten Oxides”. In: *The Journal of Physical Chemistry B* 104.6, pp. 1292–1299.

Chen, S. et al. (2021). “Propane dehydrogenation: catalyst development, new chemistry, and emerging technologies”. In: *Chemical Society Reviews* 50.5, pp. 3315–3354.

Chen, X. et al. (2017). “Characteristics and applications of plasma assisted chemical processes and reactors”. In: *Current Opinion in Chemical Engineering* 17, pp. 68–77.

Chernick, M. R. (2008). *Bootstrap methods. A guide for practitioners and researchers.* 2. ed. Wiley series in probability and statistics. Hoboken, NJ: Wiley-Interscience.

Cottrell, F. G. (1938). “Purifying gases and apparatus therefor”. US2121733A (US).

Daligaux, V., R. Richard, and M.-H. Manero (2021). “Deactivation and Regeneration of Zeolite Catalysts Used in Pyrolysis of Plastic Wastes—A Process and Analytical Review”. In: *Catalysts* 11.7, p. 770.

Danckwerts, P. V. (1953). “Continuous flow systems: Distribution of residence times”. In: *Chemical Engineering Science* 2.1, pp. 1–13.

Dautzenberg, F. M. and M. Mukherjee (2001). “Process intensification using multifunctional reactors”. In: *Chemical Engineering Science* 56.2, pp. 251–267.

Deans, H. A. and L. Lapidus (1960a). “A computational model for predicting and correlating the behavior of fixed-bed reactors: I. Derivation of model for nonreactive systems”. In: *AIChE Journal* 6.4, pp. 656–663.

— (1960b). “A computational model for predicting and correlating the behavior of fixed-bed reactors: II. Extension to chemically reactive systems”. In: *AIChE Journal* 6.4, pp. 663–668.

Dejanović, I., L. Matijašević, and Ž. Olujić (2010). “Dividing wall column—A breakthrough towards sustainable distilling”. In: *Chemical Engineering and Processing: Process Intensification* 49.6, pp. 559–580.

Deuflhard, P. and M. Weiser (2020). *Adaptive Lösung partieller Differentialgleichungen.* 2., korrigierte und ergänzte Auflage. Vol. 3. De Gruyter Studium. Berlin and Boston: De Gruyter. 456 pp.

Deutscher Bundestag (Dec. 12, 2019). *Gesetz zur Einführung eines Bundes-Klimaschutzgesetzes und zur Änderung weiterer Vorschriften.* KSG.

— (Aug. 18, 2021). *Erstes Gesetz zur Änderung des Bundes-Klimaschutzgesetzes.*

DiCiccio, T. J. et al. (1996). “Bootstrap confidence intervals”. In: *Statistical Science* 11.3, pp. 189–228.

Dinse, A. et al. (2009). “Oxidative dehydrogenation of propane on silica (SBA-15) supported vanadia catalysts: A kinetic investigation”. In: *Journal of Molecular Catalysis A: Chemical* 307.1-2, pp. 43–50.

Dittmeyer, R. and J. Caro (2008). “Catalytic Membrane Reactors”. In: *Handbook of Heterogeneous Catalysis.* Ed. by G. Ertl et al. Vol. 10. Weinheim, Germany: Wiley-VCH Verlag GmbH & Co. KGaA, pp. 2198–2248.

Dixon, A. G., M. Nijemeisland, and E. H. Stitt (2006). “Packed Tubular Reactor Modeling and Catalyst Design using Computational Fluid Dynamics”. In: *Computational fluid dynamics*. Ed. by G. B. Marin. 1. ed. Vol. 31. Advances in chemical engineering 31. Amsterdam: Elsevier/Acad. Press, pp. 307–389.

Dong, S. et al. (2023). “Catalytic conversion of model compounds of plastic pyrolysis oil over ZSM-5”. In: *Applied Catalysis B: Environmental* 324, p. 122219.

Dong, Y. et al. (2018). “What happens in a catalytic fixed-bed reactor for n-butane oxidation to maleic anhydride? Insights from spatial profile measurements and particle resolved CFD simulations”. In: *Chemical Engineering Journal* 350.17–18, pp. 799–811.

Drioli, E., ed. (2010). *Comprehensive membrane science and engineering*. Amsterdam: Elsevier.

Drioli, E. and L. Giorno, eds. (2016). *Encyclopedia of Membranes*. Berlin, Heidelberg and s.l.: Springer Berlin Heidelberg. 464 pp.

Dumez, F. J. and G. F. Froment (1976). “Dehydrogenation of 1-Butene into Butadiene. Kinetics, Catalyst Coking, and Reactor Design”. In: *Industrial & Engineering Chemistry Process Design and Development* 15.2, pp. 291–301.

Efron, B. and R. Tibshirani (1998). *An introduction to the bootstrap*. Vol. 57. Monographs on statistics and applied probability. Boca Raton, Fla.: Chapman & Hall. 436 pp.

Eigenberger, G., G. Kolios, and U. Nieken (2007). “Thermal pattern formation and process intensification in chemical reaction engineering”. In: *Chemical Engineering Science* 62.18-20, pp. 4825–4841.

Eley, D. D. and E. K. Rideal (1941). “The catalysis of the parahydrogen conversion by tungsten”. In: *Proceedings of the Royal Society of London. Series A. Mathematical and Physical Sciences* 178.975, pp. 429–451.

Ellwood, T. et al. (2021). “Process Intensification in Photocatalytic Decomposition of Formic Acid over a TiO2 Catalyst by Forced Periodic Modulation of Concentration, Temperature, Flowrate and Light Intensity”. In: *Processes* 9.11, p. 2046.

Elnashaie, S. S. E. H. (1994). *Modelling, Simulation and Optimization of Industrial Fixed Bed Catalytic Reactors*. Milton: CRC Press LLC. 510 pp.

Ene, H. I. (2004). “Modeling the Flow Through Porous Media”. In: *Emerging Technologies and Techniques in Porous Media*. Ed. by D. B. Ingham et al. Vol. 21. Springer eBook Collection 134. Dordrecht: Springer, pp. 25–41.

Estel, L. et al. (2017). “Continuous flow-microwave reactor: Where are we?” In: *Chemical Engineering and Processing: Process Intensification* 113, pp. 56–64.

European Commission, ed. (2019). *The European Green Deal. Communication from the commission to the european parliament, the european council, the council, the european economic and social committee and the committee of the regions*. Brussels.

— ed. (2020). *A new Circular Economy Action Plan For a cleaner and more competitive Europe*. Brussels.

European Parliament and Council (July 9, 2021). *Regulation (EU) 2021/1119 of the European Parliament and of the Council of 30 June 2021 establishing the framework for achieving climate neutrality and amending Regulations (EC) No 401/2009 and (EU) 2018/1999 (‘European Climate Law’)*.

Felischak, M. et al. (2021). “Analysis and experimental demonstration of forced periodic operation of an adiabatic stirred tank reactor: Simultaneous modulation of inlet concentration and total flow-rate”. In: *Chemical Engineering Journal* 410, p. 128197.

Fernandez, E., A. Helmi, J. A. Medrano, et al. (2017). “Palladium based membranes and membrane reactors for hydrogen production and purification: An overview of research activities at Tecnalia and TU/e". In: *International Journal of Hydrogen Energy* 42.19, pp. 13763–13776.

Fernandez, E., A. Helmi, K. Coenen, et al. (2015). "Development of thin Pd–Ag supported membranes for fluidized bed membrane reactors including WGS related gases". In: *International Journal of Hydrogen Energy* 40.8, pp. 3506–3519.

Froggatt, M. and J. Moore (1998). "High-spatial-resolution distributed strain measurement in optical fiber with rayleigh scatter". In: *Applied optics* 37.10, pp. 1735–1740.

Froment, G. F. and K. B. Bischoff (1961). "Non-steady state behaviour of fixed bed catalytic reactors due to catalyst fouling". In: *Chemical Engineering Science* 16.3-4, pp. 189–201.

Froment, G. F., K. B. Bischoff, and J. de Wilde (2011). *Chemical reactor analysis and design*. 3. ed. Hoboken, NJ: Wiley. 860 pp.

Gallucci, F. et al. (2013). "Recent advances on membranes and membrane reactors for hydrogen production". In: *Chemical Engineering Science* 92, pp. 40–66.

Gascón, J. et al. (2003). "Propane dehydrogenation over a Cr2O3/Al2O3 catalyst. Transient kinetic modeling of propene and coke formation". In: *Applied Catalysis A: General* 248.1-2, pp. 105–116.

Gentle, J. E. (2009). *Computational Statistics*.

Geres, R. et al. (2019). *Roadmap Chemie 2050. Auf dem Weg zu einer treibhausgasneutralen chemischen Industrie in Deutschland : eine Studie von DECHEMA und FutureCamp für den VCI*. Frankfurt am Main: DECHEMA Gesellschaft für Chemische Technik und Biotechnologie e.V. 96 pp.

German Federal Government, ed. (2021). *German Sustainable Development Strategy. Update 2021*. German Federal Government.

Goldsmith, E. and R. Allen (1972). *A Blueprint for survival*. A Penguin special. Harmondsworth: Penguin. 139 pp.

Gomez, E. et al. (2018). "Combining CO2 reduction with propane oxidative dehydrogenation over bimetallic catalysts". In: *Nature communications* 9.1, p. 1398.

Grabowski, R. (2006). "Kinetics of Oxidative Dehydrogenation of C2 –C3 Alkanes on Oxide Catalysts". In: *Catalysis Reviews* 48.2, pp. 199–268.

Grant, J. T. et al. (2018). "Aerobic Oxidations of Light Alkanes over Solid Metal Oxide Catalysts". In: *Chemical reviews* 118.5, pp. 2769–2815.

Gryaznov, V. M. et al. (1977). "Catalytic-Reactor for Carrying out Conjugate Chemical Reactions". US 4014657 A (USA).

Guettel, R. and T. Turek (2010). "Assessment of micro-structured fixed-bed reactors for highly exothermic gas-phase reactions". In: *Chemical Engineering Science* 65.5, pp. 1644–1654.

Haase, S., P. Tolvanen, and V. Russo (2022). "Process Intensification in Chemical Reaction Engineering". In: *Processes* 10.1, p. 99.

Hamel, C., Á. Tóta, et al. (2008). "Analysis of single and multi-stage membrane reactors for the oxidation of short-chain alkanes—Simulation study and pilot scale experiments". In: *Chemical Engineering Research and Design* 86.7, pp. 753–764.

Hamel, C., Á. Tóta, et al. (2010). "Packed-Bed Membrane Reactors". In: *Membrane reactors. Distributing reactants to improve selectivity and yield*. Ed. by A. Seidel-Morgenstern. Weinheim: Wiley-VCH Verlag GmbH & Co, pp. 133–165.

Hamel, C., T. Wolff, and A. Seidel-Morgenstern (2011). "Compatibility of Transport and Reaction in Membrane Reactors Used for the Oxidative Dehydrogenation of Short-Chain Hydrocarbons". In: *International Journal of Chemical Reactor Engineering* 9.1.

Hamel, C., T. Wolff, P. Subramaniam, et al. (2011). “Multicomponent Dosing in Membrane Reactors Including Recycling—Concept and Demonstration for the Oxidative Dehydrogenation of Propane”. In: *Industrial & Engineering Chemistry Research* 50.23, pp. 12895–12903.

He, S. et al. (2022). “A time- and space-resolved catalyst deactivation study on the conversion of glycerol to aromatics using H-ZSM-5”. In: *Chemical Engineering Journal* 434, p. 134620.

Helfferich, F. G., ed. (2004). *Kinetics of multistep reactions.* 2nd ed. Vol. v. 40. Comprehensive chemical kinetics. Amsterdam and Boston: Elsevier. 488 pp.

Helmi, A. (2016). “Sieverts’ Law”. In: *Encyclopedia of Membranes.* Ed. by E. Drioli and L. Giorno. Berlin, Heidelberg: Springer Berlin Heidelberg, pp. 1770–1771.

Hertwig, K., L. Martens, and C. Hamel (2018). *Chemische Verfahrenstechnik. Berechnung, Auslegung und Betrieb Chemischer Reaktoren.* In collab. with L. Martens and C. Hamel. 3rd ed. De Gruyter Studium Ser. Berlin/München/Boston: De Gruyter and De Gruyter Inc. 650 pp.

Hinshelwood, C. N. (1929). *The kinetics of chemical change in gaseous systems.* 2nd ed. Oxford: Clarendon Press.

Hirschberg, H. G. (1999). *Handbuch Verfahrenstechnik und Anlagenbau. Chemie, Technik, Wirtschaftlichkeit.* Springer eBook Collection. Berlin, Heidelberg: Springer Berlin Heidelberg.

Hou, K. and R. Hughes (2001). “The kinetics of methane steam reforming over a Ni/alpha-Al2O catalyst”. In: *Chemical Engineering Journal* 82.1-3, pp. 311–328.

Iordanidis, A. A. (2002). *Mathematical modeling of catalytic fixed bed reactors.* Enschede: Twente University Press. 195 pp.

Janssens, T. V. (2009). “A new approach to the modeling of deactivation in the conversion of methanol on zeolite catalysts”. In: *Journal of Catalysis* 264.2, pp. 130–137.

Janssens, T. V., S. Svelle, and U. Olsbye (2013). “Kinetic modeling of deactivation profiles in the methanol-to-hydrocarbons (MTH) reaction: A combined autocatalytic–hydrocarbon pool approach”. In: *Journal of Catalysis* 308, pp. 122–130.

Jiang, B. et al. (2017). “Kinetic and regenerator modeling of the coke combustion in the moving bed MTP process”. In: *Chemical Engineering Research and Design* 122, pp. 52–62.

Johnson, J. B. and K. S. Omland (2004). “Model selection in ecology and evolution”. In: *Trends in ecology & evolution* 19.2, pp. 101–108.

Joshi, M., A. Seidel-Morgenstern, and A. Kremling (2006). “Exploiting the bootstrap method for quantifying parameter confidence intervals in dynamical systems”. In: *Metabolic Engineering* 8.5, pp. 447–455.

Juan S. Martinez-Espin et al. (2017). “New insights into catalyst deactivation and product distribution of zeolites in the methanol-to-hydrocarbons (MTH) reaction with methanol and dimethyl ether feeds”. In: *Catalysis Science & Technology* 7.13, pp. 2700–2716.

Jurtz, N., M. Kraume, and G. D. Wehinger (2019). “Advances in fixed-bed reactor modeling using particle-resolved computational fluid dynamics (CFD)”. In: *Reviews in Chemical Engineering* 35.2, pp. 139–190.

Kaibel, G. (1987). “Distillation columns with vertical partitions”. In: *Chemical Engineering & Technology* 10.1, pp. 92–98.

Karagöz, S., T. T. Tsotsis, and V. I. Manousiouthakis (2020). “Multi-scale model based design of membrane reactor/separator processes for intensified hydrogen production through the water gas shift reaction". In: *International Journal of Hydrogen Energy* 45.12, pp. 7339–7353.

Keil, F. J. (2018). "Process intensification". In: *Reviews in Chemical Engineering* 34.2, pp. 135–200.

Keil, F. J. and C. Rieckmann (1994). "Optimization of three-dimensional catalyst pore structures". In: *Chemical Engineering Science* 49.24, pp. 4811–4822.

Keil, F. J., ed. (2007). *Modeling of Process Intensification.* Wiley.

Keller, T. (2014). "Reactive Distillation". In: *Distillation. Equipment and processes.* Ed. by A. Górak and Z. Olujic. Handbooks in Separation Science Ser. London: Elsevier and Academic Press, pp. 261–294.

Kelling, R. et al. (2012). "Development of a control concept for catalyst regeneration by coke combustion". In: *Chemical Engineering Science* 83, pp. 138–148.

Kern, C. and A. Jess (2005). "Regeneration of coked catalysts—modelling and verification of coke burn-off in single particles and fixed bed reactors". In: *Chemical Engineering Science* 60.15, pp. 4249–4264.

Khodakov, A. et al. (1999). "Structure and Catalytic Properties of Supported Vanadium Oxides. Support Effects on Oxidative Dehydrogenation Reactions". In: *Journal of Catalysis* 181.2, pp. 205–216.

Klose, F. (2004). "Selective oxidation of ethane over a VOx/γ-Al2O3 catalyst – investigation of the reaction network". In: *Applied Catalysis A: General* 260.1, pp. 101–110.

Kockmann, N. (2019). "A Brief History of Chemical Reactor and Reaction Technology". In: *Chemie Ingenieur Technik* 91.7, pp. 941–952.

Koleva, D., A. Atanassov, and N. Nedelchev (2008). "Nonisothermal Degradation Kinetics of Ultra-High Molecular Weight Polyethene Composites Filled with Carbon or Aramid Fibers". In: *International Journal of Polymeric Materials and Polymeric Biomaterials* 57.9, pp. 841–851.

Kolios, G., J. Frauhammer, and G. Eigenberger (2000). "Autothermal fixed-bed reactor concepts". In: *Chemical Engineering Science* 55.24, pp. 5945–5967.

Kolios, G., A. Gritsch, et al. (2005). "Enhancing Productivity and Thermal Efficiency of High-Temperature Endothermic Processes in Heat-Integrated Fixed-Bed Reactors". In: *Integrated chemical processes. Synthesis, operation, analysis, and control.* Ed. by K. Sundmacher, A. Kienle, and A. Seidel-Morgenstern. Weinheim: Wiley-VCH, pp. 1–43.

Koltzenburg, S. (2014). *Polymere: Synthese, Eigenschaften und Anwendungen.* Springer eBook Collection. Berlin, Heidelberg: Springer Spektrum. 607 pp.

Koros, W. J., Y. H. Ma, and T. Shimidzu (1996). "Terminology for membranes and membrane processes (IUPAC Recommendations 1996)". In: *Pure and Applied Chemistry* 68.7, pp. 1479–1489.

Kotanjac, Ž., M. van Sint Annaland, and J. Kuipers (2010). "Demonstration of a packed bed membrane reactor for the oxidative dehydrogenation of propane". In: *Chemical Engineering Science* 65.22, pp. 6029–6035.

Kreger, S. T. et al. (2006). "High Resolution Distributed Strain or Temperature Measurements in Single- and Multi-Mode Fiber Using Swept-Wavelength Interferometry". In: *Technical digest / 18th International Conference on Optical Fiber Sensors. OFS-18, October 23 - 27, 2006, Cancun, México.* Cancún, ThE42.

Kulkarni, M. S. and M. P. Duduković (1996). "A bidirectional fixed-bed reactor for coupling of exothermic and endothermic reactions". In: *AIChE Journal* 42.10, pp. 2897–2910.

Laidler, K. J. (1984). “The development of the Arrhenius equation”. In: *Journal of Chemical Education* 61.6, p. 494.

Lange, J.-P. (2015). “Renewable Feedstocks: The Problem of Catalyst Deactivation and its Mitigation”. In: *Angewandte Chemie (International ed. in English)* 54.45, pp. 13186–13197.

Langmuir, I. (1922). “The mechanism of the catalytic action of platinum in the reactions 2Co + O2= 2Co2 and 2H2+ O2= 2H2O”. In: *Transactions of the Faraday Society* 17, p. 621.

Lasdon, L. S. and A. D. Waren (1981). “GRG2. an all FORTRAN general purpose nonlinear optimizer”. In: *ACM SIGMAP Bulletin* 30, pp. 10–11.

Lavielle, M. (2016). *Maximum likelihood estimation in a Gaussian regression model.* URL: `http://sia.webpopix.org/regressionML.html#the-maximum-likelihood-estimator`.

Lavrenov, A. V. et al. (2015). “Propylene production technology. Today and tomorrow”. In: *Catalysis in Industry* 7.3, pp. 175–187.

Lee, M.-K. et al. (2019). “Modeling of Reaction and Deactivation Kinetics in Methanol-to-Olefins Reaction on SAPO-34”. In: *Industrial & Engineering Chemistry Research* 58.29, pp. 13227–13238.

Levenspiel, O. (1988). “Chemical engineering’s grand adventure”. In: *Chemical Engineering Science* 43.7, pp. 1427–1435.

— (1999). *Chemical reaction engineering.* 3. ed. Hoboken, NJ: Wiley. 668 pp.

Lewis, F. A. (1967). *The Palladium Hydrogen System.* Academic Press.

Liebner, C. (2003). “Einführung der Polythermen Temperatur Rampen Methode für die Ermittlung kinetischer Daten”. Institut für Angewandte Chemie Berlin-Adlershof e.V. Ph.D. Thesis. Berlin: Technische Universität Berlin.

Liu, X. et al. (2020). “Deactivation and regeneration of Claus catalyst particles unraveled by pore network model”. In: *Chemical Engineering Science* 211, p. 115305.

Lobera, M. P. et al. (2008). “Transient kinetic modelling of propane dehydrogenation over a Pt–Sn–K/Al2O3 catalyst”. In: *Applied Catalysis A: General* 349.1-2, pp. 156–164.

López, A. et al. (2011). “Deactivation and regeneration of ZSM-5 zeolite in catalytic pyrolysis of plastic wastes”. In: *Waste management (New York, N.Y.)* 31.8, pp. 1852–1858.

Lu, Y. et al. (1997). “Analysis and optimization of cross-flow reactors with distributed reactant feed and product removal”. In: *Catalysis Today* 35.4, pp. 443–450.

Lummus Technology (2022). *CATOFIN® Propane/Butane Dehydrogenation.* Lummus Technology. URL: `https://www.lummustechnology.com/Process-Technologies/Petrochemicals/Propylene-Production/Propane-Butane-Dehydrogenation` (visited on 09/30/2022).

Luo, S. et al. (2015). “Combustion kinetics of the coke on deactivated dehydrogenation catalysts”. In: *Fuel Processing Technology* 129, pp. 156–161.

Mamleev, V. and S. Bourbigot (2005). “Modulated thermogravimetry in analysis of decomposition kinetics”. In: *Chemical Engineering Science* 60.3, pp. 747–766.

Mamleev, V., S. Bourbigot, et al. (2000). “Modelling of nonisothermal kinetics in thermogravimetry”. In: *Physical Chemistry Chemical Physics* 2.20, pp. 4708–4716.

Mars, P. and D. W. van Krevelen (1954). “Oxidations carried out by means of vanadium oxide catalysts”. In: *Chemical Engineering Science* 3, pp. 41–59.

Martin, H. and M. Nilles (1993). “Radiale Wärmeleitung in durchströmten Schüttungsrohren”. In: *Chemie Ingenieur Technik* 65.12, pp. 1468–1477.

Mason, E. A., A. P. Malinauskas, and A. P. Malinauskas (1983). *Gas transport in porous media. The dusty-gas model.* Vol. 17. Chemical engineering monographs. Amsterdam: Elsevier. 194 pp.

Masson-Delmotte, V. et al., eds. (2021). *Climate Change 2021. Physical Science Basis. Contribution of Working Group I to the Sixth Assessment Report of the Intergovernmental Panel on Climate Change.* Cambridge, UK and New York, N.Y: Cambridge University Press.

Meadows, D. H. et al. (1974). *The limits to growth. A report for the Club of Rome's Project on the Predicament of Mankind.* 2. ed. New York: Universe Books. 205 pp.

Michorczyk, P., J. Ogonowski, and K. Zeńczak (2011). "Activity of chromium oxide deposited on different silica supports in the dehydrogenation of propane with CO2 – A comparative study". In: *Journal of Molecular Catalysis A: Chemical* 349.1-2, pp. 1–12.

Moulijn, J., A. van Diepen, and F. Kapteijn (2001). "Catalyst deactivation: is it predictable?" In: *Applied Catalysis A: General* 212.1-2, pp. 3–16.

Müller, K. et al. (2014). "Increasing the Equilibrium Yield of Oxidative Dehydrogenation with CO 2 by Secondary Reactions". In: *Chemical Engineering & Technology* 37.7, pp. 1261–1264.

Nam, I. S. and J. R. Kittrell (1984). "Use of catalyst coke content in deactivation modeling". In: *Industrial & Engineering Chemistry Process Design and Development* 23.2, pp. 237–242.

Nooijer, N. et al. (2019). "Long-Term Stability of Thin-Film Pd-Based Supported Membranes". In: *Processes* 7.2, p. 106.

Ochoa, A. et al. (2017). "Assessment of thermogravimetric methods for calculating coke combustion-regeneration kinetics of deactivated catalyst". In: *Chemical Engineering Science* 171, pp. 459–470.

Olsbye, U. et al. (2015). "The formation and degradation of active species during methanol conversion over protonated zeotype catalysts". In: *Chemical Society reviews* 44.20, pp. 7155–7176.

Peters, T. A. et al. (2016). "Investigation of Pd-based membranes in propane dehydrogenation (PDH) processes". In: *Chemical Engineering Journal* 305, pp. 191–200.

Petrochemical Catalysts: Olefins (2022). *Increase yields of polymer-grade propylene to meet growing demand.* Honeywell UOP. URL: `https://uop.honeywell.com/en/products-and-services/catalysts/petrochemical-catalysts/olefins` (visited on 09/30/2022).

Pfefferle, W. C. (1966). "Process for Dehydrogenation". US 3290406 A.

Pitac (2005). *Computational Science. Ensuring America's Competitiveness.* Arlington,VA: National Coordination Office for Information Technology Research and Development.

Portet, S. (2020). "A primer on model selection using the Akaike Information Criterion". In: *Infectious Disease Modelling* 5, pp. 111–128.

Pottratz, I., I. Müller, and C. Hamel (2022). "Potential and Scale-Up of Pore-Through-Flow Membrane Reactors for the Production of Prebiotic Galacto-Oligosaccharides with Immobilized β-Galactosidase". In: *Catalysts* 12.1, p. 7.

Prognos, Öko-Institut, and Wuppertal-Institut (2021). *Klimaneutrales Deutschland 2045. Wie Deutschland seine Klimaziele schon vor 2050 erreichen kann. Zusammenfassung im Auftrag von Stiftung Klimaneutralität, Agora Energiewende und Agora Verkehrswende.* Prognos, Öko-Institut, and Wuppertal-Institut.

Purvis, B., Y. Mao, and D. Robinson (2019). "Three pillars of sustainability: in search of conceptual origins". In: *Sustainability Science* 14.3, pp. 681–695.

Reiff, E. K. and J. R. Kittrell (1980). “Use of Active Site Balances for Catalyst Deactivation Models”. In: *Industrial & Engineering Chemistry Fundamentals* 19.1, pp. 126–128.

Ricca, A. et al. (2017). “Highly selective propylene production in a membrane assisted catalytic propane dehydrogenation”. In: *Chemical Engineering Journal* 330, pp. 1119–1127.

Rideal, E. K. (1939). “A note on a simple molecular mechanism for heterogeneous catalytic reactions”. In: *Mathematical Proceedings of the Cambridge Philosophical Society* 35.1, pp. 130–132.

Royo, C., J. M. Perdices, et al. (1996). “Regeneration of Fixed-Bed Catalytic Reactors Deactivated by Coke. Influence of Operating Conditions and of Different Pretreatments of the Coke Deposits”. In: *Industrial & Engineering Chemistry Research* 35.6, pp. 1813–1823.

Royo, C., J. V. Ibarra, et al. (1994). “Regeneration of Coked Catalysts: The Effect of Aging upon the Characteristics of the Coke Deposits”. In: *Industrial & Engineering Chemistry Research* 33.11, pp. 2563–2570.

Sahimi, M. (1985). “A percolation model of catalyst deactivation by site coverage and pore blockage”. In: *Journal of Catalysis* 96.2, pp. 552–562.

Satterfield, C. N. (1970). *Mass transfer in hetergeneous catalysis.* Cambridge, Mass.: MIT Press. 267 pp.

Schäfer, M. (2006). *Computational Engineering - Introduction to Numerical Methods.* Berlin, Heidelberg: Springer-Verlag Berlin Heidelberg.

Schwaab, M. and J. C. Pinto (2007). “Optimum reference temperature for reparameterization of the Arrhenius equation. Part 1: Problems involving one kinetic constant”. In: *Chemical Engineering Science* 62.10, pp. 2750–2764.

Seidel-Morgenstern, A., ed. (2010). *Membrane reactors. Distributing reactants to improve selectivity and yield.* Weinheim: Wiley-VCH Verlag GmbH & Co. 274 pp.

Sheintuch, M., O. Liron, et al. (2016). “Propane dehydrogenation kinetics on supported Pt catalyst”. In: *Applied Catalysis A: General* 516, pp. 17–29.

Sheintuch, M. and O. Nekhamkina (2018). “Architecture alternatives for propane dehydrogenation in a membrane reactor”. In: *Chemical Engineering Journal* 347, pp. 900–912.

Shelepova, E. V. and A. A. Vedyagin (2020). “Intensification of the dehydrogenation process of different hydrocarbons in a catalytic membrane reactor”. In: *Chemical Engineering and Processing: Process Intensification* 155, p. 108072.

Siirola, J. J. (2014). “The impact of shale gas in the chemical industry”. In: *AIChE Journal* 60.3, pp. 810–819.

Sokolov, S., V. Y. Bychkov, et al. (2015). “Effect of VO x Species and Support on Coke Formation and Catalyst Stability in Nonoxidative Propane Dehydrogenation”. In: *ChemCatChem* 7.11, pp. 1691–1700.

Sokolov, S., M. Stoyanova, et al. (2012). “Comparative study of propane dehydrogenation over V-, Cr-, and Pt-based catalysts: Time on-stream behavior and origins of deactivation”. In: *Journal of Catalysis* 293, pp. 67–75.

Sørensen, M. D. P. (2017). “The establishment of a coke-burn kinetic model for zeolite catalysts”. In: *Chemical Engineering Science* 168, pp. 465–479.

Sosna, B., O. Korup, and R. Horn (2020). “Probing local diffusion and reaction in a porous catalyst pellet”. In: *Journal of Catalysis* 381, pp. 285–294.

Spiess, A.-N. and N. Neumeyer (2010). “An evaluation of R2 as an inadequate measure for nonlinear models in pharmacological and biochemical research: a Monte Carlo approach”. In: *BMC pharmacology* 10, p. 6.

Stankiewicz, A. and J. A. Moulijn (2002). “Process Intensification”. In: *Industrial & Engineering Chemistry Research* 41.8, pp. 1920–1924.

Stankiewicz, A. I. and J. A. Moulijn (2000). “Process intensification: Transforming chemical engineering”. In: *Chemical Engineering Progress* 96.1, pp. 22–33.

Staszak, K., K. Wieszczycka, and B. Tylkowski (2020). *Chemical technologies and processes*. De Gruyter STEM. Berlin and Boston: De Gruyter. 301 pp.

Steen, H. (2009). *Handbuch des Explosionsschutzes*. Weinheim: Wiley-VCH. Online-Ressource (XXII, 760 S.)

Stegehake, C., M. Grünewald, et al. (2018). “Fiber–Optic Temperature Measurements in Fixed–Bed Reactors for Model–Based Evaluation of Effective Radial Thermal Conductivity”. In: *Chemie Ingenieur Technik* 90.5, pp. 602–614.

Stegehake, C., J. Riese, and M. Grünewald (2019). “Modeling and Validating Fixed–Bed Reactors: A State–of–the–Art Review”. In: *ChemBioEng Reviews* 6.2, pp. 28–44.

Strehmel, K., R. Weiner, and H. Podhaisky (2012). *Numerik gewöhnlicher Differentialgleichungen*. Wiesbaden: Vieweg+Teubner Verlag.

Sui, Z.-J. et al. (2014). “Kinetics of Catalytic Dehydrogenation of Propane over Pt-Based Catalysts”. In: *Catalysis and kinetics. Molecular level consideration*. Ed. by G. B. Marin. First edition. Advances in chemical engineering 44. San Diego, California: Academic Press, pp. 61–125.

Svehla, R. A. (1962). *Estimated Viscosities and Thermal Conductivities of Gases at High Temperatures*. Ed. by NASA Lewis Research Center Cleveland, OH, United States. Cleveland, OH: NASA Lewis Research Center Cleveland, OH, United States.

Thomas, S., C. Hamel, and A. Seidel–Morgenstern (2010). “Basic Problems of Chemical Reaction Engineering and Potential of Membrane Reactors”. In: *Membrane reactors. Distributing reactants to improve selectivity and yield*. Ed. by A. Seidel-Morgenstern. Vol. 1. Weinheim: Wiley-VCH Verlag GmbH & Co, pp. 1–27.

Tian, Y. et al. (2018). “An overview of process systems engineering approaches for process intensification: State of the art”. In: *Chemical Engineering and Processing: Process Intensification* 133, pp. 160–210.

Tiseo, I. (2021). *Production volume of polypropylene resin worldwide in 2018 and 2026*. Statista. URL: `https://www.statista.com/statistics/1103529/global-polypropylene-production/` (visited on 11/30/2022).

Tóta, Á. et al. (2004). “Theoretical and Experimental Investigation of Concentration and Contact Time Effects in Membrane Reactors”. In: *Chemical Engineering Research and Design* 82.2, pp. 236–244.

Tsakalis, K. (1984). “Deactivation phenomena by site poisoning and pore blockage: The effect of catalyst size, pore size, and pore size distribution”. In: *Journal of Catalysis* 88.1, pp. 188–202.

Tsotsas, E. (2010). “M7 Heat and Mass Transfer in Packed Beds with Fluid Flow”. In: *VDI Heat Atlas*. Ed. by VDI e. V. Vol. 96. SpringerLink Bücher. Berlin, Heidelberg: Springer Berlin Heidelberg, pp. 1327–1342.

United Nations (2015a). *A/RES/70/1: Transforming our world: The 2030 Agenda for Sustainable Development. Resolution adopted by the General Assembly on 25 September 2015*. United Nations.

— (Dec. 12, 2015b). *Paris Agreement*.

Valenzuela, R. X. et al. (2000). “Selective oxidehydrogenation of ethane with CO2 over CeO2-based catalysts”. In: *Catalysis Today* 61.1-4, pp. 43–48.

van de Graaf, J. M. et al. (1999). “Application of a silicalite-1 membrane reactor in metathesis reactions”. In: *Applied Catalysis A: General* 178.2, pp. 225–241.

van Gerven, T. and A. Stankiewicz (2009). “Structure, Energy, Synergy, Time—The Fundamentals of Process Intensification”. In: *Industrial & Engineering Chemistry Research* 48.5, pp. 2465–2474.

van Sint Annaland, M., J. Kuipers, and W. van Swaaij (2001). “A kinetic rate expression for the time-dependent coke formation rate during propane dehydrogenation over a platinum alumina monolithic catalyst”. In: *Catalysis Today* 66.2-4, pp. 427–436.

van Sint Annaland, M., H. Scholts, et al. (2002a). “A novel reverse flow reactor coupling endothermic and exothermic reactions: Part II: Sequential reactor configuration for reversible endothermic reactions”. In: *Chemical Engineering Science* 57.5, pp. 855–872.

— (2002b). “A novel reverse flow reactor coupling endothermic and exothermic reactions. Part I: comparison of reactor configurations for irreversible endothermic reactions”. In: *Chemical Engineering Science* 57.5, pp. 833–854.

Vannice, M. A. (2007). “An analysis of the Mars–van Krevelen rate expression”. In: *Catalysis Today* 123.1-4, pp. 18–22.

VDI e. V., ed. (2010). *VDI Heat Atlas*. SpringerLink Bücher. Berlin, Heidelberg: Springer Berlin Heidelberg. 1586 pp.

Vernikovskaya, N. V. et al. (2023). “Experimental and theoretical investigation of the oxidation of methanol to formaldehyde in a microstructured slit-type catalytic reactor”. In: *Chemical Engineering Journal* 451, p. 138368.

Voorhies, A. (1945). “Carbon Formation in Catalytic Cracking”. In: *Industrial & Engineering Chemistry* 37.4, pp. 318–322.

Walter, J. P., A. Brune, A. Seidel–Morgenstern, et al. (2021). “Model–based Analysis of Fixed–bed and Membrane Reactors of Various Scale”. In: *Chemie Ingenieur Technik* 93.5, pp. 819–824.

Walter, J. P., A. Brune, A. Seidel-Morgenstern, et al. (2021). “Process Intensification of the Propane Dehydrogenation Considering Coke Formation, Catalyst Deactivation and Regeneration—Transient Modelling and Analysis of a Heat-Integrated Membrane Reactor”. In: *Catalysts* 11.9, p. 1056.

Wang, S. and Z. H. Zhu (2004). “Catalytic Conversion of Alkanes to Olefins by Carbon Dioxide Oxidative DehydrogenationA Review”. In: *Energy & Fuels* 18.4, pp. 1126–1139.

Wehinger, G. D. et al. (2022). “Quo vadis multiscale modeling in reaction engineering? – A perspective”. In: *Chemical Engineering Research and Design* 184, pp. 39–58.

Weinzierl, T. (2021). “The Pillars of Science”. In: *Principles of Parallel Scientific Computing. A First Guide to Numerical Concepts and Programming Methods.* Ed. by T. Weinzierl. 1st ed. 2021. Springer eBook Collection. Cham: Springer International Publishing and Imprint Springer, pp. 3–9.

Weisz, P. B. (1982). “The Science of the Possible”. In: *CHEMTECH*, pp. 424–425.

Wen, Z. et al. (2009). “Intensification of biodiesel synthesis using zigzag micro-channel reactors”. In: *Bioresource technology* 100.12, pp. 3054–3060.

Winterberg, M., E. Tsotsas, et al. (2000). “A simple and coherent set of coefficients for modelling of heat and mass transport with and without chemical reaction in tubes filled with spheres”. In: *Chemical Engineering Science* 55.5, pp. 967–979.

Winterberg, M. and E. Tsotsas (2000). “Modelling of heat transport in beds packed with spherical particles for various bed geometries and/or thermal boundary conditions”. In: *International Journal of Thermal Sciences* 39.5, pp. 556–570.

Won, W. et al. (2009). “Repetitive Control and Online Optimization of Catofin Propane Process”. In: *IFAC Proceedings Volumes* 42.11, pp. 273–278.

Won, W. et al. (2010). “Repetitive control and online optimization of Catofin propane process”. In: *Computers & Chemical Engineering* 34.4, pp. 508–517.

Xiong, C. et al. (2019). “Structure–Performance Relationships for Propane Dehydrogenation over Aluminum Supported Vanadium Oxide”. In: *ACS Catalysis* 9.7, pp. 5816–5827.

Yan, R.-q., W. Liu, and C.-l. Song (2014). “Oxidative Dehydrogenation of Alkanes using Oxygen-Permeable Membrane Reactor”. In: *Chinese Journal of Chemical Physics* 27.6, pp. 690–696.

Yaws, C. L. (1999). *Chemical properties handbook. Physical, thermodynamic, environmental, transport, and health related properties for organic and inorganic chemicals.* McGraw-Hill handbooks. New York, N.Y: McGraw-Hill Education LLC. 779 pp.

Ye, G., H. Wang, X. Duan, et al. (2019). “Pore network modeling of catalyst deactivation by coking, from single site to particle, during propane dehydrogenation”. In: *AIChE Journal* 65.1, pp. 140–150.

Ye, G., H. Wang, X. Zhou, et al. (2019). “Optimizing Catalyst Pore Network Structure in the Presence of Deactivation by Coking”. In: *AIChE Journal*, e16687.

Ye, Y. et al. (2005). “Partial oxidation of n-butane in a solid electrolyte membrane reactor: Periodic and steady-state operations”. In: *Applied Catalysis A: General* 285.1-2, pp. 86–95.

Zagoruiko, A. N. et al. (2021). “Unsteady-state operation of reactors with fixed catalyst beds”. In: *Reviews in Chemical Engineering* 37.1, pp. 193–225.

Zanthoff, H. W. et al. (1999). “Selective and non-selective oxygen species determining the product selectivity in the oxidative conversion of propane over vanadium mixed oxide catalysts”. In: *Chemical Engineering Science* 54.20, pp. 4397–4405.

Zeeshan Nawaz (2016). “Dynamic Modeling of CATOFIN® Fixed-Bed Iso-Butane Dehydrogenation Reactor for Operational Optimization”. In: *International Journal of Chemical Reactor Engineering* 14.1, pp. 491–515.

Zeng, L. et al. (2018). “Metal oxide redox chemistry for chemical looping processes”. In: *Nature Reviews Chemistry* 2.11, pp. 349–364.

Zhdanov, V. P. (1993). “Application of Percolation Theory to Describing Kinetic Processes in Porous Solids”. In: *Advances in Catalysis*. Ed. by D. D. Eley, H. Pines, and P. B. Weisz. Vol. 39. Academic Press, pp. 1–50.

Zhu, X. and W. Yang (2017). *Mixed Conducting Ceramic Membranes*. Berlin, Heidelberg: Springer Berlin Heidelberg.

Zimmermann, H. (2010). “Propene”. In: *Ullmann’s encyclopedia of industrial chemistry*. Chichester: Wiley.

Zimmermann, H. and R. Walzl (2010). “Ethylene”. In: *Ullmann’s encyclopedia of industrial chemistry*. Chichester: Wiley.

A Appendix to Chapter 2

A.1 Details on the Momentum Balance Equations

Eq. 2.25 in section 2.3.1 describes the momentum balance equation. The mathematical correlations required to solve this equation are explained below.

The shear stress tensor can be calculated by

$$\boldsymbol{\tau} = \eta_f \left(\nabla u_0 + (\nabla u_0)^T\right) - \left(\frac{2}{3}\eta_f\right)(\nabla u)\boldsymbol{I} \tag{A.1}$$

where $\boldsymbol{I}$ denotes the unit vector and η_f being the dynamic viscosity of the fluid. An additional friction term f summarizes the Darcy resistance term and the Forchheimer resistance term (Tsotsas 2010):

$$f = 150\frac{(1-\varepsilon)^2}{\varepsilon^3}\frac{\eta_f}{d^2}\varepsilon|u| + 1.75\frac{1-\varepsilon}{\varepsilon^3}\frac{\rho_f}{d}\varepsilon^2|u|^2, \quad |u| = (u_{0,z} + u_{0,z})^{0.5} \tag{A.2}$$

Due to the incomprehensibility of the fluid the continuity equation

$$\frac{\partial(\varepsilon\rho_f)}{\partial t} + u_0\nabla\rho_f = 0 \tag{A.3}$$

is still valid. It expresses that the momentum changes in all spatial directions cancel each other.

A.2 Heat Transfer and Heat Conduction Models

For 2D modeling of chemical reactors using continuum models (see Section 2.3.1), different modeling approaches are available to describe the heat transfer from the continuous phase in the reactor to the reactor wall. In this work, the α_w model as wall heat transfer model and the $\lambda(r)$ model as wall heat conduction model are particularly emphasized. While the basic concepts of the modeling approaches and their advantages and disadvantages were briefly explained in Section 2.3.1, all equations necessary for the modeling will be presented here. These equations represent the procedure described in the VDI Heat Atlas and cover both to the description of the heat transport and also the mass transport in a reactor with a catalyst bed (VDI e. V. 2010).

A.2.1 The $\lambda(r)$ Model

In this paragraph, the equations necessary to use the $\lambda(r)$ model are presented. First the parameters needed for mass transfer are described. Later on additional parameters for heat transfer are introduced. The analogies between heat and mass transfer are highlighted.

The radial porosity profile in a tubular reactor with radius R filled with particles of a diameter of d can be approximated by

$$\varepsilon(r) = 0.4\left(1 + 1.36\exp\left(-5\frac{R-r}{d}\right)\right) \tag{A.4}$$

This equation models the porosity with an exponential function and can be seen as a good approximation of the oscillating profile that is known to form in an packed bed of spherical particles (Bey and Eigenberger 1997). Figure A.1 illustrates the differences between the approximation and the real porosity profile schematically.

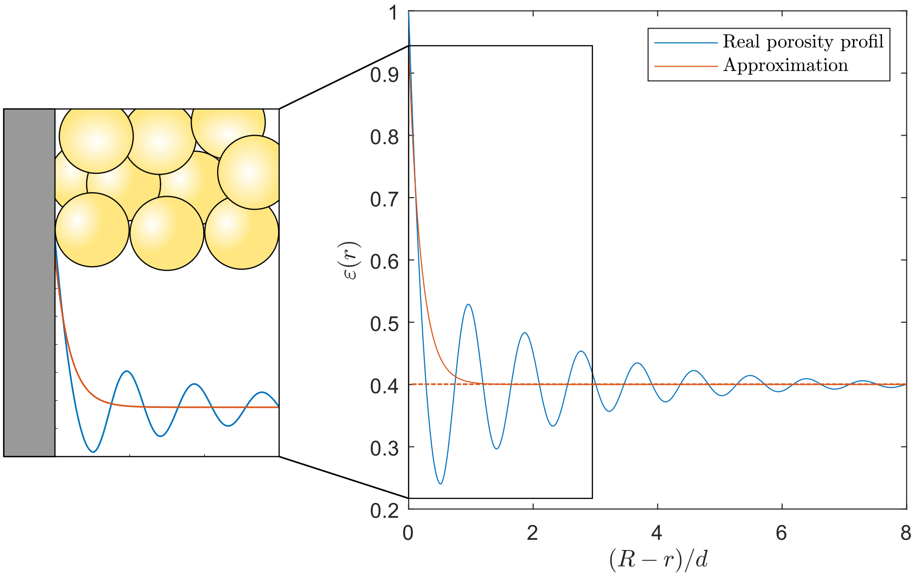

Figure A.1: Schematic representation of a porosity profile forming in a packed bed of spherical particles.

For some reactor setups discussed in this work a porosity profile for an annular gap has to be calculated. In that case the hydraulic diameter

$$D_\mathrm{h} = 2\delta \tag{A.5}$$

has been used instead of the tube diameter, where δ describes the width of the annular gap. The effective axial dispersion coefficient can be calculated as

$$D^\mathrm{eff}_{\mathrm{ax},i}(r) = D_\mathrm{bed}(r) + \frac{Pe_0}{K_\mathrm{ax}} D_{i,k}, \quad K_\mathrm{ax} = 2 \tag{A.6}$$

where D_bed is the thermal conductivity of the bed without flow, Pe_0 the molecular Péclet number at superficial velocity and $D_{i,k}$ the binary diffusion coefficient of component i in

component k. The parameter $D_{\text{bed}}(r)$ describes the axial mixing through diffusion without flow and the term $\frac{Pe_0}{K_{\text{ax}}}D_{i,k}$ adds the axial mixing caused by the flow.
Due to the radial porosity distribution a radial dependent conductivity of the bed without flow has to be taken into account. This thermal conductivity of the bed without flow can by calculated by

$$D_{\text{bed}}(r) = (1 - (1 - \epsilon(r))^{0.5})D_{i,k} \tag{A.7}$$

The molecular Péclet number Pe_0 and the superficial flow velocity u_0 resulting from a total volumetric flow of $\dot{V}_{\text{tot}}$ in a reactor with a cross sectional area A can be calculated as follows:

$$Pe_0 = \frac{\bar{u}_0 d}{D_{i,k}}, \quad \bar{u}_0 = \frac{\dot{V}_{\text{tot}}}{A} \tag{A.8}$$

To calculate the binary diffusion coefficients, a high dilution in nitrogen is assumed. Therefore a binary mixture of the specific gas in nitrogen can be assumed to calculate the diffusion coefficients. The calculation of the diffusion coefficients follows an equation by Hirschfelder as described by Bearns et al. (Baerns 2013):

$$D_{i,k} = \frac{18.583 T^{\frac{2}{3}} \left(\frac{M_j + M_k}{M_j M_k}\right)^{0.5}}{p \sigma_{i,k}^2 \Omega} \times 10^{-4} \quad \left[\frac{m^2}{s}\right] \tag{A.9}$$

with the molecular mass M_k and M_i for the components k and i respectively, the pressure p, collision diameter $\sigma_{i,k}$ and collision integral Ω. The collision diameter can be calculated by

$$\sigma_{i,k} = 0.5(\sigma_i + \sigma_k) \tag{A.10}$$

with the collision integral

$$\Omega = f\left(\frac{k_B T}{\varepsilon_{i,k}}\right) \tag{A.11}$$

depending on the Boltzmann constant k_B, the temperature T and the force constant $\varepsilon_{i,k}$ of the components i and k. The combined force constant can be calculated using the individual force constants by

$$\varepsilon_{i,k} = (\varepsilon_i \varepsilon_k)^{0.5} \tag{A.12}$$

Tabled values for σ_i, σ_k and Ω can be found in literature (Baerns 2013; Svehla 1962; Satterfield 1970). The values for Ω have been fitted by the following, empirical equation

$$\Omega = 0.9465 \left(\frac{k_B T}{\varepsilon_{i,k}}\right)^{0.694} + 0.5061 \tag{A.13}$$

to provide them for different temperatures for the simulations in this work.

The effective radial dispersion coefficient an be calculated by using the following equations:

$$D_{\mathrm{rad},i}^{\mathrm{eff}}(r) = D_{\mathrm{bed}}(r) + K_1 Pe_0 \frac{u_0(r=0)}{\bar{u}_0} \cdot f(R-r) D_{i,k} \tag{A.14}$$

$$K_1 = \frac{1}{8}\left(1 + \frac{3}{(Pe_0(r=0))^{0.5}}\right)^{-1} \tag{A.15}$$

$$f(R-r) = \begin{cases} \left(\frac{R-r}{K_2 d}\right)^n & \text{for } 0 < R-r \leq K_2 d \\ 1 & \text{for } K_2 d < R-r \leq R \end{cases} \tag{A.16}$$

$D_{\mathrm{rad},i}^{\mathrm{eff}}(r)$ consists, in analogy to $D_{\mathrm{ax},i}^{\mathrm{eff}}(r)$ (Eq. (A.6)), of a the conductivity of the bed without flow and a convective term that takes the flow around the particles into account. The parameter K_1 describes the increase of the dispersion coefficient with increasing flow velocity. The superficial velocity in the middle of the tube $u_0(r=0)$ can be derived from momentum balances. Due to the porosity increase near the wall, the convective influence on the radial dispersion coefficient decreases as the particle influence decreases. This assumption is considered in Eq. (A.16). Damping parameter K_2 describes the area where the convective influence decreases and can be calculated by

$$K_2 = 0.44 \tag{A.17}$$

Furthermore the parameter n was determined to be

$$n = 2 \tag{A.18}$$

by Winterberg et al. (Winterberg, Tsotsas, et al. 2000).

Heat transfer

The model equations for heat transfer show a lot of similarities to the mass transfer equations. The axial heat conductivity of the bed $\lambda_{\mathrm{ax}}^{\mathrm{eff}}(r)$ can be described by

$$\lambda_{\mathrm{ax}}^{\mathrm{eff}}(r) = \lambda_{\mathrm{bed}}(r) + \frac{Pe_0}{K_{\mathrm{ax}}}\lambda_f, \quad Pe_0 = \frac{\bar{u}_0 \rho_f c_{p,f} d}{\lambda_f} \tag{A.19}$$

which follows the same structure than Eq. (A.6). In these equations λ_{bed} describes the heat conductivity of the bed without flow. $K = 2$ is still valid analogous to the mass transfer equations. The heat conductivity of the fluid λ_f can be described by

$$\lambda_f = (0.3918 + 0.09814\,T + 0.0000507\,T^2 1.5 \times 10^{-8}\,T^3 \left[\frac{\mathrm{W}}{\mathrm{m\,K}}\right] \tag{A.20}$$

which is an empirical equation based on tabled values (Hirschberg 1999). Equation (A.21) describes the conductivity of the bed without flow and reads

$$\lambda_{\mathrm{bed}}(r) = \lambda_f \left(1 - (1-\varepsilon(r))^{0.5} + (1-\varepsilon(r))^{0.5} k_c\right), \quad k_c = \frac{\lambda_c}{\lambda_f} \tag{A.21}$$

where k_c describes the ration of the conductivity of the center of of the bed λ_c to the heat conductivity of the fluid λ_f. In addition, the following holds for k:

$$k_c = \frac{2}{N}\left(\frac{B}{N^2}\frac{k_{\text{cat}}-1}{k_{\text{cat}}}\ln\left(\frac{k_{\text{cat}}}{B}\right) - \frac{B+1}{2} - \frac{B-1}{N}\right), \quad k_{\text{cat}} = \frac{\lambda_{\text{cat}}}{\lambda_f} \tag{A.22}$$

In that equation N accounts for the spherical geometry of the particles and B describes a deformation factor, that are defined for spherical particles as

$$B = 1.25\left(\frac{1-\varepsilon(r)}{\varepsilon(r)}\right)^{\frac{10}{9}} \tag{A.23}$$

$$N = 1 - \left(\frac{B}{k_{\text{cat}}}\right) \tag{A.24}$$

Similar to the axial heat conductivity, the radial heat conductivity follows the structures known from the mass transfer (see Eq. (A.14)). The effective radial heat transfer can be described by

$$\lambda^{\text{eff}}_{rad}(r) = \lambda_{\text{bed}}(r) + K_1\, Pe_0 \frac{u_0(r=0)}{\bar{u}_0} f(R-r)\lambda_f \tag{A.25}$$

where the function $f(R-r)$ can be calculated by Eq. (A.16) ($n = 2$), parameters K_1 and K_2 change in comparison to mass transfer:

$$K_1 = \frac{1}{8} \tag{A.26}$$

$$K_3 = 0.44 + 4\exp\left(-\frac{Re_0}{70}\right) \tag{A.27}$$

The Reynolds number at average superficial velocity

$$Re_0 = \frac{\bar{u}_0 d\rho_f}{\eta_f} \tag{A.28}$$

is depending on the dynamic viscosity η_f, that can be described by

$$\eta_f = (3.043 + 0.04989\,T - 1.093\times10^{-5}\,T^2)\times10^{-6}[\text{Pa s}] \tag{A.29}$$

This is again an empirical equation based on tabled values (Hirschberg 1999).

A.2.2 The α_{w} Model

Analogous to the lambda r model in the previous paragraph, the equations needed to use the alpha w model are presented here. Parts of the equations are used for both models. The similarities are pointed out if necessary.

The radial dispersion coefficient is calculated by

$$D^{\text{eff}}_{\text{rad},i} = D_{\text{bed}} + \frac{Pe_0}{K_r}D_{i,k} \tag{A.30}$$

The influence of the convection does not decrease towards the reactor wall in comparison to the $\lambda(r)$ model. The factor K_r is calculated by

$$K_r = K_{r,\infty}\left(2 - \left(1 - \frac{2}{D/d}\right)^2\right), \quad K_{r,\infty} = 7 \tag{A.31}$$

$K_{r,\infty} = 7$ is valid for spherical particles. Diffusion coefficients are independent of the porosity. Therefore Eq. (A.9) to (A.13) remain valid.

Similar to the mass transfer equations in heat transfer the α_w model does consider the mean porosity $\bar{\varepsilon}$ instead of a porosity distribution. The axial heat dispersion coefficient described in Eq. (A.19) remains valid. The radial heat transfer is in analogy to Eq. (A.30) described by

$$\lambda_{\text{rad}}^{\text{eff}} = \lambda_{\text{bed}} + \frac{Pe_0}{K_r}\lambda_f, \quad K_r = 8 \tag{A.32}$$

For the determination of the heat transport coefficient α_{w} the following function depending on the wall Nusselt number

$$Nu_{\text{w}} = \frac{\alpha_{\text{w}}}{\lambda_f} \tag{A.33}$$

can be used. The wall Nusslet number Nu_{w} that can be calculated with the empirical equation

$$Nu_{\text{w}} = Nu_{\text{w0}} + 0.19 Pe^{0.75} Pr^{-0.42} \tag{A.34}$$

with

$$Pe^{0.75} Pr^{-0.42} = Re^{0.75} Pr^{0.33} \tag{A.35}$$

where $Nu_{\text{w,0}}$ is a final value, independent of the flow rate, which describes the changed radial conduction in the area of the phase boundary between the bed and the wall. It can be calculated by

$$Nu_{\text{w0}} = \left(1.3 + 5\frac{d}{D}\right)\frac{\lambda_{\text{bed}}}{\lambda_f} \tag{A.36}$$

B Appendix to Chapter 3

B.1 Kinetic Investigation of the Reaction Network

Table B.1: Directly optimized partial kinetic parameters and corresponding confidence intervals of the main and side reactions.

Parameter	Opt. Value	95 % Confidence Interval
A_1	-11.002	$\pm 2.9\,\%$
A_2	-12.551	$\pm 1.2\,\%$
A_3	-10.39	$\pm 2.7\,\%$
A_4	-9.012	$\pm 2.7\,\%$
B_1	15.976	$\pm 19.5\,\%$
B_2	13.456	$\pm 2.0\,\%$
B_3	11.667	$\pm 6.6\,\%$
B_4	11.777	$\pm 4.4\,\%$
α_1	0.500	$\pm 14.4\,\%$
α_2	1.130	$\pm 1.7\,\%$
α_3	0.814	$\pm 10.8\,\%$
α_4	0.725	$\pm 8.9\,\%$
β_2	1.051×10^{-4}	$\pm 6954\,\%$
β_3	0.212	$\pm 11.7\,\%$
β_4	0.17	$\pm 10.6\,\%$

B.2 Akaike Information Criterion

Model selection is a crucial procedure in many scientific and engineering domains. It can help to better understand the underlying mechanisms of a oberserved phenomenon, since the models available to describe an experimental data set are often based on different assumptions. A better fit of a particular model can thus indicate that the underlying assumptions of the used model are true for the fitted data set. The selection of a model is in many cases not trivial. The coefficient of determination

$$R^2 = 1 - \frac{RSS}{TSS} = 1 - \frac{\sum (y - \hat{y})^2}{\sum (y - \bar{y})^2} \tag{B.1}$$

and several variants are commonly used to describe the goodness of fit and are often used to indicate which model represents the data set best. The parameter R^2 includes the the residual sum of squares RSS and the total sum of squares TSS. These variables can be calculated from the data points y and the average of the measured data points $\bar{y}$, the calculated data point from the fitted model $\hat{y}$ but not the number of parameters of the model. Due to this structure usually models with more parameters N_{par} are preferred according to R^2. This bias towards models with a high number of parameters can be prevented by following the principle of parsimony, that states, that a model as simple as possible has to be selected. A high amount of parameters leads to overfit models with a high variance in parameter estimators. The model describes small fluctuations in the data set that can be ascribed to random noise e.g. from the accuracy of the experimental equipment. There is a risk to identify negligible parameters as important resulting in models that can not be extrapolated beyond the training data. Underfit models with to less parameters tend to show high bias in parameter estimation (Portet 2020; Johnson and Omland 2004). The error from bias results from wrong assumptions. The model therefore fails to identify important parameters. This trade-off between bias and variance is illustrated in Fig. B.1. The goal of model selection procedures is to identify the model with the lowest total error resulting from bias and variance.

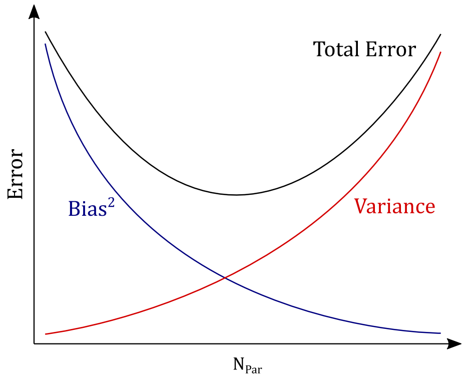

Figure B.1: Principle of parsimony: Trade-off between bias and variance in model selection.

An alternative way for model discrimination introduced by Akaike is the Akaike Information Criterion (AIC), that is based on information theory (Akaike 1978):

$$AIC = 2p - 2\log(\mathcal{L}) \tag{B.2}$$

This criterion includes the number of parameters of the tested model p and the numerical value of the log-likelihood at its maximum point $\ln(L)$. The AIC provides an estimator of the expected relative difference between the model and the true mechanism generated by the observed data set. The smaller the value of the AIC, the smaller the relative loss of information (Burnham and Anderson 2004). The AIC can be calculated for all models included in the considered model set. All models not included in the model set are disregarded according to Akaike. Consequently, the best model of a selected set does not have to be the generally best representation of reality. It may still be a poor approximation. Furthermore, the AIC can be computed for any assumed distribution, resulting in a universal range of application. A frequently assumed special case is the assumption that the errors, for example in measurements, are independent, identical and normally distributed. In the following, the AIC will be derived for this case (Lavielle 2016).
The relationship between a fitted model $f(x,\theta)$ with a parameter set θ and measured values y can be represented by

$$\begin{aligned} y &= f(x,\theta) + r && \text{(B.3)}\\ &= f(x,\theta) + \sigma\varepsilon && \text{(B.4)} \end{aligned}$$

The residual error contained in fitted model consists of a standard deviation σ and an error ε where the error ε is a sequence of independent and normally distributed random variables with mean 0 and variance 1

$$E \underset{i.i.d.}{\sim} \mathcal{N}(0,1) \tag{B.5}$$

Since ε is independent and identically distributed, it follows for y that it is also normally distributed. The expected value of this normal distribution is the model $f(x,\theta)$ and the variance is σ^2

$$y \sim \mathcal{N}\left(f(x,\theta), \sigma^2\right) \tag{B.6}$$

The general form of the Gaussian normal distribution is

$$p(y|\mu,\sigma^2) = \frac{1}{\sqrt{2\pi\sigma^2}} \exp\left(-\frac{(y-\mu)^2}{2\sigma^2}\right) \tag{B.7}$$

with the expected value μ. If the model described in Eq. (B.4) is substituted into Eq. (B.7), the normal distribution reads

$$p(y|\theta,\sigma^2) = \frac{1}{\sqrt{2\pi\sigma^2}} \exp\left(-\frac{(y-f(x,\theta))^2}{2\sigma^2}\right) \tag{B.8}$$

For a given vector of observations y, the likelihood is defined as the function of the parameter set $\beta = (\theta, \sigma^2)$ as

$$\mathcal{L}(\beta) = p(y|\beta) = \prod_{i=1}^{N_\text{point}} p(y_i|\beta) \tag{B.9}$$

The log-likelihood function is defined as the natural logarithm of the likelihood function

$$\log\left(\mathcal{L}(\beta)\right) = \mathcal{LL}(\beta) = \log\left(p(y|\beta)\right) = \log\left(\prod_{i=1}^{N_{\text{point}}} p\left(y_i|\beta\right)\right) \tag{B.10}$$

This yields the log likelihood function

$$\mathcal{LL}(\beta) = -\frac{N_{\text{point}}}{2}\log(2\pi) - \frac{N_{\text{point}}}{2}\log(\sigma^2) - \frac{1}{2\sigma^2}\sum_{i=1}^{N_{\text{MP}}}(y_i - f(x_i,\theta))^2 \tag{B.11}$$

for the normal distribution in Eq. (B.8). For the AIC, the maximum of the log-likelihood is required. Consequently, an optimization task results. The arguments $\hat{\beta} = \left(\hat{\theta}, \hat{\sigma^2}\right)$ which lead to a maximization of the likelihood or log-likelihood

$$\hat{\beta} = \arg\max(\mathcal{L}(\beta)) = \arg\max(\mathcal{LL}(\beta)) \tag{B.12}$$

are searched for.It is known that the optimized parameter set θ of the model minimizes the residual sum of squares RSS, therefore

$$\hat{\theta} = \arg\min_{\theta}\left\{N_{\text{point}}\log(2\pi) + N_{\text{point}}\log(\sigma^2) + \frac{1}{\sigma^2}\sum_{i} = 1^{N_{\text{point}}}\left(y - f(x_i,\theta)\right)^2\right\} \tag{B.13}$$

$$= \arg\min_{\theta}\left\{\sum_{i=1}^{N_{\text{point}}}\left(y_i - f(x_i,\theta)\right)^2\right\} \tag{B.14}$$

From the minimized error sum of squares, we can further estimate the variance

$$\hat{\sigma}^2 = \frac{1}{N_{\text{point}}}\sum_{i=1}^{N_{\text{point}}}\left(y_i - f(x_i,\hat{\theta})\right)^2 \tag{B.15}$$

If Eqs. (B.14) and (B.15) are substituted into Eq. (B.11), the maximum log-likelihood holds

$$\mathcal{LL}(\hat{\beta}) = -\frac{N_{\text{point}}}{2}\left(\log(2\pi) + \log(\hat{\sigma}^2) + 1\right) \tag{B.16}$$

$$= -\frac{N_{\text{point}}}{2}\left(\log(2\pi) + \log\left(\frac{1}{N_{\text{point}}}\sum_{i=1}^{N_{\text{point}}}(y_i - f(x_i,\hat{\theta}))^2\right) + 1\right) \tag{B.17}$$

$$= -\frac{N_{\text{point}}}{2}\left(\log(2\pi) + \log\left(RSS\right) + 1\right) \tag{B.18}$$

The relationship just obtained can be substituted into the definition of AIC from Eq. (B.2), yielding the following relationship for AIC for the special case of independent, identical, and normally distributed errors.

$$AIC = 2p - 2\log(\mathcal{L}) \tag{B.19}$$

As mentioned at the beginning, the absolute AIC values are not meaningful. The information content of the AIC is only unfolded by relations between the tested models of the model set. First, the AIC difference ΔAIC_i can be determined.

$$\Delta AIC_i = AIC_i - \min(AIC) \tag{B.20}$$

This indicates how large the difference between a model i and the best model j of the examined model set is. With the help of this formula the Akaike weights w_i can be calculated (Burnham and Anderson 2004):

$$w_i(AIC) = \frac{\exp(-0.5\Delta_i(AIC))}{\sum_k^K \exp(-0.5\Delta_k(AIC))} \tag{B.21}$$

The Akaike weights can be interpreted as a kind of probability with which model i is selected as the best one among those tested. The larger w_i is for a model, the smaller is the information loss between model i and the true mechanism. Further information criteria and modifications of the AIC are described by Burnham (Burnham and Anderson 2004).

B.3 Bootstrapping of Confidence Intervals

For estimating the confidence intervals of the estimated parameters of the deactivation and the regeneration kinetics, a bootstrapping algorithm has been used. Bootstrap methods describe resampling algorithms (Efron and Tibshirani 1998; Gentle 2009). The fundamental idea is, that all information about an underlying population is contained in an observed sample. Statistics about the underlying population can hence be simulated by using random samples from the original sample. Different methods of resampling are possible. The resampling method used in this contribution is semi-parametric resampling (Carpenter and Bithell 2000). It involves random resampling of the residuals r of a parametric model with the responses $y = (y_1, ..., y_n)$. A general representation of the model is given by:

$$y = g(\theta) + r \tag{B.22}$$

Fitting of the model gives the estimate $\hat{\theta}$ of the parameters θ and a set of residuals r_i with $i \in \{1, ..., n\}$. The resampling algorithm is as follows.

1. Sample with replacement from the residuals r. The new set of residuals is called bootstrap errors $r^* = (r_1^*, ...r_n^*)$.

2. Generate a bootstrap data set y^* by adding the bootstrap errors to the model values:

$$y^* = g(\hat{\theta}) + r^* \tag{B.23}$$

3. Fit the model

$$E(y^*) = g(\theta) \tag{B.24}$$

   using the bootstrap data set y^* to obtain a bootstrap estimate $\hat{\theta}^*$

4. Repeat Steps $1-3$ for $B = 1500$ times to obtain the bootstrap distribution of the estimated parameter.

Based on this parameter distribution the confidence intervals of the estimated parameters can be calculated (DiCiccio et al. 1996). A non-studentized pivotal method is used (Carpenter and Bithell 2000; Joshi et al. 2006). This method argues that the behavior of the distribution $W = \hat{\theta} - \theta$ is mirrored by the behavior of $W^* = \hat{\theta}^* - \hat{\theta}$. For a known distribution W it would be possible to find a quantile $w_{\frac{\alpha}{2}}$ such that $P(W \leq w_{\frac{\alpha}{2}}) = \frac{\alpha}{2}$. A two sided $1 - \alpha$ confidence interval would be

$$\left(\hat{\theta} - w_{\frac{\alpha}{2}}, \hat{\theta} + w_{1-\frac{\alpha}{2}}\right) \tag{B.25}$$

Since the "true distribution" W is not known, the quantiles $w_{\frac{\alpha}{2}}$ and $w_{1-\frac{\alpha}{2}}$ are replaced by the approximate quantiles $w^*_{\frac{\alpha}{2}}$ and $w^*_{1-\frac{\alpha}{2}}$ from the bootstrap distribution W^*:

$$\left(\hat{\theta}^* - w_{\frac{\alpha}{2}}, \hat{\theta}^* + w_{1-\frac{\alpha}{2}}\right) \tag{B.26}$$

In this contribution the 95 % confidence intervals have been calculated ($\alpha = 0.05$). An advantage of bootstrapping methods is their simplicity, which allow to adapt them for a wide range of applications. The major disadvantage is that the methods are generally computationally costly. Alternative methods to calculate confidence intervals analytically may be more efficient, such as the nlparci[1] function implemented in MATLAB. This function deploys the Jacobian, given by the lsqnonlin[2] function that has been used for fitting the models in this contribution (LevenbergMarquardt algorithm). Problems arise, when the Jacobian is not invertible[3]. Since bootstrapping algorithms are more robust they have been chosen in this study. Nevertheless, the results of the nlparci function can be used for verification of confidence intervals estimated by bootstrapping. Tab. B.2 summarizes the confidence intervals estimated by both methods for the kinetic parameter of the deactivation of the VO_x catalyst with propene. The confidence intervals estimated with the different methods are in good agreement, which proofs the applicability and validity of the applied methodology for this problem.

Table B.2: Optimized parameters of model C5 to describe the coking behavior of the VO_x catalyst using propene.

Parameter	Opt. Value	Confidence Intervals			Unit
		nlparci	bootstrapping		
$c_{\max}$	17.695	±1.61 %	−1.54 %	+1.35 %	% $\left(\frac{\mathrm{kg_{coke}}}{\mathrm{kg_{cat}}} \times 100\right)$
l	0.275	±1.94 %	−2.05 %	+1.55 %	-
k_0	9.59×10^5	±34.44 %	−29.71 %	+33.72 %	$(\mathrm{kg_{coke}\,kg_{cat}^{-1}\,min^{-1}})^{1-h}$
E_A	139022	±1.78 %	−1.92 %	+1.35 %	$\mathrm{J\,mol^{-1}}$
h	1.106	±2.32 %	−2.79 %	+1.47 %	-
k_{des}	3.22×10^{-3}	±3.24 %	−2.24 %	+4.09 %	$\mathrm{min^{-1}}$
c_0	5.994	±5.21 %	−4.47 %	+5.17 %	% $\left(\frac{\mathrm{kg_{coke}}}{\mathrm{kg_{cat}}} \times 100\right)$

It has to be noted, that there are other methods for estimating confidence intervals via bootstrapping which are described in literature (Chernick 2008). As an example, the distribution of the bootstrap parameters $\hat{\theta}^*$ together with the optimal parameter $\hat{\theta}$ and the estimated confidence intervals are illustrated in Fig. B.2. The numbers in the bins of the histograms in Fig. B.2 have been normalized by dividing them by $B = 1500$ to obtain the frequencies, that are easier to interpret. The optimal parameters are also listed in Table 8.

---

[1] See https://de.mathworks.com/help/stats/nlparci.html for further information

[2] See https://de.mathworks.com/help/optim/ug/lsqnonlin.html for further information

[3] A non-invertible Jacobian might be singular or singular to working precision. nlparci deploys QR decomposition to the Jacobian. For a non-invertible Jacobian this results in R being not a full upper triangle matrix which can therefore not be inverted

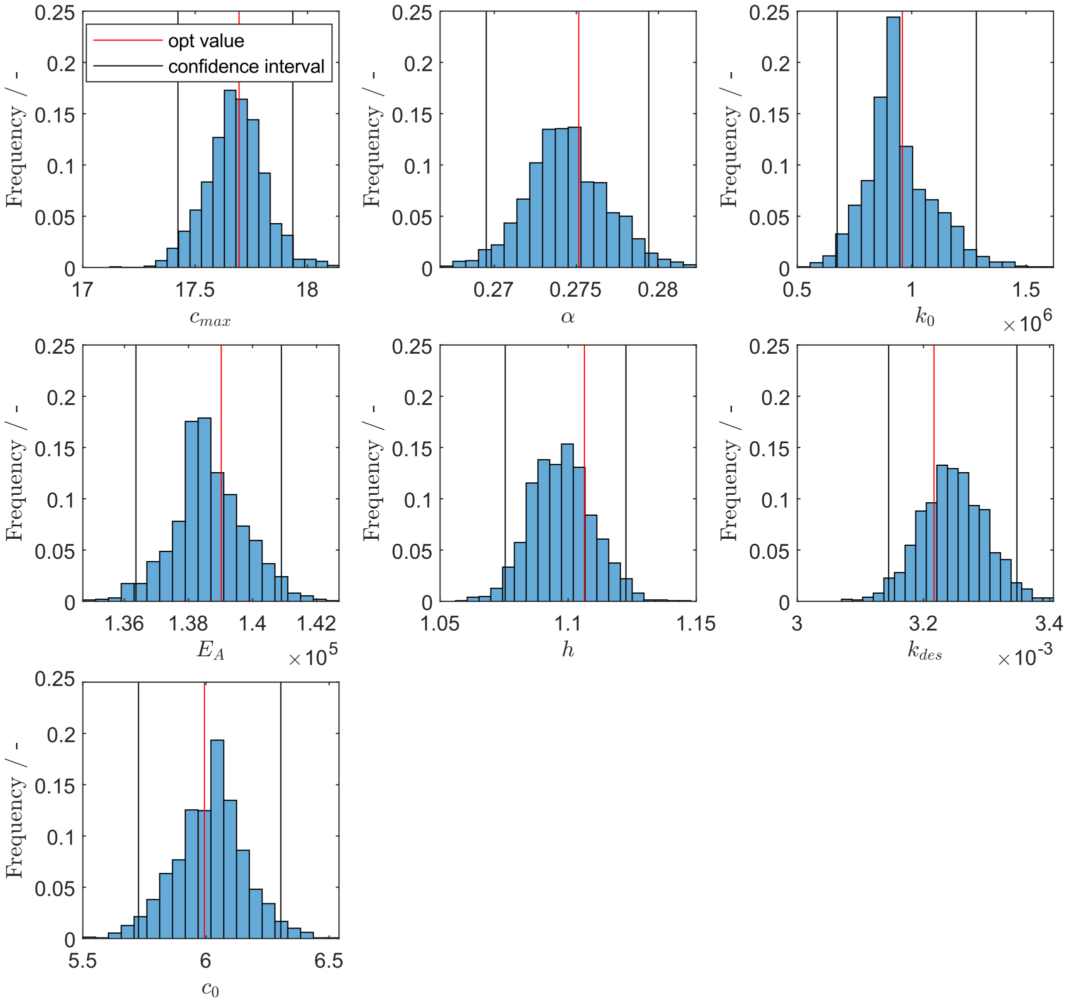

Figure B.2: Histograms of the distribution of the parameters of the bootstrapping process of model (C5) of the deactivation of the VO_x catalyst with propene.

B.4 Periodic Experiments and Validation

The diagrams in Fig. B.3 and Fig. B.4 illustrate the results of the periodic experiments (2) and (3) described in section 3.2.3. The experimental conditions are summarized in Tab. 3.14. Periodic experiment (1) is illustrated in Fig. 3.13.

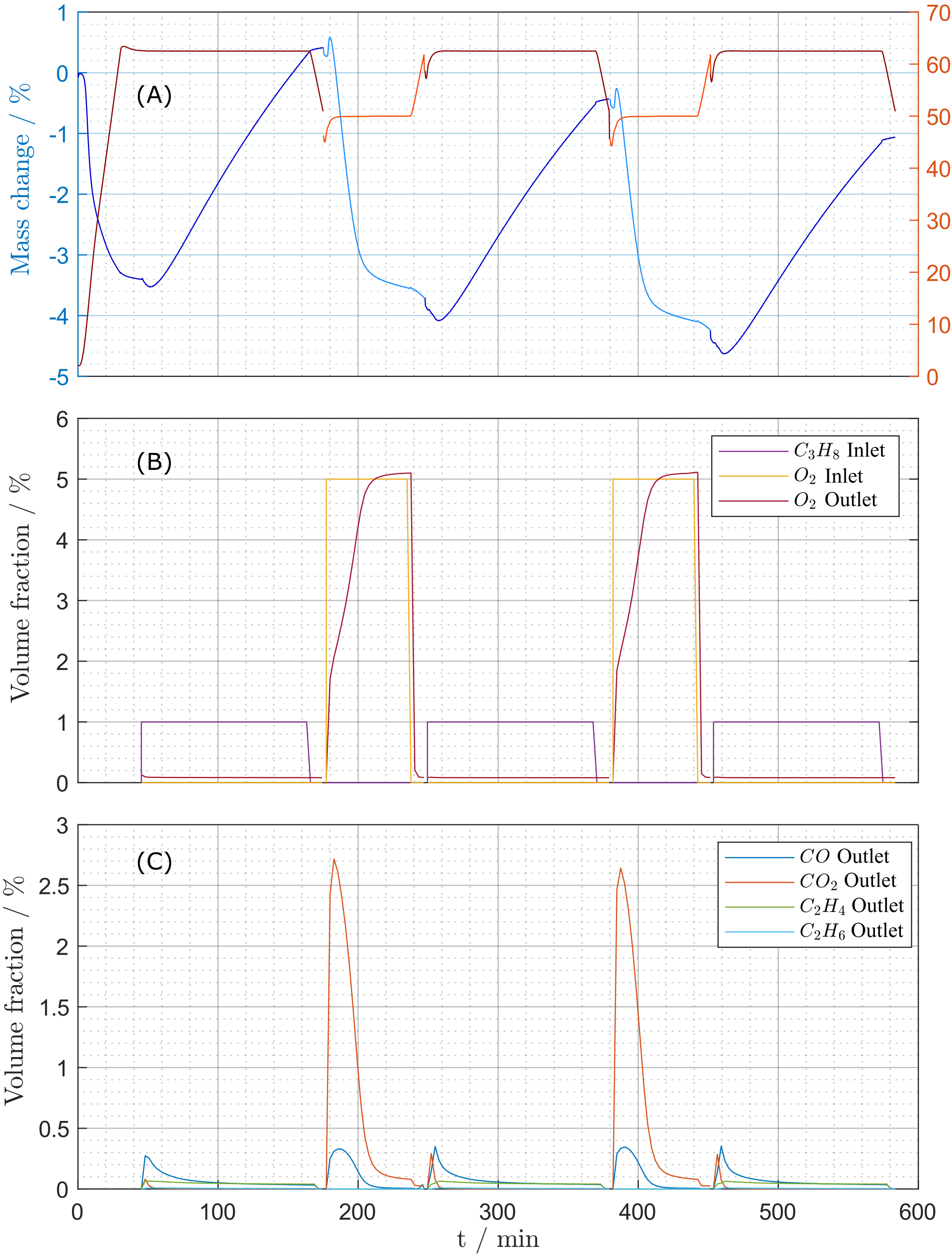

Figure B.3: Measurements during periodic experiments: (A) mass changes (TGA) and temperature, (B) oxygen and propane concentrations, (C) CO, CO_2, ethene and ethane concentrations for periodic experiment (2).

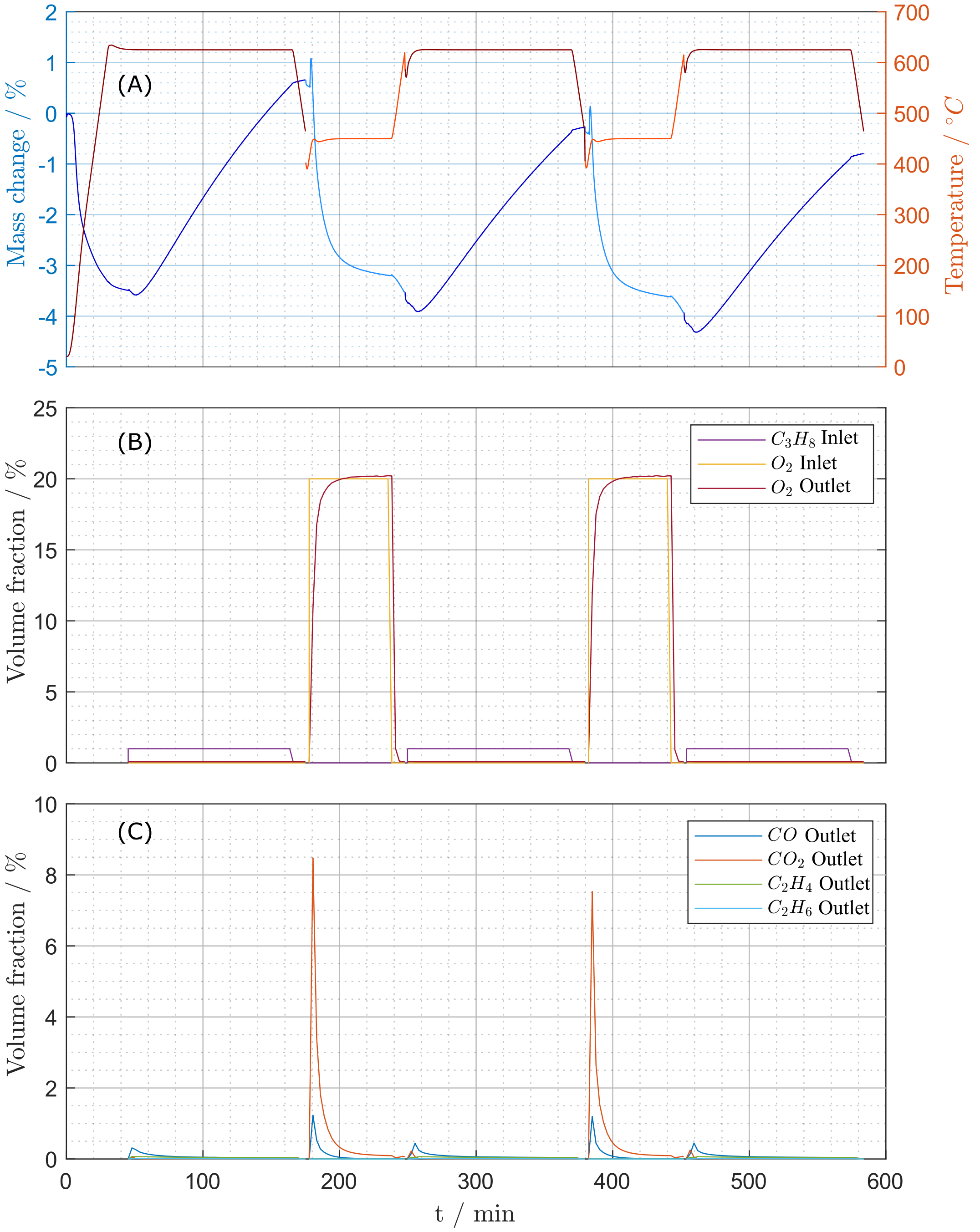

Figure B.4: Measurements during periodic experiments: (A) mass changes (TGA) and temperature, (B) oxygen and propane concentrations, (C) CO, CO_2, ethene and ethane concentrations for periodic experiment (3).

B.5 Experimental Results: Deactivation Experiments

$$S_{\mathrm{C_3H_6}} = \frac{3c_{\mathrm{C_3H_6}}}{3c_{\mathrm{C_3H_6}} + c_{\mathrm{CO}} + c_{\mathrm{CO_2}}} \tag{B.27}$$

$$S_{\mathrm{CO}} = \frac{c_{\mathrm{CO}}}{3c_{\mathrm{C_3H_6}} + c_{\mathrm{CO}} + c_{\mathrm{CO_2}}} \tag{B.28}$$

$$S_{\mathrm{CO_2}} = \frac{c_{\mathrm{CO_2}}}{3c_{\mathrm{C_3H_6}} + c_{\mathrm{CO}} + c_{\mathrm{CO_2}}} \tag{B.29}$$

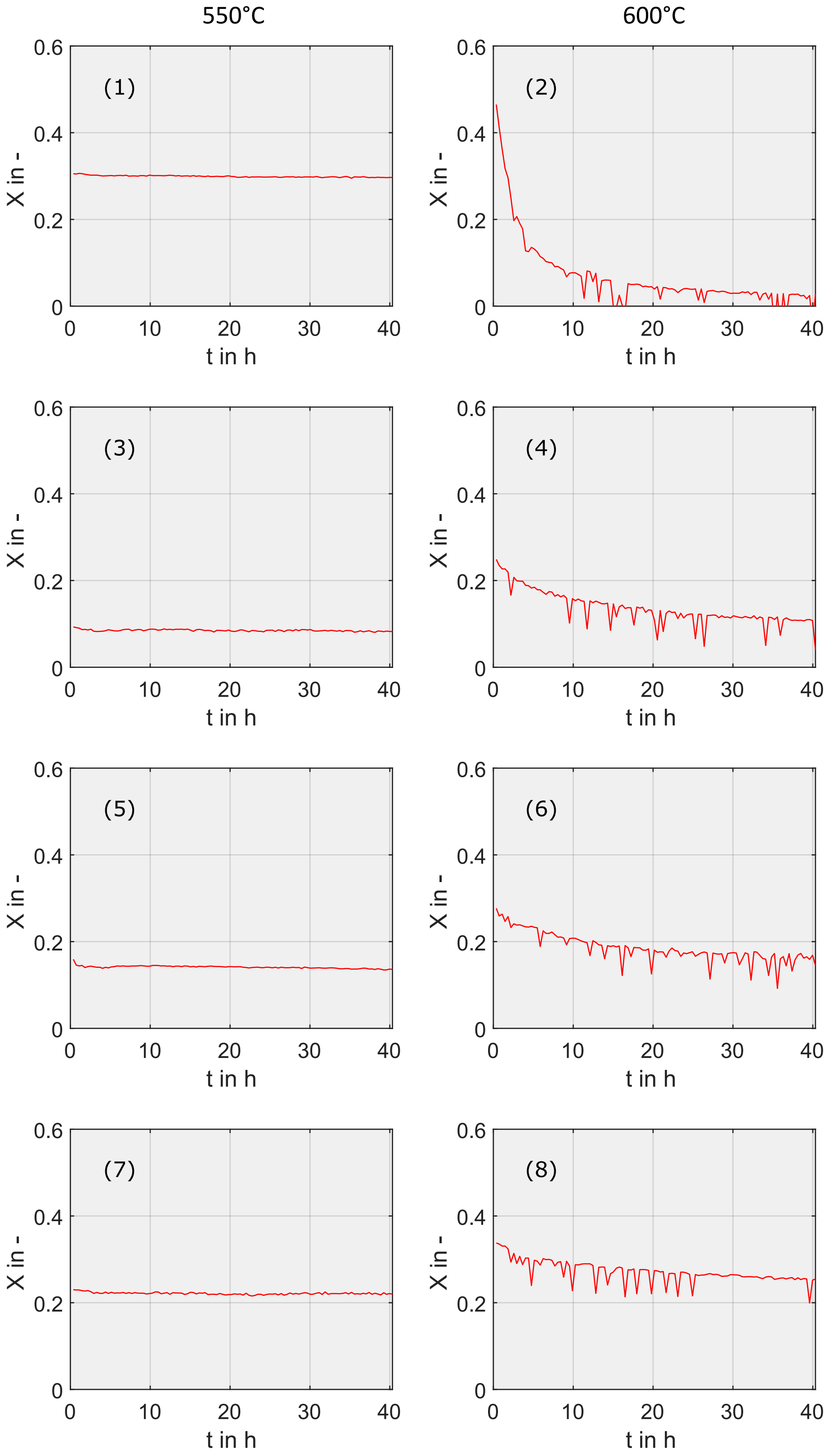

Figure B.5: Experimental determined conversion of propane in the Experiments (1) – (8) (see Table 3.16).

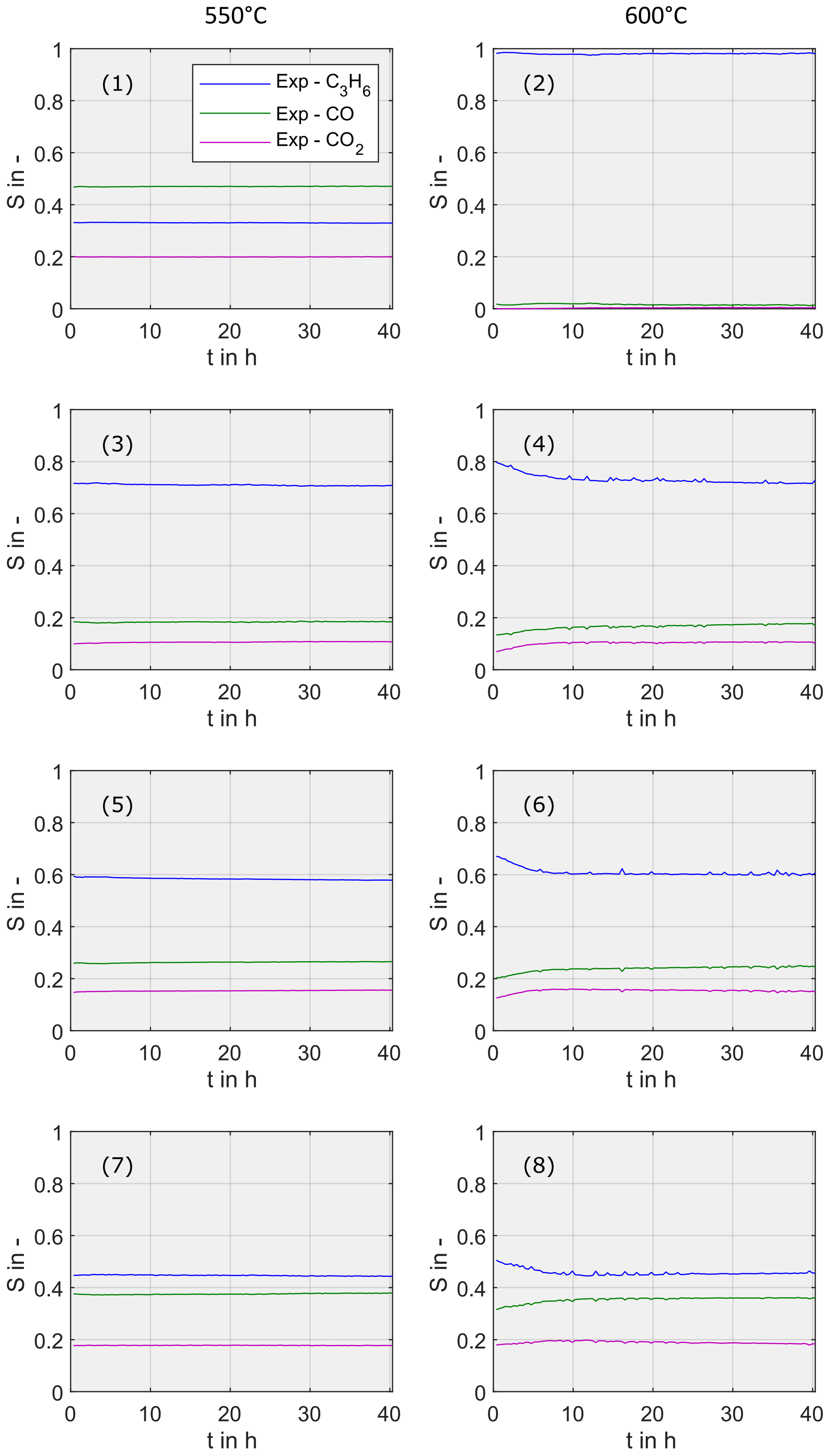

Figure B.6: Experimental determined selectivities of propene and the side products CO and CO2 in the Experiments (1) – (8) (see Table 3.16).

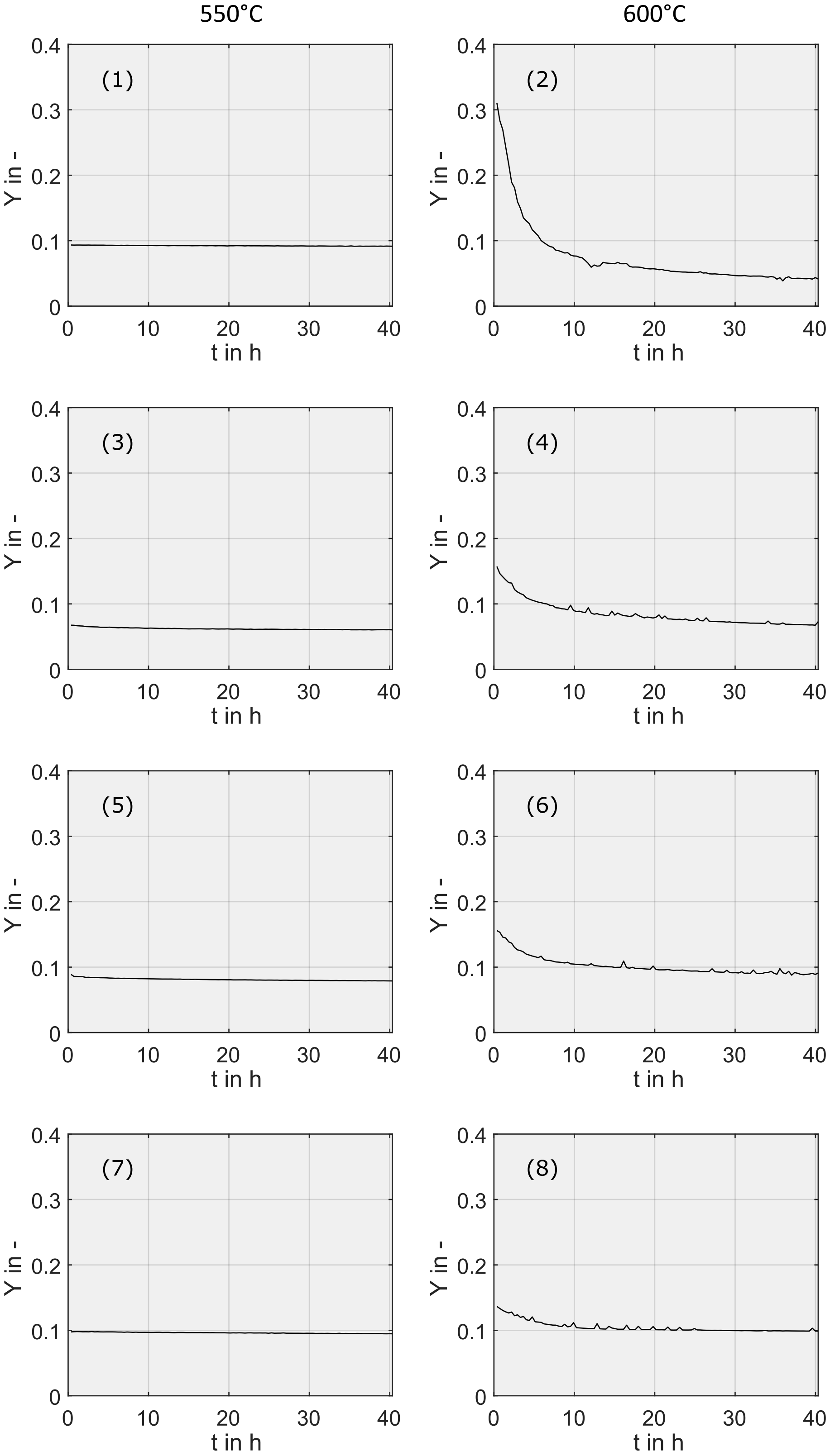

Figure B.7: Experimental determined yield of propene in the Experiments (1) – (8) (see Table 3.16).

B.6 Phenomenological Approach

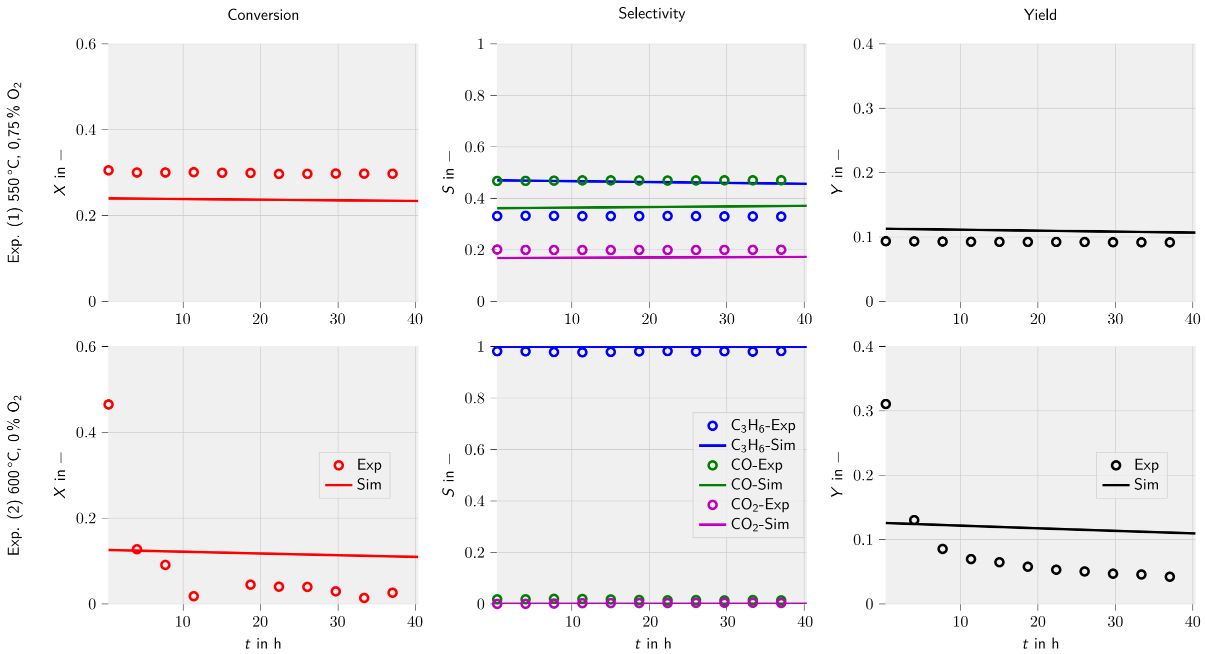

Figure B.8: Comparison of experimental and simulated performance parameters (model J1) for experiment (1): $T_{\mathrm{prod}} = 550\,^{\circ}\mathrm{C}$, $x_{\mathrm{O_2,in}} = 0.75\,\%$, $x_{\mathrm{C_3H_8,in}}) = 1\,\%$; and (2): $T_{\mathrm{prod}} = 600\,^{\circ}\mathrm{C}$, $x_{\mathrm{O_2,in}} = 0\,\%$, $x_{\mathrm{C_3H_8,in}} = 1\,\%$.

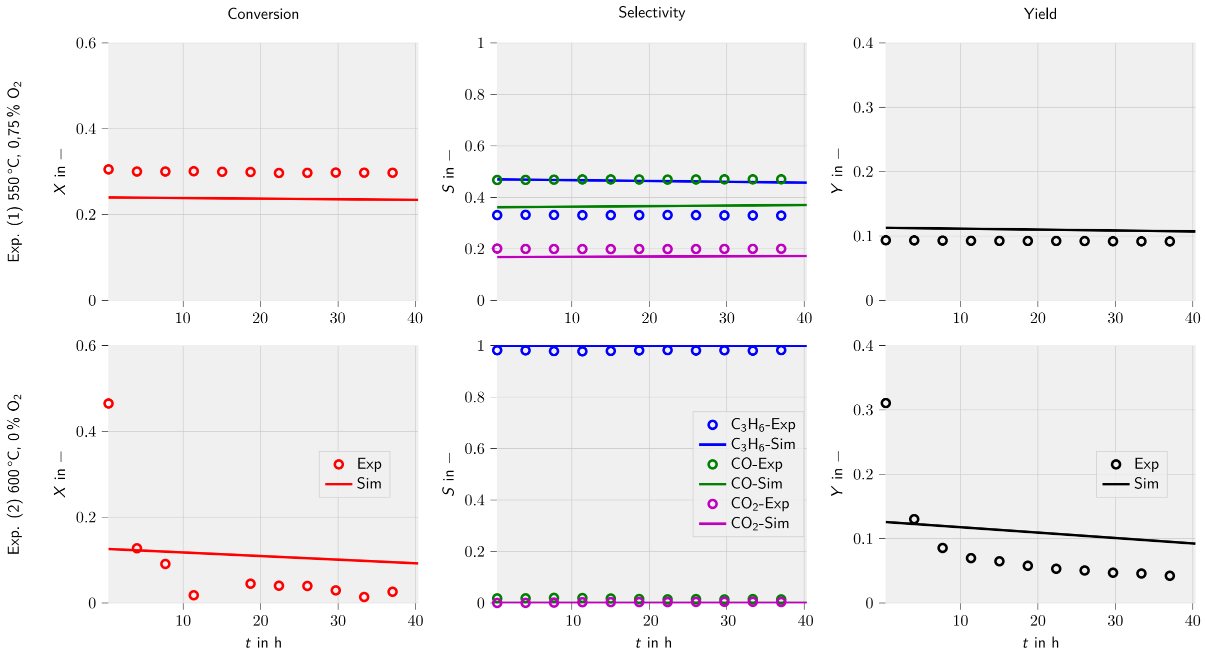

Figure B.9: Comparison of experimental and simulated performance parameters (model J2) for experiment (1): $T_{\mathrm{prod}} = 550\,^{\circ}\mathrm{C}$, $x_{\mathrm{O_2,in}} = 0.75\,\%$, $x_{\mathrm{C_3H_8,in}}) = 1\,\%$; and (2): $T_{\mathrm{prod}} = 600\,^{\circ}\mathrm{C}$, $x_{\mathrm{O_2,in}} = 0\,\%$, $x_{\mathrm{C_3H_8,in}} = 1\,\%$.

B.7 Coke Based Approach

B.7.1 Discretization

$$\frac{dc_i}{dt} = -\frac{d(uc_i)}{dz} + \sum_{i=1}^{K} \nu_{i,j} r_{j,0}(t = t_{\mathrm{deact},0}) \tag{B.30}$$

$$\frac{dc_i}{dt} = -v_{\mathrm{in}} \frac{d(c_i)}{dz} + \sum_{i=1}^{K} \nu_{i,j} a_j r_{j,0}(t = t_{\mathrm{deact},0}) \tag{B.31}$$

Forward difference quotient (Strehmel et al. 2012; Schäfer 2006)

$$\frac{df(x)}{dx} \approx \frac{f(x + \Delta x) - f(x)}{\Delta x} \tag{B.32}$$

Using Eq. (B.32) to discretize Eq. (B.31) in the nth volume element leads to

$$\frac{dc_{i,n}}{dt} = -v_{\mathrm{in}} \frac{c_{i,n+1} - c_{i,n}}{\Delta z} + \sum_{i=1}^{K} \nu_{i,j} a_j r_{j,0}, \quad n \in [2, N] \tag{B.33}$$

The length of the discrete element Δz is calculated as

$$\Delta z = \frac{L}{N} \tag{B.34}$$

Eq. (B.33) can not be used for the first volume element. To consider the boundary conditions, in this case the inlet concentrations $c_{i,\mathrm{in}}$, Eq. (B.33) has to be modified:

$$\frac{dc_{i,1}}{dt} = -v_{\mathrm{in}} \frac{c_{i,1} - c_{i,\mathrm{in}}}{\Delta z} + \sum_{i=1}^{K} \nu_{i,j} a_j r_{j,0} \tag{B.35}$$

For the calculations presented in the paper we used $N = 64$ volume elements.

B.7.2 Results

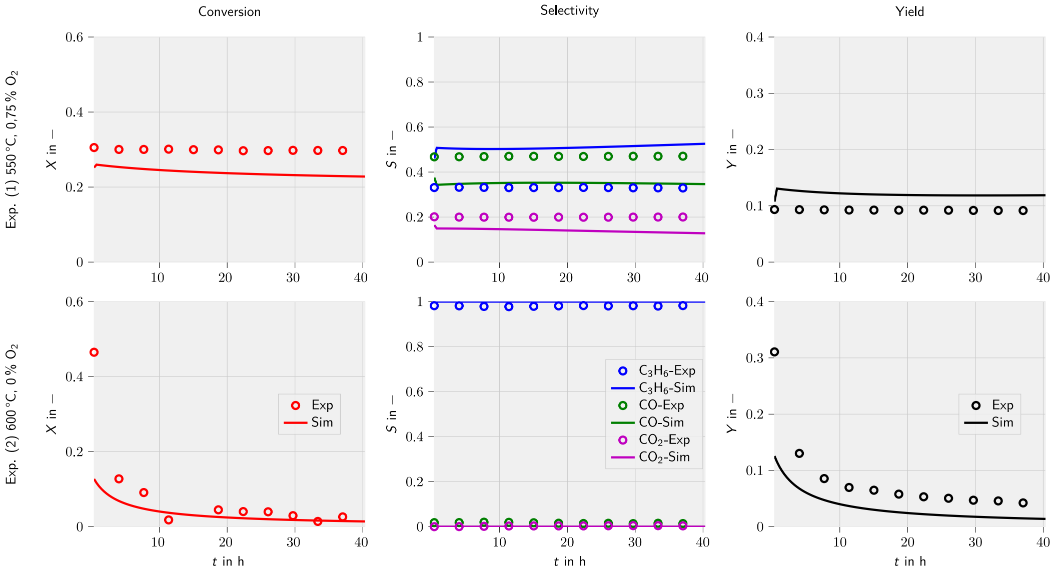

Figure B.10: Comparison of experimental and simulated values (model DF4) for experiment (1): $T_{\mathrm{prod}} = 550\,°\mathrm{C}$, $x_{\mathrm{O_2,in}} = 0.75\,\%$, $x_{\mathrm{C_3H_8,in}} = 1\,\%$; and (2): $T_{\mathrm{prod}} = 600\,°\mathrm{C}$, $x_{\mathrm{O_2,in}} = 0\,\%$, $x_{\mathrm{C_3H_8,in}} = 1\,\%$.

Qualitative Description of the Coke Loading
Modified stochiometric matrix for distinction of propene stemming from the ODH and the TDH reaction

$$\nu = \begin{array}{cccc|l} R1 & R2 & R3 & R4 & \\ -1 & -1 & 0 & 0 & \mathrm{C_3H_8} \\ 0 & -0.5 & -3 & -4.5 & \mathrm{O_2} \\ 0 & 1 & -\Phi_{\mathrm{ODH}} & -\Phi_{\mathrm{ODH}} & \mathrm{C_3H_6}^{(\mathrm{ODH})} \\ 0 & 1 & 3 & 3 & \mathrm{H_2O} \\ 1 & 0 & 0 & 0 & \mathrm{H_2} \\ 0 & 0 & 0 & 3 & \mathrm{CO} \\ 0 & 0 & 3 & 0 & \mathrm{CO_2} \\ 0 & 0 & 0 & 0 & \mathrm{N_2} \\ 1 & 0 & -\Phi_{\mathrm{TDH}} & -\Phi_{\mathrm{TDH}} & \mathrm{C_3H_6}^{(\mathrm{TDH})} \end{array} \tag{B.36}$$

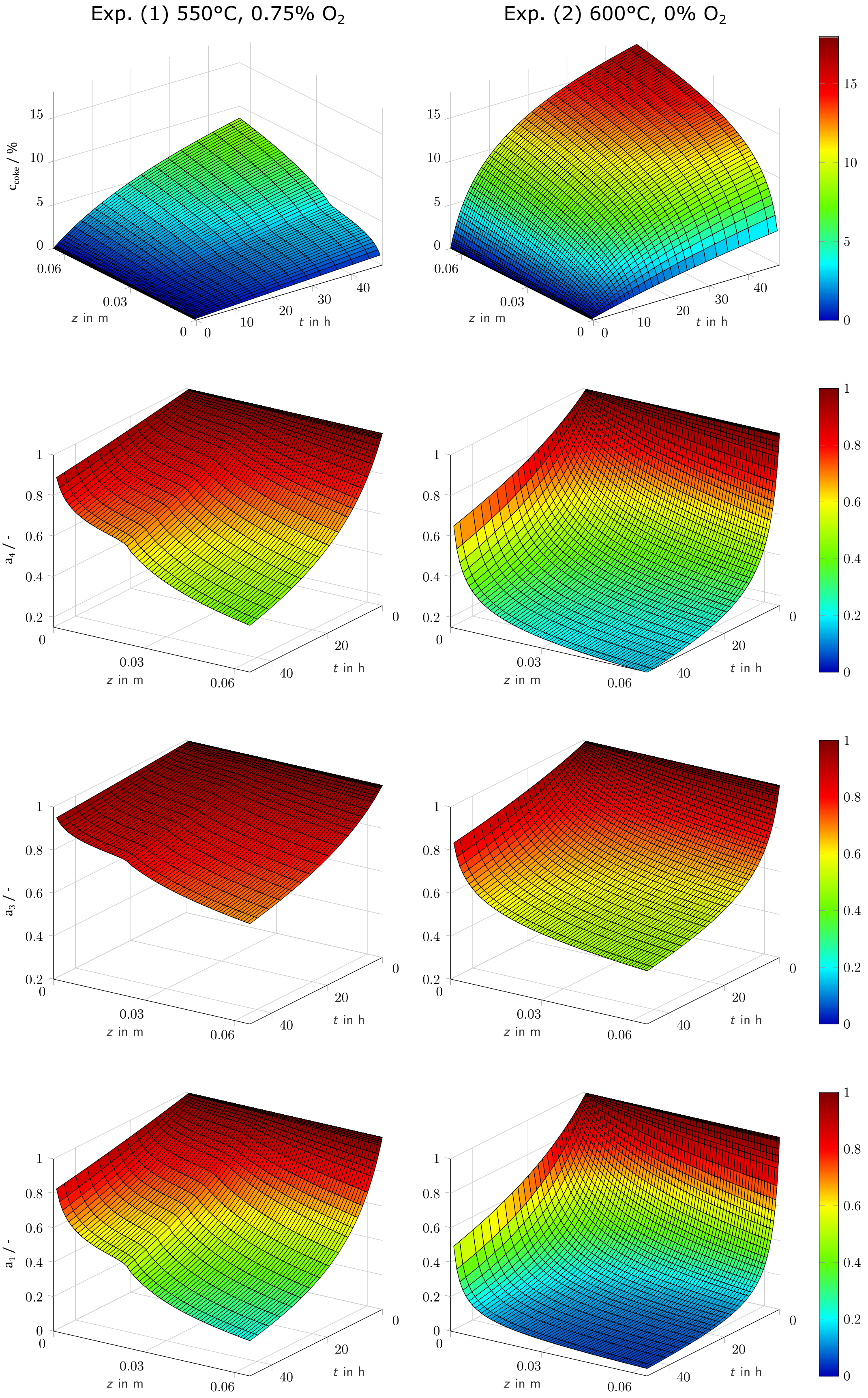

Figure B.11: Simulated coke and activity profiles using model DF4* TDH.

B.8 Optimization

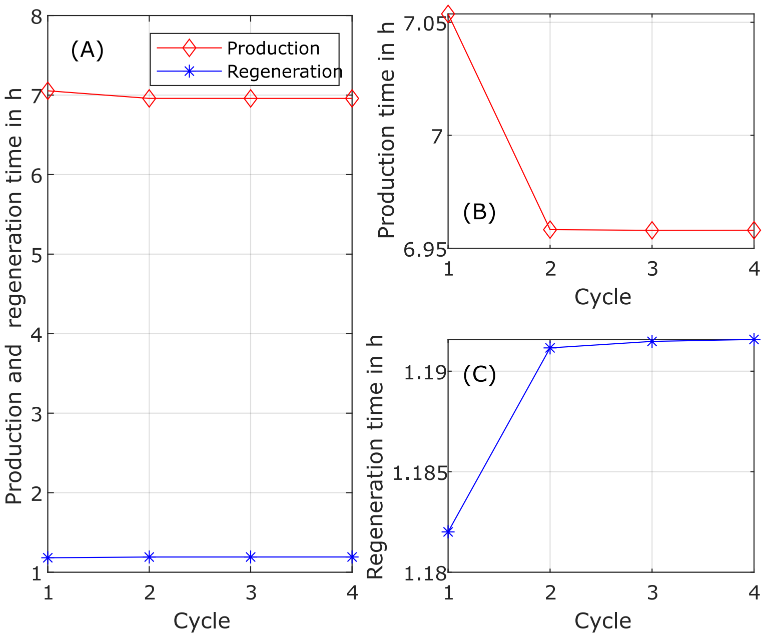

Figure B.12: (A) Regeneration and production times of the corresponding phases during propane dehydrogenation; (B) Detail: Productions times, (C) Detail: Regeneration times; ($T_{\mathrm{prod}} = 550\,°\mathrm{C}$, $x_{\mathrm{C_3H_8,in}} = 1\,\%$, $x_{\mathrm{O_2,prod}} = 0\,\%$, $T_{\mathrm{reg}} = 500\,°\mathrm{C}$, $x_{\mathrm{O_2,reg}} = 1\,\%$).

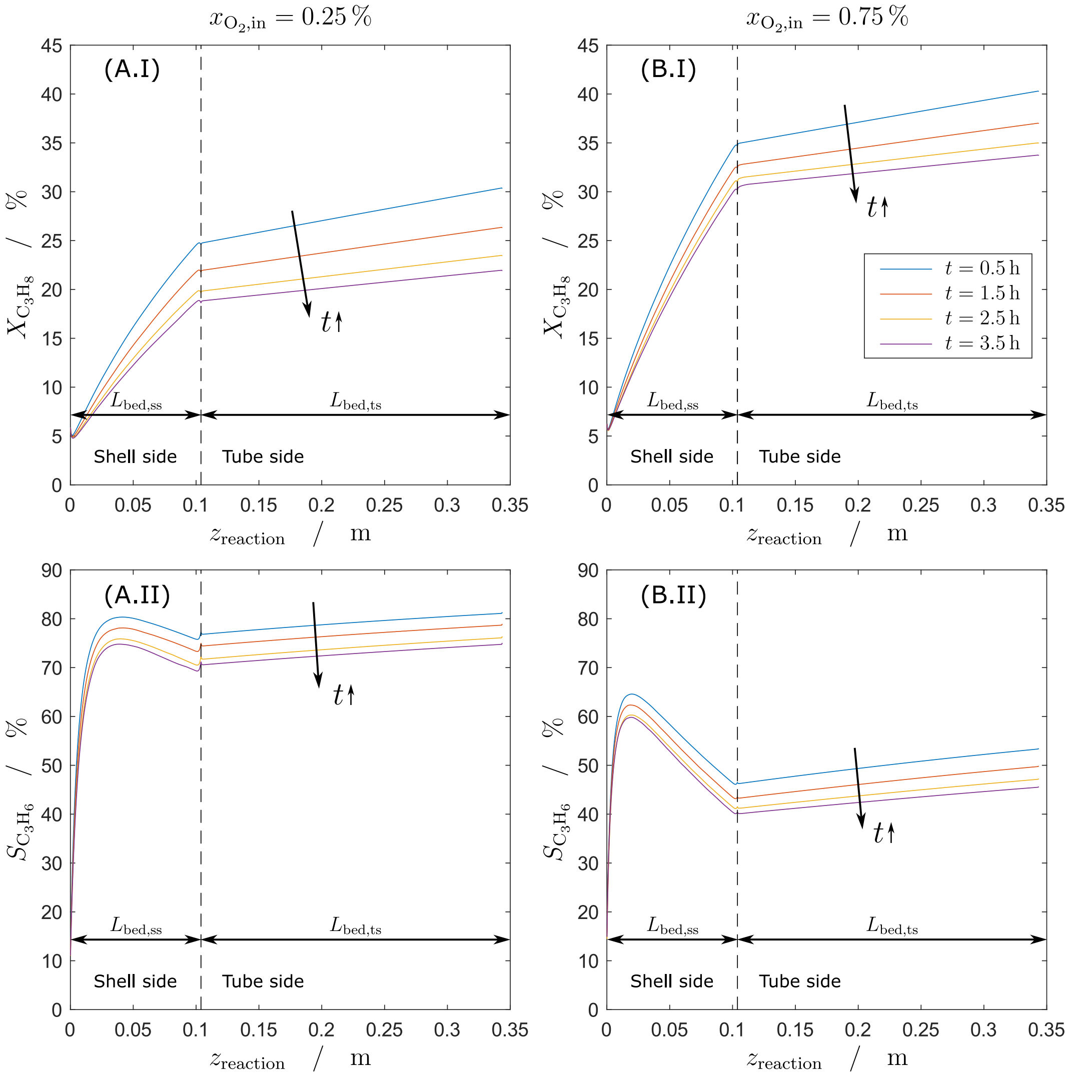

Figure B.13: Simulated propane conversion (I) and propene selectivity (II) at different times on stream (0.5 h, 1.5 h, 2.5 h and 3.5 h) with an oxygen inlet concentration of (A) $c_{O_2,in} = 0.25\,\%$ and (B) $c_{O_2,in} = 0.75\,\%$ ($T_{wall} = T_{in} = 600\,°C$, $c_{C_3H_8,in} = 1\,\%$, $\dot{V}_{TS} : \dot{V}_{SS} = 1:8$, $WHSV = 400\,kg\,s\,m^{-3}$).

C Appendix to Chapter 5

C.1 P&ID and Engineering Drawings of Pilot Scale Reactors and Pilot Plant

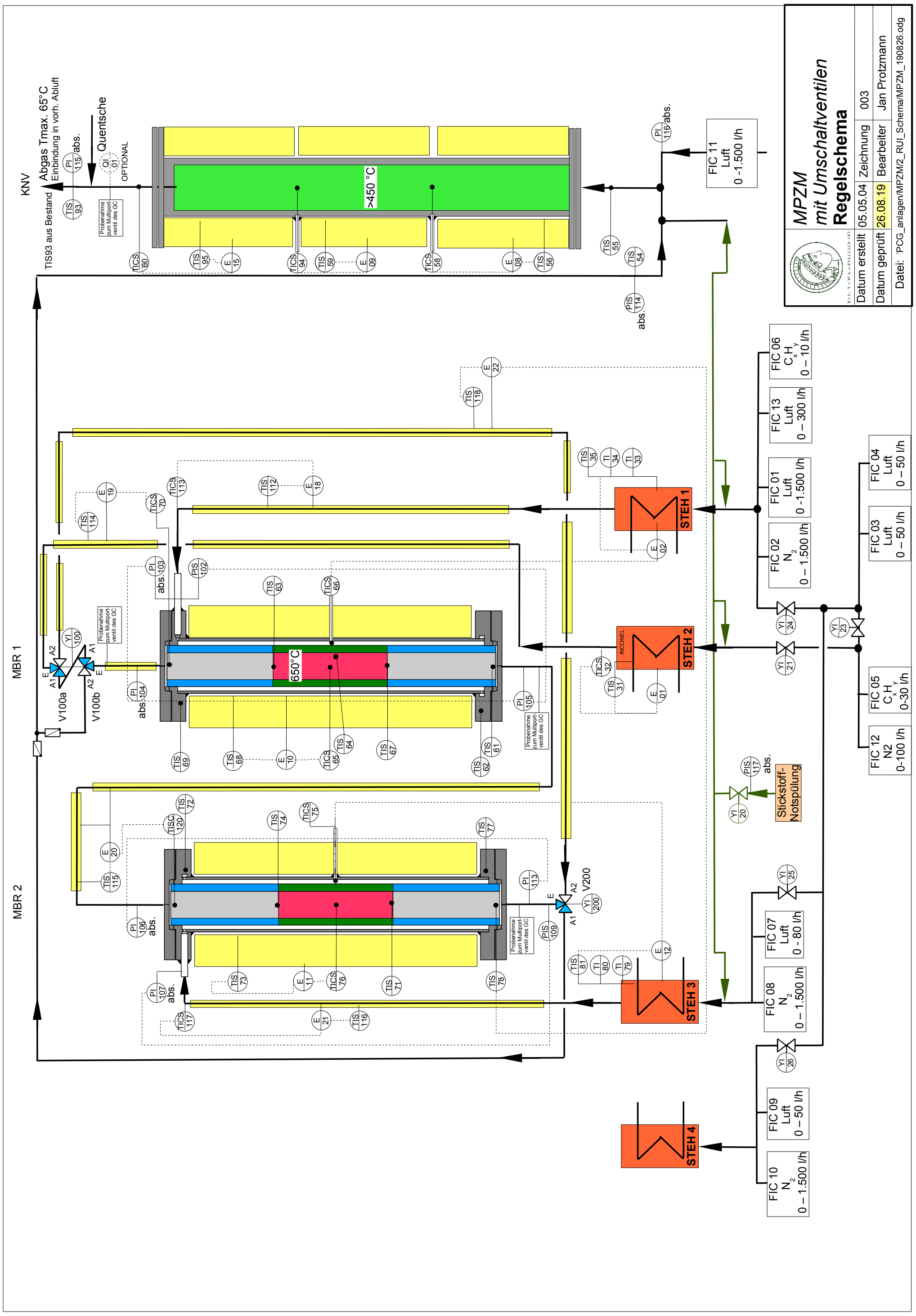
MPZM
mit Umschaltventilen
Regelschema
Datum erstellt 05.05.04
Zeichnung 003
Datum geprüft 26.08.19
Bearbeiter Jan Protzmann
Datei: PCG_anlagen/MPZM/2_RUI_Schema/MPZM_190826.odg
KNV
TIS93 aus Bestand
Abgas Tmax. 65°C Einbindung in vorh. Abluft
Quentsche
OPTIONAL
>450 °C
MBR 1
MBR 2
650°C
V100a
V100b
V200
Probenahme zum Multiport-ventil des GC
STEH 1
STEH 2
STEH 3
STEH 4
INCONEL
Stickstoff-Notspülung
FIC 11 Luft 0 -1.500 l/h
FIC 06 CxHy 0 – 10 l/h
FIC 13 Luft 0 – 300 l/h
FIC 01 Luft 0 -1.500 l/h
FIC 02 N2 0 – 1.500 l/h
FIC 04 Luft 0 – 50 l/h
FIC 03 Luft 0 – 50 l/h
FIC 05 CxHy 0-30 l/h
FIC 12 N2 0-100 l/h
FIC 07 Luft 0 - 80 l/h
FIC 08 N2 0 – 1.500 l/h
FIC 09 Luft 0 – 50 l/h
FIC 10 N2 0 – 1.500 l/h

Figure C.1: Piping and instrumentation diagram (P&ID) of pilot plant used for single PBMR/FBR and reactor cascade experiments.

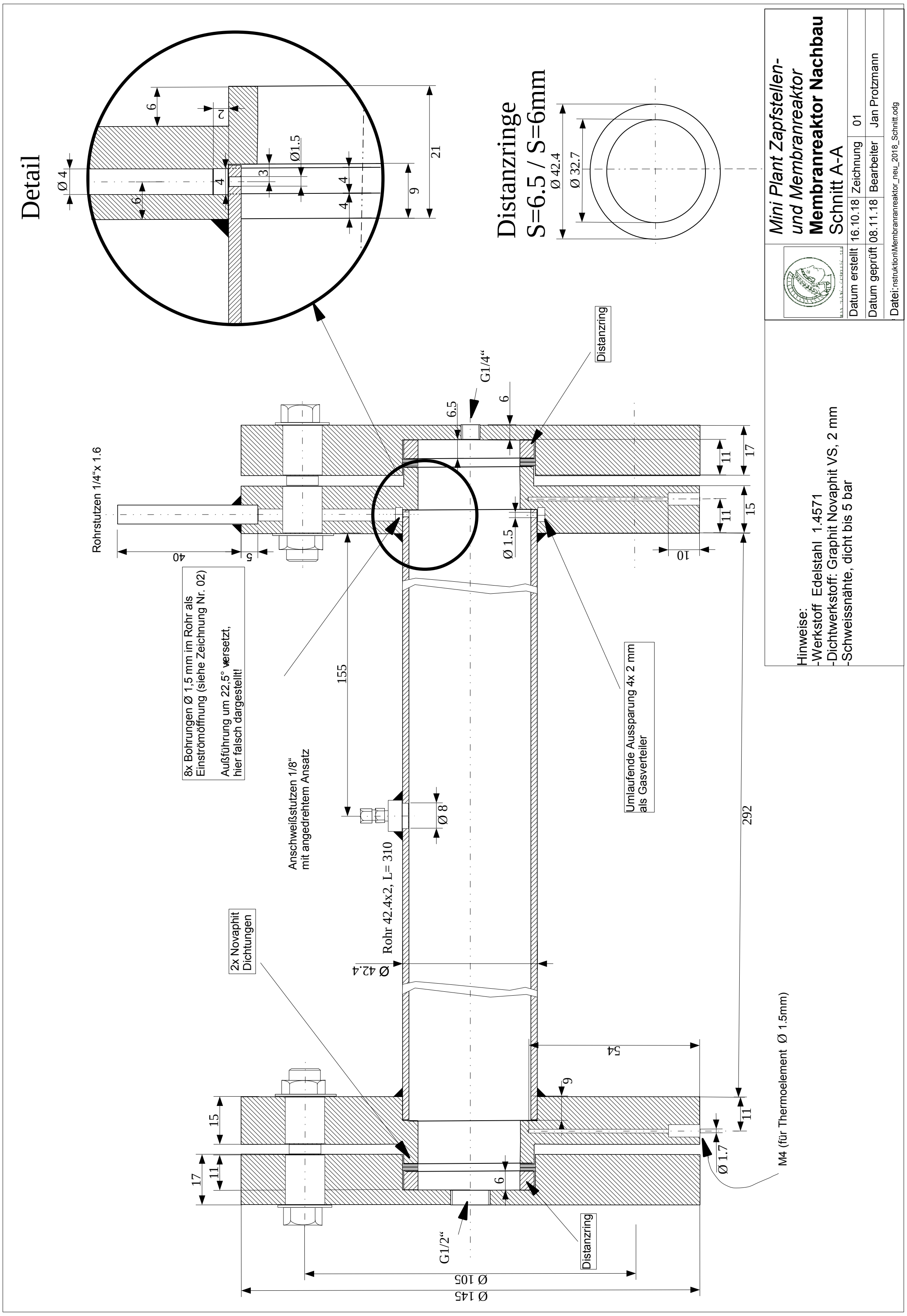
Mini Plant Zapfstellen- und Membranreaktor
Membranreaktor Nachbau
Schnitt A-A
Datum erstellt 16.10.18
Zeichnung 01
Datum geprüft 08.11.18
Bearbeiter Jan Protzmann
Datei: nstruktion\Membranreaktor_neu_2018_Schnitt.odg
Hinweise:
-Werkstoff Edelstahl 1.4571
-Dichtwerkstoff: Graphit Novaphit VS, 2 mm
-Schweissnähte, dicht bis 5 bar
Detail
Distanzringe
S=6.5 / S=6mm
Ø 42.4
Ø 32.7
Ø 4
Ø1.5
21
Distanzring
G1/4“
G1/2“
Rohrstutzen 1/4“x 1.6
8x Bohrungen Ø 1,5 mm im Rohr als Einströmöffnung (siehe Zeichnung Nr. 02)
Außführung um 22,5° versetzt, hier falsch dargestellt!
Anschweißstutzen 1/8“ mit angedrehtem Ansatz
Rohr 42.4x2, L= 310
Ø 42.4
Ø 8
155
292
54
2x Novaphit Dichtungen
Umlaufende Aussparung 4x 2 mm als Gasverteiler
M4 (für Thermoelement Ø 1.5mm)
Ø 1.7
Ø 1.5
6.5
Ø 105
Ø 145
40
17
15
11
10

Figure C.2: Engineering drawing of reactor used as FBR and PBMR.

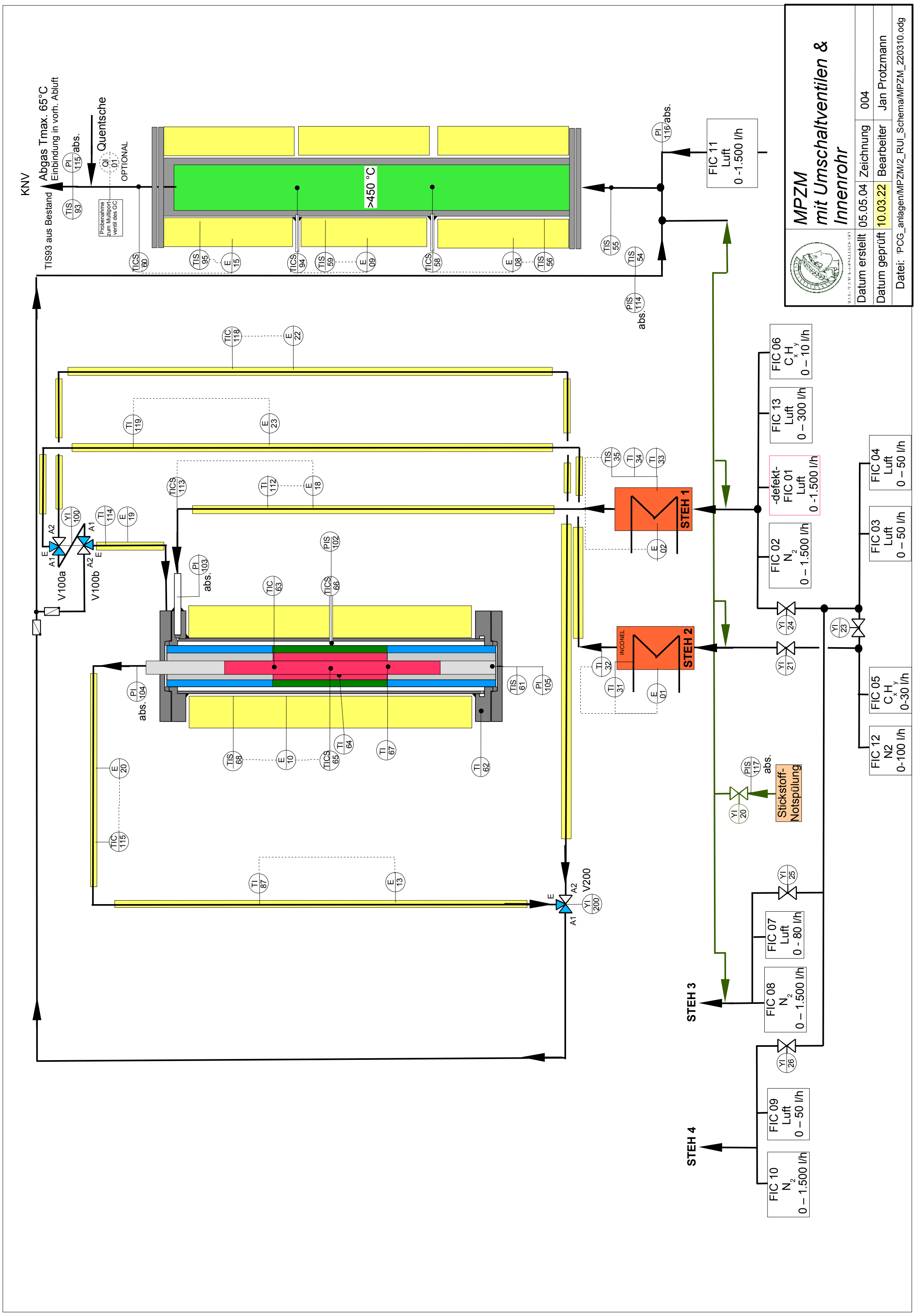
MPZM
mit Umschaltventilen & Innenrohr
Datum erstellt 05.05.04
Zeichnung 004
Datum geprüft 10.03.22
Bearbeiter Jan Protzmann
Datei: PCG_anlagen/MPZM/2_RUI_Schema/MPZM_220310.odg
KNV
Abgas Tmax. 65°C
Einbindung in vorh. Abluft
TIS93 aus Bestand
Quentsche
OPTIONAL
>450 °C
STEH 1
STEH 2
STEH 3
STEH 4
INCONEL
V100a
V100b
V200
Stickstoff-Notspülung
FIC 11 Luft 0 -1.500 l/h
FIC 06 C_xH_y 0 – 10 l/h
FIC 13 Luft 0 – 300 l/h
-defekt- FIC 01 Luft 0 -1.500 l/h
FIC 02 N_2 0 – 1.500 l/h
FIC 04 Luft 0 – 50 l/h
FIC 03 Luft 0 – 50 l/h
FIC 05 C_xH_y 0-30 l/h
FIC 12 N2 0-100 l/h
FIC 07 Luft 0 - 80 l/h
FIC 08 N_2 0 – 1.500 l/h
FIC 09 Luft 0 – 50 l/h
FIC 10 N_2 0 – 1.500 l/h

Figure C.3: Piping and instrumentation diagram (P&ID) of pilot plant used for PBMRint experiments.

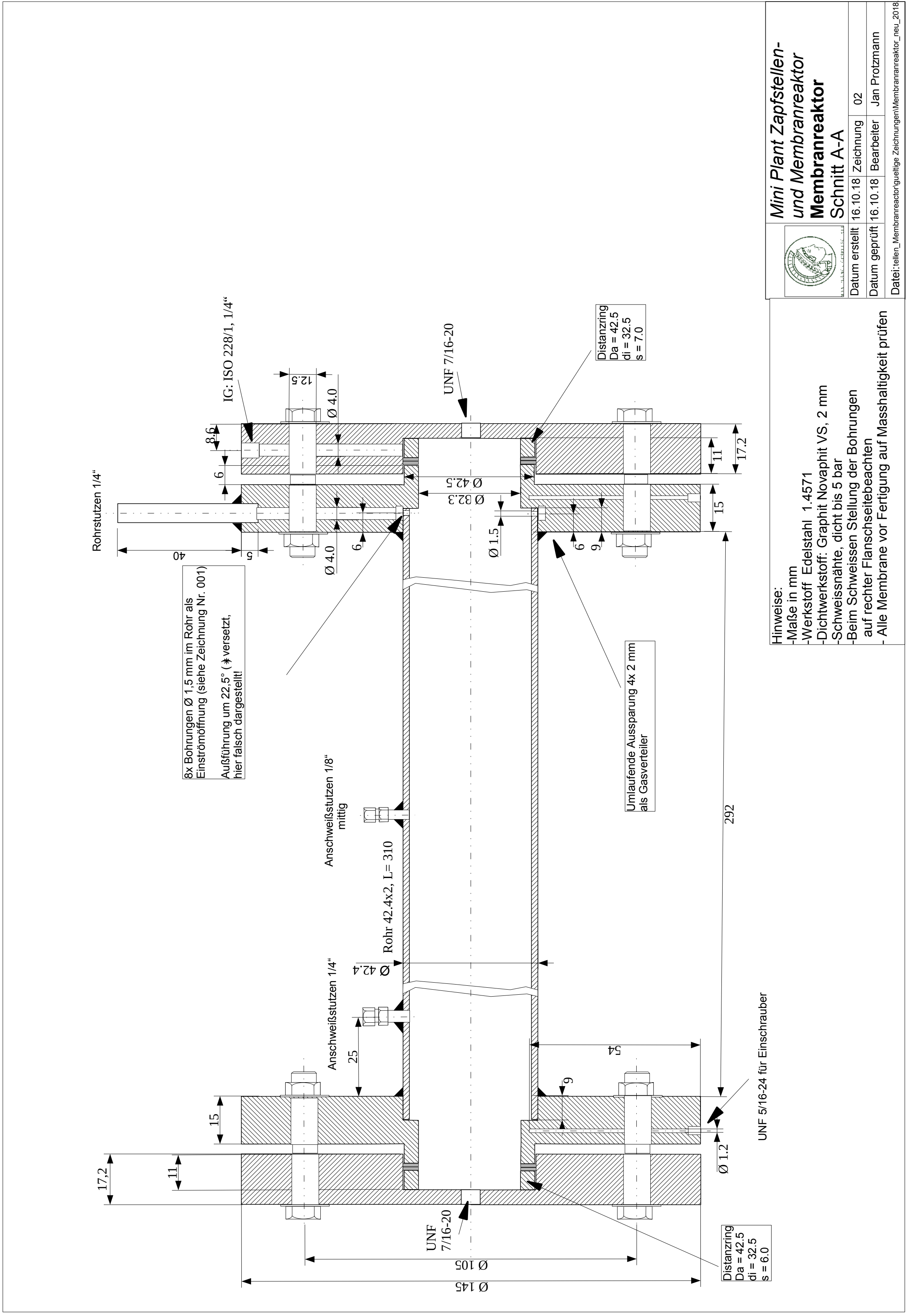
Mini Plant Zapfstellen-
und Membranreaktor
Membranreaktor
Schnitt A-A
Datum erstellt 16.10.18 Zeichnung 02
Datum geprüft 16.10.18 Bearbeiter Jan Protzmann
Datei: tellen_Membranreactor\gueltige Zeichnungen\Membranreaktor_neu_2018.o
Hinweise:
-Maße in mm
-Werkstoff Edelstahl 1.4571
-Dichtwerkstoff: Graphit Novaphit VS, 2 mm
-Schweissnähte, dicht bis 5 bar
-Beim Schweissen Stellung der Bohrungen
auf rechter Flanschseitebeachten
- Alle Membrane vor Fertigung auf Masshaltigkeit prüfen
Rohrstutzen 1/4"
IG: ISO 228/1, 1/4"
UNF 7/16-20
Distanzring
Da = 42.5
di = 32.5
s = 7.0
8x Bohrungen Ø 1,5 mm im Rohr als Einströmöffnung (siehe Zeichnung Nr. 001)
Außführung um 22,5° (✱versetzt, hier falsch dargestellt!
Umlaufende Aussparung 4x 2 mm als Gasverteiler
Anschweißstutzen 1/8" mittig
Anschweißstutzen 1/4"
Rohr 42.4x2, L= 310
Ø 42.4
Ø 42.5
Ø 32.3
Ø 1.5
Ø 4.0
Ø 4.0
12.5
8.6
6
6
40
5
6
9
11
17.2
15
292
25
54
9
15
11
17,2
Ø 1.2
UNF 5/16-24 für Einschrauber
UNF 7/16-20
Distanzring
Da = 42.5
di = 32.5
s = 6.0
Ø 105
Ø 145

Figure C.4: Engineering drawing of reactor used as PBMRint.

C.2 1D Simulations of Reactor Cascades in Pilot Scale

The simulations presented in this section are based on the 1D models derived in Section 2.3.1. Isothermal conditions were assumed. The models are not able to represent the radial profiles that form strongly in membrane reactors. In addition to the weaknesses of the kinetics used, which have already been discussed, this is the reason for the limited validity of the results. Nevertheless, general trends with variation of the reaction conditions in the simulation results can be compared with the experimental results.

C.2.1 FBR-FBR Reactor Cascade

Table C.1: Results of 1D simulations of the first reactor and of the whole FBR-FBR reactor cascade: Variation of the inlet oxygen concentration ($T_1 = 550\,°\mathrm{C}$, $T_2 = 600\,°\mathrm{C}$, $x_{\mathrm{C_3H_8,in}} = 1\,\%$, $WHSV = 400\,\mathrm{kg\,s\,m^{-3}}$)

$x_{\mathrm{O_2}}$	$X_{\mathrm{C_3H_8,FBR\ 1}}$	$S_{\mathrm{C_3H_6,FBR\ 1}}$	$Y_{\mathrm{C_3H_6,FBR\ 1}}$	$X_{\mathrm{C_3H_8,total}}$	$S_{\mathrm{C_3H_6,total}}$	$Y_{\mathrm{C_3H_6,total}}$
0.25 %	17.09 %	67.09 %	11.47 %	29.21 %	80.75 %	23.59 %
0.5 %	23.23 %	48.68 %	11.31 %	34.87 %	65.81 %	22.95 %
1 %	33.98 %	27.26 %	9.26 %	44.72 %	44.73 %	20.00 %
1.5 %	44.33 %	15.22 %	6.75 %	54.14 %	30.59 %	16.56 %
2.5 %	55.73 %	4.46 %	2.49 %	72.81 %	12.89 %	9.38 %

Table C.2: Results of 1D simulations of the first reactor and of the whole FBR-FBR reactor cascade: Variation of reaction temperatures ($x_{\mathrm{O_2,in}} = 0.5\,\%$, $x_{\mathrm{C_3H_8,in}} = 1\,\%$, $WHSV = 400\,\mathrm{kg\,s\,m^{-3}}$)

$T_{\mathrm{R1}}/T_{\mathrm{R2}}$	$X_{\mathrm{C_3H_8,FBR\ 1}}$	$S_{\mathrm{C_3H_6,FBR\ 1}}$	$Y_{\mathrm{C_3H_6,FBR\ 1}}$	$X_{\mathrm{C_3H_8,total}}$	$S_{\mathrm{C_3H_6,total}}$	$Y_{\mathrm{C_3H_6,total}}$
550 °C/600 °C	23.23 %	48.68 %	11.31 %	34.87 %	65.81 %	22.95 %
575 °C/625 °C	26.15 %	54.52 %	14.26 %	42.26 %	71.86 %	30.37 %
600 °C/650 °C	30.07 %	60.54 %	18.20 %	51.57 %	76.99 %	39.71 %

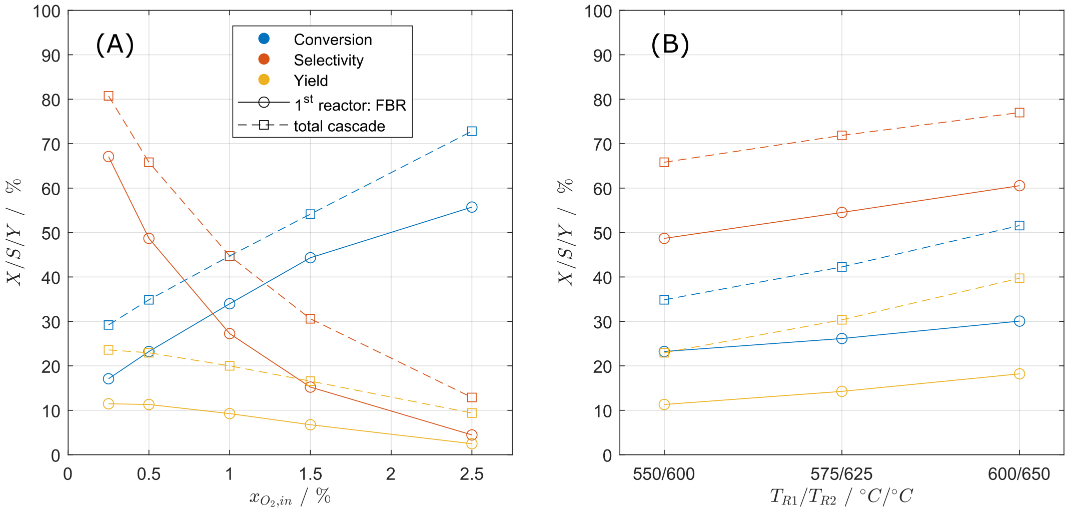

Figure C.5: Simulated conversion and yield of the first reactor and total conversion and yield of the FBR-FBR reactor cascade (1D model); (A): Variation of the inlet oxygen concentration ($T_1 = 550\,°\mathrm{C}$, $T_2 = 600\,°\mathrm{C}$); (B): Variation of reactor temperature ($x_{\mathrm{C_3H_8,in}} = 1\,\%$, $WHSV = 400\,\mathrm{kg\,s\,m^{-3}}$)

C.2.2 PBMR-FBR Reactor Cascade

Table C.3: Results of 1D simulations of the first reactor and of the whole PBMR-FBR reactor cascade: Variation of the inlet oxygen concentration ($T_1 = 550\,°\mathrm{C}$, $T_2 = 600\,°\mathrm{C}$, $x_{\mathrm{C_3H_8,in}} = 1\,\%$, $WHSV = 400\,\mathrm{kg\,s\,m^{-3}}$)

$x_{\mathrm{O_2}}$	$X_{\mathrm{C_3H_8,PBMR}}$	$S_{\mathrm{C_3H_6,PBMR}}$	$Y_{\mathrm{C_3H_6,PBMR}}$	$X_{\mathrm{C_3H_8,total}}$	$S_{\mathrm{C_3H_6,total}}$	$Y_{\mathrm{C_3H_6,total}}$
0.25 %	66.59 %	48.30 %	32.16 %	74.08 %	53.53 %	39.66 %
0.5 %	66.92 %	46.11 %	30.86 %	74.37 %	51.51 %	38.31 %
1 %	69.15 %	39.53 %	27.33 %	76.33 %	45.22 %	34.51 %
1.5 %	73.96 %	31.82 %	23.53 %	80.51 %	37.36 %	30.08 %
2.5 %	80.06 %	9.38 %	7.51 %	86.05 %	14.25 %	12.26 %

Table C.4: Results of 1D simulations of the first reactor and of the whole PBMR-FBR reactor cascade: Variation of the inlet oxygen concentration ($T_1 = 575\,°\mathrm{C}$, $T_2 = 625\,°\mathrm{C}$, $x_{\mathrm{C_3H_8,in}} = 1\,\%$, $WHSV = 400\,\mathrm{kg\,s\,m^{-3}}$)

$x_{\mathrm{O_2}}$	$X_{\mathrm{C_3H_8,PBMR}}$	$S_{\mathrm{C_3H_6,PBMR}}$	$Y_{\mathrm{C_3H_6,PBMR}}$	$X_{\mathrm{C_3H_8,total}}$	$S_{\mathrm{C_3H_6,total}}$	$Y_{\mathrm{C_3H_6,total}}$
0.25 %	78.69 %	38.12 %	30.00 %	86.85 %	43.94 %	38.16 %
0.5 %	78.89 %	35.92 %	28.34 %	87.01 %	41.90 %	36.46 %
1 %	79.20 %	30.99 %	24.55 %	87.26 %	37.36 %	32.60 %
1.5 %	82.56 %	25.28 %	20.87 %	89.84 %	31.34 %	28.15 %
2.5 %	87.04 %	6.97 %	6.06 %	93.31 %	12.41 %	11.58 %

Table C.5: Results of 1D simulations of the first reactor and of the whole PBMR-FBR reactor cascade: Variation of reaction temperatures ($x_{O_2,\mathrm{in}} = 0.5\,\%$, $x_{C_3H_8,\mathrm{in}} = 1\,\%$, $WHSV = 400\,\mathrm{kg\,s\,m^{-3}}$)

T_{R1}/T_{R2}	$X_{C_3H_8,\mathrm{PBMR\ 1}}$	$S_{C_3H_6,\mathrm{PBMR\ 1}}$	$Y_{C_3H_6,\mathrm{PBMR\ 1}}$	$X_{C_3H_8,\mathrm{total}}$	$S_{C_3H_6,\mathrm{total}}$	$Y_{C_3H_6,\mathrm{total}}$
550 °C/600 °C	66.92 %	46.11 %	30.86 %	74.37 %	51.51 %	38.31 %
575 °C/625 °C	78.89 %	35.92 %	28.34 %	87.01 %	41.90 %	36.46 %
600 °C/650 °C	88.56 %	25.15 %	22.27 %	96.05 %	30.99 %	29.77 %

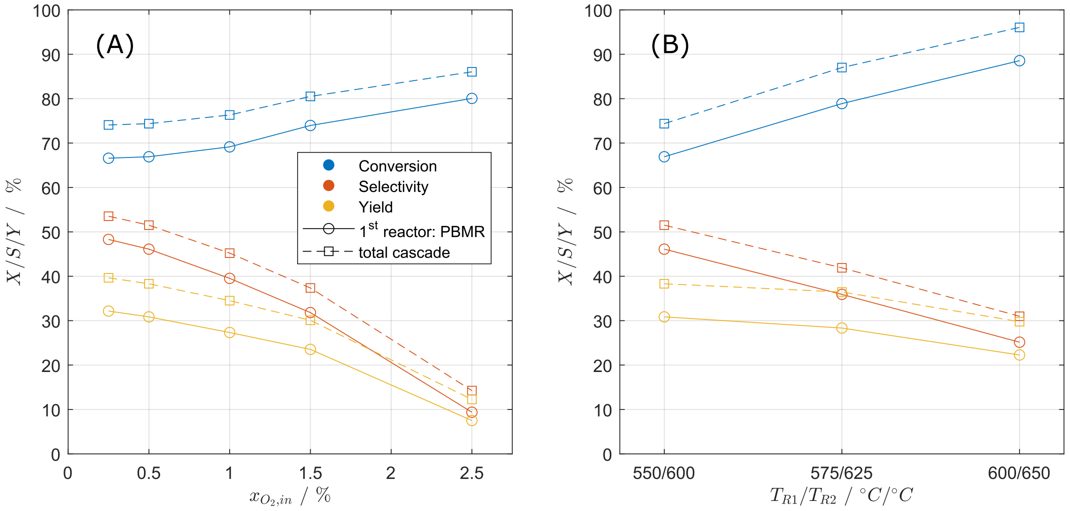

Figure C.6: Simulated conversion and yield of the first reactor and total conversion and yield of the PBMR-FBR reactor cascade (1D model); (A): Variation of the inlet oxygen concentration ($T_1 = 550\,°\mathrm{C}$, $T_2 = 600\,°\mathrm{C}$); (B): Variation of reactor temperature ($x_{C_3H_8,\mathrm{in}} = 1\,\%$, $WHSV = 400\,\mathrm{kg\,s\,m^{-3}}$)

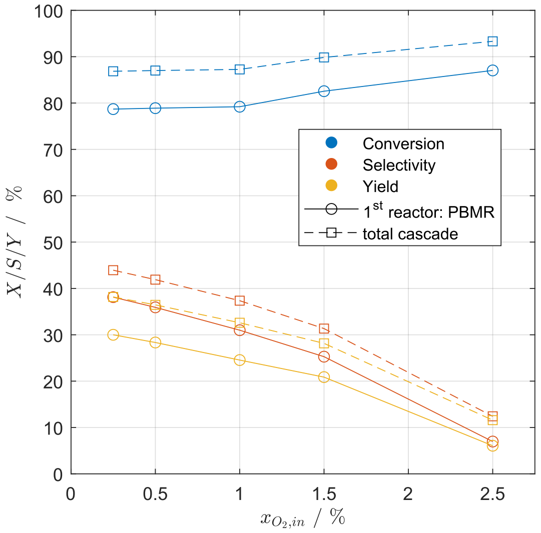

Figure C.7: Simulated conversion and yield of the first reactor and total conversion and yield of the PBMR-FBR reactor cascade (1D model)at different inlet oxygen concentration ($T_1 = 575\,°\mathrm{C}$, $T_2 = 625\,°\mathrm{C}$, $x_{C_3H_8,\mathrm{in}} = 1\,\%$, $WHSV = 400\,\mathrm{kg\,s\,m^{-3}}$)

Table C.6: PBMR ($x_{\mathrm{O_2,in}} = 0.5\,\%$, $x_{\mathrm{C_3H_8,in}} = 1\,\%$, $WHSV = 400\,\mathrm{kg\,s\,m^{-3}}$)

Temperature	1D			2D		
	$X_{\mathrm{C_3H_8}}$	$S_{\mathrm{C_3H_6}}$	$Y_{\mathrm{C_3H_6}}$	$X_{\mathrm{C_3H_8}}$	$S_{\mathrm{C_3H_6}}$	$Y_{\mathrm{C_3H_6}}$
550 °C	66.92 %	46.11 %	30.86 %	22.10 %	47.59 %	10.52 %
575 °C	78.89 %	35.92 %	28.34 %	26.12 %	53.59 %	14.00 %
600 °C	88.56 %	25.15 %	22.27 %	31.18 %	60.74 %	18.94 %

Table C.7: PBMR ($x_{\mathrm{O_2,in}} = 0.75\,\%$, $x_{\mathrm{C_3H_8,in}} = 1\,\%$, $WHSV = 400\,\mathrm{kg\,s\,m^{-3}}$)

Temperature	1D			2D		
	$X_{\mathrm{C_3H_8}}$	$S_{\mathrm{C_3H_6}}$	$Y_{\mathrm{C_3H_6}}$	$X_{\mathrm{C_3H_8}}$	$S_{\mathrm{C_3H_6}}$	$Y_{\mathrm{C_3H_6}}$
550 °C	67.19 %	42.76 %	28.73 %	25.58 %	38.98 %	9.97 %
575 °C	79.06 %	33.76 %	26.69 %	29.74 %	43.66 %	12.98 %
600 °C	88.33 %	24.02 %	21.22 %	34.80 %	49.94 %	17.38 %

C.3 Experimental Results of Pilot Scale Experiments

C.3.1 Experiments Without Membrane Dosing

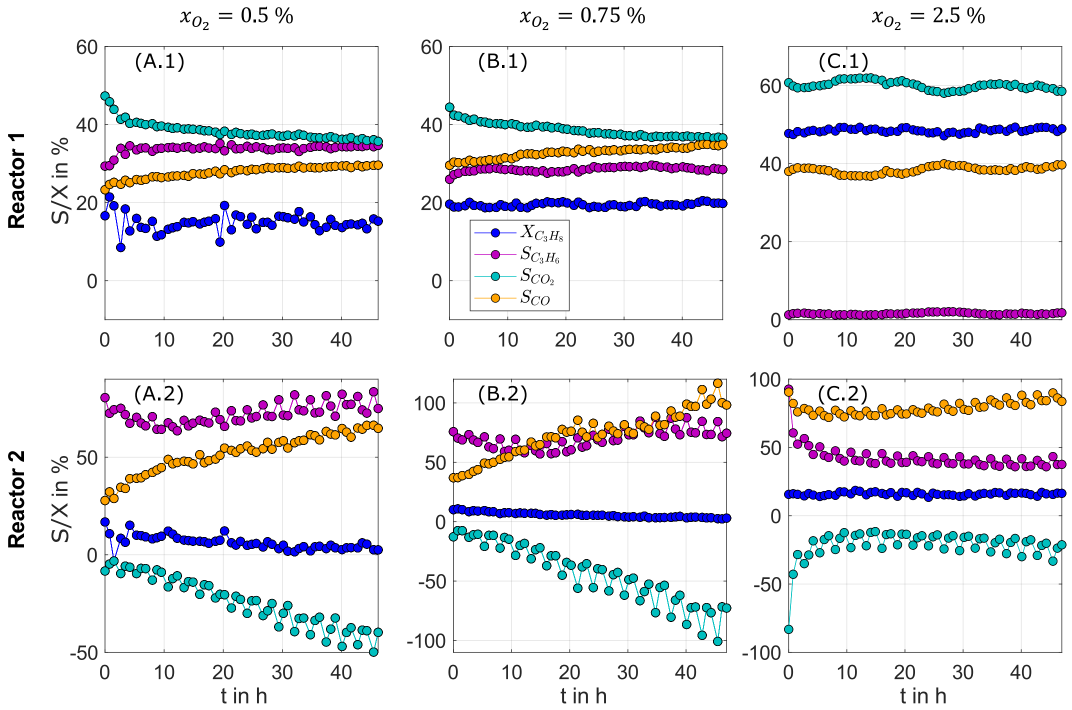

Figure C.8: Selectivities and conversion of the separate reactors in a FBR cascade at different oxygen inlet concentrations (0.5 %, 0.75 % and 2.5 %) for Reactor 1 (A.1 - C.1) and Reactor 2 (A.2 - C.2) ($T_1 = 550\,°\mathrm{C}$, $T_2 = 600\,°\mathrm{C}$, $x_{\mathrm{C_3H_8,in}} = 1\,\%$, $WHSV = 400\,\mathrm{kg\,s\,m^{-3}}$).

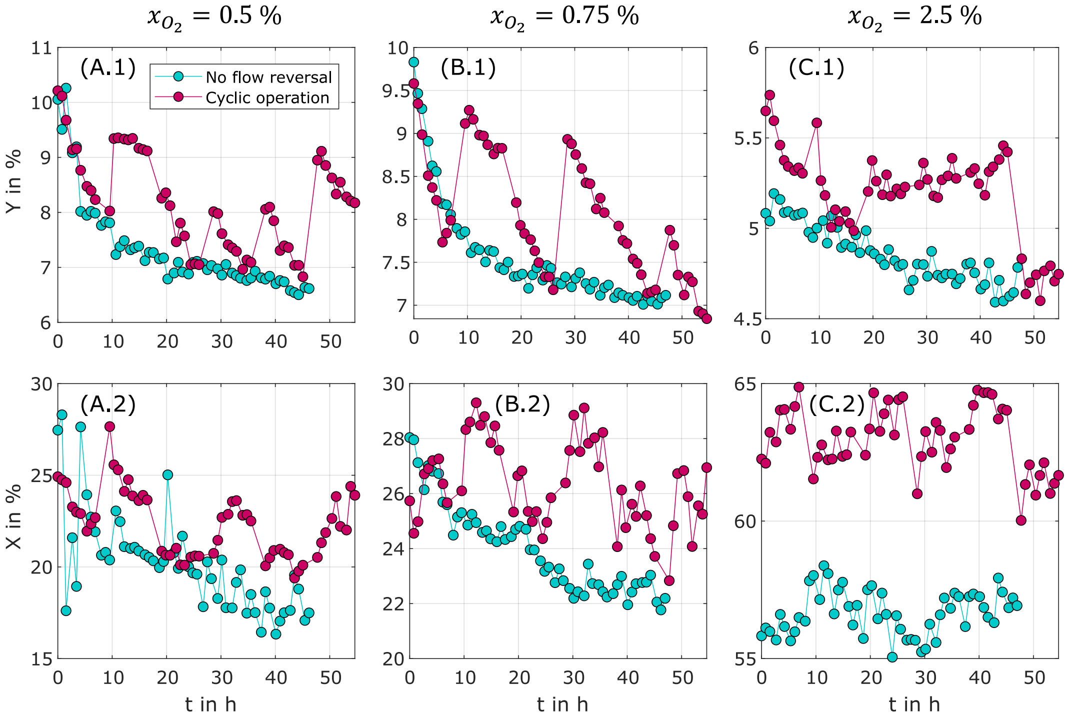

Figure C.9: Yield (A.1 - C.1) and conversion (A.2 - C.2) of the entire FBR cascade at different oxygen inlet concentrations (0.5 %, 0.75 % and 2.5 %) (T_1 = 550 °C, T_2 = 600 °C, $x_{C_3H_8,in} = 1\,\%$, $WHSV = 400\,\mathrm{kg\,s\,m^{-3}}$).

C.3.2 Experiments With Membrane Dosing

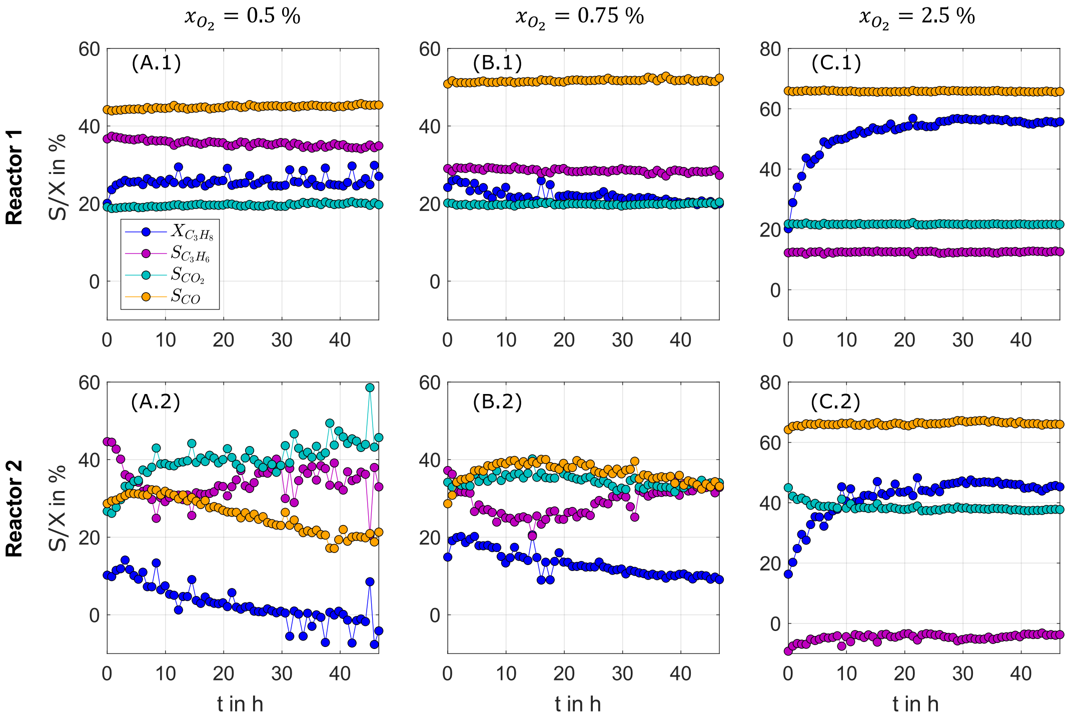

Figure C.10: Selectivities and conversion of the separate reactors in a PBMR cascade at different oxygen inlet concentrations (0.5 %, 0.75 % and 2.5 %) for Reactor 1 (A.1 - C.1) and Reactor 2 (A.2 - C.2) ($T_1 = 575\,°\mathrm{C}$, $T_2 = 625\,°\mathrm{C}$, $x_{\mathrm{C_3H_8,in}} = 1\,\%$, $x_{\mathrm{O_2,in}} = 0.5\,\%$, $WHSV = 400\,\mathrm{kg\,s\,m^{-3}}$).

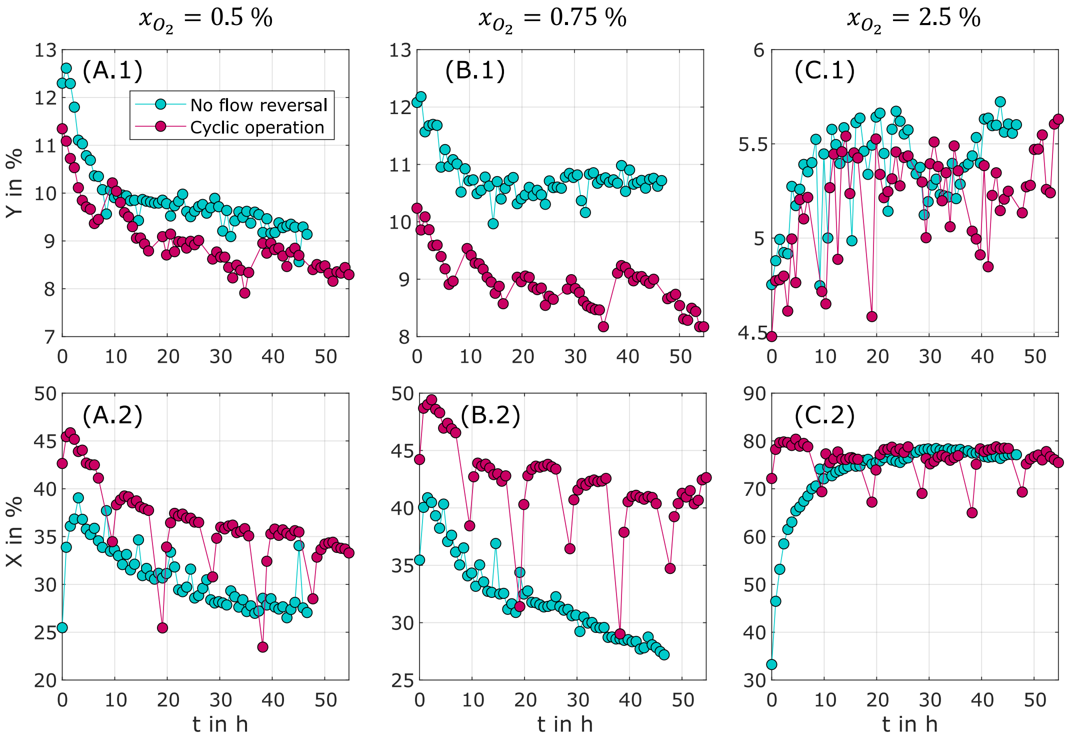

Figure C.11: Yield (A.1 - C.1) and conversion (A.2 - C.2) of the entire PBMR cascade at different oxygen inlet concentrations (0.5 %, 0.75 % and 2.5 %) ($T_1 = 575\,°\mathrm{C}$, $T_2 = 625\,°\mathrm{C}$, $x_{\mathrm{C_3H_8,in}} = 1\,\%$, $WHSV = 400\,\mathrm{kg\,s\,m^{-3}}$).

C.3.3 Experiments With Additional Membrane Dosing of CO_2

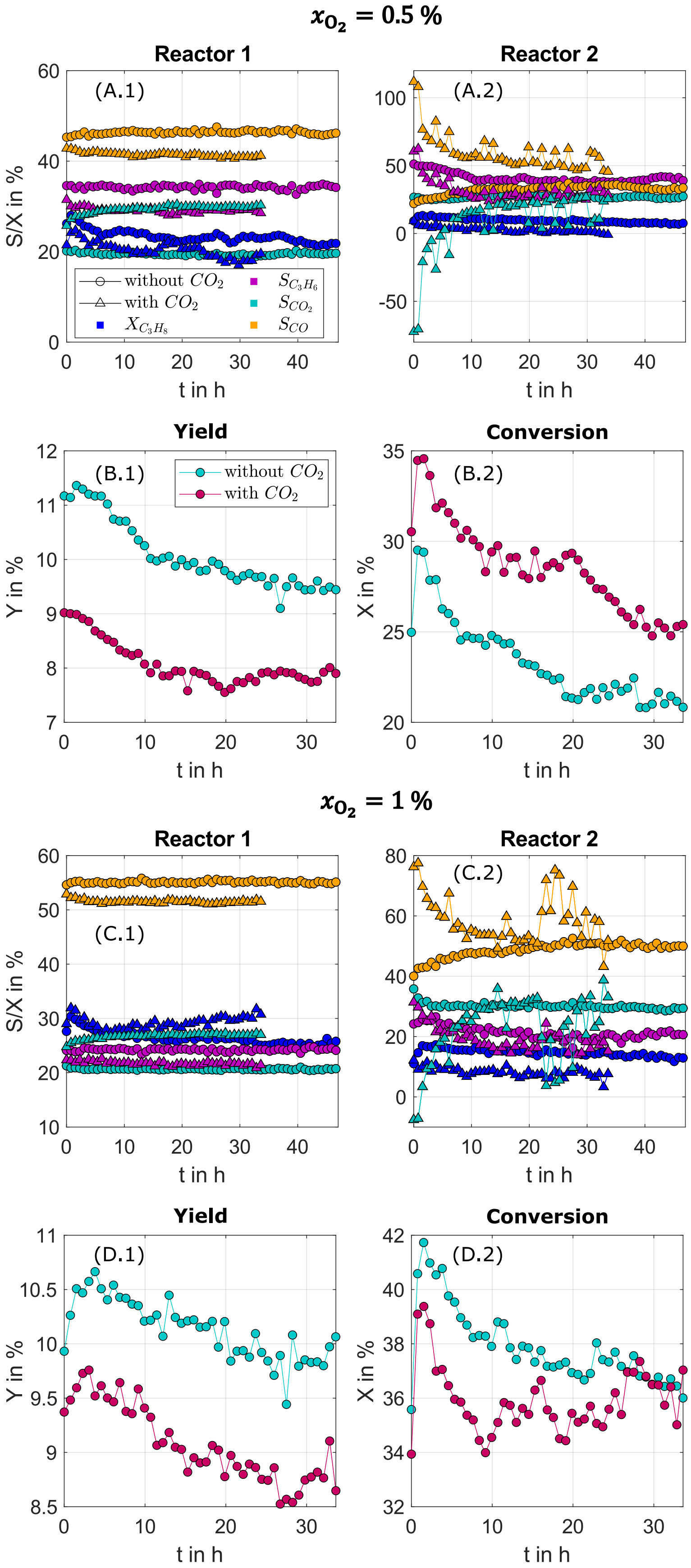

Figure C.12: Comparison of measurements in PBMR cascade operation with and without additional dosing of CO_2 without periodic flow reversal at different oxygen inlet concentrations ($T_1 = 550\,°C$, $T_2 = 600\,°C$, $x_{C_3H_8,in} = 1\,\%$, $x_{CO_2,in} = 2\,\%$).

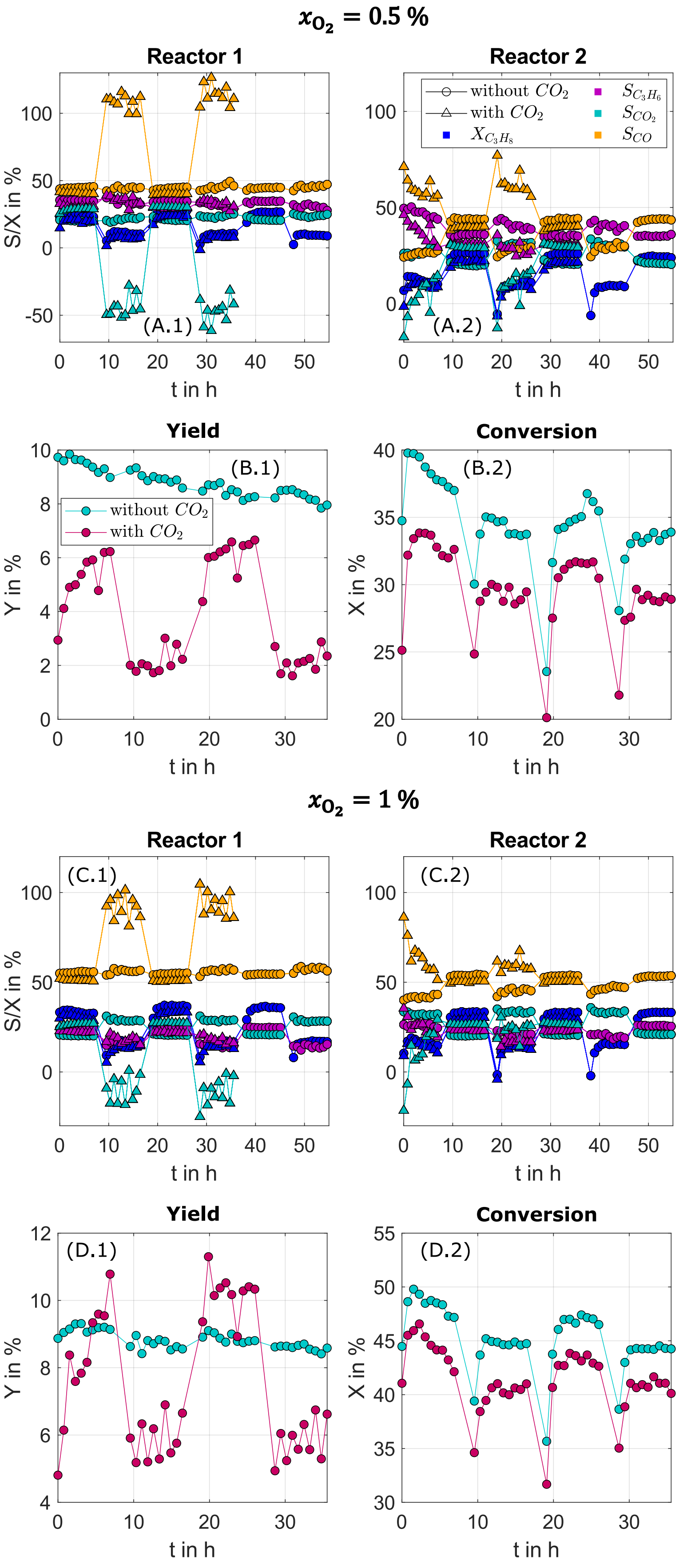

Figure C.13: Comparison of measurements in PBMR cascade operation with and without additional dosing of CO_2 with periodic flow reversal at different oxygen inlet concentrations ($T_1 = 550\,°\mathrm{C}$, $T_2 = 600\,°\mathrm{C}$, $x_{\mathrm{C_3H_8,in}} = 1\,\%$, $x_{\mathrm{CO_2,in}} = 2\,\%$).

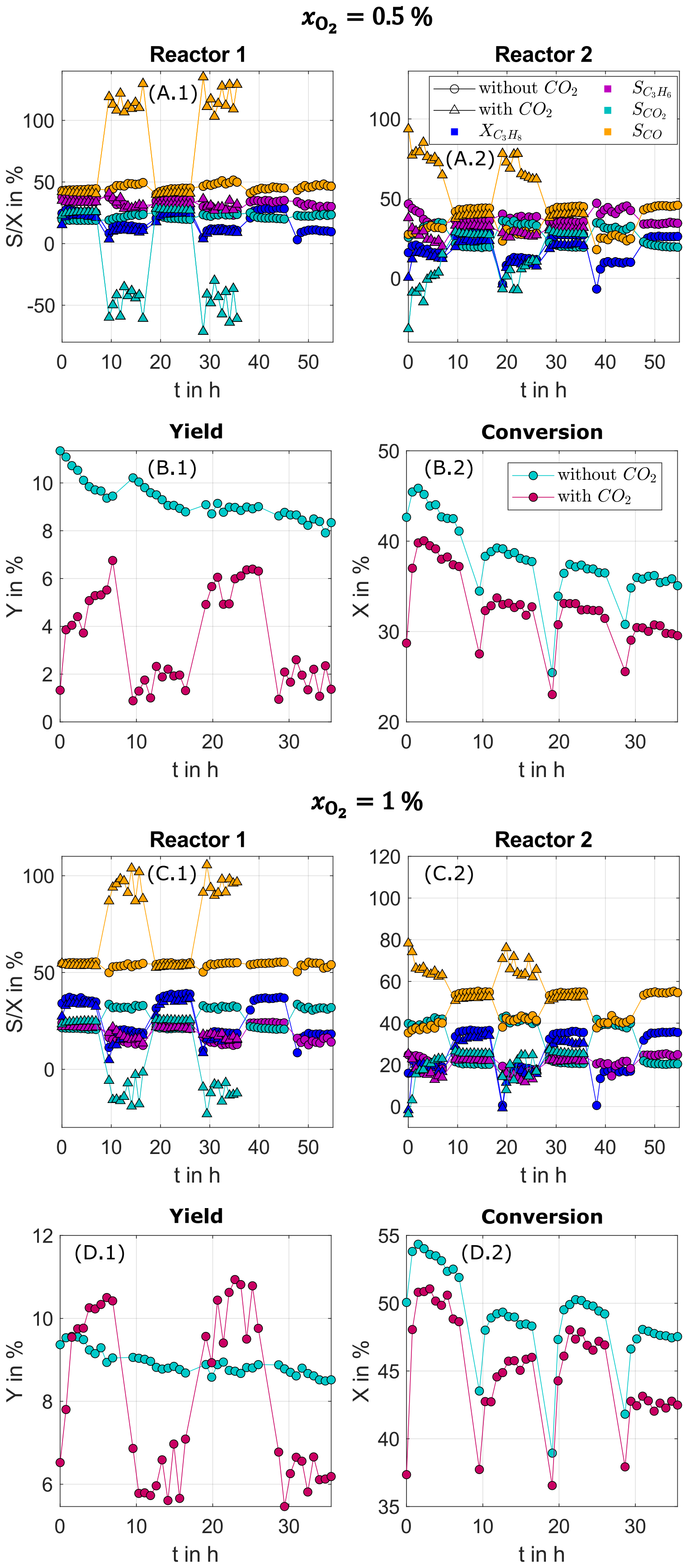

Figure C.14: Comparison of measurements in PBMR cascade operation with and without additional dosing of CO_2 with periodic flow reversal at different oxygen inlet concentrations ($T_1 = 575\,°C$, $T_2 = 625\,°C$, $x_{C_3H_8,in} = 1\,\%$, $x_{CO_2,in} = 2\,\%$).

C.3.4 Comparison of Experiments With and Without Membrane Dosing

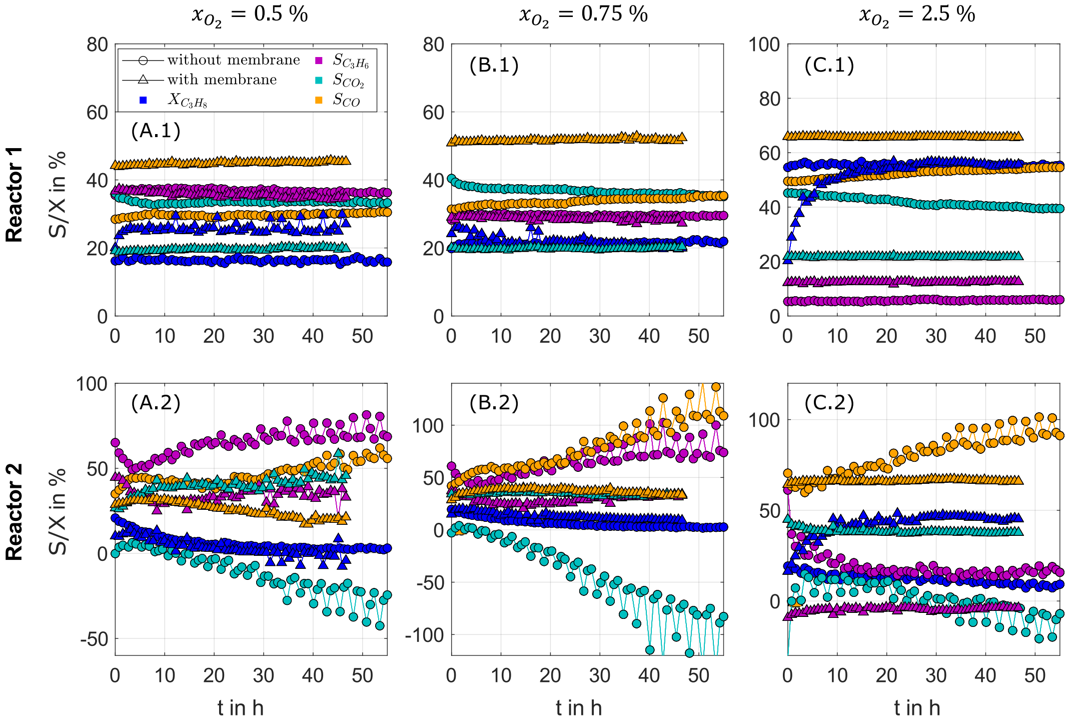

Figure C.15: Selectivities and conversion of the separate reactors in a PBMR cascade (symbol: △) and a FBR cascade (symbol: ◯) at different inlet oxygen concentrations for Reactor 1 (A.1 - C.1) and Reactor 2 (A.2 - C.2) ($T_1 = 575\,°\mathrm{C}$, $T_2 = 625\,°\mathrm{C}$, $x_{\mathrm{C_3H_8,in}} = 1\,\%$, $x_{\mathrm{O_2,in}} = 0.5\,\%$, $WHSV = 400\,\mathrm{kg\,s\,m^{-3}}$).

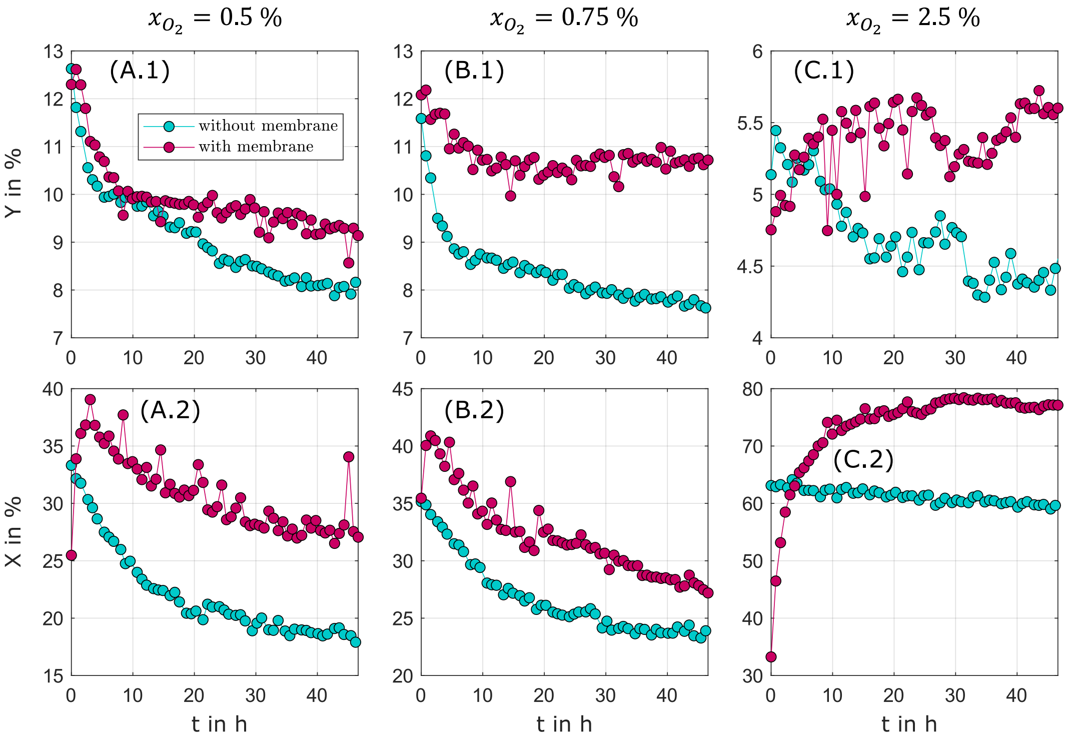

Figure C.16: Yield (A.1 - C.1) and conversion (A.2 - C.2) of the entire reactor cascade in PBMR operation (with membrane) and in FBR operation (without membrane) at different oxygen inlet concentrations (0.5 %, 0.75 % and 2.5 %) ($T_1 = 575\,°C$, $T_2 = 625\,°C$, $x_{C_3H_8,\mathrm{in}} = 1\,\%$, $WHSV = 400\,\mathrm{kg\,s\,m^{-3}}$).

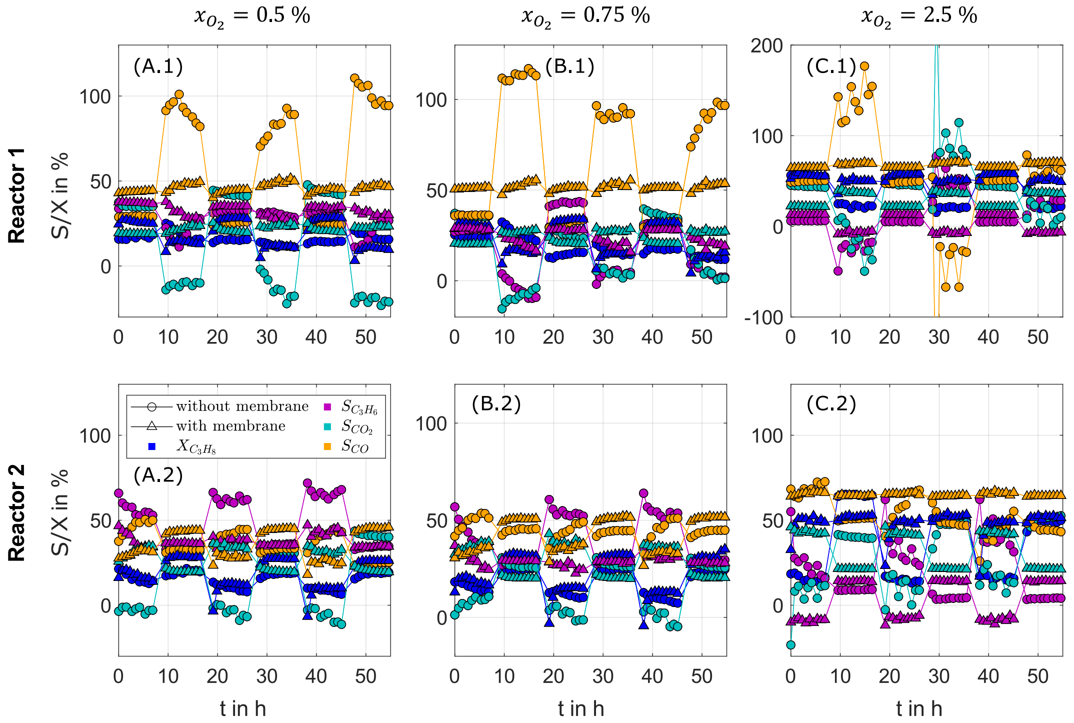

Figure C.17: Selectivities and conversion of the separate reactors in a PBMR cascade (symbol: △) and a FBR cascade (symbol: ◯) at different inlet oxygen concentrations for Reactor 1 (A.1 - C.1) and Reactor 2 (A.2 - C.2) with periodic flow reversal ($T_1 = 575\,°\mathrm{C}$, $T_2 = 625\,°\mathrm{C}$, $x_{\mathrm{C_3H_8,in}} = 1\,\%$, $WHSV = 400\,\mathrm{kg\,s\,m^{-3}}$).

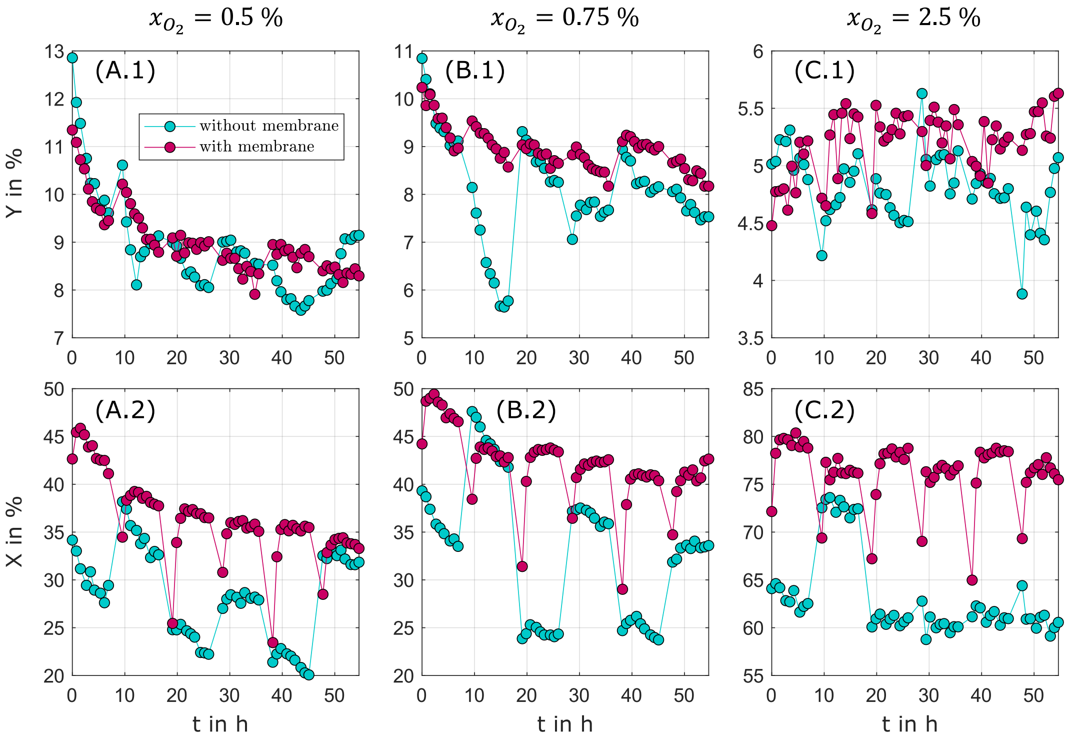

Figure C.18: Yield (A.1 - C.1) and conversion (A.2 - C.2) of the entire reactor cascade in PBMR operation (with membrane) and in FBR operation (without membrane) at different oxygen inlet concentrations (0.5 %, 0.75 % and 2.5 %) with periodic flow reversal ($T_1 = 575\,°\mathrm{C}$, $T_2 = 625\,°\mathrm{C}$, $x_{\mathrm{C_3H_8,in}} = 1\,\%$, $WHSV = 400\,\mathrm{kg\,s\,m^{-3}}$).

C.3.5 Experiments with Integrated Packed Bed Membrane Reactor (PBMRint)

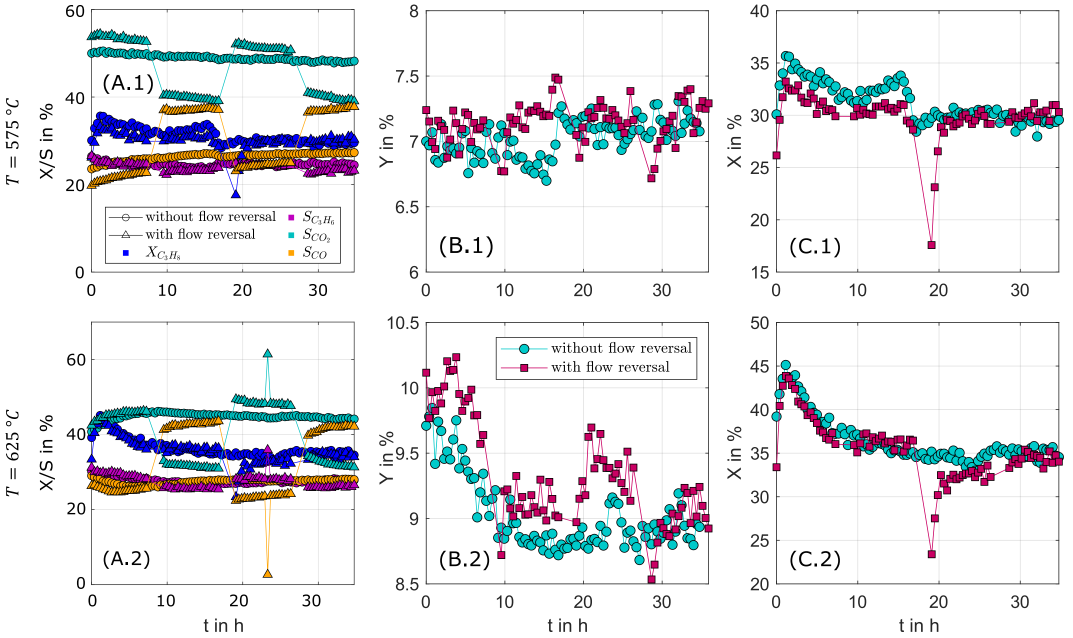

Figure C.19: Selectivities (A.1, A.2) yield (B.1, B.2) and conversion (C.1, C.2) of the PBMRint at different reactor temperatures with and without periodic flow reversal ($x_{\mathrm{C_3H_8,in}} = 1\,\%$, $x_{\mathrm{O_2,in}} = 0.5\,\%$, $WHSV = 400\,\mathrm{kg\,s\,m^{-3}}$).

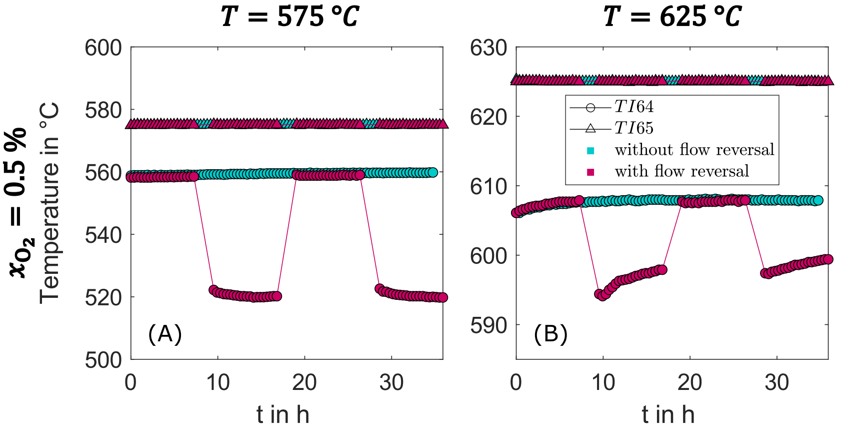

Figure C.20: Temperature of the catalyst bed in the annular gap (TI65, symbol: △) and the inner tube (TI64, symbol ◯) over time during PBMRint measurements with and without flow reversal at set point temperatures of 575 °C and 625 °C and an inlet oxygen concentration of 0.5 % ($x_{\mathrm{C_3H_8,in}} = 1\,\%$, $WHSV = 400\,\mathrm{kg\,s\,m^{-3}}$).

D Appendix to Chapter 6

D.1 Pd-Ag Membrane Characterization

The results of the measurements to characterize the Ag-Pd membrane are illustrated in Fig. D.1 A.

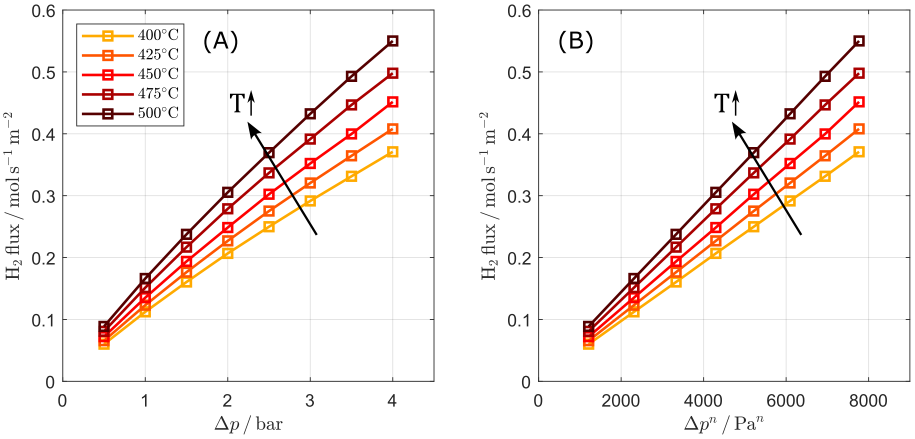

Figure D.1: Results of the membrane characterization experiments and parameter estimation: (A) H_2 flux for different temperatures T and pressure differences Δp; (B) Linearized dependency between Δp^n and H_2 flux according to Siewerts law.

As known from Siewert's law, the dependency between the pressure difference and flux is not linear but can be linearized with an optimized exponent n. This optimized exponent can be numerically estimated by minimizing the objective function

$$OF = \min_{n} \bar{r}_{\mathrm{xy}} = \frac{1}{N_{\mathrm{exp}}} \sum_{i=1}^{N_{\mathrm{exp}}} r_{\mathrm{xy},i} \tag{D.1}$$

where $\bar{r}_{\mathrm{xy}}$ denotes the Pearson correlation coefficient

$$r_{\mathrm{xy},i} = \frac{\sum_{j}^{N_{\mathrm{point},i}} (x_j - \bar{x})(y_j - \bar{y})}{\sqrt{\sum_{j}^{N_{\mathrm{point},i}} (x_j - \bar{x})^2 \sum_{j}^{N_{\mathrm{point},i}} (y_j - \bar{y})^2}} \tag{D.2}$$

with

$$x = \Delta p^n = p^n_{\mathrm{H_2,ret}} - p^n_{\mathrm{H_2,perm}}, \qquad \bar{x} = \frac{1}{N_{\mathrm{point}}} \sum_j^{N_{\mathrm{point}}} x_j \tag{D.3}$$

$$y = J_{\mathrm{H_2}}, \qquad \bar{y} = \frac{1}{N_{\mathrm{point}}} \sum_j^{N_{\mathrm{point}}} y_j \tag{D.4}$$

The Pearson coefficient is a measure of the linear correlation between the values and lies in an interval between -1 (complete negative linear correlation) and +1 (complete positive linear correlation). Based on the slope of the graph, a positive value is expected. These properties of the correlation coefficient make the value of the objective function suitable for assessing the quality of the model. The parameter estimation has been performed in Microsoft Excel by using the Solver[1] add-on that utilizes a modified GRG2 solver (Lasdon and Waren 1981). Activation energy and pre-exponential factor have been estimated afterwards by linearizing the the Arrhenius equation and performing a linear regression.

D.2 Results of Reaction Tests With Pd-Ag Membrane

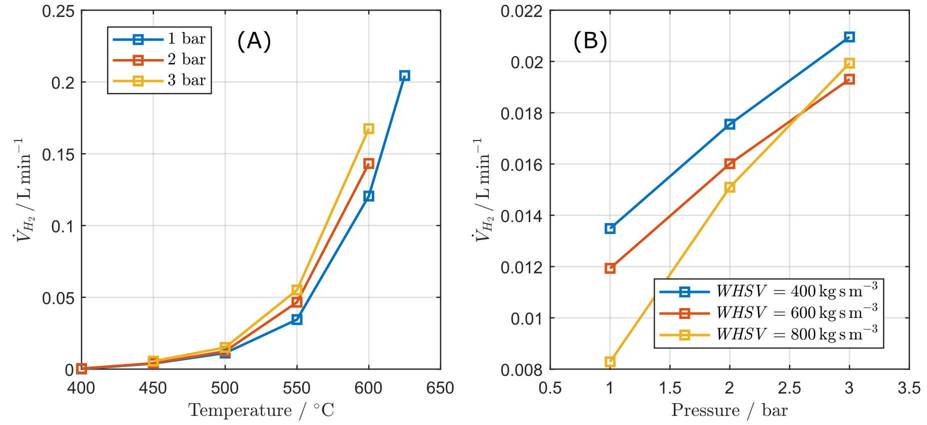

Figure D.2: Hydrogen flow at reactor outlet without membrane utilization at (A) varying pressure and temperature ($WHSV = 400\,\mathrm{kg\,s\,m^{-3}}$, $x_{\mathrm{C_3H_8,in}} = 11\,\%$) and (B) varying $WHSV$ and pressure ($x_{\mathrm{C_3H_8,in}} = 20\,\%$, $T = 500\,°\mathrm{C}$).

---

[1] https://www.solver.com/excel-solver-algorithms-and-methods-used